Final Steps Towards Production of the ITk Pixel Detector for the ATLAS High Luminosity Upgrade

Dissertation

for the award of the degree
"Doctor of Philosophy" (Ph.D.)
Division of Mathematics and Natural Sciences
of the Georg-August-Universität Göttingen

within the Physics doctoral programme
of the Georg-August University School of Science (GAUSS)

CERN-THESIS-2024-378
13/05/2024

submitted by

Yusong Tian

from Hebei, China

Göttingen, 2024

Thesis Committee:

Prof. Dr. Arnulf Quadt
II. Physikalisches Institut, Georg-August-Universität Göttingen

Prof. Dr. Ariane Frey
II. Physikalisches Institut, Georg-August-Universität Göttingen

Priv.-Doz. Dr. Markus Keil
CERN

Members of the Examination Board:

Reviewer:	Prof. Dr. Arnulf Quadt II. Physikalisches Institut, Georg-August-Universität Göttingen
Second Reviewer:	Priv.-Doz. Dr. Markus Keil CERN

Further members of the Examination Board:

Prof. Dr. Ansgar Reiners
Institut für Astrophysik, Georg-August-Universität Göttingen

Prof. Dr. Angela Rizzi
IV. Physikalisches Institut, Georg-August-Universität Göttingen

Prof. Dr. Steffen Schumann
Institut für Theoretische Physik, Georg-August-Universität Göttingen

Prof. Dr. Thomas Weitz
I. Physikalisches Institut, Georg-August-Universität Göttingen

Date of the oral examination: 13.5.2024

Reference: II.Physik-UniGö-Diss-2024/02

Final Steps Towards Production of the ITk Pixel Detector for the ATLAS High Luminosity Upgrade

Abstract

The Large Hadron Collider (LHC) upgrade to the High-Luminosity LHC (HL-LHC) will bring an unprecedentedly challenging environment to the detectors, with an instantaneous luminosity of $5 \times 10^{34}\,\mathrm{cm}^{-2}\mathrm{s}^{-1}$, which corresponds to approximately 140 inelastic proton-proton collisions per bunch crossing. Therefore, in the ATLAS detector upgrade for the HL-LHC, the current Inner Detector will be replaced with an all-silicon Inner Tracker (ITk), to operate under the higher occupancy and radiation damage.

The ITk pixel detector is the innermost part of the ITk. It will be equipped with pixel modules consisting of pixel sensors and front-end chips implemented in 65 nm CMOS technology. The ITk project is currently in the pre-production stage.

To ensure that the quality of the production components will meet the ITk specifications, practise the production workflow, and provide modules for larger scale tests, various steps are exercised in the module pre-production process. Sensors and test structures from different vendors were sent to ITk collaborating institutes for quality assurance (QA), irradiation, and follow-up testing. Test-beam campaigns were conducted to evaluate the performance of sensors in fully-assembled modules in particle beam. To guarantee smooth and uniform production of modules, all ITk institutes are required to demonstrate their ability of fulfilling their responsibilities by going through a Site Qualification. For module assembly, the ITk Pixel Quad Assembly Tooling V2 was developed, reviewed and produced. Module production involves module assembly, parylene coating for high voltage protection, mechanical wire-bond protection, as well as full electrical quality control (QC) tests.

This thesis presents the characterisation of the pre-production planar sensors for the ITk pixel detector. The results are within specifications, except for the leakage current stability from one vendor. In test-beam studies, hit detection efficiency of un-irradiated planar sensors in quad modules was measured. The Site Qualification procedure and requirements are introduced. For module assembly, the performance of the tooling was demonstrated, and 16 modules were assembled. QC tests were performed on three assembled modules. In addition to the work related to the ITk pixel detector, a small project on flavour tagging within the scope of this thesis is introduced.

Finale Schritte zur Produktion des ITk Pixeldetektors für das ATLAS High Luminosity Upgrade

Zusammenfassung

Das Large Hadron Collider (LHC) Upgrade zum High-Luminosity LHC (HL-LHC) wird in einer beispiellos anspruchsvollen Umgebung für die Detektoren resultieren, mit einer instantanen Luminosität von $5 \times 10^{34}\,\mathrm{cm}^{-2}\mathrm{s}^{-1}$, was etwa 140 unelastischen Proton-Proton-Kollisionen pro Bündelkreuzung entspricht. Dafür wird im ATLAS-Detektor-Upgrade für den HL-LHC der derzeitige Innere Detektor mit einem Inner Tracker, der nur aus Silizium besteht, ersetzt, um der höheren Auslastung und höheren Strahlenschäden standzuhalten.

Der ITk Pixeldetektor ist die innerste Schicht des ITk. Er wird mit Pixelmodulen bestückt sein, die aus Pixelsensoren und Auslesechips bestehen, die in 65 nm CMOS-Technologie implementiert sind. Das ITk-Projekt ist derzeit in der Vorproduktionsphase.

Um sicherzustellen, dass die Qualität der Detektorkomponenten für die finale Modulproduktion den ITk-Spezifikationen entspricht, den Produktionsablauf zu üben und Module für Tests in größerem Maßstab zu produzieren, werden verschiedene Schritte im Vorproduktionsprozess ausgeübt. Sensoren und Teststrukturen wurden von verschiedenen Herstellern zu kollaborierenden Instituten geschickt, um dort Qualitätssicherung, Bestrahlung und Qualitätskontrolle sowie Folgetests durchzuführen. Teststrahl-Kampagnen wurden außerdem durchgeführt, um die Performance von Sensoren in vollständig zusammengebauten Modulen im Teilchenstrahl zu testen. Um die reibungslose und gleichmäßige Produktion der Module zu gewährleisten, sind alle ITk-Institute verpflichtet, ihre Fähigkeit zur Erfüllung ihrer Verantwortungen durch eine Standortqualifizierung nachzuweisen. Für den Modulbau wurde das Werkzeug ITk Pixel Quad Assembly Tooling V2 entwickelt, geprüft und produziert. Modulproduktion beinhaltet den eigentlichen Modulbau, Parylene-Beschichtung für Hochspannungsschutz, mechanischen Drahtbondschutz und vollständige elektrische Qualitätskontrolltests (QC).

Diese Dissertation beschreibt die Charakterisierung der planaren Sensoren der Vorproduktion für den ITk Pixeldetektor. Die Testergebnisse sind innerhalb der Spezifikationen, mit Ausnahme der Leckstromstabilität eines Herstellers. Im Teststrahl wurde die Trefferdetektionseffizienz von unbestrahlten planaren Sensoren in Quad-Modulen gemessen. Der Ablauf und die Anforderungen der Standortqualifizierung werden ebenfalls vorgestellt. Für den Modulbau wurde die Funktionsfähigkeit des Werkzeugs nachgewiesen und 16 Module zusammengebaut. QC-Tests wurden an drei zusammengebauten Modulen durchgeführt. Zusätzlich zu den Arbeiten für den ITk Pixeldetektor wird ein kleines Projekt zum Flavour Tagging im Rahmen dieser Dissertation vorgestellt.

道可道，非常道。名可名，非常名。

——李耳（春秋）

Dao[1] *can be spoken of, but what was spoken of is not Dao itself. The meaning or logic of Dao can be named or expressed, but what was expressed is not the logic of Dao itself.*

— Li Er (∼4th century BC)

I would like to know about intelligent aliens one day.

— Me (now)

[1]The word “Dao” represents the world and all the fundamental functioning mechanisms of the world[2].
[2]This is also not an 100 % accurate definition, as expressed by the saying itself.

Contents

Contributions by the author xiii

1. Introduction 1

2. The Standard Model and Beyond 3
   - 2.1. The Standard Model 3
   - 2.2. Physics Beyond 5

3. ATLAS Detector and the HL-LHC Upgrade 11
   - 3.1. CERN and the LHC 11
   - 3.2. The HL-LHC Upgrade 16
   - 3.3. The ATLAS Detector 18
   - 3.4. The ATLAS Phase-II Upgrade 27

4. Particle Physics Detectors 31
   - 4.1. Interactions of Particles with Matter 31
   - 4.2. Pixel Detectors 37
   - 4.3. ITk Pixel Modules 52

5. Tracking and Flavour Tagging 57
   - 5.1. Between Collision and Tracker 58
   - 5.2. Tracking 59
   - 5.3. Vertexing 61
   - 5.4. Jet Definition 61
   - 5.5. Flavour Tagging 65

6. Planar Sensor Testing 75
6.1. Pre-production Sensor Quality Assurance 75
6.2. Test-beam 97
7. Site Qualification 113
7.1. Site Qualification Overview 113
7.2. Lab Infrastructure 117
7.3. Database 121
7.4. Coating and Wire-bond Protection 124
8. Quad Module Assembly 129
8.1. Module Assembly Goal 129
8.2. ITk Pixel Quad Assembly Tooling V2 134
8.3. Tooling V2 Gluing Procedure and Calibration 138
8.4. Tooling V2 Review and Performance 144
8.5. Assembly Site Qualification 156
8.6. Results for Site Qualification and Pre-production Module Assembly 164
8.7. Conclusions and Outlook 174
9. Module Testing 177
9.1. Module Quality Control Tests 178
9.2. Tests and Scans 180
9.3. Testing Setup 189
9.4. Results 197
9.5. Conclusions and Outlook 209
10. Conclusions and Outlook 211
10.1. Sensor 211
10.2. Assembly 213
10.3. Module QC 213
Bibliography 215
Acknowledgements 227
A. Additional Figures for Sensor Characterisation 229
A.1. Photo of Micron test structures 229
A.2. *IV* from probing different pads of the same diode 230

A.3. *CV* of unirradiated Micron quad sensors 230

B. Additional Figures for Assembly 231

B.1. Different flexes: un-populated or by a different vendor 231

B.2. Brass flex dummy and Si bare module dummy 232

B.3. Si dummy Visual Inspection 232

B.4. *CV* of quad bare modules 232

C. Additional Figures for Module Quality Control 233

C.1. ADC Calibration 233

C.2. Analog Readback 235

C.3. SLDO Qualification 237

C.4. Vcal Calibration 240

C.5. Injection Capacitance 241

C.6. Data Transmission 242

C.7. Minimum Health Test 242

Contributions by the author

The work presented in this thesis was carried out in the ATLAS experiment. As one of the largest high energy physics experiments, the ATLAS Collaboration includes about 6000 members, and 3000 scientific authors. An ATLAS member enters the author list by completing a qualification task. Various work was done to build and operate the detector, and produce physics results. The ITk pixel detector alone involves largely collaborative work. Here I highlight the contributions from various collaborators and myself. My work was conducted in the working group of my supervisor: Prof. Dr. Arnulf Quadt, who is also the local ITk project leader.

For sensor pre-production quality assurance, many ITk sites and persons were involved, including every author in the publication referenced in [1]. Their contributions are included in the results presented in this thesis. My own contributions include testing unirradiated HPK[1] test structures, as well as both irradiated and unirradiated Micron[2] sensors.

Successful test-beam campaigns cannot be done without the effort of the entire team. Since July 2021, I have participated in test-beam campaigns, contributing to the testing setup and data-taking shifts. I also performed reconstruction and analysis of test-beam data. For the results included in this thesis, the alignment was done in common effort with Christopher Krause (PhD thesis to be published), and the relevant functionality in the analysis software was implemented by Dr. Šejla Hadžić [2].

The assembly tooling was designed, manufactured, and calibrated by local mechanics technicians working in the ITk project. I was involved in the testing and the analysis of results. For module assembly, I was part of the team performing reception tests and assembling modules. The full team involved in the tooling and assembly includes: Sascha Böhlken, PD Dr. Jörn Große-Knetter, Tim Kanngießer, Janek Kluge, Niklas Grün, Prof. Dr. Arnulf Quadt, Uwe Ronsöhr, Yusong Tian, Rüdiger Widera, and Dr. Hua Ye. The manufacturing also involved the Göttingen central workshop, chemistry workshop, as well as the workshops in Wuppertal and Bern.

[1] Hamamatsu Photonics K.K.
[2] Micron Semiconductor Ltd.

For the assembly site qualification, I was involved in writing of the site qualification document block 6.7 (bare module leakage current vs voltage measurements), and I was part of the reviewing team for blocks 6.5, 6.6, and 6.7 (reception tests of bare modules). 12 out of 14 assembly sites were reviewed by me. This work was carried out together with Dr. Francesco Crescioli and Dr. Dimitris Varouchas.

Module electrical testing heavily relied on our BSc & SHK[3] intern Niklas Grün and SHK & MSc intern Ruben Förster for performing tests and parallelising the testing setup (BSc and MSc theses to be published), PD Dr. Jörn Große-Knetter, Dr. Hua Ye, and Dr. Silke Möbius [3] for developing the setup, and Orcel Thys-Dingou for developing the hardware interlock. I was involved in conducting tests and supervising students.

[3]SHK: Studentische Hilfskraft (Student Assistant).

CHAPTER 1

Introduction

Curiosity is one of the fundamental human traits. We constantly wonder why things happen as they do, and therefore turn to the study of physics. One of the most asked questions is recursive: "What are things made of?", "And what are the things that make up things made of?", etc. This drove human towards particle physics. From the contemplations of ancient philosophers – if one keeps halving things, whether there is a point to which they cannot be halved anymore[1] – to the atomic theory in the 18th to 19th century, the discovery of the first elementary particle in the Standard Model (the electron) in 1897 [4], the black body radiation that opened the door to quantum physics in 1901 [5], the formulation of the Standard Model (SM) [6–17] with quantum field theory, and the physics beyond the SM that physicists are still contemplating, particle physics has come a long way.

The research and development of particle detectors have made it possible for humans to conduct experimental particle physics research. Nowadays, accelerators and collider experiments studying particles at high energies are at the centre of the stage. One of the biggest laboratories in the field is CERN – the European Organization for Nuclear Research. Founded in 1954 and located in Geneva at the Swiss-French border, CERN is part of the ongoing effort to satisfy scientific curiosity and provide scientific understandings and technologies that benefit the earth along the way.

The Large Hadron Collider (LHC) at CERN, together with the four biggest experiments: ATLAS [18], CMS [19], LHCb [20], and ALICE [21], has been providing data for fundamental particle physics research since 2010. Not long after the start of data-taking and analysis, in 2012, ATLAS and CMS discovered a Higgs-like particle [22, 23], thereby completing the discovery of all the fundamental particle in the SM. Various physics analyses have discovered particles, their production and decay channels, and provided precise measurements of their

[1] 一尺之棰，日取其半，万世不竭。——《庄子 · 杂篇 · 天下》(Zhuang Zi)

properties. However, some of the analyses are limited by statistics and could therefore benefit from more data provided by a higher luminosity.

Studies [24–28] show that higher luminosity would enable access to Higgs pair production and rare decays. These studies can help determine the Higgs potential and investigate the Yukawa coupling. In general, more statistics allow analyses to achieve higher precision on measurements and explore physics beyond the SM (BSM), e.g. through B-physics or top physics. For instance, the top quark, as the heaviest elementary particle in the SM, is of particular interest. Studies are being done on its mass, production cross section, branching fractions of decays, searches for rare decays or production processes, and properties of its decay products, such as the polarisation and helicity of the W boson. Precision measurements can be tested for the agreement with SM prediction, potentially revealing BSM physics. The high mass also implies a strong Yukawa coupling between the top and the Higgs field, making the top-Higgs interaction especially interesting.

To provide more collisions, therefore allowing more in-depth studies and unveiling more mysteries, the LHC will be upgraded to the High Luminosity LHC (HL-LHC) from 2026 to 2030, extending the nominal luminosity from 1 to $5 \times 10^{34}\,\mathrm{cm}^{-2}\mathrm{s}^{-1}$, corresponding to an average of approximately 140 inelastic pp collisions per bunch crossing[2] [29]. This will benefit various physics analyses where the statistics is the main limitation.

However, higher luminosity brings increased occupancy and radiation damage. To deal with this challenge, the ATLAS detector is going to be upgraded. During this upgrade, the Inner Detector (ID) will be replaced with an all-silicon **I**nner **Trac**k**k**er (ITk). The ITk consists of a pixel and a strip detector. The pixel detector is the innermost layer of the ATLAS detector, which means it is the closest to the collision point and therefore faces the most challenging radiation-intensive environment[3]. It comprises modules that contains silicon sensors and 65 nm CMOS front-end chips, applying technologies that are both advanced and reliable. At the time of writing this thesis, the pixel detector upgrade is in the pre-production phase. Various studies were conducted to ensure smooth production.

This thesis first introduces the physics background – the SM and some physics beyond the SM topics – in chapter 2, then zooms into the experimental side, providing a detailed introduction to CERN, the HL-LHC ,and the ATLAS upgrade in chapter 3. A general introduction to pixel detectors, their components, functioning principle, and technologies is provided in chapter 4. The crucial role that the pixel detector plays in b-tagging, as well as the basics of flavour tagging, is described in chapter 5.

For the ITk pixel detector, sensors were tested in the lab and in testbeams (chapter 6). A tooling was developed for the assembly of sensor and front-end chip hybrids with printed circuit boards (chapter 8). Quality control tests were conducted to test the quality of the modules (chapter 9). A Site Qualification procedure was developed to qualify more than ten assembly sites and a similar number of testing sites for their respective tasks in production (chapter 7). Chapter 10 presents a summary of the conclusions and outlook.

[2] The bunch crossings are 25 ns apart.

[3] The particle fluence in the innermost layers of the detector is expected to be up to $2 \times 10^{16}\,\mathrm{n_{eq}/cm^2}$.

CHAPTER 2

The Standard Model and Beyond

The research, development and building of accelerators and detectors aims at acquiring data to investigate the most fundamental constituents of everything in the universe. In particle physics, the Standard Model (SM) is so far the best and most complete theory. It has succeeded in explaining numerous phenomena, backed up by experimental results. However, it does not explain everything that was observed. Various theories beyond the SM are postulated and investigated. This chapter introduces the SM and some examples of physics beyond the SM, both of which could benefit from the High Luminosity LHC and detector upgrades.

2.1. The Standard Model

The SM particles, their basic properties, and the fundamental interactions that they are subject to are illustrated in figure 2.1.

The leptons and quarks have half-integer spin and are collectively referred to as fermions. There are three generations of fermions. Scientists ordered the generations by mass, which is aligned with the order of discovery: as experiments reach higher energies, the possibility of observing heavier particles is unlocked. Fermions are also divided into two groups by the third component of the weak isospin vector I_3: neutrinos and up-type quarks have $I_3 = +\frac{1}{2}$, while electrically charged leptons and down-type quarks have $I_3 = -\frac{1}{2}$. For each type of fermion, there is a corresponding type of antifermion with opposite-signed quantum numbers, including but not limited to charges such as electric charge and colour charge. For example, in the SM, neutrinos are electrically neutral and colourless, but the antineutrinos have the opposite lepton number, weak isospin, and flavour. Neutrinos are

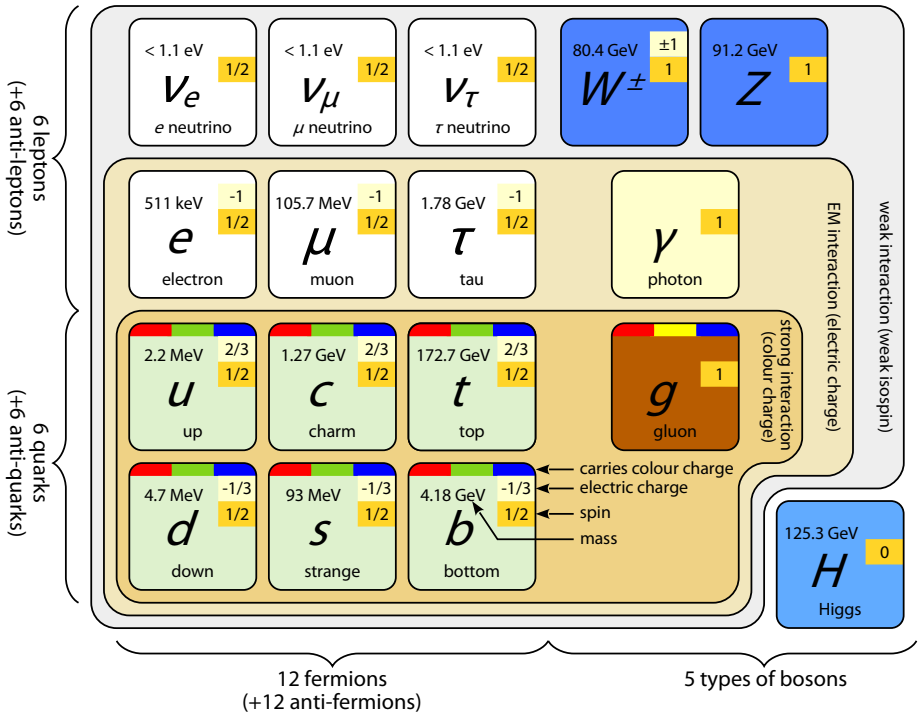

Figure 2.1: The Standard Model (SM) particles, including the interactions that they experience, the corresponding gauge (vector) bosons, and the Higgs – a scalar boson. The basic properties of the particles are marked: mass, electric charge, spin, and whether they have colour charges [30].

exclusively left-handed in chirality[1], while antineutrinos are exclusively right-handed.

In the SM, the forces arise from particles coupling to (interacting with) the force-carriers – gauge bosons. Bosons are a type of particle with integer spin, as opposed to fermions, which have half-integer spin. It is widely believed that there are four fundamental forces, as listed below, but only three of them are explained by the SM.

- Electromagnetic (EM) interaction: it is described by quantum electrodynamics (QED), and its force carrier is the photon, which couples to all charged particles.
- Strong interaction: quantum chromodynamics (QCD), mediated by the gluon. All quarks and the gluon have colour charges and undergo the strong interaction.
- Weak interaction: quantum flavour dynamics (QFD), propagated through the massive W^+, W^-, and Z. All SM particles are subject to the weak interaction. Charged leptons couple only to their corresponding flavours of neutrinos. The gauge coupling strengths of the strong, weak, and EM interactions are $g_s \approx 1$, $g \approx \frac{2}{3}$, and $g' \approx \frac{2}{3\sqrt{3}}$, respectively [31], at the scale of the Z boson mass, and run closer as the energy scale increases. The

[1]Chirality is an intrinsic property of a particle's wave function and is Lorentz invariant (independent of the inertial frame of reference). Another parameter that is described by a handedness is helicity, which is the projection of spin onto the direction of motion. If the helicity is positive (when the projection is in the same direction as the direction of motion), the particle is right-handed in helicity. For massless particles, chirality and helicity becomes the same.

electroweak unification [6–8] unified the weak and the EM interactions.
- Gravity: despite being the first fundamental force explained by physics – in 1687 by Newton, gravity is NOT in the SM.

In gauge theory, the SM of particle physics describes the strong, weak, and EM interactions based on the $SU(3) \times SU(2) \times U(1)$ symmetry group, where $SU(3)$ is the gauge group for QCD, $SU(2)$ is for QFD, and $U(1)$ is for QED. Other gauge interactions can be added to this model, making it more complete. This is done by many theoretical extensions of the SM, such as SUSY and string theory.

The Higgs boson is a scalar field. Unlike the gauge bosons (which are vector fields), instead of carrying force, the Higgs field gives rise to particle masses. Particles acquires masses when they couple to the Higgs field via the Higgs mechanism, also called the Brout-Englert-Higgs mechanism [32–35]. The SM Lagrangian is the mathematical description of the interactions. The Higgs mechanism adds terms to the SM Lagrangian that breaks the electroweak gauge symmetry (spontaneous symmetry breaking) and thereby making particle masses possible. The Higgs boson is the latest addition to the SM: it was one of the main motivations for the LHC, and indeed, in 2012 – only two years after the start of data-taking – a Higgs-like particle was discovered [22, 23]. After the discovery, Higgs and Englert were awarded the 2013 Nobel Prize in Physics[2].

An introduction to a complete mathematical description of the SM Lagrangian is beyond the scope of this thesis. For further information please refer to, for example, a quantum field theory textbook. Readers of general interest could turn to the science education paper referenced in [36] over a cup of tea or coffee.

2.2. Physics Beyond

The SM is an extremely useful model that successfully explains numerous observed phenomena. However, this model has its limitations. Gravity and neutrino masses are not yet formulated and added mathematically into the SM Lagrangian, and are therefore not included in the SM. Human also to this day do not know the true colour of dark matter and dark energy, as well as numerous other mysteries in the universe. Here a few such unanswered questions, and various theories and experiments that attempt to answer them.

2.2.1. Antimatter and CP Violation

The matter-antimatter asymmetry in the observable universe is one of the biggest questions that remains to be understood. Therefore, CP violation has been an important research topic. Our universe is dominated by matter. In 1967, Sakharov proposed 3 conditions for this to happen [37]: baryon number[3] violation, C and CP violation, and the previous two conditions having happened before the universe reaches thermal equilibrium.

[2] Brout had unfortunately passed away before the discovery.
[3] Baryon number is $\frac{1}{3}$ for quarks and $-\frac{1}{3}$ for antiquarks.

Noether's theorem states that continuous symmetry means conservation. But this theorem does not cover discrete symmetries, which include charge (C), parity (P)[4] and time (T) symmetries. In 1956, Lee and Yang found that parity, despite being conserved in EM and strong interactions, may not be conserved in weak interactions, and proposed possible experiments [38]. Wu then designed and conducted an experiment based on the β decay of cobalt-60 [39]: $^{60}\mathrm{Co} \rightarrow ^{60}\mathrm{Ni}^* + \mathrm{e}^- + \bar{\nu}_\mathrm{e}$. She cooled ^{60}Co to 0.01 K to decrease the disturbance from thermal effects, applied a magnetic field to align the atomic spins, and observed the direction of the electron emission with respect to the direction of the B-field. It was found that one direction is favoured over the other, which means parity violation.

This was a big shock, but it was still believed that CP could be an exact symmetry, until CP violation was found in 1964 by an experiment performed on neutral kaons [40]. The flavour states $K^0(d\bar{s})$ and $\overline{K}^0(\bar{d}s)$ of neutral kaons are eigenstates of the strong interaction[5]. Due to kaon mixing, a neutral kaon propagate as a whole system with a linear combination of both K^0 and $\overline{K}^0$. These physical states are the mass eigenstates K_S^0 and K_L^0[6]. They decay via the weak interaction, mainly to two pions, three pions, or semi-leptonically. Consider also the CP eigenstates K_1 and K_2:

$$\begin{aligned} \mathbf{CP}\,|K_1\rangle &= +1\,|K_1\rangle\,, \\ \mathbf{CP}\,|K_2\rangle &= -1\,|K_2\rangle\,. \end{aligned} \tag{2.1}$$

If CP is conserved, K_S^0 and K_L^0 would also be eigenstates of CP, with $|K_S^0\rangle = |K_1\rangle$ and $|K_L^0\rangle = |K_2\rangle$. As the $\pi\pi$ final state is CP-even and the $\pi\pi\pi$ final state is CP-odd[7], if $|K_L^0\rangle$ is the same as the CP eigenstate $|K_2\rangle$ and is therefore with CP -1, when it decays into pions, it must decay into three pions for CP to be conserved. However, decay events of K_L into two pions were observed. The experiment was conducted by bombarding 30 GeV protons on a beryllium (Be) target, using a detector that consists of two spectrometers, and calculating the momentum of each charged particle observed in the decay. For a two-body decay, the angle θ between the vector sum of the momenta and the direction of the K_L^0 beam would be zero. For a three-body decay, the angle would almost always be non-zero due to the missing neutral pion. The result showed an excess of events at $\theta = 0$, showing that CP is violated in the weak interaction[8]. However, the branching fraction is small.

CP violation is expected in the SM from the CKM (Cabibbo-Kobayashi-Maskawa) matrix [41], and three is the minimum number of generations needed for CP violation. In the SM, there are indeed three generations of fermions, but the level of CP violation is not enough to explain the matter-antimatter asymmetry in the universe. This leaves CP violation that deviates from the level of SM prediction yet to be found.

[4] Charge conjugation reverses a particle's charge, parity conjugation reverses the particle's spatial coordinates, and CP symmetry is the symmetry in the product of C and P conjugations.

[5] And the strangeness is conserved.

[6] K-short and K-long. They have well-defined mass and lifetime. The lifetime of K_L^0 is around two orders of magnitude higher than that of K_S^0.

[7] $\mathbf{CP}(\pi^+\pi^-) = \mathbf{CP}(\pi^0\pi^0) = +1$ and $\mathbf{CP}(\pi^+\pi^-\pi^0) = \mathbf{CP}(\pi^0\pi^0\pi^0) = -1$.

[8] Then the only symmetry left is the CPT symmetry, which is still believed to be conserved to this day.

The B-factories have been a popular sector for CP violation studies. The first detection of the time-dependent CP asymmetry was in 2001 in the $B^0 \to J/\psi K^0$ decay by Belle [42] and BaBar [43] experiments. With the HL-LHC bringing more data to the B-factories like the LHCb, physicists hope to find more sources of CP violation.

2.2.2. Dark Matter

Studies of the cosmic microwave background shows that 68.5 % of our universe is dark energy, 26.5 % is dark matter, and the familiar matter we know only accounts for 5.0 % [44]. The origin and interactions of the dark matter and dark energy remains unexplained by the SM, which motivates extending the SM to include a "dark sector". Dark sector (also called hidden sector or uncharged sector) is a collection of particles that are under gravitational interactions, but not the other SM interactions. Or say, the dark sector consists of fields with no SM gauge charges.

The dark sector could explain the existence of the large amount of dark matter and their lack of interactions, origin of neutrino masses, baryon asymmetry, dynamics of galactic structure formation, photon charge radius, etc., and the interaction of the dark sector could possibly produce matter-antimatter asymmetry. The theory of dark sector is also compatible with theories about supersymmetry breaking and mediation, as well as the theory of unifying the SM gauge groups at a high scale. These all motivate studies of the dark sector. For further information please refer to [45, 46].

Collider experiments have been searching for dark sector particles supported by different theories, and putting limits on the phase space (various sets of parameters, the most typical is the mass of the particle). For instance, one of the possibilities of how dark sector particles couple to the SM particles is via an unknown force felt very weakly by the SM particles. The force carrier is assumed to be the massive dark photons. This idea of a new neutral spin-1 gauge boson was originally proposed by P. Fayet, motivated by supersymmetry, and was then studied outside this context. He proposed different theories [47, 48], e.g. extending the SM $SU(3) \times SU(2) \times U(1)$ gauge by adding an extra $U(1)$ factor that is responsible for spontaneous symmetry breaking, which requires a new neutral gauge boson, and proposed various experiments to search for this boson [49]. Searches by collider experiments, e.g. NA48/2 at the SPS and LHCb at the LHC, did not observe either prompt-like or long-lived dark photons, but some regions of the phase space was excluded [50, 51].

With future data-taking incorporating higher luminosity, optimised trigger schemes, and larger detector acceptance, the collider experiments can access more processes, larger region of the phase space could be probed, and more data could be used, decreasing the statistical uncertainty, and bring possibility of new findings in the dark sector.

2.2.3. Higher Dimensions

Gravity is a mystery in the SM. How can it be added to the SM, together with the other fundamental forces? Why is it so weak? Is the inverse square law still valid at extra small

scale of distance? Theories of higher dimensions are part of the attempts to answer these questions.

The higher dimensions theory originates from the Kaluza-Klein theory. In 1921, Kaluza proposed a fifth dimension of spacetime by extending Einstein's theory of gravity to five dimensions. It succeeded in making the theory consistent with the Einstein equations, Maxwell equation and massless Klein-Gordon equation, and proposed fields that correspond to graviton, photon and dilaton in QFT. However, the 5D world in this theory is the same as a 4D world with a special infinite mass spectrum. Klein in 1926 revived the theory by assuming that the fifth dimension is circular with one of the coordinates being periodic, which means that there is a tiny circle at each point of the four-dimensional spacetime, but also results in an infinite number of 4D fields and symmetries. The studies of higher dimensions continued. One later theory interpreted Kaluza-Klein strings as black holes [52], in some other studies, different numbers of dimensions were studied, e.g. supergravity studies from four to eleven dimensions [53].

For explaining the much weaker scale of gravity compared to the other fundamental forces, some theory proposed extra time dimensions, stating that the SM particles are in the regular time that we are in, but gravity propagates also in higher time dimensions, which causes it appear to be weaker [54]. This theory could be an explanation to the cosmological constant problem, which is that the energy density from cosmological observations is not consistent with the theoretical calculation of quantum mechanics. The dark energy density from cosmological observations corresponds to a distance of around 85 µm, at a distance around or less than such a small scale, if the gravitational force no longer follows the inverse square law of gravity, it could indicate new physics like higher dimensions. If gravity becomes weaker, it could be caused by a "fat" graviton with a size at around the same scale [55]. However, low energy torsion balance experiments found that the inverse square law does hold at the length scale as low as 56 µm [56]. The same experiment also tested the prediction in the M theory of extra space dimension [57] that gravity becomes stronger at sufficiently low size scale that correspond to the size of the extra dimension. The experiment set the upper limit of the size of extra dimensions as 44 µm. Further experimental research is needed.

Theories on large extra dimensions are also considered a possible solution of the hierarchy problem. The weak scale set by the Higgs boson is around 246 GeV, which is the scale of all the particle masses. However, the Planck scale is at the Planck mass 10^{19} GeV, which is also the scale where gravity becomes prominent. Except for supersymmetry and technicolour, higher dimensions is also proposed as a theoretical solution [58].

Higher dimensions could be studied in collider experiments via exotic searches by searching for e.g. particles from extra dimensions dis- or re-appearing, narrow Regge-excitations of SM particles, events that produce microscopic black holes, and events with energy conservation violation if energy is carried away by gravitons [57, 58]. For example, the ATLAS experiment has searched for microscopic black holes with between two and six extra dimensions, the signature that was looked for is at least one electron or muon and two additional leptons or jets with high transverse momentum (p_{T}). The result is within the SM prediction, but some

limits were put on the phase space [59]. Hopes are put on future astrophysics researches, smaller scale experiments, and collider experiments, to unveil the mystery of gravity and test the theories of higher dimensions.

2.2.4. The Higgs Boson

The Higgs mechanism is an important part of the electroweak sector in the SM, through which the particles acquire mass via interacting with the Higgs boson – a scalar field whose self-interaction results in a field strength where the ground state is not where the field is zero, but at a non-zero vacuum expectation value v, spontaneously breaking the electroweak $SU(2) \times U(1)$ symmetry to the electromagnetic $U(1)$ symmetry. The SM Higgs has mass $m_H = 125.25 \pm 0.17\,\text{GeV}$ [30], it is the only spin 0 particle and is electrically neutral. It also has no colour charge, which means it is not subject to the EM and strong force. Since its discovery, one has not stopped wondering: is the Higgs that was discovered the SM Higgs? Is there only one type of Higgs? Is the Higgs a fundamental particle or a composite particle?

Various properties of the Higgs boson have been studied, like the production cross section and the branching fractions of its decays. In the SM, the coupling strengths between the Higgs and other particles is positively related to the particle mass[9] – heavier particles interact stronger with the Higgs field. Experimental results are so far consistent with SM prediction [60]. However, the coupling strength to in particular charged fermions in the 1st and 2nd generation as well as the Higgs itself is still unclear.

The potential of multiple Higgs self couplings is:

$$V = \frac{m_H^2}{2}H^2 + \frac{m_H^2}{2v}H^3 + \frac{m_H^2}{8v^2}H^4, \tag{2.2}$$

where:

- H is the Higgs field
- v is the field strength $v = \frac{2m_W}{g_W} \approx 246\,\text{GeV}$, also called the Higgs vacuum expectation value, where m_W is the W boson mass and g_W is the weak coupling constant, both of which are measured experimentally to determine v
- $m_H = \sqrt{2\lambda}v$ is the Higgs mass, where λ is the Higgs trilinear (cubic) coupling

Even before the discovery of the Higgs, researchers have already studied how to measure the triple Higgs self-coupling constant, because this is important for calculating the Higgs potential, therefore understanding electroweak symmetry breaking [61]. $\lambda = \frac{m_H^2}{2v^2}$ can be measured at a three Higgs vertex experimentally. Results that deviate from the SM could indicate different BSM theories like the Higgs portal model, or composite Higgs.

Collider experiments with larger centre-of-mass energy could give access to Higgs pair production, see figure 2.2 for examples of the dominant Feynman diagrams. Figure 2.2(a)

[9] The Yukawa couplings of fermions $g_f = \sqrt{2}\frac{m_f}{v}$. For gauge bosons W and Z, $g_{HWW} = g_W m_W$, $g_{HZZ} = g_Z m_Z$, where $g_Z = \frac{g_W}{\cos\theta_W}$ is the Z boson coupling constant and θ_W is the weak mixing angle.

gives access to the Higgs trilinear coupling. This production channel is important because its cross section is higher than double-Higgs-strahlung and vector boson fusion. Lepton colliders cannot measure the trilinear coupling via Higgs pair production due to their lower energy scale, but it is possible to access it through loop corrections of single Higgs production processes. For lepton collider measurements please refer to [62].

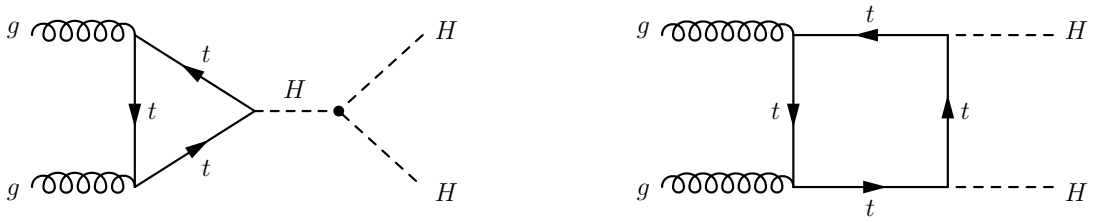

Figure 2.2: Dominant Feynman diagrams for Higgs pair-production from gluon fusion. (a) involves Higgs self-interaction.

Studies show that Higgs pair-production from gluon fusion requires $3000\,\mathrm{fb}^{-1}$ to measure the tri-Higgs coupling constant with precision of up to 20–30 % at 95 % confidence level [24–27]. This is one of the main motivations for the High-Luminosity LHC, with a designed nominal integrated luminosity of $3000\,\mathrm{fb}^{-1}$.

CHAPTER 3

ATLAS Detector and the HL-LHC Upgrade

This chapter brings you into the accelerator complex of CERN – the European Organization for Nuclear Research (Conseil Européen pour la Recherche Nucléaire), introducing the Large Hadron Collider (LHC), the upcoming High Luminosity LHC (HL-LHC) upgrade, and the ATLAS detector upgrade for successful data collection in the HL-LHC era.

3.1. CERN and the LHC

The CERN accelerator complex consists of a series of smaller accelerators, each boosts the energy of the beam particles and injects them into the next, or redirects the beam towards a fixed target experiment. See figure 3.1 for the layout. The largest accelerator in the complex is the LHC, which accelerates and collides protons (pp collisions) or heavy-ions. Filling the LHC takes 12 cycles from the SPS synchrotron (each cycling takes 21.6 s), and for each SPS fill, 3-4 cycles from the PS (3.6 s cycling time), making the LHC fill time 4 min per beam. Practically, the turnaround time[1] including the whole operational cycle of the LHC is much longer, at the order of around a few hours, due to various reasons like not all injections fill the LHC successfully with protons with target energy, machine faults and recovery, and procedures like a few SPS cycles needed for setting up the injection, evaluation of such pilot bunches and adjustment of machine settings done by the LHC operators, ramping up and down of the beam energy, checking of the systems, etc.

The LHC is to date the largest accelerator and collider in the world. It was built in the tunnel of the previous collider called LEP (Large Electron–Positron Collider). The circumference of the accelerator ring is 26.7 km, which lies, depending on the landscape,

[1] Turnaround time: the time between beam dump during stable beam and the beginning of the next stable beam mode.

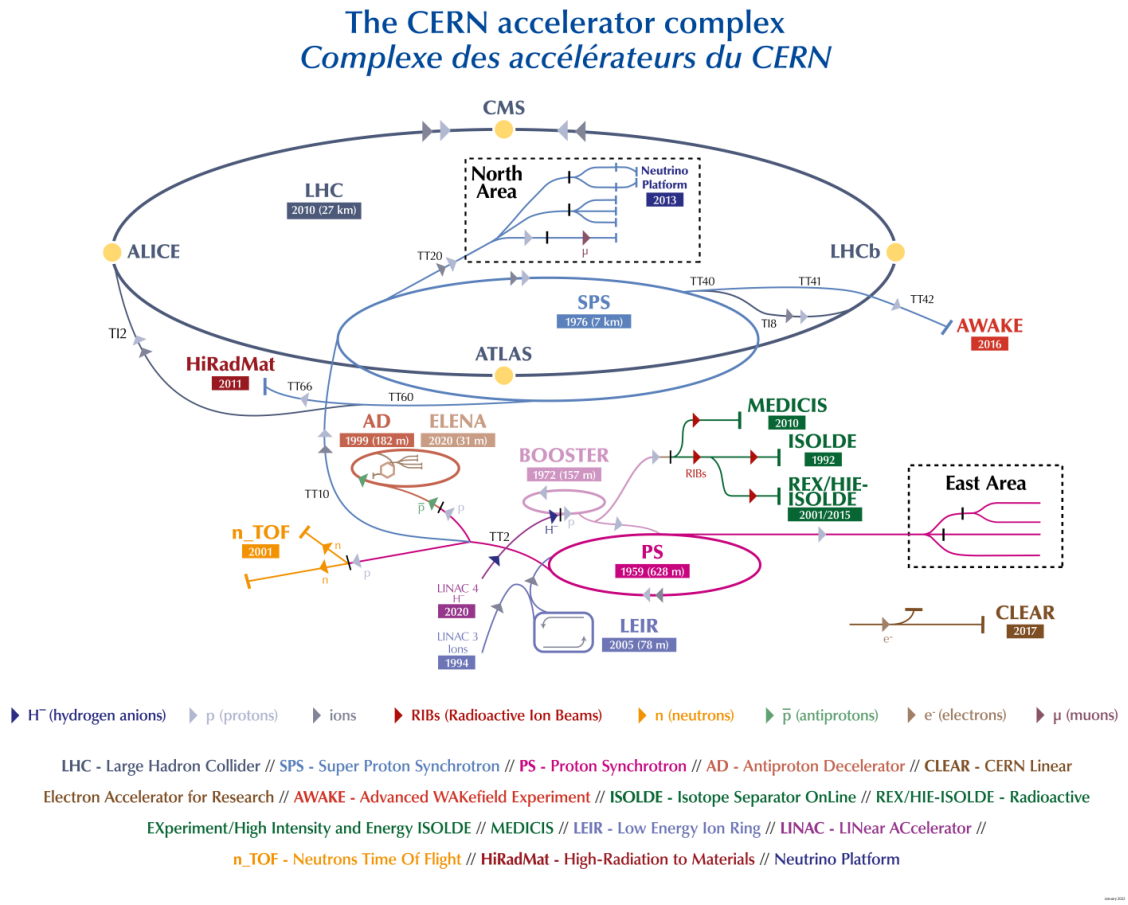

Figure 3.1: The CERN Accelerator complex layout in 2022. The starting point of feeding the LHC with protons is LINAC4 (LINAC3 in case of ions), which replaced LINAC2 in 2020 (LINAC1 continued to provide light ions after its role of proton source was replaced by LINAC2 [63], and eventually LINAC3 took over to produce heavier ions [64]). H^- ions are accelerated to energy of 160 MeV by the end of LINAC4, then stripped of electrons to leave only protons, which enter the following accelerators in sequence: the Proton Synchrotron Booster, where the energy is increased to 1.4 GeV, Proton Synchrotron (25 GeV), Super Proton Synchrotron (450 GeV), and then into the LHC (7 TeV for proton and 2.8 TeV for Pb ion) [65, 66]. Image from [67].

between 45 and 170 m underground. The slope of the ring plane is 1.4 %. With 90 % being in molasse rock and 10 % in limestone under the Jura mountains, the geological structure provides a suitable environment for the construction. The original LEP tunnel was constructed during 1984–1989. The LHC project was approved in 1994, then LEP was closed in 2000 for the LHC construction, and the LHC machine first started up in 2008.

The LHC ring contains two beam pipes for two beams to circulate in opposite directions in vacuum. There are eight arc sections and eight straight sections, as shown in figure 3.2. The straight sections host the four beam crossing points and the superconducting radio frequency (RF) cavities, which contain EM fields that accelerate the particles again to compensate

for the energy loss due to synchrotron radiation. The arc sections comprise smaller base blocks referred to as cells, which consists of cryostat, short straight section assembly, and dipole magnet sections. The main magnet system includes multiple superconducting dipole magnets and quadruple magnets for beam bending and focusing, respectively. Other components includes quadrupole, sextupole, octupole and decapole magnets as corrector magnets and beam position monitors. In practice, the beam oscillates around the designed closed orbital trajectory, the frequency of which is described by the betatron tune. Also, the momentum spread of the beam particles results in different focal lengths from the quadrupole, leading to a dependency of the betatron tune with particle momentum, which is described by chromaticity. All accelerator components work together to obtain good performance on these crucial parameters for a circular collider.

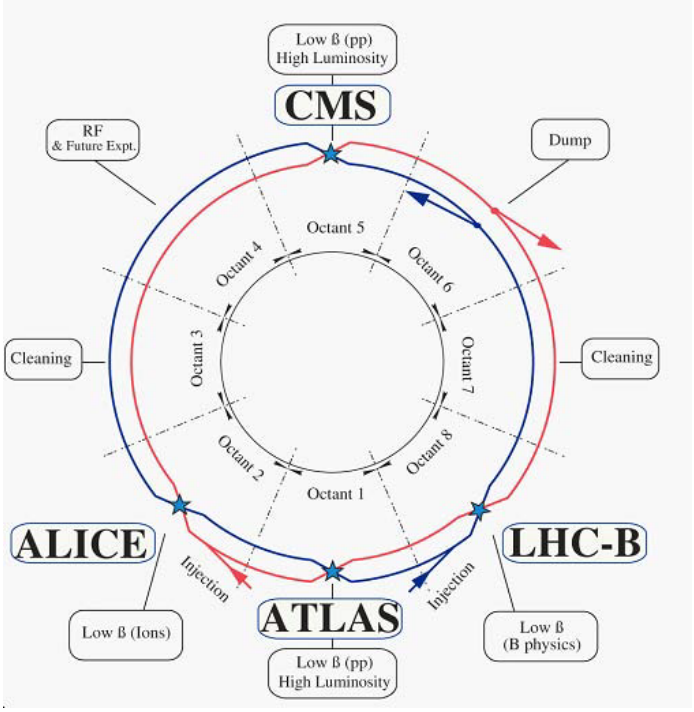

Figure 3.2: Schematic of the LHC. The two beams (denoted in red and blue) are counter-rotating. The ring is divided into eight octants, where they are referred to as Interaction Region or Point 1 to 8. ATLAS and CMS are at Point 1 and 5, respectively. The injection systems for the two beams are at Point 2 and Point 8, where the ALICE and the LHCb experiments are located. Injections come from below the LHC plane. The insertions at the other points contain: momentum and betatron cleaning systems (collimators) at Point 3 and 7, RF systems at Point 4, and beams are dumped at Point 6, where the beams are deflected vertically by magnets to another tunnel into absorbers. Image from [66].

In the LHC, a proton beam consists of smaller bunches[2], and the time between neighbouring bunches, which is called the bunch spacing, is 24.95 ns. The beams cross each at an angle referred to as the crossing angle, and then the remaining beams continue to travel to the next IP. The rate of collisions is typically measured through the luminosity. The number

[2]A bunch is a group of particles in one RF bucket.

of events[3] per unit time is determined by:

$$\frac{dN_{\text{event}}}{dt} = L\sigma_{\text{event}}, \tag{3.1}$$

where L is the machine luminosity and σ_{event} is the cross section, which differs according to the type of event. The machine luminosity depends only on parameters of the beam. Assuming round beams with small bunch length, the machine luminosity is

$$L = \frac{\gamma}{4\pi}\frac{N_b^2 n_b f_{\text{rev}}}{\beta^* \epsilon_n} R, \tag{3.2}$$

where:

- γ is the relativistic gamma factor
- N_b is the number of protons per bunch
- n_b is the number of bunches per beam
- f_{rev} is the revolution frequency, which is the frequency that the bunches circle around
- β^* is the beam beta function at the collision point, which is the focal length
- ϵ_n is the normalised transverse emittance
- R is the geometric reduction factor, which is from the crossing angle at the interaction point, and is defined as:

$$R = \frac{1}{\sqrt{1 + \frac{\theta_c \sigma_z}{2\sigma}}}, \tag{3.3}$$

where:

- θ_c is the crossing angle between the colliding beams
- σ and σ_z are the transverse and longitudinal root mean square (RMS) beam size and length, respectively

Luminosity changes with time mainly due to the protons consumed at collisions ("luminosity burn-off"). The effect is approximated by an exponential decay of the luminosity [68] with lifetime τ_L, therefore the integrated luminosity for one run is:

$$\mathcal{L}_{\text{int}} = L_0 \tau_L \left(1 - e^{-T_{\text{run}}/\tau_L}\right), \tag{3.4}$$

where L_0 is the initial luminosity and T_{run} is the duration of the run.

The integrated luminosity is the total collisions created, and can be used to gauge the amount of data that was collected:

$$\mathcal{L}_{\text{int}} = \int_{\Delta t} L_{\text{ins}}. \tag{3.5}$$

Luminosity levelling is used during the LHC operation to achieve optimal data collection: instead of colliding with the highest possible luminosity, which will then fast decay from the initial peak value, the LHC is operated such that the luminosity starts lower but is kept

[3] An event is an occurrence of particle interactions and decay processes, typically from one pp collision.

almost constant for longer, before decaying slowly. This luminosity profile is illustrated in figure 3.3, which shows the planned luminosity levels for the HL-LHC, but the luminosity levelling behaviour is qualitatively the same for the LHC.

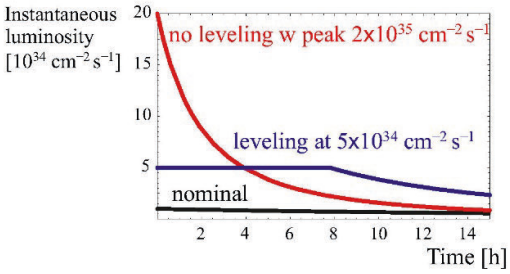

(a) Black line shows the level of the nominal peak luminosity at the LHC. After the high luminosity upgrade, the luminosity without and with levelling are approximately shown by the red and the blue lines.

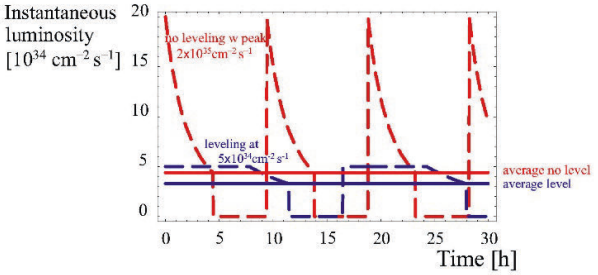

(b) To optimise the run time, beam is dumped when the luminosity decreases to a threshold. The average luminosity with levelling is expected to be similar to (despite a bit lower than) that without levelling.

Figure 3.3: Luminosity levelling and run time optimisation. The values for the red and blue lines are around the expected values at HL-LHC. Figures from [29].

With luminosity levelling, the maximum peak luminosity is lower, therefore mitigating pile-up (events in the same bunch crossing), and the average luminosity is comparable to that without levelling, making luminosity levelling a good data-taking strategy.

The designed centre of mass (CoM) collision energy of the LHC is 14 TeV[4] and the luminosity delivered depends on the experiment.

- ATLAS (A Toroidal LHC ApparatuS[6]) [18] and CMS (Compact Muon Solenoid) [19] are general-purpose detectors. They take advantage of the high energy and luminosity of the LHC, and investigate new physics in proton or heavy-ion collisions. During proton-proton collisions, both detectors get a high peak luminosity of $L \sim 10^{34}\,cm^{-2}s^{-1}$.
- ALICE (A Large Ion Collider Experiment) [21] is a general-purpose heavy-ion detector that focuses on QCD. During nominal lead-ion–lead-ion operation, the target of the peak luminosity is $2 \times 10^{27}\,cm^{-2}s^{-1}$.
- LHCb (Large Hadron Collider beauty) [20] is a single-arm spectrometer aims at looking for new physics in CP violation and rare decays of beauty and charm hadrons[7]. The peak luminosity is aimed at $10^{32}\,cm^{-2}s^{-1}$.

[4] Beam energy 7 TeV. However, the designed energy is not necessarily reached, but depends on various factors, which can be as big as an accident[5] leading to the CoM energy for Run 1 being limited to 7 and 8 TeV [69] and as small as tidal effects from the moon deforming the earth crust, therefore changing the circumference of the LHC [70, 71].

[5] Thermal runaway led to the melting temperature of a solder being exceeded, breaking the electrical circuit connection between a dipole and a quadrupole magnet, developing an electrical arc, vapourising and destroying components, causing huge damage that involved even the civil engineering structures.

[6] Also the name of a giant in Greek mythology.

[7] Beauty or charm hadrons: hadrons that contain b or c quarks.

3.2. The HL-LHC Upgrade

To collect enough statistics to analyse rare processes with small cross-section, larger luminosity is needed (as shown by equation 3.1). Therefore, the LHC is going to be upgraded to the HL-LHC, to improve the precision of existing measurements and probe new physics.

In the past, the LHC and the detectors have taken data in Run 1 and Run 2 since 2011, and at the time of this thesis, Run 3 is ongoing. Each Run is separated by a Long Shutdown (LS) period, when the accelerator, collider machine and the detectors are maintained and upgraded. See figure 3.4 for the Run and LS timeline. The HL-LHC upgrade will be conducted during the LS 3 from 2026 to 2030, together with the ATLAS and CMS phase II upgrades.

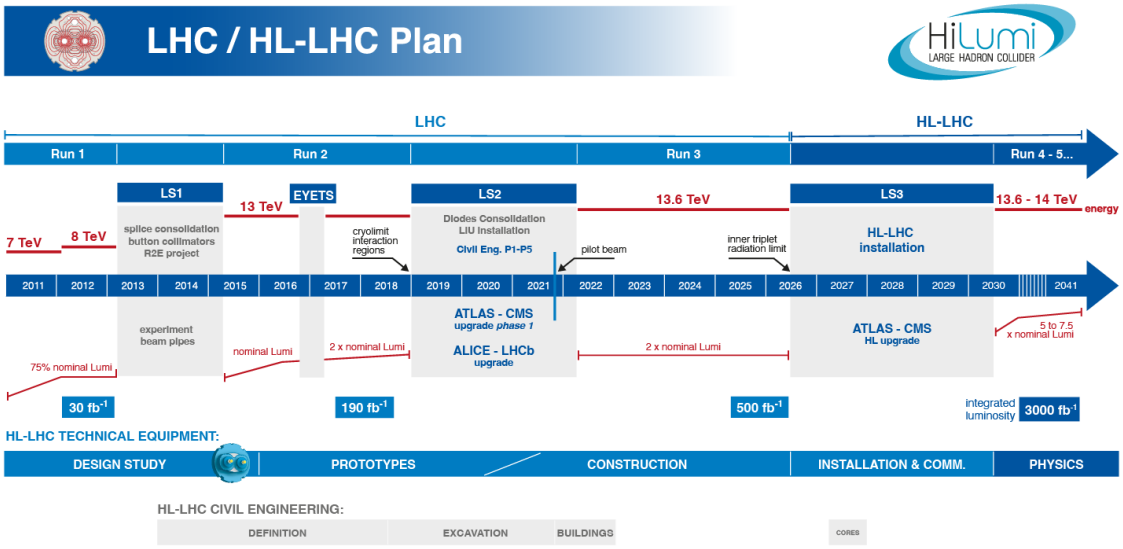

Figure 3.4: Schedule of LHC and the HL-LHC upgrade including Runs, Long Shutdowns (LS), and an Extended Year-End Technical Stop (EYETS). Image from [72], last update January 2025, modified.

A comparison between the parameters of the LHC and the planned HL-LHC upgrade for proton collisions is shown in table 3.1 [29, 66]. In Run 3, the LHC is running at 13.6 TeV instead of the designed CoM energy of 14 TeV, which is planned to be reached for the HL-LHC. The nominal luminosity will be upgraded from $10^{34}\,\mathrm{cm}^{-2}\mathrm{s}^{-1}$ at the LHC to $5.32\times10^{34}\,\mathrm{cm}^{-2}\mathrm{s}^{-1}$ at the HL-LHC. For the planned operation time, the nominal integrated luminosity will be $3060\,\mathrm{fb}^{-1}$.

The increase in luminosity is achieved via different measures, especially the beam parameters. The beam will be brighter, which means a larger number of protons per bunch crossing. Stronger quadrupole magnets focus the beam more. The stronger and larger aperture at the quadrupole magnets reduces the minimum beam beta function β^*, which decreases the size of the luminous region and increases peak luminosity. The brand new technology

Parameter	LHC	HL-LHC
Ring circumference [m]	26658.87 [73]	26658.883
Centre of Mass energy $\sqrt{s}$ [TeV]	14	14
Nominal luminosity [$10^{34}\,\mathrm{cm}^{-2}\mathrm{s}^{-1}$]	1	5.32
Pile-up† μ	27	140
Integrated luminosity [$\mathrm{fb}^{-1}\mathrm{yr}^{-1}$]	35	250
Number of protons per bunch N_b	1.15×10^{11}	2.2×10^{11}
Number of bunches per beam n_b	2808	2748
Relativistic gamma γ	–	7461
Revolution frequency f_{rev} [kHz]	11.2455 [73]	11.2455
Minimum beam beta function β^* [m]	0.55	0.2
Normalised transverse emittance ϵ_n [µm]	3.75	2.50
Crossing angle θ_c at IP1/5 [μrad]	285	510
Longitudinal RMS bunch length σ_z [cm]	7.55	8.1
Transverse RMS bunch size at IP1/5 [µm] σ	16 [73]	7.1
Peak dipole field of the magnets [T]	8.33	11 to 12

Table 3.1: Comparison of nominal design parameters of the LHC and HL-LHC. †With crab cavities and luminosity levelling, calculated with inelastic cross-section 85 mb.

called "crab cavities" is also a key to the luminosity increase. They are RF cavities that tilt bunches with respect to their direction of motion, as if they are travelling slightly sideways like crabs, see figure 3.5. This maximises the overlap between the bunches, increasing the collision rate.

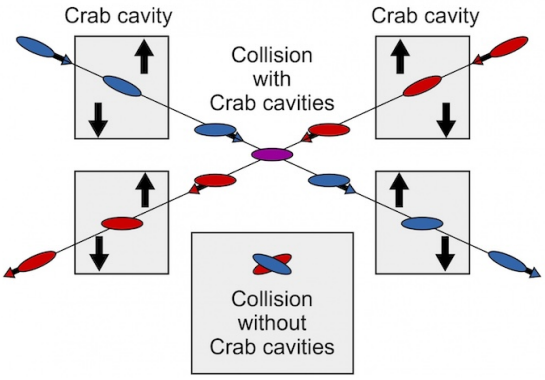

Figure 3.5: The effect of crab cavities. © CERN.

In addition, there is larger beam current benefiting the powering of many systems, and decrease of numbers of hardware, software and beam-induced faults, time of recovering from faults, need of tunnel access for intervention, turnaround time[8], and unnecessary beam dumps. Everything comes together to achieve a high integrated luminosity.

[8]The turnaround time is estimated to be 3 h at the HL-LHC.

3.3. The ATLAS Detector

The ATLAS detector is located in the experimental hall of the LHC Point 1 at CERN, the cavern is 100 m below the ground level. It is cylindrical-shaped and symmetric in the forward and backward direction with respect to the IP. The different sub-detector layers wrap around the beam pipe like layers in the stem of a leek, as shown in figure 3.6. Being the largest detector in a particle collider, it is 44 m in length (along the beam-line), 25 m in diameter, and weighs about 7000 tons[9].

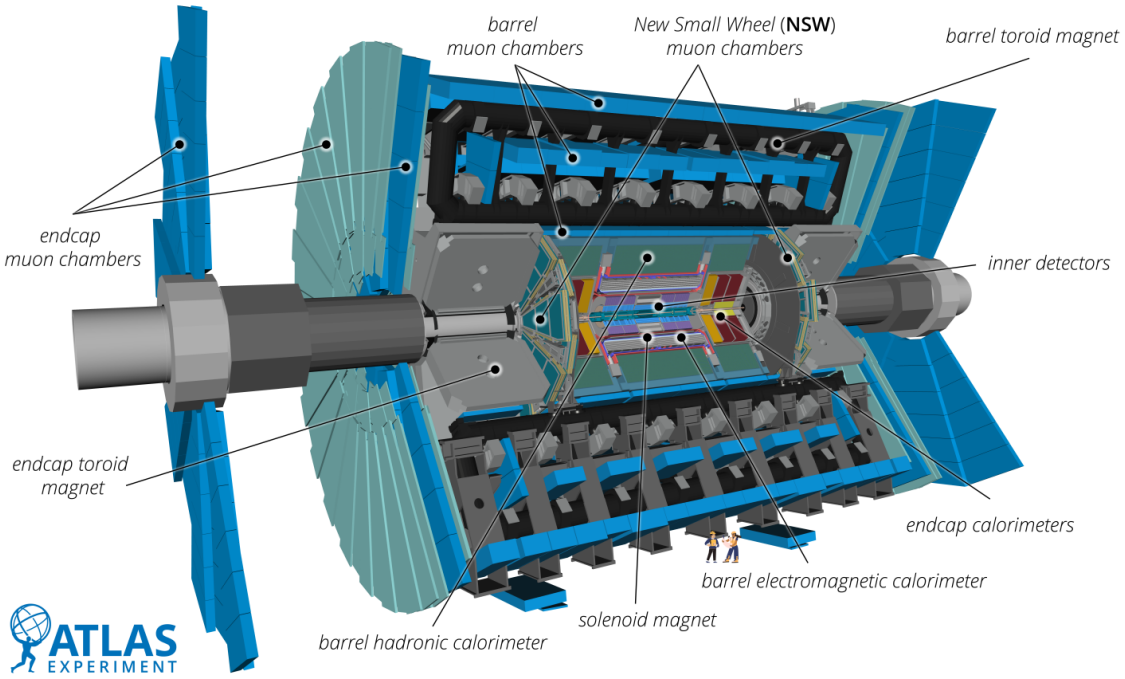

Figure 3.6: The ATLAS detector, including the new systems installed during the Long Shutdown 2, the different layers of sub-detectors are marked. Image from [74], ATLAS Experiment © 2022 CERN.

3.3.1. The Coordinate System

The coordinate system used to describe the detectors and the kinematic variables of the particles is defined as follows, see figure 3.7 for an illustration. The origin of the coordinate is the nominal interaction point. The x-axis is along the LHC ring plane, with the positive being defined as the direction from the interaction point to the centre of the ring. The y-axis points upwards. The z-axis is along the beam direction, and forms a right-handed coordinate system with the x and y-axis.

The more commonly used coordinate system is expressed with an azimuthal angle ϕ around the beam axis and a polar angle θ from the beam axis. The polar angle can also be expressed

[9]The weight of the ATLAS detector is similar to that of the Eiffel tower. Despite ATLAS being the largest by size, CMS is the heaviest detector.

with pseudorapidity:

$$\eta = -\ln \tan\left(\frac{\theta}{2}\right), \tag{3.6}$$

or rapidity:

$$y = \frac{1}{2}\ln\left(\frac{E + p_{\mathrm{L}}}{E - p_{\mathrm{L}}}\right), \tag{3.7}$$

where p_{L} is the momentum in the longitudinal (beam) direction.

Rapidity and pseudorapidity is preferred over θ due to being Lorentz invariant along the beam axis. For massless particles, or when the momentum is much higher than the mass, the rapidity and pseudorapidity become the same.

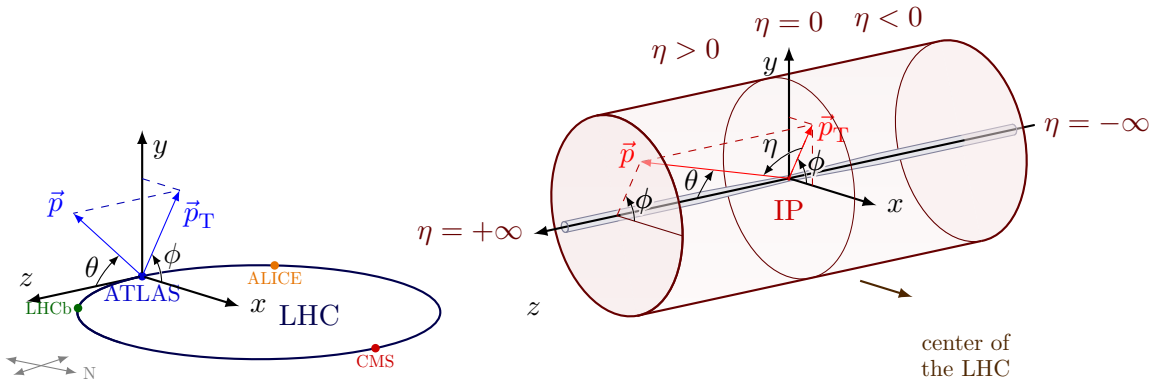

(a) The coordinate system w.r.t. the LHC ring. (b) The coordinate in the cylindrical ATLAS detector.

Figure 3.7: The coordinate system. © Copyright 2021 – TikZ.net, license: CC BY-SA 4.0, modified.

The transverse momentum p_{T}, transverse energy E_{T}, and missing transverse energy $E_{\mathrm{T}}^{\mathrm{miss}}$ is defined in the plane transverse to the beam axis. This is because in a pp collision, what interacts are the partons (quarks and gluons in the protons), and each parton carries an unknown fraction of the proton energy across the z-axis. However, the conservation law can be applied on the complete measurements in the x–y plane.

If the ATLAS cylinder is unwrapped, it forms a plane where a geometric distance ΔR_{12} between two particles or objects can be defined. This plane is defined by the pseudorapidity and azimuth angles, and the distance between object 1 and 2 in the (η, ϕ) plane is:

$$\Delta R_{12} = \sqrt{\Delta\eta_{12}^2 + \Delta\phi_{12}^2}. \tag{3.8}$$

See figure 3.8 for an example of a dijet[10] event shown in the (η, ϕ) plane.

3.3.2. Particle Detection in the ATLAS Sub-detectors

Particle detectors in HEP commonly consists of sub-detectors, each of which is sensitive to different types of particles, and provides various information about them. These detector

[10] A jet is a cone of hadronised high-energy quarks and gluons.

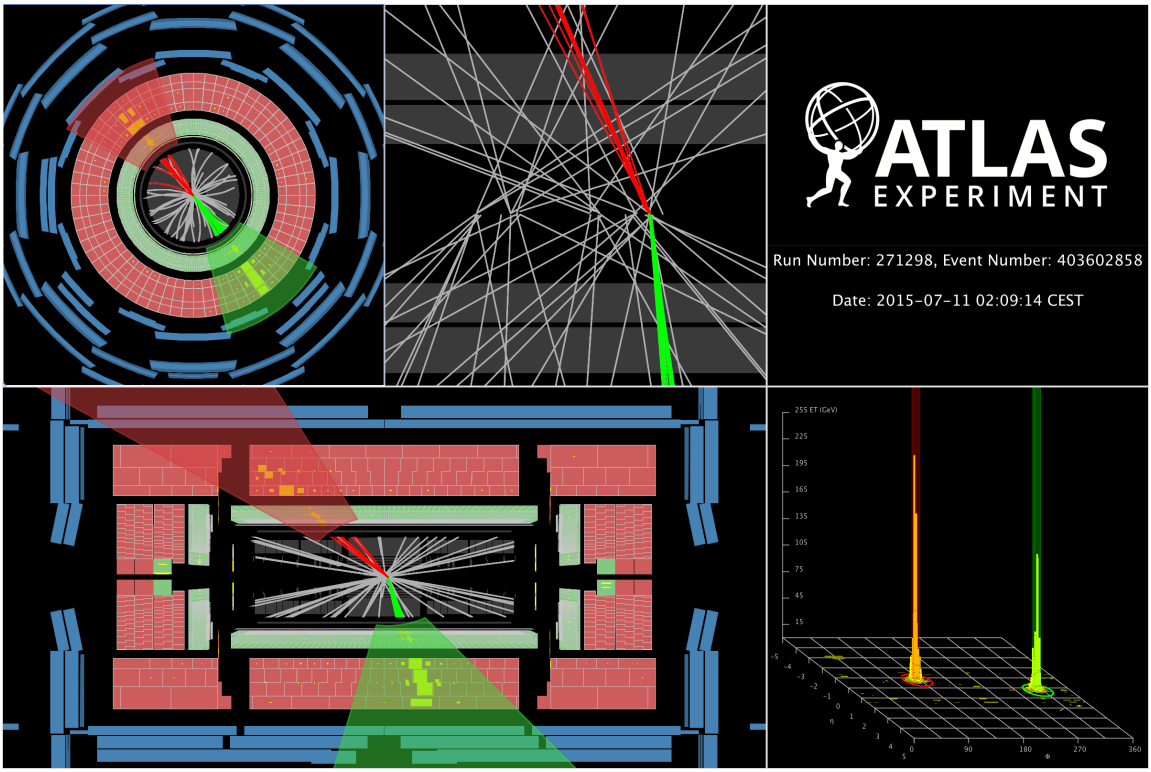

Figure 3.8: Display of a dijet event in the ATLAS detector. Bottom right shows the two jets in the (η, ϕ) plane. Image from [75].

information can be reconstructed to recover the kinematic properties of the particles, identify the particles, and provide data for analysis to give physics results.

Figure 3.9 highlights how particles show up in the ATLAS sub-detector layers. Charged particles leave bended tracks in the tracking system due to the magnetic field from the solenoid magnet outside the tracker. Electrons, photons, and hadrons produce showers in the calorimeters, and the hadrons penetrate to the hadron calorimeter, where they are completely absorbed. During this process, the energy, mass and spatial information is recorded. Muons do leave tracks in the ID and deposit minimum energy in the calorimeters, but they pass through the entire detector instead of being stopped at the calorimeters, and are measured mainly by the muon spectrometer at the outmost layer. Neutrinos are invisible to the detector, but after all the other particles are measured, as the total transverse momentum (hence energy) is conserved, neutrinos show up as missing transverse energy.

The systems are mainly divided into: magnets, tracker, calorimeter, muon system, and trigger and data acquisition (TDAQ). There are also forward detectors that measure the luminosity and centrality of collisions.

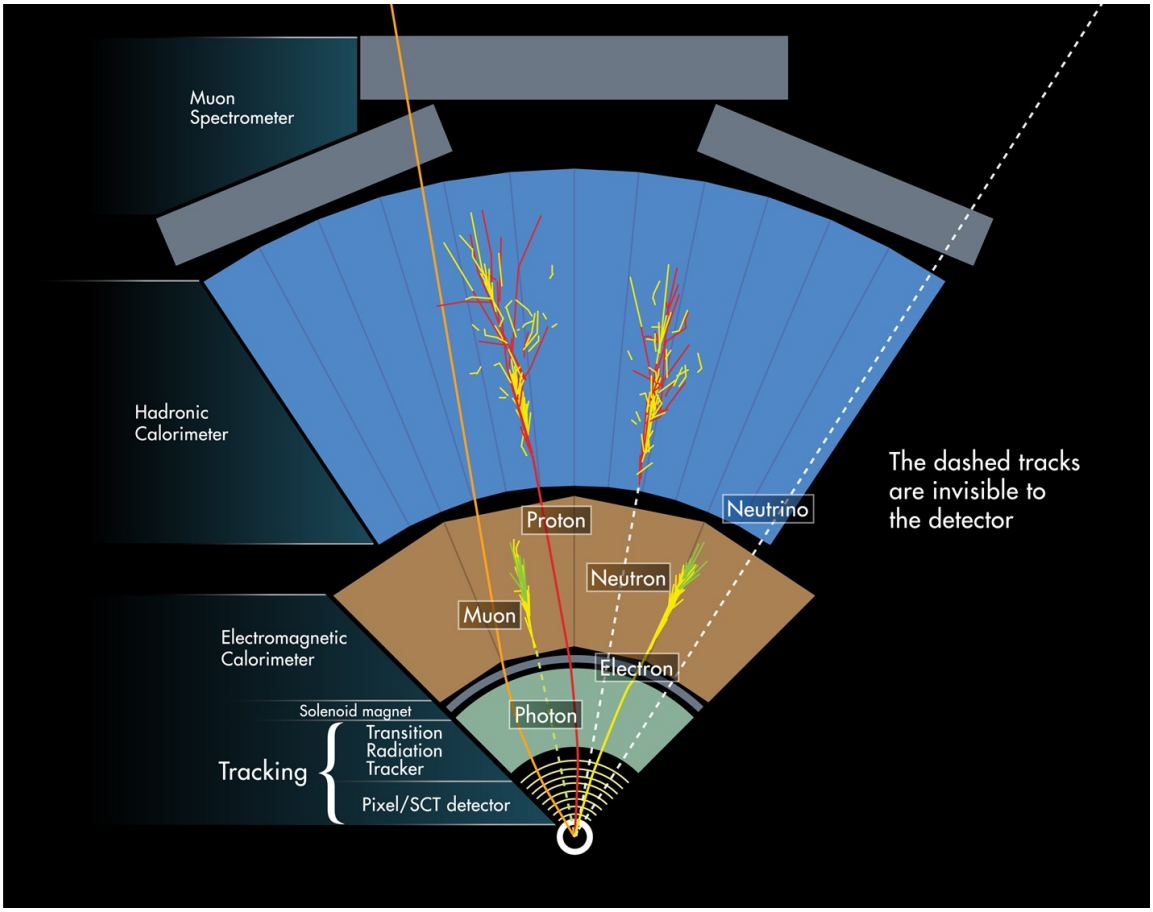

Figure 3.9: Paths of different types of particles in the sub-detector layers of ATLAS. Image from [76], ATLAS Experiment © CERN.

3.3.3. Magnets

The superconducting magnets are cooled to 4.5 K with liquid He and provide strong magnetic fields, which bend the tracks of the charged particles, so that the momentum and the charge can be calculated according to the curvature of the track. There are two magnet systems in the ATLAS detector:

- The central thin solenoid magnet around the ID cavity. The solenoidal field is 2 Tesla for the ID and is along the beam direction, but affects the barrel EM calorimeter as little as possible.

- Three large superconducting toroids (one barrel and two end-caps), which enclose the muon spectrometer barrels and small wheels. Each toroid consists of eight coils radially and symmetrically distributed around the inner layers of the detector. They provide a toroidal magnetic field of around 0.5 to 1 T for the muon spectrometer.

See figure 3.10 for an illustration of the magnetic fields that the magnets generate, and figure 3.11 for photos of the solenoid and toroid (only the barrel toroid is visible) magnets.

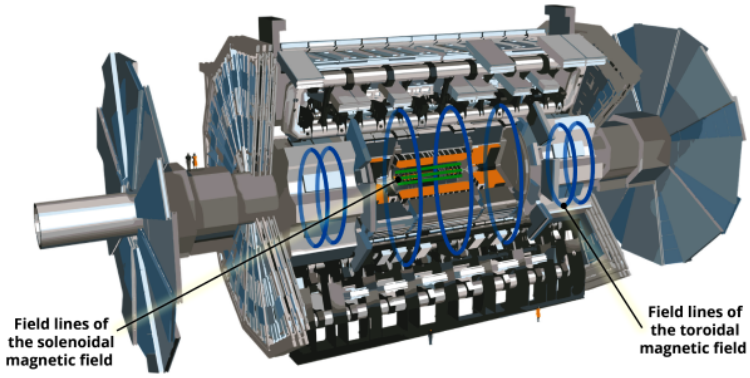

Figure 3.10: The magnetic fields in the ATLAS detector. Image from [77], ATLAS Experiment © 2021 CERN.

(a) The bare central solenoid magnet.

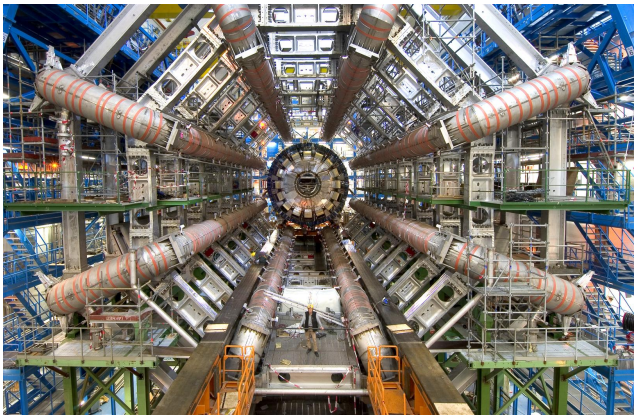

(b) The barrel toroid magnet in the underground cavern.

Figure 3.11: Photos of the magnets. Images from [18].

3.3.4. Inner Detector (ID)

The Inner Detector (ID) is the tracking system at the innermost and central layer of the ATLAS detector. It measures the tracks of charged particles with p_{T} higher than 0.5 GeV, or in the case of minimum-bias events, above 0.1 GeV. The tracks are used for primary and secondary vertex, as well as impact parameter reconstruction. It also provides electron identification within the acceptance range over a wide energy range from 0.5 to 150 GeV.

The ID needs to have high granularity (to provide good spatial and momentum resolution in both the R-ϕ and the z coordinates), good pattern recognition, and high reconstruction efficiency. Because it is the closest to the beam-pipe, it also needs to be radiation-tolerant. Being in a solenoidal field, the p_{T} of the particle can be calculated from the curvature of the track. Combined with the vertex measurements, the ID plays the crucial role in flavour tagging (details in chapter 5).

The ID consists of three parts: Pixel detector, Silicon Microstrip Tracker (SCT), and

Transition Radiation Tracker (TRT). The first two are cooled and operated at -5 to -10 °C, while the TRT is operated at room temperature.

The Pixel Detector and the Insertable B-Layer (IBL)

The Pixel detector has the highest granularity in the ID. It is a silicon detector and consists of hybrid modules[11]. Initially, three barrel layers and three end-cap disks were installed[12]. Later, during the LS1 and before the start of Run 2, a fourth layer – the Insertable B-Layer (IBL) – was added close to the beam-pipe. This is to maintain or even improve the performance and robustness of the tracking system due to the radiation damage of the pixel detector modules during Run 1, the planned higher peak and integrated luminosity in Run 3 causing the read-out bandwidth to reach its limitation, and further radiation damage. The IBL is planned to be operated until the end of Run 3, before the upgrade of the whole ID for the HL-LHC. For details of the sensor and FE of the pixel and IBL modules, as well as comparison with the modules for the ITk pixel upgrade, see section 3.4.

Silicon Microstrip Tracker (Semiconductor Tracker – SCT)

The SCT is the middle layer of the ID. The barrel region of the SCT consists of four layers of modules, and each of the two end-caps contains nine disk layers. Each module has four sensors separated into two layers, one axial and the other at a 40 mrad stereo angle, to provide improved spatial resolution. For the barrel modules, each sensor layer comprises two 6.4 cm long sensors that are daisy-chained together, and the strip pitch is 80 µm. The sensors in the end-cap regions are trapezoidal-shaped, with sizes that vary but are similar to the rectangular barrel sensors.

Transition Radiation Tracker (TRT)

The TRT is a gaseous detector operated at room temperature. It makes use of the transition radiation: when charged particles like electrons or pions traverse the border of two different materials that have different dielectric constants with a velocity higher than a threshold, photons are emitted.

The TRT consists of barrels and end-caps made from polymide drift tubes ("straw"s) with 4 mm diameter, the cathode is the polymide tube, which is coated with Al and biased at −1530 V. The gas mixture in the tube is 70 % Xe, 27 % CO_2 and 3 % O_2, over-pressured at around 5 to 10 mbar. The anode is gold plated tungsten, and is connected to FE electronics and grounded. The resulting gain is 2.5×10^4.

Between the straw are polypropylene fibres (for the barrel) or foils (for the end-cap). The transition radiation traverses these materials, get absorbed by the Xe atoms in the gas and

[11] For detailed introduction to hybrid pixel detectors, see chapter 4.

[12] Three is the minimum number of hits needed to reconstruct a curve. How tracking is performed and how p_T is obtained from the tracks are explained in section 5.2.

ionise the gas, depositing higher energy than the usual ionising particles. This feature is used for electron identification. Pions are identified by setting a higher threshold.

For the barrels, there are three layers of rings, each with 32 modules, with 52544 straws per module (144 cm long, along the z-axis), forming a total of 73 layers. The end-caps on each side consists of two sets of 20 wheels, each with eight layers spaced around 1 cm apart (160 layers in total). Each layer has 768 straws of 37 cm long aligned along the radial direction. There are on average 36 hits per track, which provides good tracking and momentum resolution, as well as longer track length measurements.

3.3.5. Calorimetry

Calorimeters measure the energy and position of the incoming particles, and identify electrons, photons, hadrons, and $E_{\mathrm{T}}^{\mathrm{miss}}$ (neutrinos). It should also absorb the energy, and stop the particle showers from passing through to the muon system. The ATLAS calorimetry consists of the EM calorimeter and the hadronic calorimeter.

Electromagnetic Calorimeter (ECal)

The ECal is a Liquid-Argon (LAr) electromagnetic sampling calorimeter, the inner layer of the calorimeters. It identifies electrons and photons, and measure their energy and the position of the energy deposition. It consists of a barrel and two end-caps, and is completely symmetric around the ϕ direction. It is kept at $-184\,^{\circ}\mathrm{C}$ to keep the Ar liquid.

The most characteristic feature of the ATLAS ECal is the accordion shape (see figure 3.12) from alternating layers of metal (lead) and thin LAr. The structures with honeycomb pattern in the LAr layers are the electrodes (made of kapton: a type of polyimide film), from which the position of energy deposition can be measured with good resolution due to the fine segmentation.

Figure 3.12: Accordion shaped calorimeter. Image from [78], © 2003-2024 CERN.

The incoming particles interact with the metal part of the calorimeter, and leave almost all the energy in the form of a shower of secondary particles with lower energy, which ionise the LAr. This process happens recursively, until the energy is too low and is completely

absorbed by the metal layer. The resulting free electrons from the ionisation, under the HV applied to the LAr layer, are extracted and detected as current, with a constant current per particle in the shower. Therefore, the number of particles in the shower can be measured by the total current, and the mass (or energy) of the original incoming particle is calculated by summing up all the currents from the LAr layers.

Hadronic Calorimeter (HCal)

The HCal measures the energy of jets accurately for jet and E_T^{miss} reconstruction. It is located directly outside the ECal, and has lower granularity, but is still sufficient for its purpose. Unlike electrons and photons, which are completely absorbed in the ECal, hadrons reach the HCal through the ECal, and are stopped (absorbed) here.

HCal consists of three parts: the tile calorimeter (TILE, three consecutive barrels), hadronic end-cap calorimeter (HEC, two wheels per end-cap), and the forward calorimeter (FCal, three layers/modules per end-cap).

- TILE is a scintillator-tile sampling calorimeter. It is the outmost layer, aims at completely absorbing the particles (except for muon and neutrinos), and measures the energy of the hadronic particles since they do not deposit all energy in the ECal. It consists of alternating layers of steel and plastic scintillating tiles. Similar to the description in the ECal section, the steel acts as the absorber and generates a shower, producing photons in the scintillators, which are then detected as currents. The proportionality between the current and the numbers of shower particles and therefore the energy of the original incoming particle also holds.
- The HEC and FCal are also LAr sampling calorimeters, with the same principle as the LAr ECal, just with different absorber material and geometry.
  - HEC has flat layers with honeycomb electrodes and the absorber plates are copper.
  - FCal consists of absorber material with regularly spaced cylindrical electrodes parallel to the beam-line. The absorber is copper in the first layer, and tungsten in the other two, for optimised EM and hadronic measurements, respectively.

3.3.6. Muon Spectrometer

Outside the calorimeters is the muon spectrometer. This is also the outmost layer. Unlike most particles, muons and neutrinos are not stopped by the calorimeters. Muons are subject to weaker Bremsstrahlung due to their higher mass. Therefore, unlike electrons and photons that create EM showers through Bremsstrahlung and pair-production (as detailed in section 4.1.3), muons do not generate EM showers in the ECal. Being leptons, muons also do not undergo nuclear interactions as hadrons do, and therefore do not produce hadronic showers in the HCal. The muon spectrometer reconstructs and identifies muons with GeV to TeV level p_{T}, and can identify the charge of high p_{T} muons.

The muon spectrometer is also a gaseous detector. It consists of four different types of chambers: the Monitored Drift Tubes (MDT), the Cathode Strip Chambers (CSC), the Resistive Plate Chambers (RPC), and the Thin Gap Chambers (TGC).

- The first two, MDT and CSC, are the precision tracking chambers. With tubes perpendicular to the beam direction, they can measure the muon tracks bent by the toroid magnets in the direction of the beam (the η).
- The other two – the RPC in the barrel region and the TGC in the end-cap regions – are trigger chambers, and provide an extra coordinate of tracking information. They identify bunch-crossings, define the p_{T} thresholds, and measure the tracks in the direction orthogonal to the precision tracking chambers (the ϕ). They send information quickly to the Level-1 trigger logic, to determine the multiplicity and approximate energy range of the muon tracks.

To accurately determine the momentum of the muons, the muon chamber layers are very well aligned, and the B-field is reconstructed, to determine the bending power of the tracks. The monitoring of B-field, combined with simulation, allows reconstruction of the positions of the toroid coils, and correction of the influences on the B-field from the metallic structures nearby, like the tile calorimeter.

In the Phase-I upgrade of the LHC, because of the higher luminosity, the inner part of the muon end-caps (Small Wheel) were replaced by the New Small Wheel (NSW), which has two more chamber technologies: the Micromegas detectors (MM) for precision tracking, and the small-strip Thin Gap Chambers (sTGC) for Level-1 trigger and tracking functionalities [79].

3.3.7. Forward Detectors

At the forward regions of both sides of ATLAS, there are three small systems: LUCID (LUminosity measurement using Cerenkov Integrating Detector), ALFA (Absolute Luminosity For ATLAS), and Zero-Degree Calorimeter (ZDC). LUCID and ALFA detect the luminosity delivered to ATLAS, and ZDC measures the centrality of heavy-ion collisions.

- LUCID is located at $\pm$ 17 m from the IP. It consists of Cherenkov tubes, and is the main monitor of the relative luminosity for ATLAS. It detects inelastic pp scattering in the forward region, therefore measures the integrated luminosity, and monitors the instantaneous luminosity and the beam conditions.
- ALFA is located at $\pm$ 240 m from the IP, and is as close as 1 mm from the beam. It consists of scintillating fibre trackers, and measures the absolute luminosity by measuring the elastic scattering in the forward direction with very small scattering angle (3 µrad).
- ZDC is at $\pm$140 m from the IP and measures the centrality of heavy-ion collisions by detecting the forward neutrons in the collisions. It consists of alternating quartz rods and tungsten plates.

3.3.8. Trigger and Data-Acquisition System

The Data-Acquisition (DAQ) system is responsible for read-out, conversion, and storage of data from the detector systems. Due to the limitation of resources, the data-taking must be limited to around 200 Hz, despite that the pp interaction rate is around 1 GHz at the designed luminosity of $10^{34}\,\mathrm{cm}^{-2}\mathrm{s}^{-1}$. Therefore, a trigger system that is responsible for online (real-time) selection of the events is needed. With an appropriate trigger rate, it rejects background events to reduce the amount of data while keeping events for the physics processes that are of interest.

There are three levels of triggers: Level-1 (L1) hardware trigger and High level trigger (HLT), which consists of Level-2 (L2) trigger and event filter. The DAQ system transmits the results between the levels and eventually puts the data into permanent storage.

- L1 trigger is based on hardware (electronics on or close to the detector, fast, not intended for flexible modification), it takes limited information from the calorimeters and the muon spectrometer, discards events with $< 2.5\,\mu$s latency, and reduces the data rate to 75 kHz[13]. This limit is from the bandwidth of the readout system. It looks for high p_{T} objects like photons, charged leptons, jets (including tau-jets), large missing and total E_{T}, and provides regions of interest to the L2 triggers. The data is saved in buffers during this process, and after the events pass the L1 trigger, the data is transferred from the detector to the Readout Drivers.
- L2 trigger is a software trigger, it uses all the detector data from the regions of interest, which is around only 2 % of the total data. After the L2 trigger, the trigger rate is reduced to around 3.5 kHz, and the average event processing time is 40 ms.
- The event filter is an offline analysis procedure. It reduces the data to the final rate of 200 Hz with an average event processing time of 4 s. The data is then saved to a permanent storage system.

3.4. The ATLAS Phase-II Upgrade

Detectors at hadron colliders at the scale of the LHC need fast and radiation-hard electronics and sensor, high detector granularity for better spatial resolution and pile-up mitigation, and large acceptance in η and ϕ. The ATLAS detector has collected data successfully at CoM energy of 7 to 8 TeV in Run 1, 13 TeV in Run 2, and 13.6 TeV at Run 3, as indicated in figure 3.4. Each Run was followed by a corresponding LS period, when certain sub-detectors were upgraded to continue to perform smooth data-taking.

During the LS1, the IBL was added to the tracking system [80]. And during the LS2, the Phase-I upgrade was performed, which includes improving the TDAQ of the LAr Calorimeter [81], adding the NSW and its readout system to the muon spectrometers [79], improving the TDAQ system [82], and adding the ATLAS Forward Proton spectrometer [83].

[13] Up to 100 kHz in Run 2 and Run 3.

A Phase-II upgrade is ongoing to deal with the challenges brought by the HL-LHC: with higher luminosity comes higher radiation dose, pile-up, and particle energy. The muon spectrometer [84] and TDAQ [85] will be upgraded, a High-Granularity Timing Detector (HGTD) will be added [86] to mitigate pile-up by using high-precision timing information, distinguish events that are close in space but not in time, and improve the performance in the forward region. As the ID will reach its lifetime, it is going to be replaced with a radiation-hard all-silicon Inner Tracker (ITk) [87, 88]. The data-taking in the Run 4 after the upgrade is planned to start in 2030 and last for around 10 years.

The ITk consists of the pixel detector and the strip detector, see figure 3.13 for the comparison between the layout of the ID and the ITk. This thesis will focus on the ITk pixel detector.

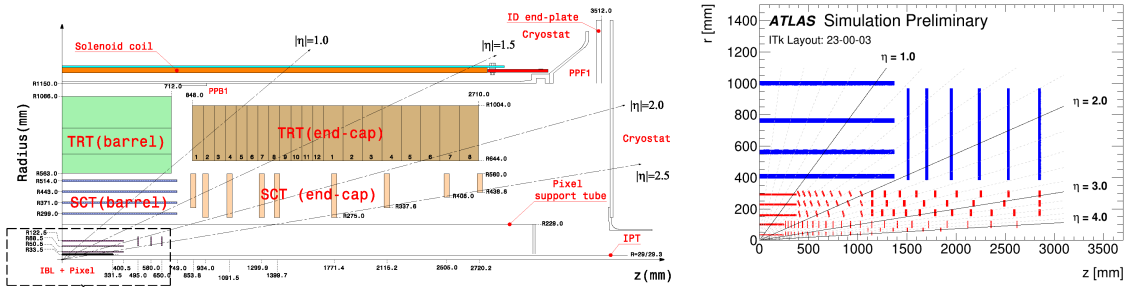

(a) A quarter-section of the ATLAS Inner Detector (ID).

(b) A quadrant of the ITk.

Figure 3.13: Layout of the ID and the ITk. In the ITk layout, the pixel detector is shown in red and the strip detector in blue. Figures from [80, 89].

The ITk pixel consists of five active layers of flat barrels and inclined rings (which are referred to as B0 to B4) and 5.5 layers of end-cap rings (R0, R0.5, R1 to R4). For details about the different layers, including r (the radius), $|z|$, and module type, see ref. [89]. The outer barrel and end-caps are designed to deal with an integrated luminosity of 4000 fb^{-1}, while the inner system (inner barrel and end-caps) is planned to be replaced after 2000 fb^{-1}. The different sections and expected fluence during the lifetime of operation in the HL-LHC are shown in figure 3.14. After taking a safety factor of 1.5 into account, the 1 MeV neutron equivalent fluence on the Layer 0 flat barrel at 3.9 cm radius (closest to the interaction point) is expected to be $1.31 \times 10^{16}\,\text{n}_{\text{eq}}/\text{cm}^2$, which is about 10 times that of the ID pixel Layer 0 ($1.35 \times 10^{15}\,\text{n}_{\text{eq}}/\text{cm}^2$) [18, 87].

Being the innermost layer, the ITk pixel detector faces high requirements. After the upgrade, it is more radiation-hard, has better granularity thus allows more accurate tracking of particles, and has an increased acceptance. See table 3.2 for a comparison between the pixel detector in Run 1 and Run 2, the IBL in Run 3, and the ITk pixel in the planned Run 4. Details about the sensors and front-end chips are introduced in chapter 4.

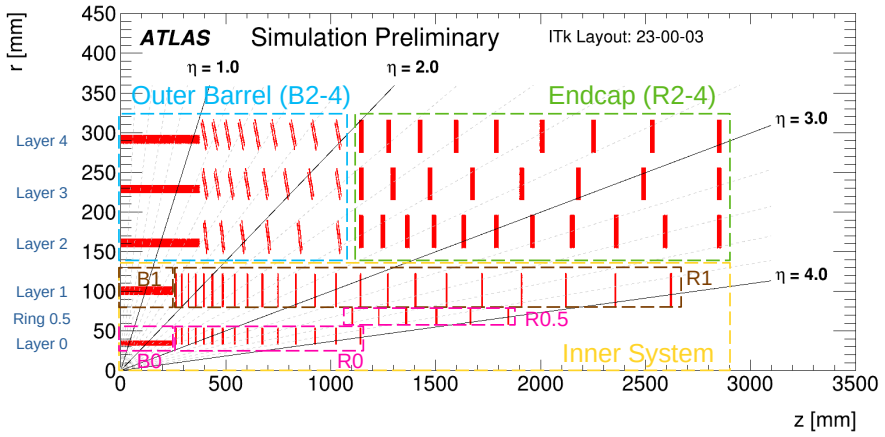

(a) Different sections of the ITk Pixel detector layers. The innermost layers marked in pink are equipped with 3D sensors. Image from [89].

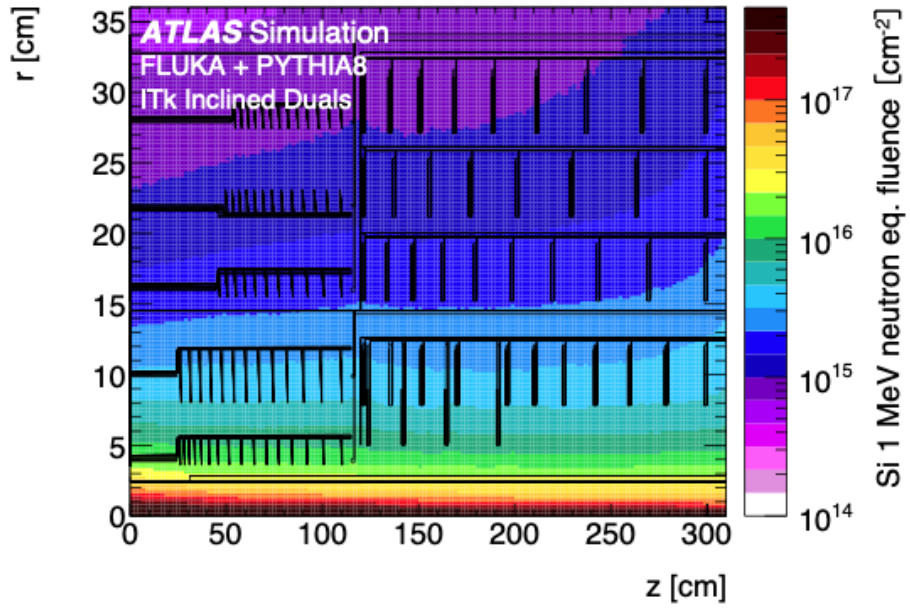

(b) The 1MeV neutron equivalent fluence distribution in the ITk Pixel detector normalised to 4000 fb^{-1} without safety margin. The geometry in this figure is outdated. Image from [87].

Figure 3.14: Different pixel regions and the simulation of the fluence.

Parameter		Pixel	IBL	ITk Pixel
Pixel pitch [µm^2]		50×400	50×250	50×50 25×100
Number of pixels per sensor (columns × rows)		160×18	$336 \times (80 \times 2)$	400×384
Sensor type	Planar 3D	n^+-in-n –	n^+-in-n n^+-in-p	n^+-in-p n^+&p^+columns in p^-
Sensor thickness [µm]	Planar 3D	250 –	200 230	100/150 150
Operation bias voltage [V] (Non-irrad/5×10^{15} n_{eq}/cm^2)	Planar 3D	-80/-600 –	-80/-1000 -20/-160	TBD TBD
FE chip		FE-I3	FE-I4B	RD53B
FE thickness		180 µm	150 µm	150 µm
Acceptance $\|\eta\|$		< 2.5	< 3.0	< 4.0
Number of modules	Planar 3D	1774 0	168 112	8276 396

Table 3.2: Comparison of the ATLAS Pixel, IBL, and ITk Pixel Detectors [18, 80, 87]. The bias voltages for ITk pixel module sensors are yet to be determined (TBD).

CHAPTER 4

Particle Physics Detectors

Particles are detected based on their interactions with the detector material. Therefore, the research and development of particle detectors require a thorough understanding of the various interactions between particles and matter. This chapter also introduces the principles of semiconductor detectors, concentrating on hybrid silicon pixel detectors, which were selected for the ATLAS ITk pixel detector. Since highly granular pixel detectors are usually the closest to the interaction point in high energy physics (HEP) experiments and are therefore subject to severe radiation damage, the principles of radiation damage are also discussed. The last section presents specific features of the ATLAS ITk pixel detector.

4.1. Interactions of Particles with Matter

Various types of particles interact differently with matter, mainly through ionisation, excitation, and multiple scattering.

- Charged particles mainly interact electromagnetically through the Coulomb potential with the electrons or nuclei of atoms in matter, exciting and ionising the atoms. The incoming charged particle itself loses energy and gets deflected.
  - Heavy charged particles: particles with masses significantly higher than the electron mass, such as $\mu^{\pm}$, p, and α. With enough kinetic energy, they are highly ionising and cause both ionisation and excitation.
  - Light charged particles: $e^{\pm}$, which mainly lose energy via Bremsstrahlung.
- Neutral particles:
  - Light neutral particles: γ and ν. Photons interact through the photoelectric effect, Compton scattering, and pair production, generating electrons that subsequently

interact with matter. Neutrinos do not go through strong or electromagnetic interactions and therefore almost do not interact with detector material. Neutrino detectors therefore utilises, for example, Cherenkov radiation emitted by the charged particles produced when neutrinos interact with water, as in the Super-Kamiokande [90].

– Heavy neutral particles: neutrons scatter in dense materials such as lead in calorimeters.

This section focuses on particles that interact with the tracker: heavy charged particles, electrons, and photons.

4.1.1. Heavy Charged Particles

Heavy charged particles easily carry high kinetic energy. In comparison, the binding energy of the shell electrons in the detector material is small. Therefore, the shell electrons can be considered free, and the incoming particles ionise the atom by knocking out shell electrons. The free charge carriers created from ionisation can then drift in an externally applied electric field, inducing a signal, therefore gets detected. This is explained in section 4.2.2.

The *average energy loss per path length* for heavy charged particles is illustrated in figure 4.1. It is also referred to as the *stopping power*, as it is normalised to the density of the material. In the region with $\beta\gamma$[1] between approximately 0.1 and 1000, the stopping power is described by the Bethe-Bloch formula [91–93], the form with shell correction term is given in equation 4.1.

$$-\left\langle \frac{dE}{dx} \right\rangle = K \frac{Z}{A} \frac{z^2}{\beta^2} \left[\frac{1}{2} \ln \frac{2m_e c^2 \beta^2 \gamma^2 T_{\max}}{I^2} - \beta^2 - \frac{\delta(\beta\gamma)}{2} - \frac{C}{Z} \right], \tag{4.1}$$

with $K = 4\pi N_A r_e^2 m_e c^2$, where:

N_A	is the Avogadro constant
r_e	$= \frac{e^2}{4\pi\varepsilon_0 m_e c^2}$ is the classical electron radius, where e is the electron charge, m_e is the electron mass, ε_0 is the vacuum permittivity, and c is the speed of light
Z	is the atomic number of the matter ($Z_{\text{silicon}} = 14$)
A	is the mass number of the matter ($A_{\text{silicon}} = 28$)
z	is the charge of the incoming particle in electron charge
β	$= \frac{v}{c}$, $\gamma = \frac{1}{\sqrt{1-\beta^2}}$ are the relativistic parameters, where v is the particle velocity
$T_{\max}$	is the maximum kinetic energy transfer in one collision
I	is the effective excitation energy of the material
C	is the sum of corrections from shell electrons, and is effective at lower energy range

[1] $\beta\gamma = \frac{p}{Mc}$ and therefore represents the momentum of a particle with mass M.

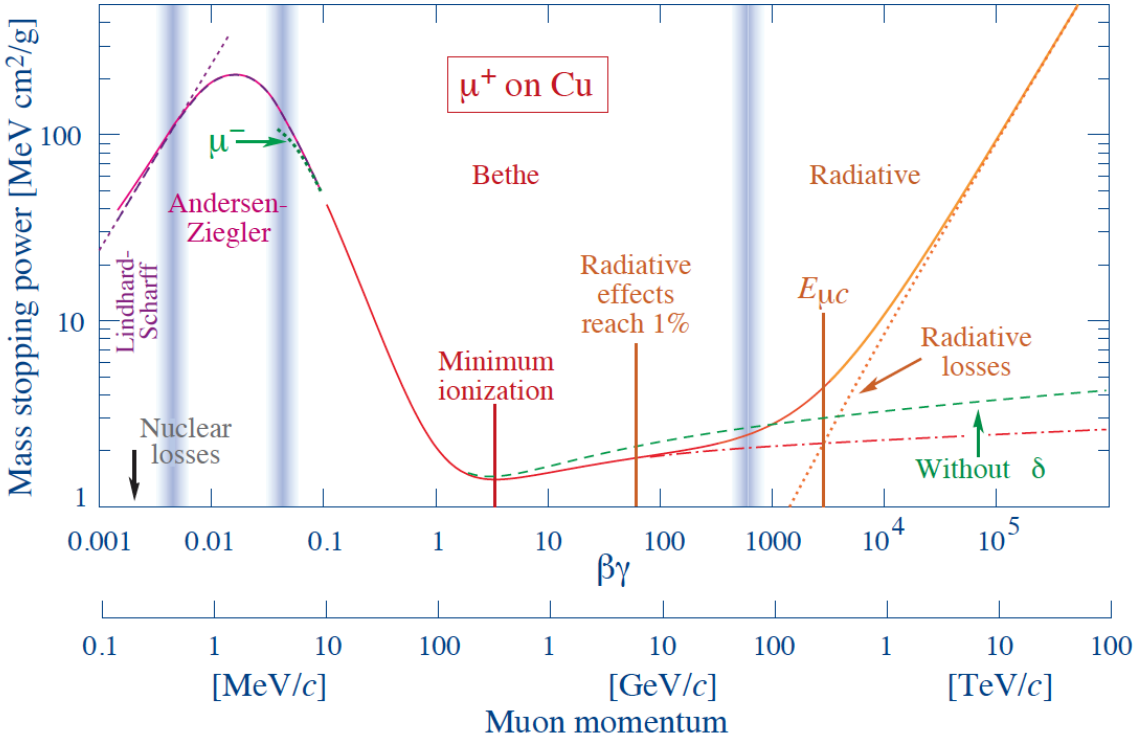

Figure 4.1: The stopping power $\left\langle \frac{dE}{dx} \right\rangle$ (energy loss per path length normalised to material density) of μ^+ in Cu versus $\beta\gamma$. The solid lines are the total stopping power. The vertical bands indicate the separation of regions with different approximations. Figure from [30].

The dependency of the stopping power on $\beta\gamma$ varies in different regions:

- In the region with $\beta\gamma < 0.1$, the Bethe-Bloch formula is not valid. Due to the low energy, ionisation is not the dominating process, since the electron binding energy is considerable in comparison, and the electrons are therefore not free.
- As momentum increases, the $\frac{1}{\beta^2}$ term dominates. It can be seen from figure 4.1 that the curve reaches its minimum when $\beta\gamma$ is around 3 to 4, where the particle loses the smallest amount of energy, and is referred to as a *minimum ionising particle* (mip).
- The rising green dashed line is the logarithmic part, where the stopping power is proportional to $\ln \beta\gamma$.
- At higher momentum, $\delta(\beta\gamma)$ – an attenuation coefficient from density effect – comes in. It originates from the polarisation effects where the electric field of the particle polarises the medium instead of ionising it. This effect is material dependent.
- The Bethe-Bloch formula only describes the electronic losses, but not the radiative losses, which dominates for e.g. energetic muons in cosmic rays. In the region with $\beta\gamma$ over 1000, radiative effects – e^+e^- pair production, Bremsstrahlung, and photonuclear interactions [94] – overpower ionisation. However, the cross sections for these processes are small.

The logarithmic rise is small for relativistic particles, which is the case for almost all particles to be detected in a high energy particle detector. Therefore, most relativistic particles are considered mips. This means smaller signals, which is not ideal for detection. However, it also means that when studying the response of the detector, there is no need to consider the type of the particle. In addition, effects from the detector material are also small because most materials have $\frac{Z}{A} \approx \frac{1}{2}$.

Therefore, a good estimation of the stopping power can be made for a mip, independent of the particle type or detector material: $\left\langle \frac{dE}{dx} \right\rangle_{\text{mip}} \approx 1.5\,\text{MeVcm}^2/\text{g}$. This can be used to estimate the number of charge carriers[2] generated by a mip, using the thickness and density of the detector material that the mip passes through. For example, for a Si layer with 100 µm thickness, a mip generates around 10 k electron-hole pairs.

It is worth mentioning that the Bethe-Bloch formula describes the mean energy lost by the incoming particle, but this is not necessarily equal to the energy that is deposited in the sensor to form the signal. The latter can be smaller: when a very energetic incoming particle transfers a large amount of energy to a single electron, the ejected high energy electron (which is called a *delta electron*) exits the detector without depositing all of its energy. This can be accounted for by replacing T_{max} – which is a limit that is purely kinematic – with T_{cut}, a lower value for the maximum energy transfer in one collision. In this case, T_{max} in equation 4.1 is replaced by T_{cut}, and the $-\beta^2$ term takes the form $-\frac{\beta^2}{2}\left(1 + \frac{T_{\text{cut}}}{T_{\text{max}}}\right)$, which effectively makes a cut on $-\left\langle \frac{dE}{dx} \right\rangle$. The resulting $-\left\langle \frac{dE}{dx} \right\rangle$ is known as the *restricted energy loss* [30].

The Bethe-Bloch formula is useful for the basic understanding of the energy loss of incoming charged particles. However, since it describes the mean value, it is heavily influenced by rare cases when a single collision has a large energy loss. These collisions increase the average, despite that most collisions are from mips. Since these incidences are rare, they also introduce large experimental fluctuation when determining the average of the energy loss experimentally. Instead, the *most probable energy loss* is useful in describing single particle energy losses. The actual distribution of the energy loss per distance follows the Landau distribution [95] – the most probable value of the energy loss is small, and there is a long tail at the higher energy loss end. This means that most particles deposit a small amount of energy.

When a particle with high momentum travels across matter, it loses energy along the path, and falls back to the low momentum range, where it is no longer a mip, and the energy loss is large within a very short distance. Therefore, the particle gets stopped, depositing almost all energy at the end of the path. This peak in energy loss at the end of the depth is the *Bragg peak*. It is beneficial in applications like radiation therapy for tumours, as the energy deposition is mostly targeted at the tumour, and healthy tissue that was traversed before the tumour gets a smaller radiation dose.

[2] Electron-hole pairs in Si, and electron-ion pairs in gas detectors.

4.1.2. Electrons

For electrons, the shell electrons in the detector material can no longer be considered free. Ionisation and excitation are still present, but it is important to consider in addition the effect of *Bremsstrahlung* radiation. This is when a charged particle with sufficient energy is deflected by the electromagnetic field of the electron or nucleus of an atom, and radiates a photon. The energy loss by Bremsstrahlung is $\propto \frac{Z^2 E}{m^2}$, and that by ionisation is $\propto \frac{Z \ln E}{m}$, where Z is the charge of the nucleus, and E and m are the energy and mass, respectively, of the incoming decelerated particle. Therefore, the effect of Bremsstrahlung dominates for incoming particles with low mass and high energy, and for material with high atomic number. As the energy of the incoming particle goes up, the energy loss by Bremsstrahlung reaches that by ionisation. This is referred to as the *critical energy* [96]. In Si, the energy loss of electrons through Bremsstrahlung exceeds that through ionisation at 47.87 MeV [97].

The energy loss per path length from Bremsstrahlung is proportional to the energy of the incoming particle, and is material dependent:

$$-\left\langle \frac{dE}{dx} \right\rangle = \frac{E}{X_0}, \tag{4.2}$$

where X_0 is the material dependent parameter called *radiation length*. It is defined as the average distance that the incoming electron travels until its energy is only $\frac{1}{e}$ of the initial energy due to Bremsstrahlung. The radiation length of Si is 9.365 cm [98]. This leads to another common definition of critical energy, which is when the energy loss via ionisation per X_0 equals the energy of the incoming electron [99]. With this definition, the critical energy is 40.19 MeV for Si [30].

A related concept is the *material budget*, which describes the thickness of the material in the number of radiation lengths. For multiple layers of different material with different radiation lengths, the material budget ε is the sum of all the materials along the path [100]:

$$\varepsilon = \sum_i \frac{x_i}{X_{0,i}}, \tag{4.3}$$

where x_i is the material thickness, and i is the index for the different materials.

4.1.3. Photons

Photons are charge neutral and therefore interact differently. They mainly interact through photoelectric effect, Compton scattering, and electron-positron pair production.

- *Photoelectric effect* occurs when an incoming photon gets absorbed by an electron. If the photon energy exceeds the binding energy, the electron is freed.
- *Compton scattering* refers to when the photon carries higher energy and is therefore not completely absorbed by the electron, but just scatters the electron off. The energy transfer depends on the scattering angle.

- *Pair production* happens when the incoming photon has an energy higher than double the electron mass, i.e. $> 1.022\,\text{MeV}$, and the energy turns into an electron-positron pair.

For high energy particle detectors, pair production is the most important process. The electrons and positrons created by photons then interact subsequently with the detector material, and emit Bremsstrahlung radiation (photons). This is the process that happens in the ECal: starting with either a photon or an electron, and a shower of photons and electrons is created.

For tracking detectors, pair production is undesirable. The photon either loses a considerable amount of energy or gets absorbed, therefore, the properties of the photon change, making them harder to detect and measure at the following sub-detector layers. Tracking of the $e^{\pm}$ pairs is also difficult. The mean free path for pair production is $\frac{9}{7}X_0$, and the tracker must minimise the radiation length and material budget to reduce pair production.

4.1.4. Multiple Scattering

Charged particles undergo *multiple scattering*: the elastic scattering via the Coulomb potential of the nuclei in the detector material, which occurs multiple times along the way, resulting in a zigzag path. A scattering angle can be defined as the overall angle after multiple smaller deflections. The cross section of the Coulomb scattering with a nucleus is determined by the Rutherford formula, which defines the Rutherford cross section, and shows that it is smaller for larger scattering angles:

$$\frac{d\sigma}{d\Omega} = z^2 Z^2 \alpha^2 \hbar \frac{1}{\beta^2 p^2} \frac{1}{4\sin^4(\theta/2)}, \tag{4.4}$$

where

θ is the scattering angle
z is the charge of the scattered particle
Z is the charge of the nucleus
$\alpha = \frac{e^2}{4\pi\varepsilon_0\hbar c}$ is the fine structure constant
β is the velocity of the scattered particle
p is the momentum of the scattered particle

The distribution of the overall scattering angle is approximately Gaussian with the mean at zero, and the standard deviation is given by [101]:

$$\theta_{\text{rms}} = \frac{13.6\,\text{MeV}}{\beta pc} z\sqrt{\varepsilon}\left[1 + 0.038\ln(\varepsilon)\right], \tag{4.5}$$

where ε is the material budget[3]. It can be seen that the effect of multiple scattering is larger for particles with lower momentum and detectors with a higher material budget.

Multiple scattering is not ideal for the tracker, since the incoming particles go through multiple changes of direction along the way, introducing angles to the path, which adds

[3]Which is simply $\frac{x}{X_0}$ for one single material, where x is the thickness of the material.

difficulty to track reconstruction. Therefore, the material budget needs to be minimised in the detector, to minimise multiple scattering.

4.2. Pixel Detectors

A *pixel*[4] is the smallest element of an image or imaging device. A regular camera can be regarded as the most common pixel detector, where photons are sensed by the pixels during a certain time of exposure, and the image is essentially the intensity distribution.

The pixel detector in HEP shares the high granular nature, which results in a better spatial resolution. However, pixel detectors in HEP need to be fast, so that they can transmit the data of the hits caused by the previous particles before the next hits arrive. They must have good time resolution, so that the particle can be assigned to the correct collision time (bunch-crossing). They must be radiation hard, so that they can be operated for longer before reaching the end of their lives. Instead of only visible light, they need to detect relativistic charged particles or photons, which are in keV to MeV energy regime. The hits need to be spatially separable so that the tracks can be easily distinguished and reconstructed. These requirements come from the need of being the closest to the interaction point of a particle accelerator and collider, where the rate of collision, as well as the particle energy is very high, as well as the need of being able to see short-lived particles. The tracking of pixel detectors, and how it is important for identifying particles for analyses is detailed in chapter 5, with the example of the ATLAS ID.

4.2.1. Silicon Hybrid Pixel Detectors

Silicon (Si) is the most commonly used material for semiconductor pixel detectors because of its small band gap, short radiation length, fast signal collection, low cost, availability, and the possibility of growing large and pure crystals. The band gap of Si is only 1.12 eV. Compared to other materials, less energy is needed to excite an electron in or below the valence band to the conduction band, or higher energy levels. With only 3.6 eV, an electron-hole pair can be created. Stronger signals can be created due to the production of more electron-hole pairs. A gas-filled ionisation chamber functions with basically the same principle, but with gas as the medium, it takes ∼20 eV for ionisation to happen. This means a Si semiconductor sensor provides better energy resolution.

Various semiconductor materials have been used in the past. GaAs was used in an early era before Si was easily available, but it is not radiation-hard enough for HEP experiments. Diamond is not massively available and has a larger band gap, which means the generation of charge carriers requires more energy, resulting in small signals. For CdTe and SiC, it is difficult to produce wafers with good quality. However, different materials are preferred in other fields due to the benefits that are not significant for particle physics. Please refer to section 2.7 in ref. [102] for more information, and for research on using diamond as an alternative for the ATLAS pixel detector, see ref. [103].

[4] "Pixel" is short for "picture element", with "pix" or "pics" being short for "pictures".

Pixel detectors nowadays fall mostly in two categories: *hybrid pixel detectors*, and *monolithic pixel detectors*.

Hybrid Pixel Detectors

"Hybrid" refers to the hybrid of sensor and readout chip. The active electronics are on the readout chip. The sensors and readout chips are produced separately before being connected together, each sensor pixel is connected to a readout pixel. Figure 4.2 illustrates the structure of one single hybrid pixel cell, with bump-bonding technology. The thicknesses for the sensor and chip are typically in the range of 0.1 mm. When a particle traverses through the sensor, it creates free charge carriers, which drift across the volume, inducing a current. The charges then get collected through the bump-bond, forming a signal, which is read out by the front-end readout chip. This process, as well as the principles of sensors are explained in detail in section 4.2.2. The readout chip is introduced in section 4.2.3.

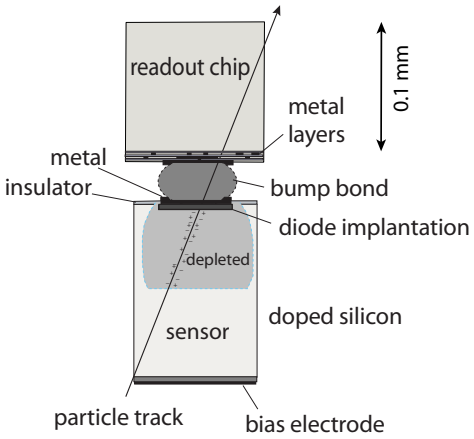

Figure 4.2: One hybrid pixel cell: a sensor pixel bump-bonded to a readout pixel. Image from [97].

The readout pixel and its sensor pixel are usually the same in size and geometry, but having different sizes is also possible, see [104]. The pixel is typically rectangular, and there are recent developments on hexagonal pixels [105]. When the length and width of the pixel electrodes differ largely, e.g. a few cm vs tens of µm, the structure is called a strip instead of a pixel.

The connection between sensor and readout pixels can no longer be done via wire-bonding as for strip detectors, as arrays of pixels, compared to lines of strips, result in one more dimension to interconnect. The tiny size and the large amount of pixels also increase the difficulty. This makes special interconnection technologies with high-density necessary. The step of interconnecting the sensor and the readout chip is called *hybridisation*. The most prevalent hybridisation technology is the *bump-bonding* technology, it is performed in three steps: dicing of wafers, under bump metallisation on the sensor, and flip-chip to connect the bumps deposited on the chip with the under bump metallisation on the sensor. Hybridisation can also be done with Anisotropic Conductive Films, which is an adhesive epoxy film with conductive micro-particles. This technology is still under development [106].

Thousands of these sensor-readout chip ensembles can be put together by planar integration technology into a matrix of pixels. For a hybrid pixel detector, each of these matrices can be assembled with other components into an independent unit called a *module*. A module typically covers a few cm^2, and a large number of modules can cover a large area, making up a pixel detector with large spatial acceptance range.

Monolithic Pixel Detectors

For monolithic pixel detectors, the readout electronics and the sensor are built on the same wafer (piece of silicon) in the same process. The manufacture process is simpler since there is no need of bump-bonding, which avoids the accompanying restrictions like cost, logistics, and the minimum pixel pitch (size of one pixel). The material budget is also smaller. Infusing the three items (sensor, FE chip, and interconnection) into one design before producing makes it easier than making three separate designs and complicating the production tasks.

However, the structure is more complex, the stitching between sensor and readout is complicated, and some compromise between the function of sensor and readout is often needed. Having to fuse the sensor and chips takes away the liberty of using some technologies. In the case of the hybrid pixel detectors, the separation of tasks facilitates making use of novel chip design.

For the ATLAS ITk pixel detector, Si hybrid pixel modules were chosen, which is the main focus of the later sections.

4.2.2. Sensors

A sensor "senses" the particles to be detected. From interaction between the particles and the sensor material (normally Si), signals get generated and propagated to the readout electronics. The main part of a sensor is the *pn-junction*.

The pn-junction

A pn-junction is formed when an n-doped and p-doped material contact each other, see figure 4.3(a) for a pn-junction with high n-doping concentration and low p-doping concentration. n-doped material is rich in electrons as charge carriers, and in p-doped material, holes are the majority charge carriers. The charge carriers diffuse to the other side, recombine with the local majority charge carriers, forming a region that is depleted of free charge carriers at the interface. This region is called the *depletion zone*. It is also named the *space-charge region*, because the region is electrically charged locally (while the whole space-charge region is still charge neutral to the outside).

As the depletion zone is electrically charged, an electric field is built up. When particles pass through, they ionise the material, therefore generating signal charges, which drift due to the electric field. This induces a current, which gets detected as the signal.

Because the depletion zone is free from free charge carriers, there is less interference with the signal charges, allowing a larger primary signal. Therefore, it is beneficial to have a large depletion zone. This is done by applying an external voltage to further remove the majority charge carriers from the corresponding sides, this voltage is called the *reverse bias voltage*, as shown in figure 4.3(b).

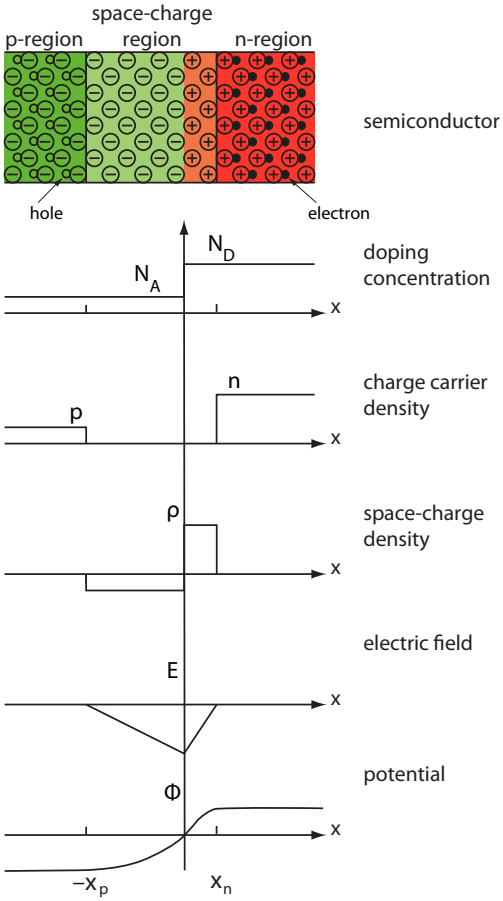

(a) A pn-junction & depletion zone (space-charge region), the doping concentration, charge carrier density, space-charge density, and electric field is also illustrated.

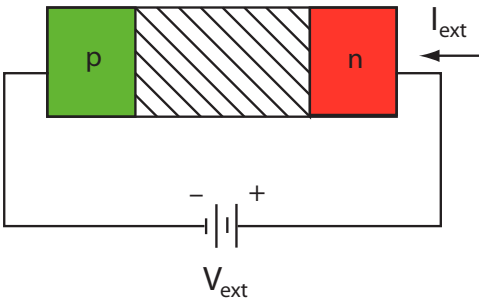

(b) Reverse bias widens depletion zone.

Figure 4.3: pn-junction and reverse bias. Images from [97].

Normally, a high-doped shallow implant is put in a low doped substrate bulk. Due to the low doping concentration, a larger volume is needed to provide the same amount of charge carriers, therefore the depletion zone is mostly in the bulk. Assuming that the doping concentration is homogeneous in both the bulk and the implant, and boundaries of the junction are cleanly separated, the depleted depth is:

$$d \approx \sqrt{\frac{2\varepsilon_0 \varepsilon_{\mathrm{Si}}}{eN} V}, \tag{4.6}$$

where:

- d is the depth of the depletion zone
- N is the bulk doping concentration (the lower one)
- V is the bias voltage
- e is the electron charge
- ε_0 is the vacuum permittivity
- $\varepsilon_{\mathrm{Si}}$ is the relative permittivity of Silicon

When the reverse bias voltage is increased, the depth of the depletion zone increases. This increases the signal-to-noise ratio (S/N).

Signal Formation

When the signal charge starts to drift because of the electric field, a signal is already detectable at the collecting electrode due to the induced electric current. This means faster detection, as opposed to only being able to detect the signal when the signal charge arrives at the collecting electrode. The instantaneous current induced is given by the Shockley-Ramo theorem [107]:

$$i = e\boldsymbol{E_W} \cdot \boldsymbol{v}, \tag{4.7}$$

where:

- i is the instantaneous current induced on the electrode
- e is the electron charge
- $\boldsymbol{E_W}$ is the weighting field, which is the electric field in the sensor when a unit potential was applied to the electrode (while the other electrodes are at 0 potential)
- $\boldsymbol{v}$ is the drift velocity

Leakage Current

Even without radiation coming through the sensor to generate current, a current still exists in the sensor. This is known as *leakage current* (or *dark current*). Main contributors to leakage current include volume generation, surface generation, and avalanche breakdown. Volume generation leakage current comes from free charge carriers diffusing from the volume that is not depleted to the depletion zone, as well as thermal generation.

For detectors, thermally induced current generated in the sensor volume dominates. Thermally generated electron-hole pairs can come from impurities, which add extra energy levels in the band gap, facilitating generation and recombination of electron-hole pairs.

The leakage current in a depleted bulk is proportional to the volume of the depletion zone:

$$I_{\text{leak}} = -e\frac{n_i}{\tau_g}Ad = -e\frac{n_i}{\tau_g}A\sqrt{\frac{2\varepsilon_0\varepsilon_{\text{Si}}}{eN}V}, \tag{4.8}$$

where:

- I_{leak} is the leakage current in the depleted bulk
- A is the depleted area
- d is the depletion depth
- n_i is the intrinsic charge carrier concentration
- τ_g is the generation lifetime

This means that volume-generated leakage current is proportional to $\sqrt{V}$. When the depletion zone reaches the backside, a (small) surface generation contribution comes in. Avalanche breakdown starts at regions with high electric field, at this stage, the leakage

current increases steadily. Further voltage increase leads to electrical breakdown at the junction. This is a hard breakdown, where the current increases suddenly by a few orders of magnitude and could be deadly to the sensor. The voltage at which this occurs is called the *breakdown voltage*.

Leakage current also increases with temperature. This temperature dependency comes from the intrinsic charge carrier concentration n_i and the generation lifetime τ_g. The standard parametrisation of the relation between leakage current and temperature is [108]:

$$I_{\text{leak}} \propto T^2 \exp\left(\frac{-E_{\text{eff}}}{2kT}\right), \tag{4.9}$$

where:

- T is the absolute temperature
- E_{eff} is the effective band gap (also called activation energy or effective energy) with a best-fit value 1.21 eV
- k is the Boltzmann constant

An IV (leakage current vs bias voltage) curve could give information on almost all defects of the sensor, and the main characteristics to be checked are the breakdown status and the level of the leakage current. The measurements need to be taken at a defined temperature. Otherwise, scaling of results according to equation 4.9 needs to be considered when comparing measurements.

Capacitance

A sensor is fully depleted when the depletion zone expands across the entire sensor. It can be approximated as a parallel plate capacitor, and functions as a pn-diode under reverse bias with voltage V. Substituting in the expression for the depletion zone depth (equation 4.6) into that of the capacitance for a parallel plate capacitor gives:

$$C(V) = A\frac{\varepsilon_0\varepsilon_{\text{Si}}}{d(V)} \approx A\begin{cases}\sqrt{\frac{\varepsilon_0\varepsilon_{\text{Si}}eN}{2V}} & \text{for } V \leq V_{\text{dep}} \\ \frac{\varepsilon_0\varepsilon_{\text{Si}}}{D} & \text{for } V \geq V_{\text{dep}}\end{cases}, \tag{4.10}$$

where:

- C is the capacitance
- A is the area of the sensor
- d is the thickness of the depletion zone, which depends on the reverse bias voltage
- D is the thickness of the depletion zone when fully depleted, which is the sensor thickness
- V_{dep} is the full depletion voltage

Rearranging gives:

$$\frac{1}{C(V)^2} \approx \frac{1}{A^2}\begin{cases}\frac{2V}{\varepsilon_0\varepsilon_{\text{Si}}eN} & \text{for V} \leq \text{V}_{\text{dep}} \\ \left(\frac{D}{\varepsilon_0\varepsilon_{\text{Si}}}\right)^2 & \text{for V} \geq \text{V}_{\text{dep}}\end{cases}, \tag{4.11}$$

Therefore, after plotting $\frac{1}{C^2}$ against the reverse bias voltage, the two regions separated by V_{dep} behave linearly, being a ramp and a constant plateau, to which one can fit two straight lines, and the voltage that corresponds to the intersection point is the *full depletion voltage* V_{dep}.

Also, because increasing bias voltage decreases the capacitance of the sensor, the signal to noise ratio S/N is larger at higher bias voltage.

Punch-through

The depleted zone under the doped implant also grows laterally with voltage, as illustrated in figure 4.4: consider two neighbouring p^+-type implants, one is biased with V_{B}, the other is floating. When increasing V_{B}, the depletion zone under this implant grows both vertically along the thickness, and laterally toward the other floating implant, which is at voltage $V_{\text{S}} \approx 0$.

The *punch-through* (PT) voltage V_{PT} corresponds to the voltage when the depletion zone under V_{B} reaches the one under V_{S}. Due to the difference in electric potential, the depletion zone under V_{S} gets depleted further, the holes under V_{B} move to the implant under V_{S}, forming a PT hole current (the arrows), therefore changing the potential of V_{S}. V_{PT} depends mainly on the distance between the implants and the substrate doping.

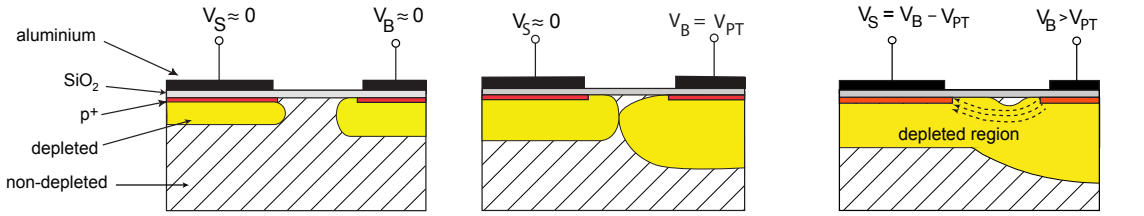

(a) Without bias.

(b) The reverse bias voltage at which depletion zones just connect is V_{PT}.

(c) Reverse bias voltage exceeds V_{PT}, depletion zone continues to expand.

Figure 4.4: Punch-through mechanism. V_{B}: reverse bias voltage; V_{S}: pixel/strip potential; V_{PT}: punch-through voltage. Image from [97].

The PT effect makes it possible to bias the pixel sensors via the PT biasing technique. All pixel implants (electrodes connected to the bump-bonds) need to be biased, however, they cannot be directly connected, since this would conduct the signal across all pixels, losing the point of having high granular pixels for spatial resolution. Therefore, neighbouring each pixel electrode, there is also a PT implant. All PT implants are connected to a *bias grid*, and biasing one point on the bias grid would bias all PT implants, therefore biasing all the pixel electrodes indirectly through the PT mechanism.

4.2.3. Front-End Readout Chips

Front-end (FE) electronics in detector physics normally refers to all the on-detector electronics. "Chip" in general refers to a piece of silicon, as well as the additional structures on it. For hybrid pixel detectors, a FE chip, or also called a readout chip, is an Application-Specific Integrated Circuit (ASIC) chip. It consists of the same number of pixels as the corresponding sensor, each FE pixel bump-bonded to a sensor pixel, and reads out the signal from the sensor pixel. In the context of the ATLAS ITk pixel detector, the FE chip is often simply referred to as the "FE" or the "chip".

A FE readout pixel is a pixel unit cell (PUC) with an integrated circuit. The circuitry transfers hit information to the bottom of the chip for the next process. As technology develops and the size of transistors shrinks, more complicated integrated circuits can be put on even smaller FE pixels.

There are a lot of different designs for FE chips. But in general, a FE chip is divided into an active area and a periphery. The active area contains the PUCs, and the periphery contains global control functions. See figure 4.5 for an illustration of PUCs in the active area and the peripherals, as well as a circuit diagram for a generic PUC.

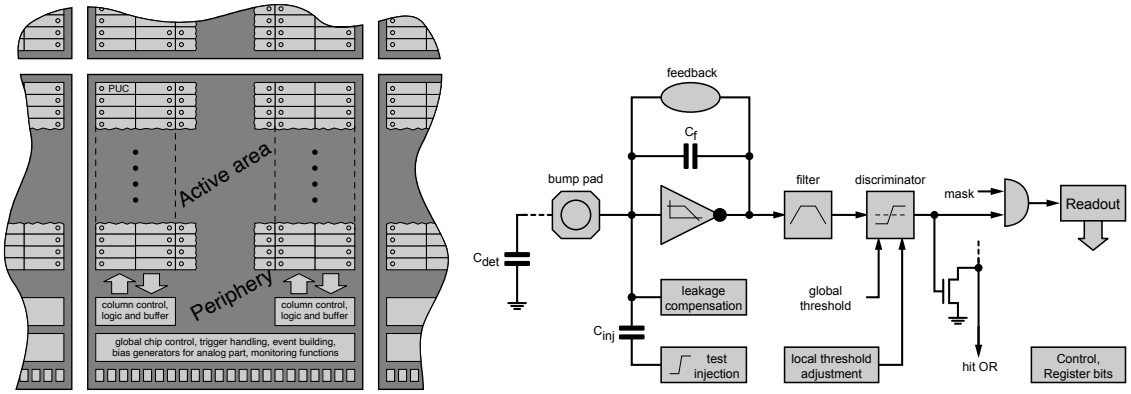

(a) Areas of a front-end chip.

(b) Generic internal circuit in a pixel unit cell.

Figure 4.5: A front-end chip consists of an active area with an array of pixel unit cells and a chip periphery. Each pixel unit cell includes various components, generally as shown in (b). Images from [102].

Pixel Unit Cell

A PUC has an analog part and a digital part. The sensor pixel bump-bonded to it can be considered as a capacitor C_{det}. The capacitance is from the bulk and inter-pixel capacitance. The signal is essentially a current, which is charges moving for a period of time. For a mip, the drift time is around 10 ns, with a charge around 4 fC. The signal travels through the bump bond, and since it is very small, firstly goes through a *charge-sensitive preamplifier*. Together with the *feedback capacitor* C_{f} at the fF level, it converts the input charge to a *voltage* (in an ideal scenario $\Delta U_{\text{out}} = \frac{Q_{\text{in}}}{C_{\text{f}}}$). For the use of particle physics, the preamp

should have a high gain (more than 100), high bandwidth, and low power consumption (around 50 µW).

The voltage then goes through a filter (also called a *shaper*), which is a *band-pass filter*. A pulse consists of waves of different frequencies, the shaper filters away the frequencies at the low and high end, which is more from noise due to e.g. leakage current and input transistor, and could also shorten the pulse.

Then the *discriminator* takes the shaper output, and digitises the signal according to a threshold, as shown in figure 4.6. The threshold needs to be low enough to have a higher detection efficiency, but not too low to allow too much noise. The duration for which the signal passes the threshold (the "*time-over-threshold*" – ToT) can be used to determine the charge of the particle.

As illustrated in figure 4.6, the signals with larger and smaller amplitudes start at the same time, but after the discriminator, it seems as if they started at different times, since the response time for the higher signal is shorter. This time difference is called the *time-walk*. This can cause a hit with smaller charge to be detected later, therefore matched with the wrong bunch-crossing or trigger[5]. If the amplification is larger, the signal has a steeper rise (shorter rise time), which causes smaller time-walk. However, this would cause higher signal and leakage current, therefore higher power dissipation.

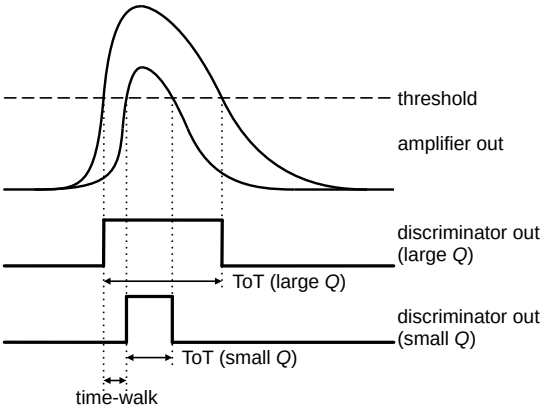

Figure 4.6: A discriminator digitises the signal according to the set threshold. As a result, two signals occur at the same time but with different amplitudes appear to start at different times. The resulting time difference is the time-walk, and the time that the signal exceeds the threshold level is the time-over-threshold (ToT). The pulse shape in this figure is for illustrative purpose only.

Each pixel may have a different threshold due to individual differences of their components, like the transistors, preamplifier, and the pixel resistance. Therefore, to even out the threshold, it is possible to tune each pixel individually. In practice, the threshold is implemented by a Digital to Analog Converter (DAC), and trim values can be stored in each pixel as a few bits in a few digital registers. This allows tuning of individual pixels

[5] A trigger is a fast signal that marks the time of a hit.

with high precision.

A HitOR logic exists on either every column, or one on the whole chip. This combines the hit information on all the pixels with an "OR" logic: as long as one pixel detects a hit, the HitOR sends a trigger. This is called the *self-triggering mode*. When doing tests with a radioactive source, self-triggering mode saves a lot of time compared to random-triggering. Since the event may happen at any time, a random trigger requires the trigger and event to coincide. However, self-triggering makes sure that an event is recorded, as long as it creates a hit anywhere on the chip.

There are also controls on the chip that can, for example, mask a pixel by disabling the readout of an individual PUC when a FE pixel is broken or when a sensor pixel is noisy, disable the HitOR, or switch the chip to a mode for digital tests.

An injection circuit makes it possible to test the PUCs at wafer level via injecting a known amount of charge into the pre-amplifier input. The circuit can work via applying a voltage to an *injection capacitor* with a known value C_{inj}. This voltage can be generated either globally, e.g. from the chip periphery, or per pixel from the voltage input. Alternatively, a current can be injected for a certain time interval, to give a defined amount of charge.

The PUCs must be small, fast, radiation-hard, have a well-defined threshold, with low heat dissipation, and give low noise after amplification of the signal charge.

Chip Periphery

Chip periphery controls the active part of the FE chip. It contains all the global analog and digital circuits for system functionalities of the chip: biasing, configuring, monitoring and read out. It performs global tasks like receiving and buffering the data (hit information) from the signals, sending the data to the DAQ, receiving the configuration of the chip, which contains the threshold configurations like global and per pixel threshold trim values, disabling or switching off pixels, switching readout modes, and injecting capacitance or digital signal. It can also process trigger information and build events. It contains all the global analog and digital circuits for system functionalities of the chip: biasing, configuring, monitoring and read out.

The wire-bond pads are also at the periphery. There are redundancies – multiple of the wire-bond pads with the same function – so that there are back-ups when some wires are damaged or malfunction. Especially for supplying voltages for the analog and digital parts, multiple wires connected in parallel reduce the voltage drop due to resistance of the thin wires, and allow supplying sufficient power.

4.2.4. Printed Circuit Board

In addition to the sensor and the FE chip, another piece of electronics that needs to be connected, to bias the sensor, power the FE chips, and transmit the signal to the DAQ system. This can be done through either connecting a printed circuit board (PCB), or

integrating the functionalities to the sensor, using e.g. the Multichip Module Deposited (MCM-D) technology, which was proposed as one of the prototypes for the innermost layer of the ATLAS ID [104].

The ATLAS ITk pixel detector uses the PCB option to hold passive components, and interfaces with the FE chip and the sensor. The PCB is flexible, and is therefore referred to as a "flex". It has a power connector to connect to both the LV and the HV, to distribute power to the module, and bias the sensor. The voltages are routed through Cu traces and wire-bonds, LV to the wire-bonding pads on the FE chips, and HV to the back of the sensor. A data connector interconnects the signal from the module to the rest of the DAQ system. There is also an NTC on the flex, which provides module temperature measurements.

4.2.5. Radiation Damage

The high fluence in collider experiments, especially in the HL-LHC, can severely damage both the sensors and the electronics. Silicon is easily subject to radiation damage due to its crystalline structure, and abundant research exists on radiation damage of pixel detectors.

Radiation damage to Si is commonly divided into two categories: bulk damage and surface damage.

- Bulk damage is the damage of the Si crystal lattice, therefore of the substrate. It happens in general due to non-ionising energy loss (NIEL). NIEL is caused by the incoming particle interacting with the nuclei of the lattice atoms. The result is phonon excitation of the lattice (which does not result in damage), and dislocation of the lattice atoms or other types of distortions of the lattice. This affects the sensor characteristics, especially the charge collection efficiency.
- Surface damage is the damage of the surface and interfaces (normally between Si and SiO_2). It originates from ionisation energy loss (IEL). Surface damage happens to both sensors and chips, but mainly damages the readout electronics, since it causes threshold shifts of transistors or undesirable currents between transistors.

Bulk Damage

Figure 4.7 shows possible damages of the crystal lattice from NIEL. When particles collide with the nuclei of the atoms in the lattice, they can knock off atoms, thus create vacancies. The knocked off atoms become interstitials if they are displaced to another location in the lattice. Other types of possible damages are e.g. when neutrons get captured into the nucleus of an atom.

The fluence Φ is the number of particles traversing a unit area, normally per cm^2, during a certain amount of time. To allow quantification and comparison of radiation damage from different types of particles, the fluence from various particles is by convention normalised to 1 MeV *neutron equivalent fluence* Φ_{eq}, with the unit n_{eq}/cm^2. The conversion to neutrons and the specifics of the conversion were established for Si via many studies [109–111].

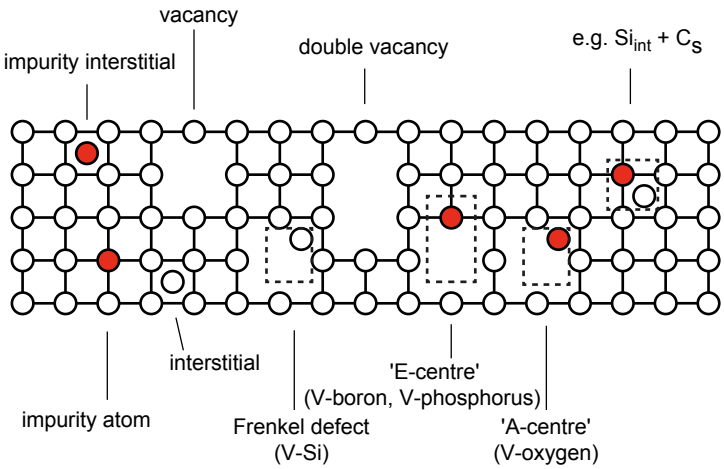

Figure 4.7: Types of radiation damage in a Si lattice. Red circles: existing impurity atoms e.g. from crystal growth; V: vacancy; Si_{int}: lattice interstitial; C_S: carbon atom which substituted a Si atom in the lattice. Image from [97].

The innermost layer of the ATLAS ID pixel detector, which is 5 cm from the beam-pipe, was designed to survive a fluence of $\Phi_{eq} \approx 10^{15}$ n_{eq}/cm^2 at the LHC for ten years of operation [18]. And for the HL-LHC, the maximum fluence for the innermost layer (at 3.9 cm) is 1.31×10^{16} n_{eq}/cm^2 [87] before the planned replacement when reaching the integrated luminosity of 2000 fb^{-1} after 5 years of operation.

Effects of substrate damage:

- Increase of leakage current

  The defects, similar to impurities, add extra energy levels in the band gap, facilitating the generation and recombination of charge carriers, therefore causing larger leakage current. The increase of leakage current is proportional to the fluence Φ [112]:

  $$\frac{\Delta I_{leak}}{V} = \alpha\Phi, \tag{4.12}$$

  where V is the depleted volume, and α is the damage rate.

  Parametrisation of α was done in various studies [113, 114], and α is related to the annealing temperature and time[6].

  The higher leakage current leads to higher power dissipation, which in turn increases the temperature, which leads to an even higher leakage current. This vicious circle is called *thermal runaway* and could lead to the inability to operate the sensor. This is why cooling is needed in detector operation and components testing.

- Change of effective doping concentration

[6] Annealing is the treatment of a solid at certain temperature over a certain period of time, it causes changes to the defects, as introduced later in this section.

After substrate damage, the doping concentration is, instead of pure donor or acceptor concentration, an *effective doping concentration*[7] N_{eff}. It can be determined from the full depletion voltage [102]:

$$|N_{\text{eff}}| = \frac{2\varepsilon_0\varepsilon_{\text{Si}}V_{\text{dep}}}{ed^2}. \tag{4.13}$$

This is the effective space charge density defined by the sum of all donor and acceptor-like states, with one of them being defined as negative. By convention, N_{eff} is defined as positive for n-type material, and negative for p-type material. This equation assumes simple diodes and constant space charge.

$|N_{\text{eff}}|$ is related to the fluence. See figure 4.8 for the relation between V_{dep} and fluence Φ_{eq} of short range α-particles on an n-doped material. After irradiation of $\Phi_{\text{eq}} \sim 2$ to $5\times\ 10^{12}/\text{cm}^2$, the space charge density drops to close to 0. With further irradiation, the material starts to behave like p-type, since the concentration of acceptor-like defects (with negative space charge) starts to overpower. This is called type inversion or space charge sign inversion. There is no type inversion for sensors with a p-type bulk, the V_{dep} behaves as on the right side of the figure and increases directly.

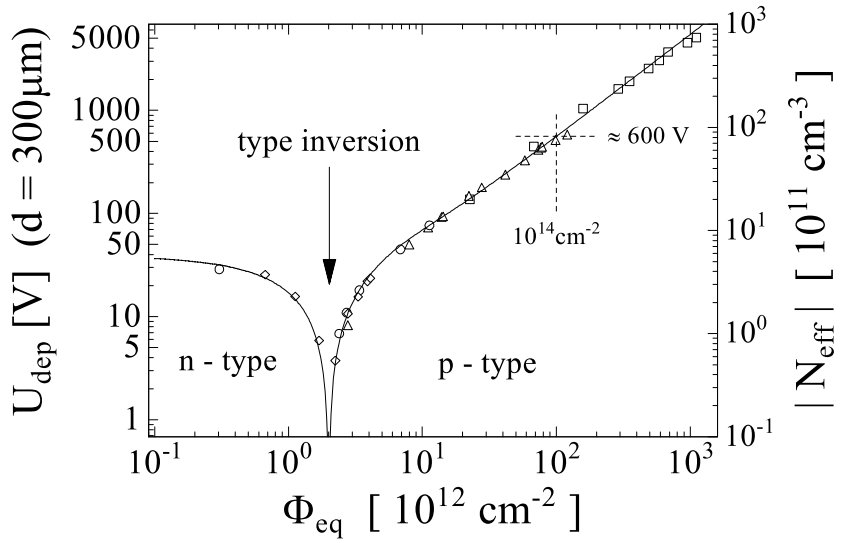

Figure 4.8: Type inversion, shown via V_{dep} or absolute effective doping concentration of a 300 µm thickness Si sensor immediately after irradiation vs fluence [113]. Figure from [102].

The influence on sensor operation is that if the sensors are already irradiated till type inversion, the rise of net doping concentration leads to increase of V_{dep}. This means that the sensors need to be biased at a higher operation voltage, which has technical limits like causing sparks. This means one might need to continue to take data with partially depleted sensors, therefore getting decreased signals.

- Carrier trapping

[7] Also called net doping concentration.

The defects can also trap the signal charge in the depletion region for some time. When the trapping time τ_t is longer than the charge collection time, the signal height is reduced. The relation between the trapping time and fluence is [102]:

$$\frac{1}{\tau_t(\Phi)} = \frac{1}{\tau_t(\Phi = 0)} + \gamma\Phi, \tag{4.14}$$

where γ is a coefficient that was measured and is different for different types of irradiation.

Surface Damage

Surface damage is mostly caused by IEL, it can happen to both semiconductor sensors and electronics. Compared to NIEL, IEL is a smaller problem in semiconductor lattices: because ionisation is mostly reversible there, it normally does not leave any permanent damage in the crystal. However, it does cause permanent damage at surface or interfaces, mostly in the SiO_2 layer overlaid on the surface, and the interface between Si and SiO_2.

The problematic damage caused by IEL is when ionisation happens in the oxide, creating electron-hole pairs. Even though most of the electron-hole pairs immediately recombine, some remain and cause change to the total charge at the oxide layer (oxide charge): electrons have high mobility in SiO_2, therefore they are collected by nearby electrodes. But the hole mobility is $\sim 10^6$ times lower, because of the abundant shallow hole traps in SiO_2 capturing the holes. The holes may also remain at the interface between Si and oxide due to the deep hole traps (e.g. interstitial oxygen atoms) there. The Si lattice can contain H^+ impurities, which after being released could form traps at the interface. It is also possible to create positive oxide charges from Si atoms with a dangling bond [115–117].

These effects increase the total oxide charge, therefore shift the threshold of the transistors and generate parasitic transistor structures [118]. Surface damage could also generate extra states at the interface and add to the surface generation current when the depletion zone extends to the surface [117].

Single Event Upset

Single event upset (SEU) refers to a bit flip of a storage element caused by ionising radiation. It is especially induced by slow heavy ions that cause very strong ionisation, which can deposit a large amount of charge on a small point of the Si. If this happens to be on a storage node, like a flip-flop, latch, or a static or dynamic random access memory cell itself, it can cause a bit flip. This could lock up the whole system. Standard solutions include error correcting logic, checksum, and triplicating the most critical control storage elements, where the decision can be corrected by majority voting.

Annealing

Annealing is the physical change of the defects in a solid at a certain temperature after a period of time. In a crystal, this can happen when defects migrate, recombine to form a

complex (a defect consists of multiple constituents), or when a complex dissociates. This process can lead to formation of the original lattice structure, or new defects. Therefore, the effect of annealing can be either beneficial (referred to as *short-term annealing* or beneficial annealing), or adverse (*reverse annealing*).

The Hamburg model is the most well-accepted parametrisation of the effective doping concentration and its dependence with time [114, 119]. The expression is:

$$\Delta N_{\text{eff}}(\Phi_{eq}, T_a, t) = N_A(\Phi_{eq}, T_a, t) + N_C(\Phi_{eq}) + N_Y(\Phi_{eq}, T_a, t), \tag{4.15}$$

where:

T_a is the annealing temperature
N_A, N_C and N_Y are different terms, their effects are shown in figure 4.9.
- N_A is the short-term annealing component and is beneficial
- N_C is the stable damage, it is independent of annealing time and temperature
- N_Y is the reverse annealing component, and it is the term that is responsible for the increase of V_{dep} at a longer time scale

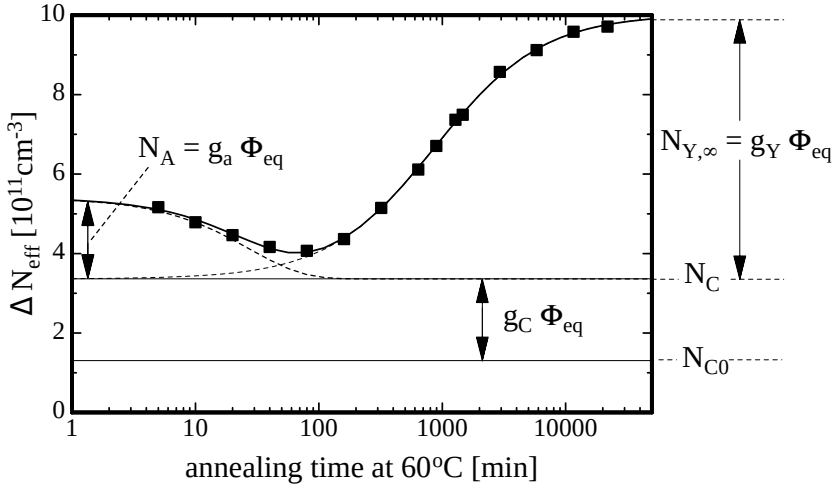

Figure 4.9: Annealing of a sample irradiated with fluence $\Phi_{\text{eq}} = 1.4 \times 10^{13}\,\text{cm}^{-2}$: radiation-induced changes in effective doping concentration vs annealing time at 60 °C [114, 120]. Figure from [102].

To prevent reverse annealing, the detectors at the LHC keep the cooling system operating even during shut-down periods, because at room temperature, reverse annealing causes V_{dep} to increase considerably after just a few weeks.

Annealing of surface damage can happen via electrons either tunnelling from Si, or released via thermal effect from the valence band, and move into the oxide traps [97].

4.3. ITk Pixel Modules

This section introduce specifically ATLAS ITk pixel detector modules. They are hybrid modules consisting of sensors bump-bonded with FE readout electronics. This bump-bonded sensor and FE hybrid is called a bare module (BM), which is in addition assembled via a homogeneous glue layer and wire-bonded to a flexible PCB referred to as a "flex". Two types of modules are used: quad modules and triplet modules. Quads consist of four FEs bump-bonded to one $4 \times 4\,\mathrm{cm}^2$ sensor, and triplets comprises three FEs, each bump-bonded to a $2 \times 2\,\mathrm{cm}^2$ sensor.

The modules are referred to by the type of the FE chip. The ongoing studies are on RD53B (in ATLAS also called ITkPix). Figure 4.13 shows an ITkPixV1.1 quad module from the flex side[8], cross section schematics, and both sides of an ITkPixV1.1 BM.

4.3.1. ITk Pixel Sensors

Different sensor technologies – 3D and planar – are used for modules in different parts of the detector. Table 4.1 summarises the active thickness, pixel pitch, position, and overall sensor size of different types of sensors in the pixel detector, and the types of modules into which they are planned to be assembled. The pixel pitch of the central part (barrel) of the innermost layer (B0) is $25 \times 100\,\mu\mathrm{m}^2$, as opposed to $50 \times 50\,\mu\mathrm{m}^2$ for the rest. The division of layers (including barrels and rings) in the ITk pixel detector is illustrated in figure 3.14(a).

3D sensors have n^+-type and p^+-type columns in p^--type substrate. For details of 3D sensors, including the cross-section view, see ref. [121]. They have a shorter drift distance, therefore faster charge collection, which leads to them being more radiation-hard. Hence they are chosen for the inner layer. They also require lower bias voltage, therefore lower power dissipation. 3D sensors will equip the innermost layers: L0 (Layer 0, which includes B0 and R1 – Barrel 0 and Ring 0) and R0.5.

Planar sensors are n^+-in-p type (n^+-type implants in p-type substrate). They will be used for the outer layers, with the layer that is the second closest to the interaction point (L1) using thinner sensors (100 µm instead of 150 µm as for the other outer layers) due to smaller material budget and lower power dissipation. The downsides are the risks and complications of processing such thin substrates and the consequently larger production cost.

	Active Thickness	Pixel Pitch	Position	Sensor Size	Module Type
Planar	150 µm 100 µm	$50 \times 50\,\mu\mathrm{m}^2$	B2-4, R2-4 B1, R1	$4 \times 4\,\mathrm{cm}^2$	Quads
3D	150 µm	$50 \times 50\,\mu\mathrm{m}^2$ $25 \times 100\,\mu\mathrm{m}^2$	R0, 0.5 B0	$2 \times 2\,\mathrm{cm}^2$	Triplets

Table 4.1: Geometry and planned positions of planar and 3D sensors in the pixel detector, and the types of modules into which they will be assembled [87, 89].

[8] And without parylene coating or mechanical wire-bond protection, which are introduced in section 7.4.

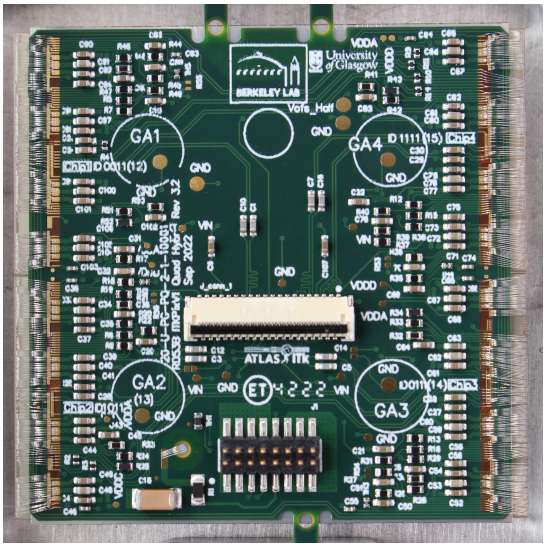

(a) An ITkPixV1.1 quad module (flex side).

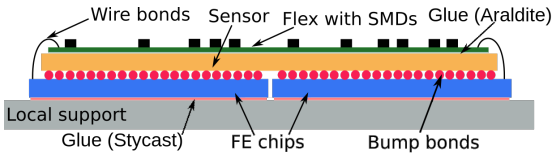

(b) Cross section schematics of a hybrid quad module [87]. The sensor is bump-bonded to 4 FEs and glued to a flex. The flex is wire-bonded to the FEs.

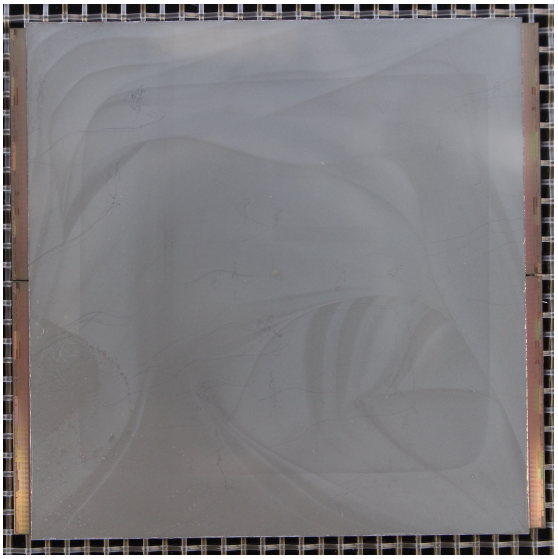

(c) An ITkPix V1.1 bare module, sensor back side.

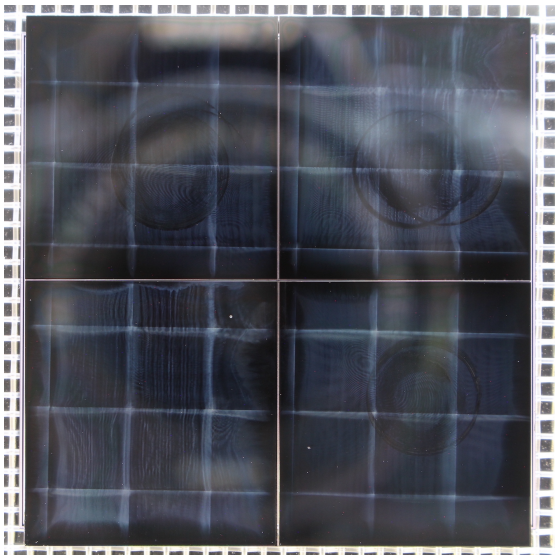

(d) An ITkPix V1.1 bare module viewed from the other side, showing four front-end readout chips.

Figure 4.10: ITkPixV1.1 quad module, schematics, and both sides of a bare module.

To cover the gaps between the four FE chips on a quad module, planar sensors are designed with an *inter-chip region*, as shown in figure 4.11. They are the four middle columns and rows on the sensor. The $50 \times 50\,\mu m^2$ pixel pitch refers to the pitch of the nominal-sized pixels. In the inter-chip region, the 16 central pixels are of size $100 \times 100\,\mu m^2$. The other pixels in the inter-chip region are of $50\,\mu m$ in one dimension, and $100\,\mu m$ in the other dimension.

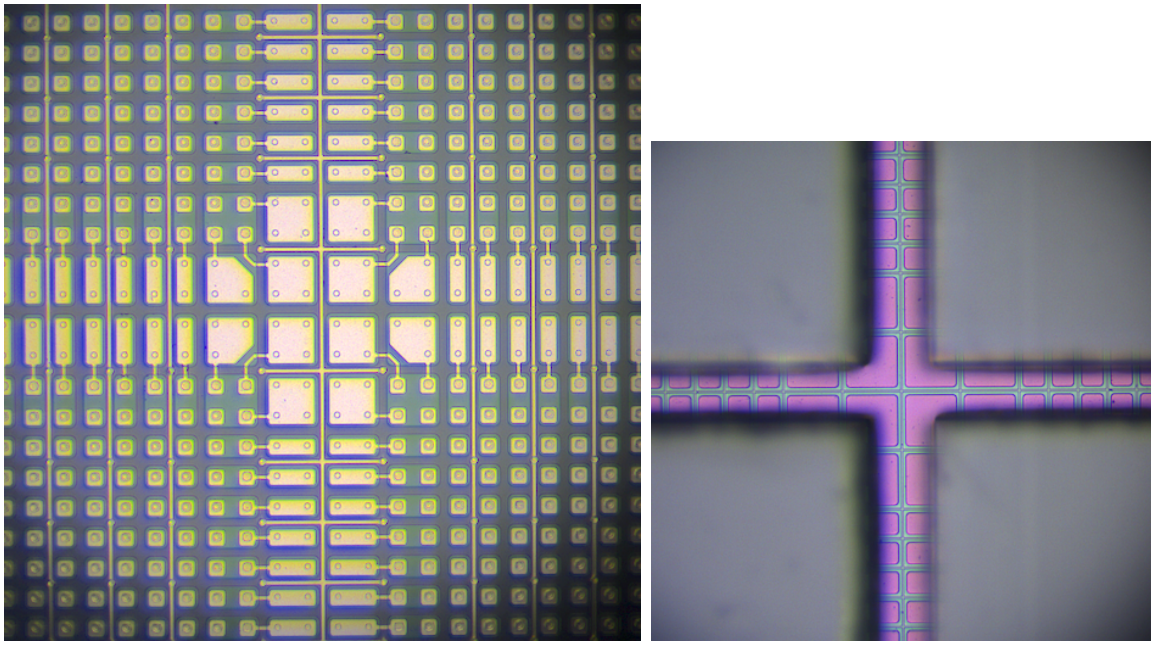

(a) Inter-chip region of a Micron quad sensor.

(b) Inter-chip region of an HPK quad BM.

Figure 4.11: Inter-chip region of a quad sensor and a quad bare module from different vendors. The four rows and columns at the centre are of double the size in one or both dimensions, resulting in sixteen $100 \times 100\,\mu m^2$ pixels. The rest of the pixels in these rows and columns are $50 \times 100\,\mu m^2$ or $100 \times 50\,\mu m^2$.

4.3.2. ITk Pixel Readout Chips

For the purpose of the ATLAS and CMS pixel detector upgrade for the HL-LHC, a chip was developed by the RD53 collaboration [122]. It is a pixel readout circuit equipped with 65 nm CMOS technology. A prototype ASIC version called RD53A was produced and tested for development purpose, which has different flavours of the analog FE integrated in one chip: synchronous, linear and differential. For detailed explanation please refer to [123].

Then ATLAS and CMS chose slightly different designs for their pre-production and production FE chips [124]. The ATLAS versions are referred to as ITkPix. The pre-production modules are with ASIC version ITkPixV1.1, production modules are ITkPixV2 (RD53C [125]). The analog FE flavour is the differential FE. The differential analog FE has a differential gain stage before the discriminator. This brings good performance of noise occupancy and low power consumption. The CMS versions are referred to as the CROC FE chip. They have a different numbers of pixels (column $\times$ row $= 432 \times 336$), and chose the linear analog FE, which has a linear pulse amplification stage before the discriminator.

The ITkPixV1.1 FE chips can be tuned to and operated at low threshold (1k electron charge), and have a data handling rate of 1.28 Gbps per lane. The radiation dose tolerance was tested up to 1 Grad, fulfilling the total ionising dose in the HL-LHC [126].

Each FE chip is separated into a pixel matrix and a chip bottom, as shown in figure 4.12(a). Each FE pixel in the pixel matrix has an analog front-end and a digital logic. The pixels

are grouped into fours, forming an "analog island". 16 analog islands (4×4) make up a "pixel core", i.e. each pixel core consists of 64 pixels. Figure 4.12(b) shows the analog islands (there are four complete ones in the picture). The green part is the "sea" of digital circuits that the analog FEs are embedded in. The chip bottom (peripheral circuitry) can be divided into the analog chip bottom, digital chip bottom, and the wire-bonding pad frame.

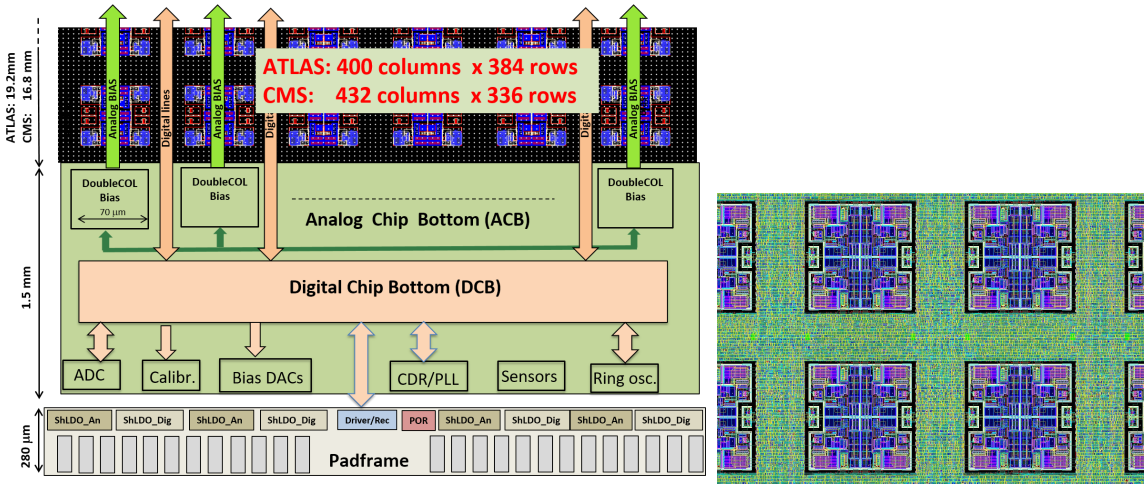

(a) Floorplan of the RD53B chip.

(b) Analog islands.

Figure 4.12: The RD53B chip overall floorplan and analog islands. There are four complete analog islands in (b). Each analog island contains 4 pixels. Images from [124].

To be more resistant to single event upset, a reset scheme was added to reset the chip global configuration registers to default when needed. The registers are also triple redundant, and the selection of the configuration can be done via any permutation with one bit-flip of the key codes, which is the key that the user needs to write to the registers to switch configuration.

Data Merging

The FE chips output data blocks that use Aurora 64b/66b protocol encoding. Data merging is one of the important features of the RD53B FE chips, it means that data from multiple FE chips (secondaries) can be merged into one FE chip (primary). The primary has three Aurora receivers to receive the data, and then merges all the output together. In this case, the secondary chips are operated at 320 Mbps due to the constraint of the data receivers, and the primary chip output needs to be increased to 640 Mbps for one secondary, and 1.28 Gbps for more than one secondaries. The DAQ then distinguishes which chip the Aurora block comes from via the chip ID that is included in the Aurora block.

Serial Powering

In the detector, the modules are connected in serial, in order to reduce material budget from the large number of cables. The serial powering scheme requires providing constant

input current I_{in} to multiple modules, which cannot be achieved by conventional shunt regulators. Therefore, a Shunt LDO (SLDO) regulator is included in the FE chips.

The SLDO contains a linear Low Drop-Out voltage (LDO) regulator and a shunt, see figure 4.13(a) for a diagram. The shunt circuit is in addition to the LDO, and can be turned on or off to switch between SLDO and LDO mode. The SLDO regulates the input voltage, and shunts the extra current. By shunting away the excessive current, it controls and provides constant power consumption. The LDO regulator powers the main load L, which is the chip, and the shunt element – an internal load L_{s} connected in parallel. L_{s} can be controlled independently of the behaviour of L, to achieve constant current:

$$I_{\text{in}} = I_L + I_s = \frac{V_{\text{in}} - V_0}{R_{\text{eff}}}, \tag{4.16}$$

where V_{in}, V_0 and R_{eff} are the input voltage, the offset voltage and the effective resistance, as shown in figure 4.13(b).

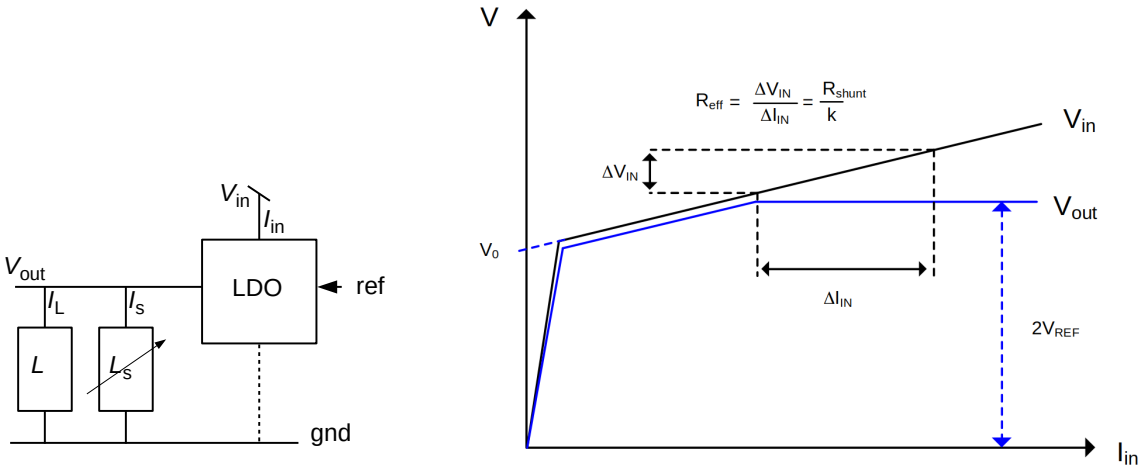

(a) SLDO regulator.

(b) Target SLDO voltage vs current behaviour.

Figure 4.13: Shunt LDO structure and VI. In operation, the LDO regulator powers both the main load L, and the variable shunt load L_{s} connected in parallel. V_{in} is the input voltage, and V_{out} is the output voltage that is regulated by SLDO. Images from [124].

LDO, shunt, and offset are different parts of the SLDO regulator circuit. The offset voltage V_0 is controlled by a reference voltage V_{ofs}. The effective resistance R_{eff} is controlled by an external resistor R_{shunt}: $R_{\text{eff}} = \frac{R_{\text{shunt}}}{1000}$. The SLDO *VI* curve is measured in module electrical tests, to check that the V_{in} and I_{in} show ohmic behaviour. In addition to the SLDO circuit, there are additional circuit parts for low power mode, under-shunt protection and overvoltage protection. These functionalities are performed using the SLDO regulation, and are tested as part of the module electrical tests, as discussed in section 9.2.

CHAPTER 5

Tracking and Flavour Tagging

After the proton–proton (pp) collisions, the collision products arrive at the detector, first the tracker. Tracking is the process of determining the trajectory of the particles in the sub-detectors. It is the key of event reconstruction, and needs to be done fast and with low fake rate. This can be achieved with high granular and radiation-hard trackers like the ATLAS ID, and in the future, the ITk. With the tracks, the particle p_{T} can be obtained, but particularly importantly is the reconstruction of the primary (production) vertex at the collision point, and the possible secondary (decay) vertex of the hadrons. This provides information on the decay life-time and impact parameter of the object, and is important for particle identification.

Particle identification is important for physics analyses. In particular, quarks show up as "jets": they cannot show up as free particles, but form hadrons that contain the corresponding flavours of quarks, and then go through a series of processes before arriving at the detector as other types of hadrons. The jets that originate from b- and c- quarks are the heavy-flavour jets. Light-flavour jets originate from light quarks and gluons. τ leptons, due to their high mass, also form jets, and are normally separated into their own category. Some heavy-flavour jets have a secondary vertex, while light jets do not. Therefore, the information from tracking and vertexing is used to distinguish heavy-flavour jets and light-flavour jets. Identification of the jet flavour is called "tagging" or flavour tagging. Through tagging of the hadrons, the flavour of the original particle created in the collision can be distinguished.

Especially, b-hadrons have distinctive features: they are particularly long-lived, with a lifetime τ_b at the level of 1.5 picosecond. With b-hadrons with mass around 5 GeV and e.g. momentum of 10 GeV, the mean flight length $\langle l \rangle = \beta\gamma c\tau_b$ is 0.9 mm[1]. Other features include

[1] The decay length for τ leptons is also long: 0.5 mm for 10 GeV momentum.

high mass and decay multiplicity[2]. Also, top quark decay is the main background for a lot of analyses, and top quarks couple predominantly to b quarks (as they are weak-isospin partners, and the rate is specified in the CKM matrix). These make b-tagging the centre of flavour tagging.

This chapter first introduces the processes that quarks go through in the detector, to understand the object to be tracked and reconstructed. Track and vertex reconstruction are described with example of the ATLAS ID. Then jet and jet algorithms, as well as flavour tagging (in particular b-tagging) are explained. As part of the work of the thesis, tools were developed for automated derivation of b-tagging working points and production Monte-Carlo-to-Monte-Carlo scale factors. The relevant concepts and procedures are introduced.

5.1. Between Collision and Tracker

A pp collision and the processes that the involved particles go through are illustrated in figure 5.1 and explained below.

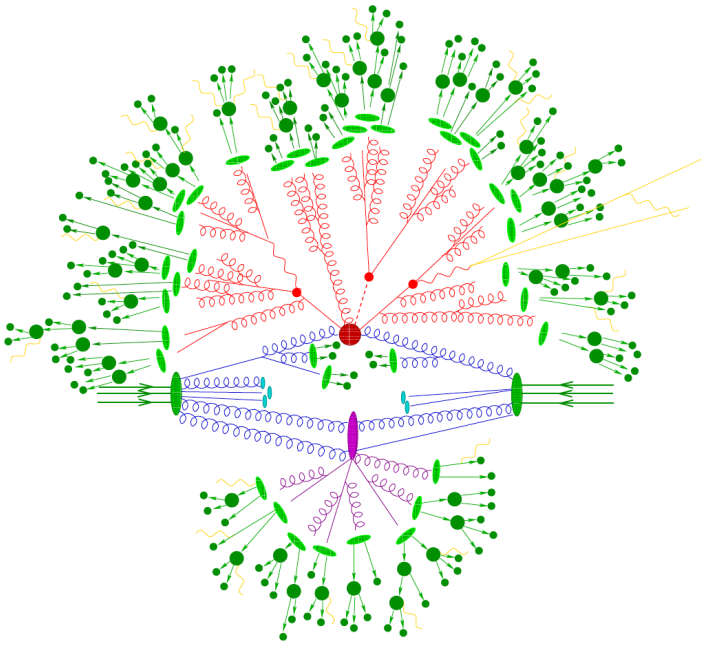

Figure 5.1: Depiction of a $t\bar{t}H$ event. Protons (there are two protons in this illustration, each shown as a big green ellipse from three parallel lines with arrows) come in and collide. Part of the protons undergo hard interaction (the bigger red circle at the centre), producing two top quarks and a Higgs boson (small red circles). They then produce hard QCD radiation, and parton showering happens (red lines), the final state partons hadronise (light green ellipses) and then decay into other hadrons – mostly pions and kaons (small dark green circles). The light yellow lines represent photons, they are radiated in all processes. The underlying event takes place at the same time (big purple ellipse). Image from [127].

[2]Decay multiplicity: the numbers of decay product particles.

Protons consist of many "partons" – quarks and gluons. Partons create initial-state radiation by emitting more partons and photons. In the collision, the hard interaction between partons produces final state particles like leptons, quarks, bosons, and possible new particles. The particles radiated by the final state particles from the hard process is referred to as final state radiation. Some of the final state particles then create a "shower" of partons through QCD and electroweak interactions: they decay into quarks and radiate gluons, which branch successively, resulting in more quarks and gluons. This process is called parton showering.

The partons in the shower then go through hadronisation: they form hadrons (for example, b- and c- quarks form b- and c- hadrons), which then decay into mostly π and K mesons, and get detected as jets.

In the two colliding protons, some of the partons are the initial states of the hard interaction process, and the rest ("spectator partons") also interact and radiate. The events from spectator partons are called Underlying Events (UE), and give rise to background jets. The other protons in the same bunch could scatter off each other, leading to hadronic activity. These are the pile-up events. Radiation from pile-up is much softer (with smaller p_{T}) than the jet produced from hard interaction, but can distort the kinematic relation of them.

5.2. Tracking

The ATLAS ID performs tracking of charged particles with a high acceptance ($|\eta| < 2.5$ and full ϕ). At each bunch-crossing, the high pile-up, underlying event and decay product multiplicity result in very high numbers of hits, therefore clusters in the ID, making it difficult to associate the clusters correctly to the track, which can distort the track and lead to wrong track parameters. Therefore, tracking is a difficult combinatorial problem.

In ATLAS, track reconstruction is first done inside out (from pixel to TRT), then outside in. These two processes are called the primary tracking and the back-tracking, respectively [128]. The procedure of primary tracking is described below and illustrated in figure 5.2.

1. Clustering: a charged particle can leave hits on multiple pixels, forming a cluster of hits. Therefore, the first step is to combine neighbouring hits to form clusters, based on hit information from the Pixel and SCT.

2. Seed finding: select three suitable hits as a "seed" in either pixel or SCT.

3. Find track candidates: only considering clusters on modules that are on the path of the seed, extend seeds to form a smooth trajectory across the whole of pixel and SCT. For electrons, due to Bremsstrahlung radiation, the track might change direction. Therefore a kink is allowed, if there is corresponding information from the calorimeter.

4. Ambiguity resolution: a hit might come from multiple charged particles hitting the same pixel/strip. This can happen e.g in the core of a collimated jet (high-energy jet). In this ambiguous case, a neural network algorithm assigns a probability to the number of charged particles by which the cluster is formed (1, 2, or 3). Clusters from multiple

charged particles are assigned to multiple track candidates. Then a global χ^2 fit is done on the track candidates, to extract the track parameters and make up for uncertainties from measurements and physics effects like multiple scattering.

5. Extend the track to TRT, which is done similar to the track candidate finding, and do a re-fit after including the TRT hit information. This improves momentum resolution and particle identification.

Primary tracking finds tracks from particles in the primary interaction (the pp collision). However, particles could be produced further from the beam-line, e.g. when a photon interacts with the detector and creates electrons. To find these tracks, back-tracking is done using the hits remaining from the primary tracking. The hits from ECal are matched to the hits in TRT, and then go back to the SCT and pixel, using the same procedure as primary tracking.

This whole process gives a collection of tracks for physics analyses.

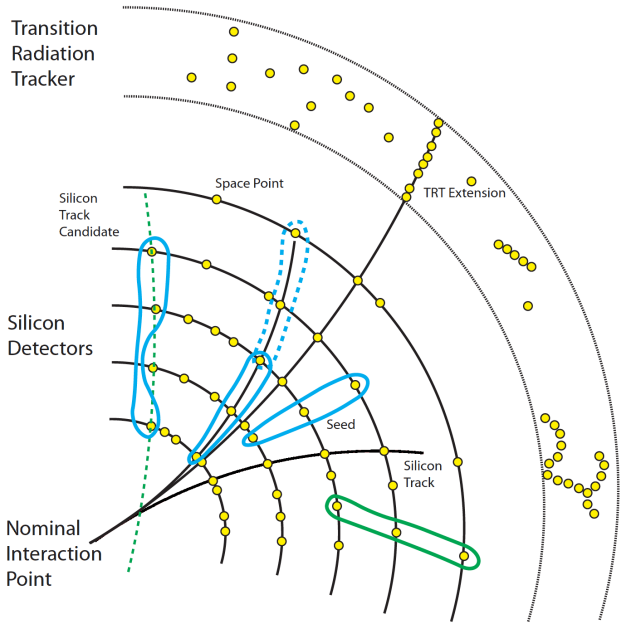

Figure 5.2: Illustration of processes in the tracking algorithm. The seeds are circled out, and the track candidates are the lines connecting the space points in different layers. The seed marked in a dashed blue line is from the track of one charged particle. The green seed and the track marked in a dashed green line are not from the nominal interaction point, and would be rejected. One of the tracks reached the TRT. Image from [129], with modification.

Charged particles leave curved tracks due to the B-field along the beam-line in the ID. From the curvature of the tracks, p_{T} can be determined. This starts with equating the centripetal force and the force of the charged particle in a B field – $m\frac{v^2}{r} = qvB$. For particles with elementary charge (which is the case for most particles with a lifetime long enough to leave

a measurable curved track), and after converting the unit of p_{T} to GeV, p_{T} is given by:

$$p_{\mathrm{T}} = 0.3Br, \tag{5.1}$$

where

p_{T} is the transverse momentum in GeV
B is the magnetic field strength in T
r is the radius from the curvature in m

Only tracks with p_{T} higher than a threshold (e.g. 500 MeV in ATLAS Run 2 [130]) are used for flavour tagging.

5.3. Vertexing

Because of the high pile-up (around 25 and 50 inelastic pp collisions per bunch crossing for ATLAS Run 1/2 and Run 3, respectively), it is important to find the correct primary vertex – the interaction point. This is also an iterative fitting procedure using the tracks. Interested reader on primary vertex finding algorithms can refer to ref. [131]. A good tracking system with high granularity close to the interaction point is necessary for reconstructing the primary vertex, secondary vertex, and impact parameters.

- Primary Vertex (PV): the interaction point of the original collision in the beam.
- Secondary Vertex (SV): the decay point. Some long-lived particles travel for a noticeable distance before decaying, and the decay point shows up as an SV. It is one of the features used to tag the long-lived particles, like τ leptons and b-jets.
- Impact parameter: the closest distance of a track to the primary vertex. The impact parameter is often projected in the longitudinal and transverse direction. The distance between the extension of the track and the PV in the transverse plane is often denoted d_0, and in the longitudinal direction z_0.

See figure 5.3 for an illustration of PV, SV and impact parameter.

To reach higher spatial resolution of the vertex reconstruction, a few items could benefit the tracker: an innermost layer that is closer to the beam, large total tracking length, high granularity (which brings higher resolution to the hits), and – for particles with low momentum – minimised multiple scattering, which requires lower material budget (thinner walls of beam pipe and tracker layers). These bring better extrapolation, and improve the resolution of the impact parameter on both directions of projection.

5.4. Jet Definition

The definition of "jet" is rather ambiguous: it is not certain whether two particles belong to the same jet, especially in collimated jets where the particles are boosted. Therefore,

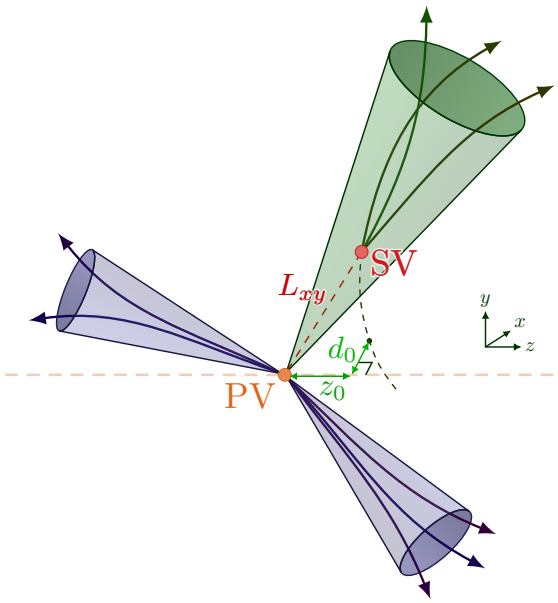

Figure 5.3: A three-jet event with one long-lived particle, showing the primary vertex (PV), secondary vertex (SV), and the longitudinal and transverse impact parameters z_0 and d_0. © Copyright 2021 – TikZ.net, license: CC BY-SA 4.0.

a "jet definition" is simply a well-defined procedure to reconstruct jets, and includes two essentials [132]:

- Recombination scheme – it gives the kinematic properties of the jet by taking information from the detector as inputs and combining the kinematic properties of jet constituents. The commonly used scheme is the four-momentum scheme, which simply sums the components of the four-vectors of the jet constituents.
- Jet Algorithm – or jet clustering algorithm, is the recipe to group particles into jets. They need to be infra-red and collinear safe, and normally have a few parameters for the user to adjust and give desired performance. The recent most commonly-used jet algorithm in the LHC experiments is the anti-k_t algorithm.

Starting from objects taken from the sub-detectors, jets are reconstructed by the jet algorithms, and then go through pile-up mitigation, to be cleaned/identified by the jet substructure techniques like various grooming techniques: mass-drop filtering, trimming, and pruning. Afterwards, they are calibrated for e.g. E, η, mass. Here we introduce a few jet algorithms, and explain the "PFlow" jet collection, which is the jet collection used for the b-tagging related work presented in this chapter. For detailed study of the performance of the jet substructure techniques and the calibration process please refer to [133].

5.4.1. Jet Algorithms

There are two typical categories of jet algorithms: cone algorithms and sequential recombination algorithms. Cone algorithms start with a given set of "seeds" and then try to find a

"stable cone": for a cone centre with y_c, ϕ_c, sum the 4-momenta of all the particles with a fixed radius R around it, if the sum has rapidity and azimuth y_c, ϕ_c (points in the direction of the centre of the cone), it is a stable cone. As the stable cones could possibly overlap, some procedures are done to split or merge the cones. The LHC uses almost exclusively a type of sequential recombination algorithm: the anti-k_t algorithm. A parton branches successively and produces jets. Sequential recombination algorithms invert this process by combining two particles into one successively. Most sequential recombination algorithms are in the generalised-k_t algorithm family:

- k_t algorithm [134, 135]
- Cambridge/Aachen algorithm [136, 137]
- Anti-k_t algorithm [138]

Each algorithm is sensitive to different effects, and has different characteristics.

Generalised-k_t algorithm

The clustering process of the generalised-k_t algorithm family is:

1. Find the initial list of objects (the particles in the event).
2. Find the inter-particle distance and the beam distance.
   Inter-particle distance is calculated by:
   $$d_{ij} = min(p_{t,i}^{2p}, p_{t,j}^{2p})\Delta R_{ij}^2, \tag{5.2}$$
   where: i and j are the labels of the two particles, p is a free parameter, p_{T} is the transverse momentum, and ΔR_{ij} is the geometric distance in the rapidity-azimuthal angle plane.
   And the beam distance is:
   $$d_{iB} = p_{t,i}^{2p} R^2, \tag{5.3}$$
   where R is the jet radius, a free parameter.
3. Find the smallest d_{ij} and d_{iB}. If the smallest $d_{ij} < d_{iB}$, recombine object i and j into a new object k (using the recombination scheme), add object k to the objects list.
   If $d_{iB} < d_{ij}$, object i is defined as a jet. Remove i from the list.
4. Find the new smallest d_{ij} and d_{iB}, loop this process until there is only one object left in the list and cannot be clustered further.

k_t algorithm

This is the case when $p = 1$. This makes the soft emissions[3] have a small distance, and thus recombine early in the clustering process. Therefore, it inverts the process of emitting radiation with a very intuitive process: starts with recombining soft radiation, then go to the hard ones. The disadvantage is that the jets are sensitive to extra soft background radiation in the event (like UE and pile-up).

[3] Soft emission: particles with small p_{T}.

Cambridge/Aachen algorithm

This is the case when $p = 0$, and the distance is purely geometrical.

Anti-k_t algorithm

This is the case when $p = -1$. It clusters the hard particles first, and then gathers soft particles around it. The cluster grows gradually, until it reaches a distance R away from the jet axis.

This algorithm is insensitive to soft radiation, the shape of the jets are more circular in the $y - \phi$ plane, as shown in figure 5.4, which is easy for calculating the jet kinematic variables and easy for calibration. It is the default jet clustering algorithm in LHC experiments.

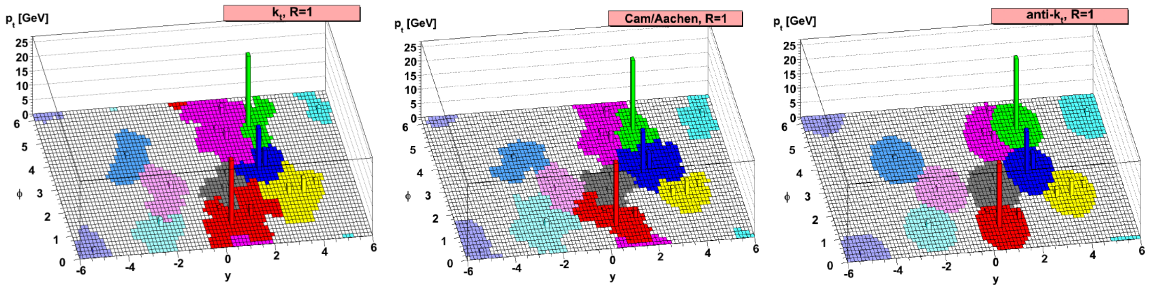

Figure 5.4: The catchment areas (coloured regions) for different algorithms. The hard jets from the anti-k_t algorithm are more circular than the other two. Figures from [138].

5.4.2. Particle-Flow Jet Collection

The input to the jet algorithm and recombination scheme can be topological clusters, particle-flow objets, etc. Topo clusters are reconstructed from calorimeter information– energy deposit, while particle-flow objects combine information from both the tracker and the calorimeter.

For ATLAS Run 2, a new type of jet collection – particle-flow (PFlow) jets – were used [139]. In the particle-flow algorithm, for tracks of the neutral particles, only topo clusters are used. But for charged particles, first match the tracks from the ID and the deposit from the calorimeter, then replace the energy deposit in the calorimeter using the momenta measured by the ID. This improves the measurement accuracy for charged hadrons. Then, these reconstructed objects are used as input to the anti-k_t algorithm to reconstruct the PFlow jets, with a chosen jet radius of R=0.4. The previously used jet collection is EMTopo jets, which only uses calorimeter information. In comparison, PFlow jets have better jet energy and angular resolution, better rejection of pile-up, and higher reconstruction efficiency. The jet collection then goes through jet flavour identification, i.e. flavour tagging.

5.5. Flavour Tagging

Flavour tagging is crucial for physics analyses, with b-tagging playing a significant role in it. The ATLAS flavour tagging group provides various b-tagging related information needed by analyses via a central Calibration Data Interface (CDI) file, the information includes working points (WP) and Monte-Carlo-to-Monte-Carlo scale factors (MC/MC SF).

5.5.1. Taggers

In ATLAS, b-tagging algorithms are divided into low-level taggers and high-level taggers. Different low-level algorithms, benefiting from various b-jet signatures, reconstruct different characteristic properties of the jets. High-level taggers take and combine the output information from low-level taggers, as well as jet kinematics like p_{T} and η. The taggers used in Run 2 are [140]:

- Low level taggers
  - Impact Parameter based algorithms: IP2D (uses d_0), IP3D (uses both d_0 and z_0), and RNNIP (a Neural Network).
  - Secondary Vertex based algorithms: JetFitter (decay chain multi-vertex finder) and SV1 (inclusive secondary vertex reconstruction algorithm).
  - Soft-muon based algorithm: SMT (soft muon tagger).
- High level taggers
  - MV2: Boosted Decision Tree (BDT)-based.
  - DL1: Deep Learning Neural Network-based.

However, displaced vertices can come from – other than b-hadrons – other particles or detector effects, such as other long-lived particles, photon conversions, uncertainty of measurement of tracks, or interaction with detector material. Therefore, the high-level algorithms are multivariable classifiers that give scores to a jet. MV2 and DL1 taggers give different outputs. The algorithms of MV2 family output only one score, while DL1 algorithms give three. They are combined to form the final output multivariate discriminant, which is defined as:

$$D_{DL1} = \ln\left(\frac{p_b}{f_c \cdot p_c + (1 - f_c) \cdot p_{\mathrm{light}}}\right), \tag{5.4}$$

where p_b, p_c, and p_{light} are the possibilities that the jet is a b-jet, c-jet, and light-flavour jet, respectively, and f_c is the effective c-jet fraction in the background training sample [141]. The output discriminant score D reflects the probability that a jet is a b-jet. The distributions of D for the MV2 and DL1 taggers in a Monte Carlo (MC) simulated $t\bar{t}$ sample are shown in figure 5.5.

Each type of high-level tagger has several variants that differ in the lower level taggers that they take as inputs, and on which samples they were trained. The DL1 series taggers include DL1, DL1r, and DL1rmu. DL1 uses information from IP2D, IP3D, SV1, jetFitter,

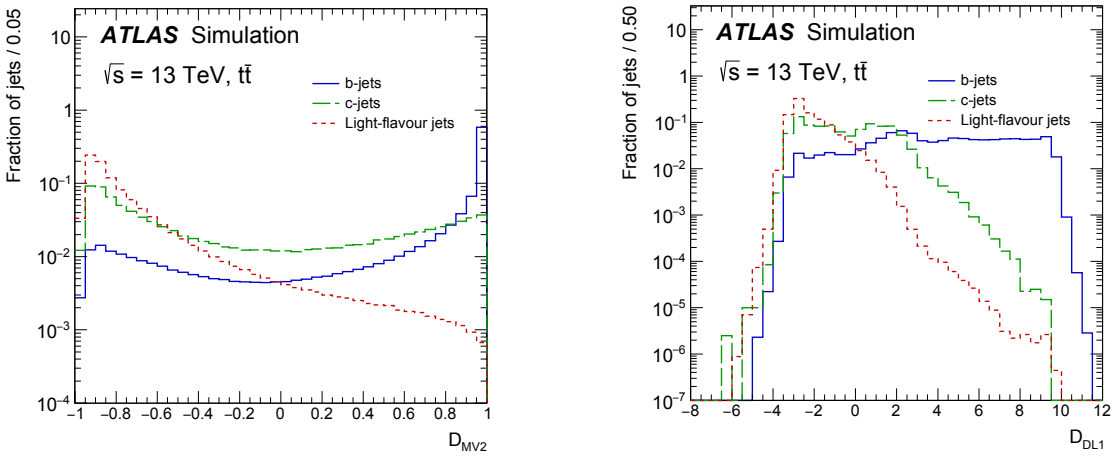

(a) MV2 tagger output discriminant.

(b) DL1 tagger output discriminant.

Figure 5.5: Distribution of the output discriminant from the MV2 and DL1 high-level taggers in Monte Carlo (MC) simulated $t\bar{t}$ events. Figures from [141].

and the jet kinematics. DL1r in addition uses RNNIP, and is used as the default. DL1rmu takes information also from SMT.

5.5.2. *b*-tagging Efficiency and Rejection

Since the taggers only provide a discriminant value corresponding to the probability of the jet being a b-jet, analyses need to find a balance between the amount of statistics and the purity of the b-jets. This can be gauged via the b-tagging efficiency ε_b, and the background (c- or light-) jet rejection. They are defined as:

$$\varepsilon_b = \frac{\text{number of true } b\text{-jets tagged as } b\text{-jet}}{\text{total number of true } b\text{-jets}}, \tag{5.5}$$

$$\text{rejection} = \frac{1}{\text{mistag rate}} = \frac{\text{total number of true background jets}}{\text{number of background jets tagged as } b\text{-jet}}. \tag{5.6}$$

ε_b or rejection can be obtained from MC samples, where the truth flavours of the jets are known.

5.5.3. Working Point (Operating Point)

Different analyses may prefer different strategies for object selection: more statistics, b-tagging efficiency, purity (having more or less of correctly tagged b-jets), or rejection of certain type of jets. It is always a balance between these factors.

In practice, a "Working Point" (WP) or "Operating Point" definition was made to characterise the b-tagging efficiency choices. In analyses, the object selection step includes selecting a suitable b-tagging WP. This is done essentially by choosing a cut value of the tagger output discriminant D that corresponds to a certain ε_b, and jets with a score higher

than this cut value are tagged as b-jets. In ATLAS, there are four centrally provided WP: 60%, 70%, 77%, and 85%. This is the ε_b that the D corresponds to, i.e. an X% WP means the b-jet tagging efficiency as measured in $t\bar{t}$ events is X%. An analysis that has large statistics would choose the 60% WP – the tightest one. In figure 5.5(b), this corresponds to a higher D value, and all jets at the right side of this value on the histogram are considered b-jets. This leaves a smaller number of jets compared to extending the jets accepted to further left of the histogram, but as seen in the figure, more jets on the right are actual b-jets.

An alternative approach referred to as "pseudo-continuous" b-tagging is used by a lot of analyses. Using all four fixed cut WPs, the distribution of five bins covers a full range of b-jet efficiencies. A pseudo-continuous b-tagging score defines if a jet passes a given WP, but fails the adjacent tighter one. The bin that corresponds to 85% to 100% WP contains mostly c- and light- jets, whereas the bin from 0% to 60% gives the same jets as the fixed cut 60% WP. Each bin contains jets that correspond to a certain b-tagging quality.

5.5.4. The WP Derivation Framework

Some analyses could benefit from non-standard WPs, for example, jet-p_{T}-dependent WP profiles. Deriving a WP is essentially getting the cut value for the tagger output discriminant D that corresponds to the desired value of another parameter. In the case of the fixed cut WP profile, it is one cut value that corresponds to the desired ε_b. For p_{T}-dependent profiles, the cut value varies with p_{T}.

The extended and automated WP derivation framework[4] takes the tagger discriminant D, jet p_{T}, jet η, and the true flavour of the jet from the input MC samples. Analysers can specify the desired efficiency or rejection values, and the code returns the cut value(s) on D. Multiple working point profiles are supported: the jet-p_{T}-independent fixed cut profile, and three p_{T}-dependent profiles: flat b-efficiency, hybrid, and flat rejection.

1. The fixed cut profile is the only profile included in the central CDI file and is p_{T} independent. As previously described, there is one cut value that gives an overall b-efficiency ε_b. There are four officially supported WPs, and this framework allows specifying other values.

2. The flat b-efficiency profile is a D vs p_{T} curve that provides the same ε_b WP across the jet p_{T} spectrum.

3. The hybrid WP profile is a combination of the fixed cut and flat efficiency profiles: with a fixed cut, as jet p_{T} goes up, ε_b first rises to a maximum, then decreases. When ε_b decreases to the specified WP, the profile changes to flat efficiency.

4. The flat rejection profile gives D vs p_{T} that provides the specified c- or light-jet rejection across the p_{T} spectrum.

[4] GitLab repository: https://gitlab.cern.ch/tiany/FTag-WorkingPointDerivation

Different profiles suit different scenarios in different analyses. Examples are shown below. All the results are solely for illustrative purposes to demonstrate the functionality of the framework, with example WPs derived from a MC sample generated by the Powheg + Pythia 8 event generator, using PFlow jets tagged by the DL1r tagger, and targeting at 70% WP or a light-rejection of 502, which is the rejection value that is given by a 70% fixed cut WP profile for a test sample with limited statistics and unspecified generator and simulation details. In the samples used for these figures, a fixed cut WP between 70% and 77% would give a light-rejection of 502.

Fixed Cut

Taking the histogram of the tagger output discriminant for true b-jets, as illustrated in figure 5.6, for a certain cut value on D, the entries on the right side of the histogram will be tagged as b-jets. The full expression of the corresponding b-tagging efficiency with statistical uncertainty is given by:

$$\varepsilon_b = \frac{N_b(\text{tagged})}{N_b(\text{total})} \pm \sqrt{\frac{\varepsilon_b \times (1 - \varepsilon_b)}{N_b(\text{total})}}. \tag{5.7}$$

This is simply equation 5.5 with the uncertainty and in a different notation, where $N_b(\text{tagged})$ and $N_b(\text{total})$ are the number of true b-jets tagged as b-jets, and the total number of entries in the true b-jets histogram, respectively. In practice, as illustrated in figure 5.6, the histogram is binned. After finding the bin that contains the cut value that gives the desired ε_b, the exact cut value in the bin is determined via interpolation.

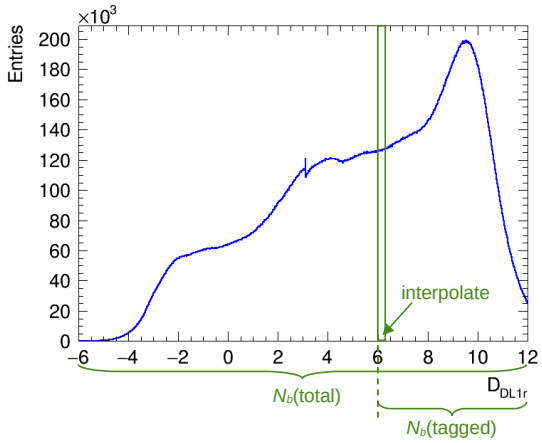

Figure 5.6: Finding cut value for a WP from histogram of tagger output discriminant score D for true b-jets in an MC sample.

See table 5.1 for the D cut values obtained from the automated framework compared to the values in the CDI file released in December 2020 that was used by analyses. The b-tagging efficiency ε_b vs p_{T} given by the D value that corresponds to the 70% WP is shown in figure 5.7(b). ε_b peaks at around 150 GeV p_{T}, possibly influenced by the track and secondary vertex reconstruction quality – which is related to the distance that the particles

WP [%]	Automated Framework	2020-12-2 CDI
60	4.83	4.57
70	3.47	3.25
77	2.44	2.20
85	0.90	0.67

Table 5.1: Tagger output discriminant cut values for the four official working points derived by the automated framework, and from the official CDI file. The values agree with each other, with differences arising from the different MC samples used.

travel before decaying and the collimation of decay products – and the number of tracker layers that the tracks traverse[5].

Flat Efficiency

The algorithm is similar to the above, except that in this case, the procedure is applied for each p_{T} bin of a 2D histogram of D and p_{T}. Doing this across the whole p_{T} range gives a series of D cut values corresponding to the same ε_b. The cut values and the corresponding ε_b for all WP profiles are presented in figure 5.7.

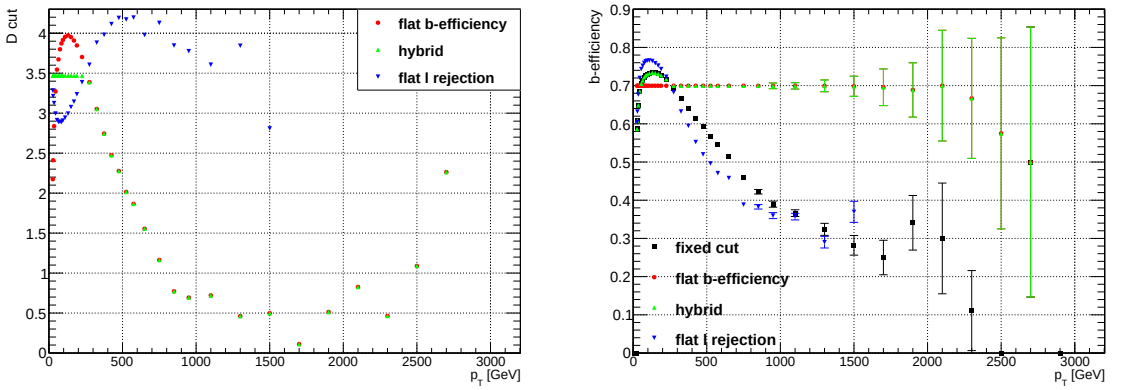

(a) D cut value vs p_{T} for p_{T}-dependent WP profiles.

(b) b-efficiency ε_b vs p_{T} for all WP profiles. The large uncertainty in ε_b at high p_{T} is due to lower statistics.

Figure 5.7: Tagger discriminant D cut values and b-efficiency vs p_{T} for all WP profiles (DL1r, 70% ε_b or 502 light-rejection).

The ε_b vs p_{T} plot in figure 5.7(b) is for validation, showing that applying the cut values presented in figure 5.7(a) gives an almost flat efficiency across full range of p_{T}, with some fluctuations at high p_{T} region, due to statistics. The values of the flat efficiency profile partly overlap with that of the hybrid profile (in green).

The flat efficiency WP profile is suitable for analyses that need a stable quality of b-jets independent of p_{T}.

[5] At 150 GeV, around 5% of the b-jet constituents already exceed the innermost layer of the pixel detector when they decay [141].

Hybrid

The Hybrid WP profile is derived starting with the cut value on D that corresponds to the desired WP, looping through jet p_{T}, and calculating ε_b. When ε_b decreases to the desired WP, the corresponding cut value that keeps the same ε_b is obtained. The cut value vs p_{T} and the resulting ε_b are included in figure 5.7.

This profile takes full advantage of the statistics at higher p_{T}. It keeps more statistics by lowering the D requirement, while maintaining ε_b, i.e. the fraction of the b-tagged jets.

Flat Rejection

The flat rejection profile has two options: a flat c-jet or light-jet rejection. The procedure to derive a flat rejection WP is the same as for the other profiles, except that when looping through the D bins for each p_{T} bin, instead of calculating ε_b, the rejection is calculated by integrating over the mistagged jets:

$$\text{rejection} = \frac{1}{\varepsilon_{\text{bkg}}} = \frac{N_{\text{bkg}}(\text{total})}{N_{\text{bkg}}(\text{tagged})} \pm \sqrt{\frac{\text{rejection} \times (\text{rejection} - 1)}{N_{\text{bkg}}(\text{tagged})}}, \tag{5.8}$$

where background (bkg) can be c- or light- flavours, and the mistag rate of background jets are simply the "efficiency" ε_b or $\varepsilon_{\text{light}}$, which is the number of true background jets tagged as b-jets[6] – $N_{\text{bkg}}(\text{tagged})$[7], over the total number of true background jets – $N_{\text{bkg}}(\text{total})$.

See figure 5.7 for the spectra of cut value and the resulting b-efficiency, and figure 5.8 for the cross-check of light-jet rejection. The cut value fluctuates, and the light-rejection is almost flat across the p_{T} spectrum. A rejection value of 502 is used for demonstrative purpose. This value roughly corresponds to the light-rejection of 70% to 77% fixed cut WP.

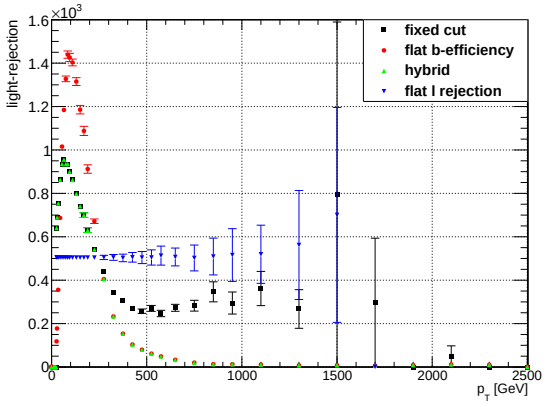

Figure 5.8: Light-rejection vs p_{T} from flat light-rejection WP.

The flat rejection profile is useful for analyses that are sensitive to c- or light- backgrounds and need better control of the background rejection.

[6] Therefore "mistag".

[7] In the histogram, these are the background jets with higher D values than the bin that is looped to.

5.5.5. Monte Carlo / Monte Carlo Scale Factors

Several corrections are applied to the flavour tagging efficiencies. Data-to-MC scale factors (SF) correct for different ε_b in data and MC simulated samples[8], and MC/MC SFs[9] correct for different MC generators (which have e.g. different parton shower, hadronisation, or decay models) with respect to the nominal one, which is used to derive corrections to data, to avoid systematic bias.

$$\mathrm{SF}_{\mathrm{X/MC}(p_\mathrm{T})} = \frac{\varepsilon_{\mathrm{X}(p_\mathrm{T})}}{\varepsilon_{\text{Nominal MC}}(p_\mathrm{T})} \tag{5.9}$$

where:

X is the label for the data or alternative MC sample
ε is the b-tagging efficiency
Nominal MC generator setup used for calibration to data is the PowhegPythia 8

The MC/MC SFs are derived for alternative showers like Herwig and Sherpa and variations of the Pythia parameters. The overall SF for an alternative MC generator combines the data/MC and MC/MC SFs:

$$\mathrm{SF}_{\text{Alternative}(p_\mathrm{T})} = \frac{\varepsilon_{\text{Data}}(p_\mathrm{T})}{\varepsilon_{\text{Nominal MC}}(p_\mathrm{T})} \times \frac{\varepsilon_{\text{Nominal MC}}(p_\mathrm{T})}{\varepsilon_{\text{Alternative MC}}(p_\mathrm{T})} = \frac{\mathrm{SF}_{\mathrm{Data/MC}}(p_\mathrm{T})}{\mathrm{SF}_{\mathrm{MC/MC}}(p_\mathrm{T})} \tag{5.10}$$

The SFs are produced using $t\bar{t}$ samples, assuming that they also work for other processes, e.g. W+jets, Z+jets, because SFs depend mainly on p_T. The efficiencies are calibrated.

A $t\bar{t}$ decay can happen in the hadronic, di-lepton or single-lepton channels. See figure 5.9 for the tree level decays and the branching fractions for each decay channel.

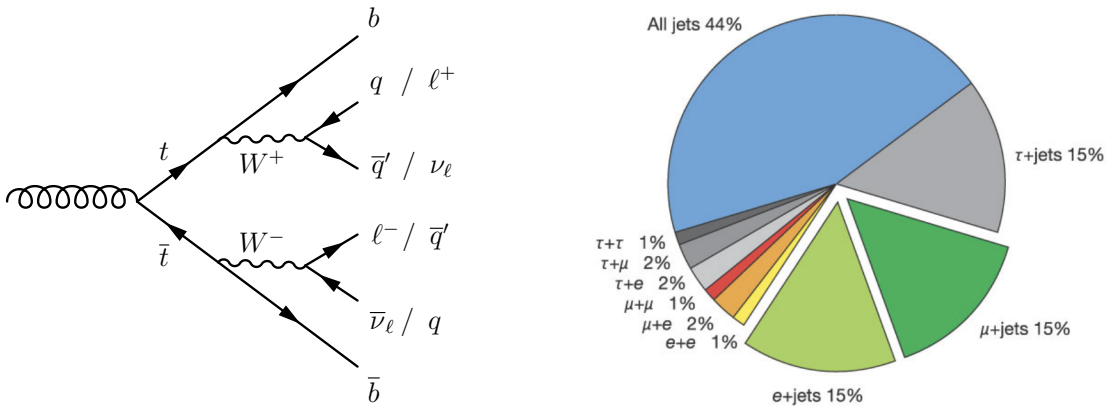

Figure 5.9: $t\bar{t}$ decay channels and the corresponding branching fractions.

The MC samples can be generated either as $t\bar{t}$ non-all-hadronic samples, or separately for di-lepton and single-lepton channels. The later brings various benefits, like when the sample for one of the channels is used for calibration or machine learning purposes, larger statistics can be generated for this sample. Therefore, samples for the two channels are

[8] The b-tagging efficiency ε_b is determined by measurements like in [141] using $t\bar{t}$ sample.
[9] Also called efficiency maps.

often not generated with cross sections in proportion to their respective branching ratio. Samples are also generated separately for data-taking campaigns in different years, which are with different luminosity and pile-up profiles, and should therefore be normalised to the respective luminosity of the data taking period. A dataset ID (DSID) is given as a label for each MC sample, which can include one or more decay channels[10] and one of the campaigns. In the work for this thesis, the normalisation implemented into the MC/MC SF derivation framework[11] is as follows.

The weight of each MC event[12] is:

$$w_{\text{MC}} \times w_{\text{JVT}} \times w_{\text{pu}} \times w_{\text{lepton}} \tag{5.11}$$

where w_{MC} is the MC weight assigned by the MC generator. w_{JVT}, w_{pu}, and w_{lepton} are weights from the Jet Vertex Tagger, pile-up, and lepton, respectively. These weights are also taken into consideration in the previous version of the framework.

For each sample in a different campaign or decay channel, events are weighted by:

$$L_{\text{campaign}} \times \left(\frac{\text{XSec} \times \text{kfactor}}{\text{totalEventsWeighted}} \right)_{\text{DSID}} \tag{5.12}$$

where L_{campaign} is the integrated luminosity, which is different for each campaign. XSec $\times$ kfactor gives the full cross section, and the denominator totalEventsWeighted is the sum of all MC weights. Both of these are different for each DSID.

In the scope of the thesis work, MC/MC SF derivation was made on various alternative generators. The SFs made for the $tt(H \to b\bar{b})$ analysis [142] feature the new normalisation, and are presented in figure 5.10 as an example. The alternative generators are Herwig 7.1.3 and Powheg + Pythia 8 with dipole recoil shower. The figures show examples of the SFs using PFlow jets tagged with the DL1r tagger and passing the 70% WP.

The SFs for the Powheg + Herwig 7.1.3 samples are big. They are around 3 % at low p_{T} for b-jets, which is big enough for an analysis that uses one or more b-jets to require corrections from SFs. For light jets, the SFs are even larger: they can go up to around 9.5%. The SFs are around 4 % for the whole p_{T} spectrum of c-jets and at higher p_{T} for τ-jets. The dipole recoil sample deviate from nominal at higher p_{T} and only for light and τ-jets, being about 4 % and 2 %, respectively. The SFs labeled "PhPy8EG_old" is also a Powheg + Pythia 8 sample with nominal configuration, but is an older version. The SFs between the new and old nominal Powheg + Pythia 8 samples are negligible. Compared to the previous normalisation, the SFs from the new normalisation for Powheg + Herwig 7.1.3 is visibly different, with a difference of around 1 % at high p_{T} for c-jets and at low p_{T} for light jets.

[10] E.g. di-lepton, single-lepton, both together as non all-hadronic, or all-hadronic.
[11] The MC/MC SF derivation framework: https://gitlab.cern.ch/tiany/efficiency-maps.git
[12] The unweighted MC event generated is referred to as the "raw" MC event.

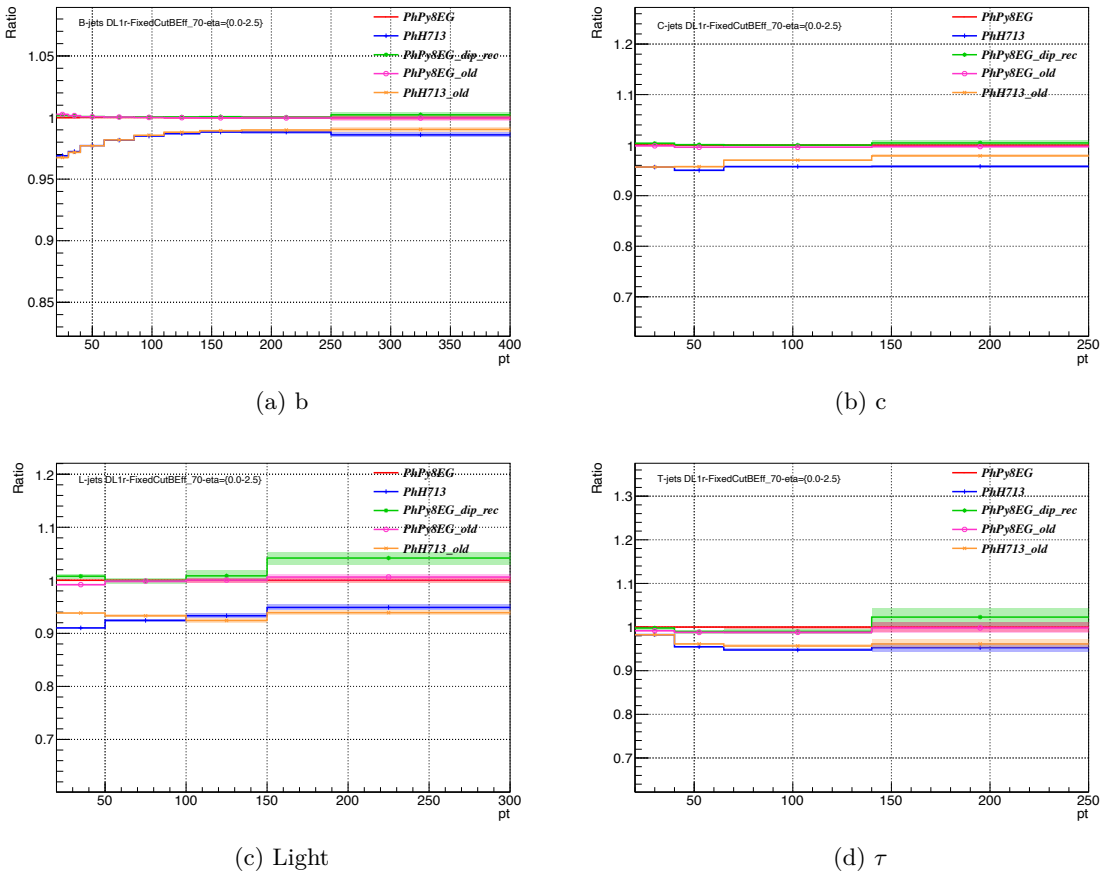

(a) b

(b) c

(c) Light

(d) τ

Figure 5.10: Examples of scale factors vs p_{T} (PFlow jets, DL1r tagger, 70% working point) for alternative generators vs the nominal generator, for b-, c-, light-, and τ-jets. The alternative generators are Powheg + Herwig 7.1.3 and Powheg + Pythia 8 with dipole recoil. The nominal sample is Powheg + Pythia 8 used in the $tt(H \rightarrow b\bar{b})$ analysis. Comparison is also made with an older Powheg + Pythia 8 sample that has been used as nominal for SFs, and Herwig 7.1.3 sample without the new normalisation (the pink lines and the orange lines).

5.5.6. Conclusions and Outlook

Frameworks were developed for the purpose of providing WP and MC/MC SFs. The WP derivation framework provides four different WP profiles: fixed cut, flat efficiency, hybrid, and flat rejection. The MC/MC SF framework implemented a new normalisation method, taking the luminosity for different campaigns and cross-sections for different decay channels into consideration. These developments provide support to both SM analyses like ttV ($V = W$, Z, H), $t\bar{t}$, and four tops, and BSM physics searches. Further work should be done on making sure that the non-standard WPs derived can be calibrated correctly to data, and unifying the two frameworks so that MC/MC SFs could be provided for the non-standard WPs. It is important to investigate if different SFs arise from the difference between single-lepton and di-lepton events by deriving SFs with only the leptonic half of single lepton $t\bar{t}$ decays, and comparing to those derived with di-lepton samples. Furthermore,

when applying the MC/MC SFs to analysis, the uncertainty on the SFs are not yet taken into account in the final uncertainties. This should be implemented. There is also effort on deriving MC/MC SFs using optimal transport in machine learning [143], which allows continuous calibration instead of binned SFs with a certain WP.

CHAPTER 6

Planar Sensor Testing

A general introduction to ITk pixel detector sensors is included in section 4.3.1 and comparisons to the current ATLAS pixel and IBL are in table 3.2. In pre-production, to determine if the sensors are going to meet the requirements in the ATLAS ITk pixel detector, they are tested in lab (section 6.1) for the characteristics and in particle beam (section 6.2) for the hit detection efficiency. These tests provide important information, for instance, for choosing the vendors from which to procure the sensors and on the expected performance.

6.1. Pre-production Sensor Quality Assurance

At the pre-production stage of the ATLAS ITk pixel detector upgrade, a small fraction of sensors was procured from several vendors: Hamamatsu Photonics K.K. (HPK), Micron Semiconductor Ltd (Micron), and Future Built on Knowledge (FBK, Fondazione Bruno Kessler). After the sensor wafers were produced, the vendors conducted initial quality control (QC) measurements, after which part of the wafers were diced by the sensor or hybridisation vendors, then sent to ITk testing sites for quality assurance (QA). Sensors are accepted if both QC and QA meet the requirements. Some sensors went through under-bump-metallisation, dicing, and bump-bonding at the hybridisation vendors to form bare modules, which were subsequently tested, selected, and assembled into modules[1]. This process ensures that the sensors meet the specifications for the final production.

The planar sensor characterisation measurements for QA are described in [1]. The following section focuses on these measurements and follow-up tests. Some of the measurements presented in this section were performed by other ITk sites, including High Energy Accelerator

[1] Module QC are then performed on fully assembled modules, finishing the module production chain. Module assembly is introduced in chapter 8 and module QC in chapter 9.

Research Organization (KEK, in Tsukuba, Japan), Max-Planck-Institut für Physik (MPP, in Munich, Germany), and Lancaster University (Lancaster, in the United Kingdom).

6.1.1. The Measurements

The tests for sensor QA are listed below. The purposes, as well as the corresponding specifications for passing sensor QA are also introduced in this subsection.

- Basic measurements performed on sensor tiles and diodes:
  - *IV*– leakage current as a function of reverse bias voltage
  - *CV*– bulk capacitance as a function of reverse bias voltage
  - *It*– leakage current stability
  - Visual inspection and metrology
- Additional measurements performed on dedicated test structures (TS):
  - Inter-pixel resistance (on strip TS), inter-pixel capacitance
  - Charge collection efficiency
  - Other technological TS (e.g. poly-Si resistance)
- Follow-up tests:
  - *It* after sensor baking

For QC, the vendors measure *IV* on all sensor tiles and *CV* on part of the sensor tiles/diodes. Results from sensor QA include *IV*, *CV*, *It* tests on unirradiated and irradiated HPK and Micron planar sensors (irradiation done at CYRIC). On HPK TS, inter-pixel and poly-Si resistance were performed in addition. Results for other optional tests, FBK planar sensors, and 3D sensors were also obtained by ITk sites, but are out of the scope of this thesis. The follow-up tests are baking and *It* curves of a sensor (tested as a fully assembled module).

IV curves, as introduced in section 4.2.2, test the breakdown voltage and the level of the leakage current (I_{leak}), which is temperature-dependent and is also affected by radiation damage and annealing. Therefore, temperature requirements are essential for making sensible specifications and ensuring cross-comparability between measurements, especially between ITk sites. Irradiated sensor measurements are required to be performed at a colder temperature due to the higher I_{leak}. This is also the reason for the low temperature environment required during the operation of the detector.

For sensor QA, I_{leak} (in both *IV* and *It*) should be measured at 20±1 °C before irradiation, and at -25±1 °C after irradiation and after annealing at room T for 10 days. The breakdown voltage (V_{bd}) is defined as the voltage at which I_{leak} increases by >20% in steps of 5 V, excluding 0 to 5 V.

Relative humidity (RH) was also found to affect I_{leak}, possibly due to H^+ ions increasing the conductivity around the guard ring implants [3]. RH $< 50\,\%$ is therefore required when performing QA measurements.

The effects from temperature, RH, radiation damage and annealing also impose requirements on the storage of sensors. Irradiated sensors were therefore kept in a freezer at $-20\,^{\circ}\text{C}$ to avoid annealing. The freezer is flushed with dry air, and when taken out for testing, the

sensors are put in a box and flushed by dry air for 10 min while warming up before being put in probe station, in order to prevent condensation.

As described in section 4.2.2, the full depletion voltage (V_{dep}) can be obtained from *CV* measurements. Since this is determined by the bulk doping concentration, *CV* results can be used to cross-check the doping. To ensure that the sensor is fully depleted during operation, the operation voltage is also defined relative to V_{dep}.

For taking the *CV* curves, the LCR meter generates an AC voltage, and the frequency of the measurement AC voltage affects the result. QA requires *CV* to be taken at 10 kHz.

To test if the leakage current is stable during operation, *It* curves were taken by measuring the leakage current every 10 minutes for 48 hours, skipping the first 10 min, while the sensor is biased at $V_{\text{dep}} + 50$ V (the operating voltage). There is no unified definition of fluctuation for planar sensor QA. In this thesis, it is defined as $\frac{\text{max}-\text{min}}{\text{average}}$, where average is the average of all measurements.

The inter-pixel resistance measurements test the inter-pixel isolation, which is commonly achieved using isolation implants with p-stop or p-spray techniques[2]. Poly-Si resistance provides information on the poly-Si bias structures, which is introduced in section 6.1.2. When the incoming particle hits a pixel, it not only generates an output signal on the electrode of the said pixel, but also induces signals in the neighbouring ones due to inter-pixel capacitance. This is the capacitance between neighbouring pixel electrodes, and should be minimised to reduce crosstalk.

The QA specifications are summarised in table 6.1.

Detailed settings of the measurements are summarised in table 6.2. The number of repetitions per step for *CV* and *It* measurements, as well as the waiting time for *CV* are not specified by QA requirements, but are decided locally by ITk sites. Table 6.2 therefore shows the local setup at Göttingen. For *It*, initially, only one measurement was taken per time step. This was later increased in the baking test to five repetitions and these repetitions finish within 2.5 s.

Measurement	Step Size	t_{steps}	t_{reps}	n_{reps}	Additional Information
IV	5 V	2 s	100 ms	10	Current compliance set at 100 µA
CV	5 V	5 s	1 s	5	Measure at 10 kHz
It	10 min	–	–	1 or 5	–

Table 6.2: Details of *IV*, *CV*, and *It* measurements: step size, settling time between steps t_{steps}, settling time between each repetition t_{reps}, number of repetitions at each (voltage or time) step for averaging n_{reps}, and additional information about the measurements.

[2]The two differs in the dose of the implant. For more details please refer to [102].

Measurement	Irradiation [n_{eq}/cm^2]	Sensor Info.	Requirement
I_{leak}	0	–	<0.75 µA/cm^2 at V_{dep} +50 V
	5×10^{15}	150 µm	<45 µA/cm^2 at 600 V
		100 µm	<35 µA/cm^2 at 400 V
V_{bd}	0	–	>V_{dep} +70 V
	5×10^{15}	150 µm	>600 V
		100 µm	>400 V
V_{dep}	0	150 µm	<100 V
		100 µm	<60 V
It fluctuation	0	–	<25 % for 48 h at V_{dep} +50 V
Inter-pixel R	-	Poly-Si	>2 MΩ
		Other permanent	>20 MΩ

Table 6.1: The specifications on leakage current I_{leak}, breakdown voltage V_{bd}, depletion voltage V_{dep}, I_{leak} stability, and inter-pixel resistance R. Specifications for sensors irradiated with 2×10^{15} n_{eq}/cm^2 are omitted. The specifications on I_{leak} and V_{bd} for sensors irradiated with 5×10^{15} n_{eq}/cm^2, as well as V_{dep} are different according to the sensor thicknesses. The inter-pixel resistance requirements differ between sensors with poly-Si bias rails and other permanent bias structures [144].

6.1.2. Sensors and Test Structures

Three vendors – HPK, Micron, and FBK – were selected via a market survey [3] and a tender, to produce planar sensors. On each produced wafer there are quad sensors and various TS. It is planned to use the TS to monitor the quality during production. The arrangement of the wafers are illustrated in figure 6.1.

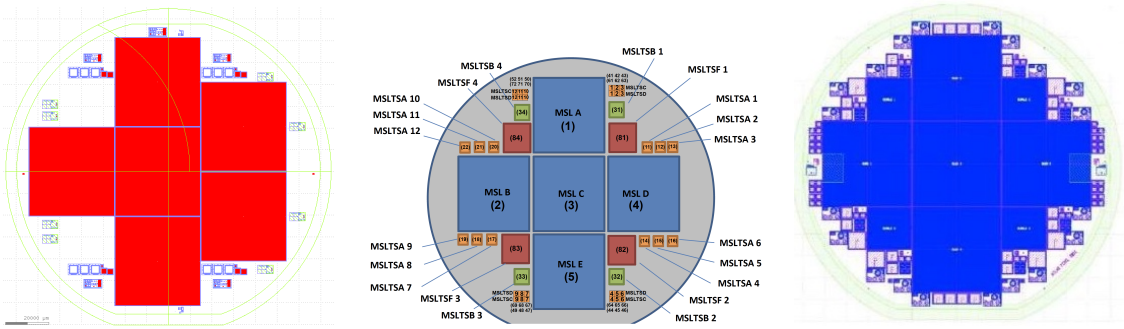

(a) HPK wafer map.

(b) Micron wafer map, MSL is short for "Micron Semiconductor Ltd".

(c) FBK planar 100 µm wafer map. Image from [145].

Figure 6.1: Arrangements of wafers for all three vendors for planar sensors.

After the sensors are bump-bonded to the FE chips, the bias voltage can be applied through the bump-bonds. However, to test wafers or bare sensors without FEs, bias structures are needed. The bias structures used by the three vendors are illustrated in figure 6.2. The active thicknesses and bias structures used by each vendor, as well as the numbers of quad sensors per wafer, are summarised in table 6.3.

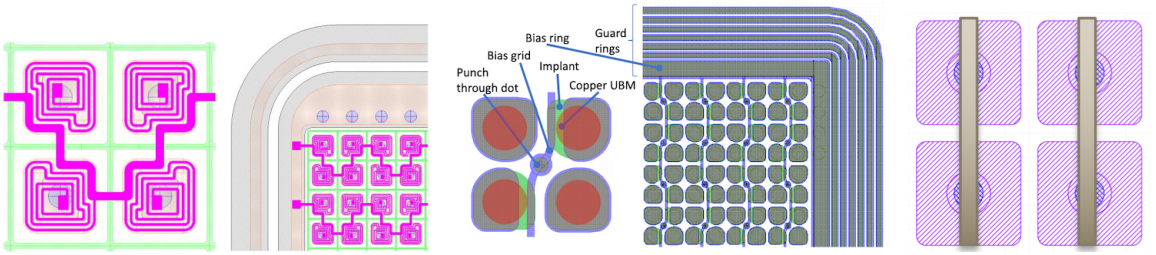

(a) Bias resistor [146]. Image from [147]. (b) Punch through. Image from [148]. (c) Temporary metal. Image from [149].

Figure 6.2: Illustrations of three types of bias structures.

- HPK sensors have poly-Si bias resistors on the top of the pixel implants. In addition, a wiggly metal bias rail passes by every four implants, as illustrated in figure 6.2(a). The wiggly shape maximises the overlap with the pixel implants.
- Micron uses the punch-through biasing scheme, which was introduced in section 4.2.2. The punch-through dot (punch-through implant) and bias grid are shown in figure 6.2(b). The pixel implant, as well as the under-bump metallisation are also labeled in the figure.
- FBK deposits a temporary metal layer on the top of the sensor. This metal layer will be removed before hybridisation.

Vendor	Active Thickness	Bias Structure	Sensor Tiles per Wafer
HPK	150 µm	Poly-Si	6
Micron	150, 100 µm	Punch-through	5
FBK	100 µm	None (temporary metal)	5

Table 6.3: Planar sensors with different active thicknesses and bias structures produced by different vendors, and the numbers of quad sensor tiles produced on each wafer. FBK sensors have no permanent bias structure but temporary metal deposition, making it possible to take e.g. *IV* measurements. The temporary metal will be removed before further processing of the sensors, like hybridisation.

Figure 6.3 shows an example of a die[3] from HPK with TS and a 150 µm quad sensor from Micron. The sizes of the die and the quad sensor tile in this picture are not adjusted to the actual proportion. A photo of a Micron TS die can be found in appendix A.1.

6.1.3. Testing Setup

The testing setup used at Göttingen, with various voltage sources and meters, the probe station, and the chiller, is shown in table 6.4 and figure 6.4.

For *IV*, *CV*, and *It* measurements, a die is placed on the chuck of the probe station, with the back side facing down, in contact with the chuck, and fixed by vacuum. The chuck is connected to HV (apply negative voltage for reverse bias). A probe needle is connected

[3]Die: pieces of wafer. It can either contain multiple TS and sensor, or be a single sensor die / TS die.

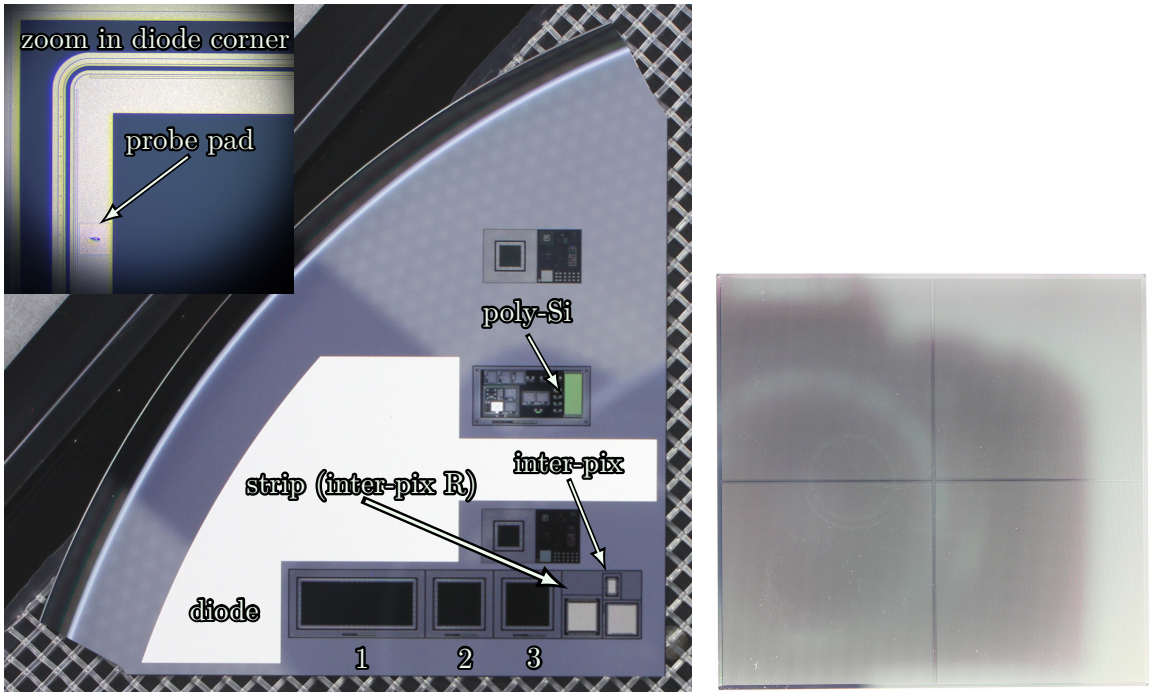

(a) A die with HPK test structures.

(b) A Micron 150 µm quad sensor.

Figure 6.3: An HPK TS die with zoom-in photo of a diode showing a probe pad, and a Micron 150 µm quad sensor. The sizes between the TS die and the sensor is not to the actual proportion.

Tests	Voltage Source	I or C Meter
IV, It	Keithley 2410	Keithley 2410 or 6487
Inter-pixel R	Keithley 2410	Keithley 6487
CV	Keithley 6487	HM8118 LCR bridge

Table 6.4: Voltage sources and meters.

to the ground, and is used to contact the probe pads on the die. On sensors, the probe pads are connected to the bias grid. There are normally multiple pads on each die, and measurements on RD53A bare modules show that contacting different pads give compatible results (appendix A.2). The connections for the resistance and inter-pixel capacitance measurements are described in the respective sub-sections.

The Süss PA300 probe station provides shielding of ambient light, to prevent it from interfering with the I_{leak} measurements. Inlets for dry air allows keeping the RH $< 10\,\%$ during measurements. The chuck is connected via an inlet to a vacuum pump, the vacuum pressure fixes the die on the chuck, keeps them flat, and prevents them from slipping when probing. The temperature of the chuck is controlled by a Huber Unistat 380 chiller.

Environmental monitoring is achieved through a PT1000 sensor connected to the chuck via kapton tape, and an NTC sensor and a HIH4000 sensor placed close to the chuck. These three sensors measure the sensor T, ambient T, and RH, respectively.

(a) Probe station: Süss PA300.

(b) Chiller and controller: Huber Unistat 380.

Figure 6.4: The probe station and the chiller. The probe station has inlets for connection to dry air for humidity control, and vacuum for fixing the die on the chuck. It also provides shielding from ambient light. The temperature of the chuck is controlled by the chiller.

During measurements, the target T of the chiller is set at around the required T for the respective measurements. For unirradiated dies, the measured T is 20 ± 1°C at the chiller, and typically around 24 °C at the chuck. Depending on the thermal contact, the T measured at chuck by the PT1000 could be between 20 and 28 °C. For irradiated dies, the measured T is -25 ± 1°C at chiller, and typically around -18 °C at the chuck. Due to the unknown thermal contact quality between PT1000 and the chuck, chiller T instead of chuck T was chosen for consistency. This would make the leakage current results more conservative, since the measurement at a higher T result in higher leakage current than what it would have been at the required T.

Keithley 6487 was used for CV measurements because Keithley 2410 source meters were found to be incompatible with the CV setup. The HM8118 LCR meter is equipped with a bias-T soldered according to the circuit in [114], with only minor differences. For all the CV data measured at Göttingen, an offset of 11 pF was subtracted, this value was obtained by averaging a CV curve with the probe needles disconnected from the die.

In the baking test, baking of the fully assembled module was conducted with a Binder ED 23 heating chamber, the temperature control during It scan was done by putting the module in a Vötsch VTM 4004 climate chamber, and the module temperature was taken via the module NTC.

Other lab infrastructure, including a dry box for storage of the sensors and modules is described in section 7.2.

6.1.4. Leakage Current vs Bias Voltage (*IV*)

30 unirradiated HPK diodes from four wafers were tested in pre-production QA. 29 of them showed no breakdown, see figure 6.5(a) for IV curves of nine diodes on wafer 5 (W5). These IV curves are from three TS dies, on each die there are one larger diode of size $5 \times 10\,\text{mm}^2$

(labelled D1), and two small diodes of size 5×5 mm^2 (D2 and D3). Due to the size difference, D1s have almost double the I_{leak} that of D2 and D3. The I_{leak} level at V_{dep} +50 V (which is around 120 V) are all well within specification, which amounts to 375 nA for D1, and 188 nA for D2 and D3. The scale of these limits is too large to be shown in the figure.

Sensors from HPK and Micron were also tested to ensure that the measurements made by the vendor can be reproduced. See figure 6.5(b) for the results on HPK sensors. Results showed good agreement on both the breakdown status and the I_{leak} level.

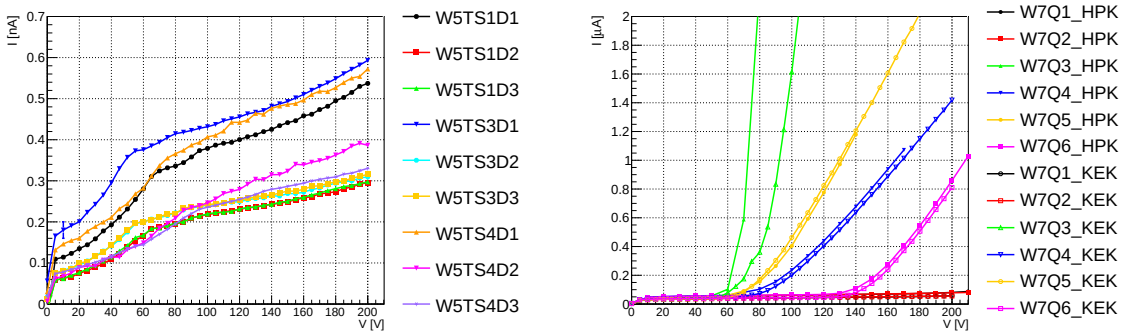

(a) *IV* of nine unirradiated HPK diodes from wafer 5. Diodes on three TS dies were tested, on each die there are three diodes, the diodes labelled D1 are of size 5×10 mm^2, D2 and D3 are of size 5×5 mm^2.

(b) *IV* for unirradiated HPK quad sensors showing agreement between vendor and ITk site. HPK measured at 23 °C, RH∼40%, and KEK at 20 °C, RH<5%.

Figure 6.5: *IV* of unirradiated HPK sensors and diodes.

Micron 100 µm quad sensors were measured at the vendor and two ITk sites: Göttingen and MPP. The results from MPP on all sensors from wafer 0121 ITk sites are illustrated in figure 6.6(a) and are consistent with that of the vendor, as shown in ref. [2]. Sensor C, D, and E meet the specifications, showing no breakdown and I_{leak} is within the limit at 120 V. The limit on I_{leak} is marked in the fiture with the red vertical line and a bar at the top. The default size of quad sensor tiles (41.1 mm × 39.5 mm) was used in the calculation of I_{leak} limit.

MPP observed large variation in *IV* behaviour after the sensor is biased for an extended amount of time due to an *It* measurement. The measurements were performed on sensor D, which was subsequently sent to Göttingen for crosscheck of results. The comparison is illustrated in figure 6.6(b). The two curves taken at Göttingen were only 22 min apart, but the change is clearly present, which indicates instability of I_{leak}. More investigations were conducted through *It* studies and led to baking tests, the results of which are discussed in section 6.1.6 and section 6.1.7.

Seven of the unirradiated quad sensors that were tested to be within specification were sent for irradiation and then tested, for a direct comparison before and after irradiation. They are HPK W7Q1, Q2, and Q6, Micron 100 µm 0121C and 0121E[4], and Micron 150 µm 0006A and 0022C. They were irradiated at a fluence of approximately 5×10^{15} n_{eq}/cm^2, and the

[4]Micron 100 µm 0121D was not irradiated but was instead used to investigate instability in I_{leak}.

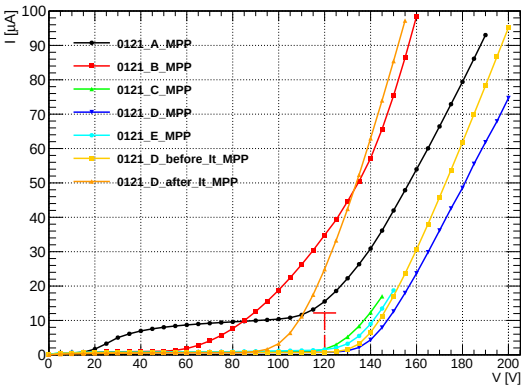

(a) *IV* of five sensors on wafer 0121. Additional *IV* curves for sensor D were taken before and after an *It* measurement.

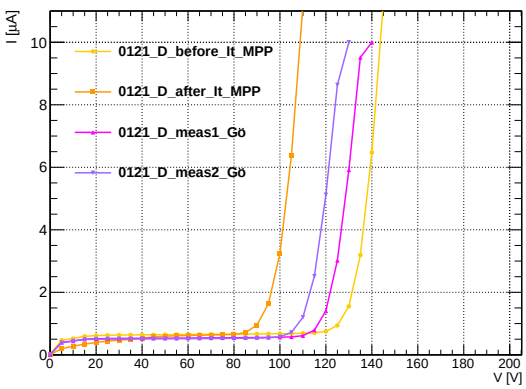

(b) Crosscheck of sensor D *IV* between MPP and Göttingen. Gö measurement 1 and 2 were taken 22 min apart.

Figure 6.6: *IV* for unirradiated Micron 100 µm quad sensors. Sensor C, D and E are within specification, as indicated by the red line at 120 V, with the short horizontal bar on the top indicating the I_{leak} limit calculated using the default size of quad sensors. After being biased continuously for longer, the leakage current increases significantly, with an earlier breakdown. This was confirmed by measurements at Göttingen. The MPP results were published in ref. [2].

results are shown in figure 6.7.

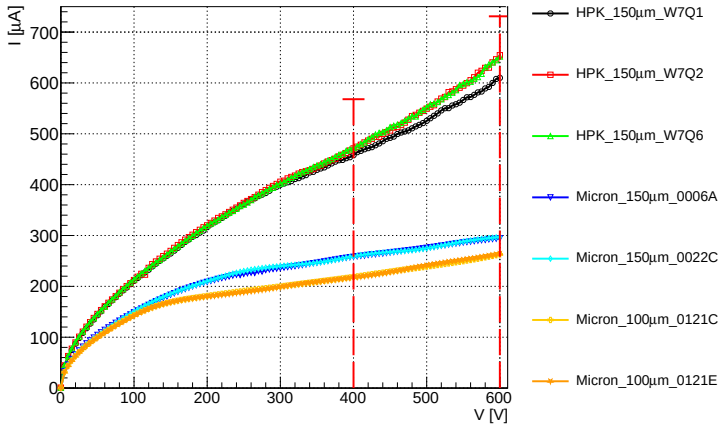

Figure 6.7: *IV* curves of irradiated quad sensors. The specifications are indicated by the dashed red lines: at 400 V for 100 µm sensors and at 600 V for 150 µm sensors, the short horizontal lines on the top of the dashed lines indicate the I limit calculated using the default size of quad sensor tiles.

The Micron 150 µm irradiated sensors remained in Cologne for around one month without temperature monitoring, therefore, the annealing effect is unknown. HPK sensors were tested by KEK. Micron 150 µm and 100 µm sensors were tested in Göttingen at around −25°C chiller temperature, and around −18 °C at the chuck, making the results more

conservative. The leakage current for all the seven sensors are within specification, as indicated by the dashed red lines. No breakdown was observed.

6.1.5. Bulk Capacitance vs Bias Voltage (*CV*)

During pre-production QA, ITk sites obtained CV curves on 33 unirradiated HPK diodes from four wafers. Figure 6.8 shows results for dies from two of the wafers, obtained by two different sites.

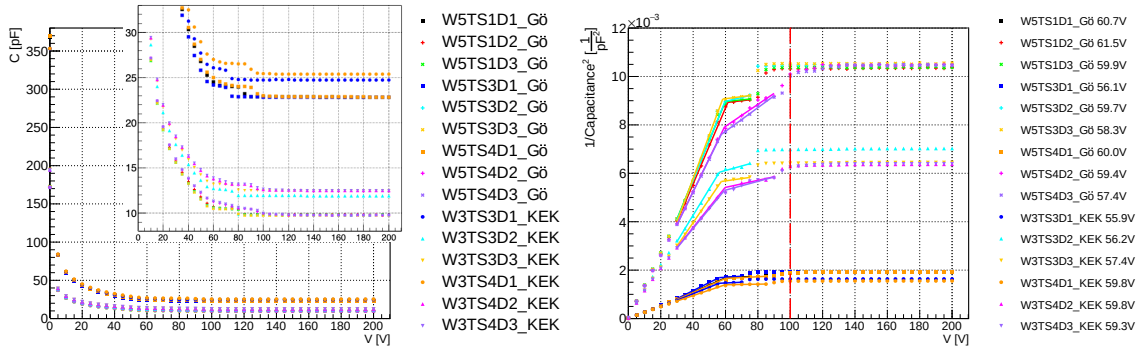

(a) CV (b) $\frac{1}{C^2}$

Figure 6.8: CV and $\frac{1}{C^2}$ of HPK diodes. The overlayed figure in (a) is a zoom-in of the lower C region. Diodes named D1 are larger ($5\times10\,\mathrm{mm}^2$) than D2 and D3 (both $5\times5\,\mathrm{mm}^2$). The results are from two different testing sites: Göttingen and KEK, each site tested dies from a different wafer. The full-depletion voltages V_{dep} written in the legend correspond to the first intersection point (with lower V) of the fitted lines. The dashed red line indicates the limit on V_{dep} required by the specification.

Capacitance decreases rapidly at low bias voltage, and the capacitance of D1s is approximately twice that of D2 and D3 due to their sizes. A slight shift is observed in results for same-sized diodes on dies from different wafers tested by different sites, which is explained by differences between wafers and the testing setups. There are two kinks in the $\frac{1}{C^2}$ plot, possibly due to edge effects: there are extra p^+-doped rings outside the active area of the diodes, which causes further lateral depletion. The capacitance decreases at this point, possibly because the centre of the diode and the ring, as two electrodes, provide extra capacitance. When the depletion zones connect, the extra capacitance disappears. Thus, the first intersection point at lower V reflects better the V_{dep} needed to fully deplete the sensors across the thickness, and the voltage at which further depletion occurs is the punch-through voltage. The slope of further depletion from TS4, which is the die at the bottom right of the wafer if viewed in the direction as in figure 6.1(a), consistently differs from the other dies, indicating presence of manufacturing variations across the circular wafer.

The $\frac{1}{C^2}$ curves for unirradiated Micron quad sensors are shown in figure 6.9 (for CV curves see appendix A.3). Sensors on wafer 0016 were tested without dicing. No edge effect was observed, possibly due to the larger area of quad sensors compared to diodes, which makes the edge effect negligible.

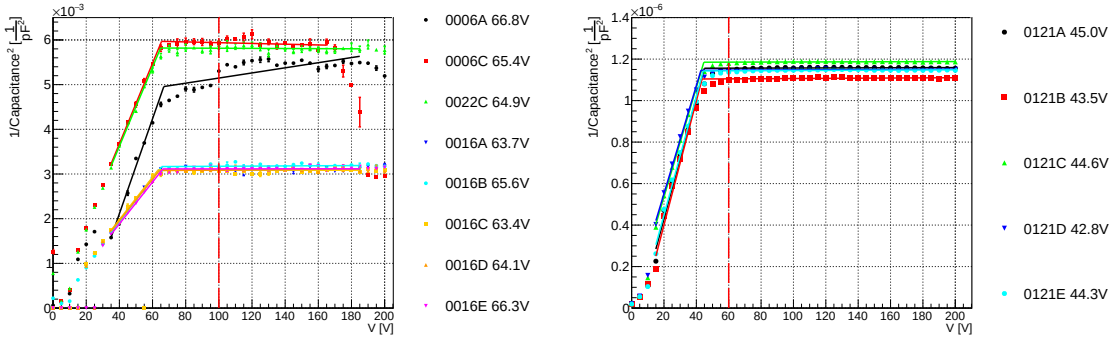

(a) Micron 150 µm, measured by Lancaster. Wafer 0016 was measured without dicing.

(b) Micron 100 µm, measured by MPP.

Figure 6.9: $\frac{1}{C^2}$ vs V of unirradiated Micron quad sensors with two active thicknesses. V_{dep} results are indicated in the legend and the required limit is indicated by dashed red lines.

The V_{dep} obtained from HPK diodes is 58 ± 5 V, results from 33 diodes were taken into account. As the first plateau is short, the result is subject to significant variation from the fit. Therefore, the uncertainty is estimated by varying the data points that are included in the fit. V_{dep} for Micron quad sensors is 65.0 ± 0.4 V for 150 µm and 44.0 ± 0.4 V for 100 µm sensors. These uncertainties are simply the standard error of the mean, as the ramp and plateau region of these curves are less ambiguous. All results meet the specifications, as indicated by the dashed red lines.

CV curves for Micron sensors of both thicknesses after irradiation at around 5×10^{15} $n_{\text{eq}}/\text{cm}^2$ are shown in figure 6.10. The range is up to 505 V due to the available range of the Keithley 6487 voltage source.

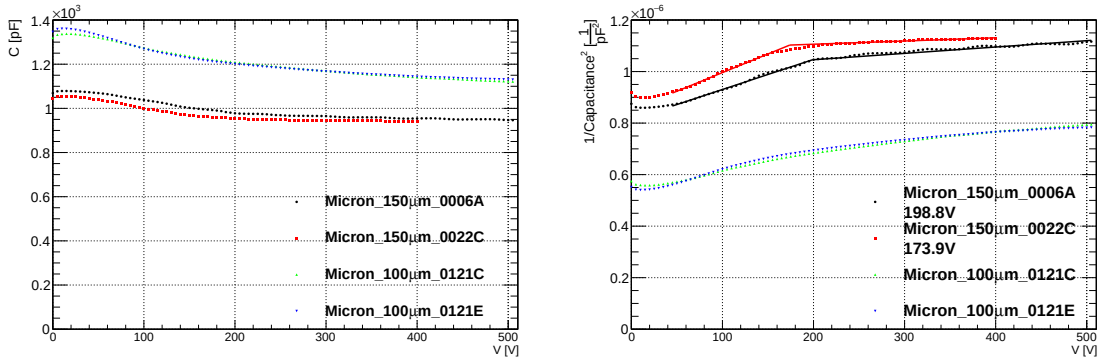

(a) CV.

(b) $\frac{1}{C^2}$ vs V. The markers are the measured results and the solid lines are the fitted lines.

Figure 6.10: *CV* and $\frac{1}{C^2}$ for irradiated Micron quad sensors, measured at 10 kHz. V_{dep} was obtained only for 150 µm sensor results based on visual estimation of the ramp and plateau regions, due to nonlinearity of the $\frac{1}{C^2}$ curves for 100 µm sensors.

Compared with the results of unirradiated diodes and sensors, C becomes larger after irradiation, at first increasing slightly with V, then decreases slowly. This is possibly due to

the lower electric field in the sensor [150]. Also, since the free charge carriers in an irradiated bulk are lower in quantity and mobility, the dependence of C on V could be smaller, when measured at high frequency [102]. In the $\frac{1}{C^2}$ plot, the distinction between the ramp and plateau regions is unclear as they are no longer linear, and V_{dep} is thus not clearly defined. An attempt was made to determine V_{dep} for the Micron 150 µm sensors from their vaguely distinguishable ramp and plateau regions. The result is $V_{\text{dep}} \approx 186 \pm 18\,\text{V}$ on average.

6.1.6. Leakage Current Stability (*It*)

Figure 6.11 shows the results for unirradiated HPK diodes. The diodes on W5 were biased at 120 V, W1 at 100 V, and W3 at 125 V, due to different choices of V_{dep} by different testing sites. The fluctuations in all measurements are within the required limit.

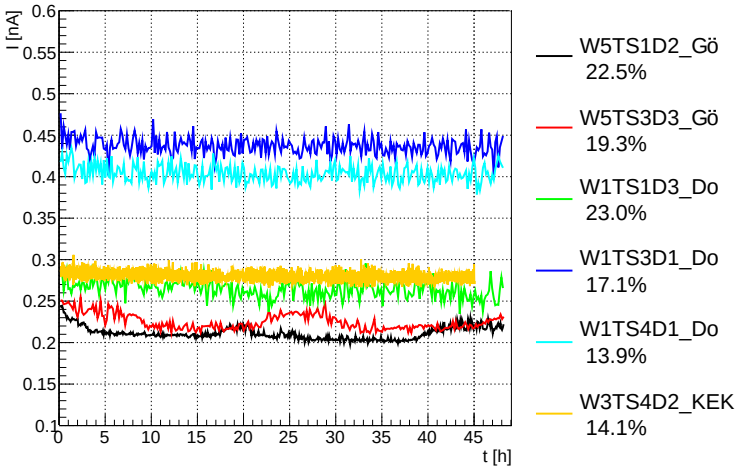

Figure 6.11: *It* curves for unirradiated HPK diodes. The current is not corrected for temperature fluctuations. The curves for W5TS1D2 and W5TS3D3 show periodic fluctuation, likely caused by environmental influences like ambient light. The fluctuations for all curves are written in the legend and are within the required limit.

However, unirradiated Micron sensors showed unstable I_{leak}, as illustrated in figure 6.12(a). The 100 µm quad sensor 0121D was tested at two different bias voltages (90 V and 70 V) at 20 °C chiller T. When biased at 90 V, the *It* curve increases rapidly and then decreases steadily with respect to time. A shorter curve was obtained at 70 V – I_{leak} still increases, but with no obvious subsequent decrease. The fluctuation, as written in the legend, is out of specification in both cases. This result is consistent with that of MPP (figure 8.4 a in ref. [2]). For a 150 µm sensor, I_{leak} only decreases and also exceeds the limit (figure omitted for simplicity).

This effect disappears after irradiation. As presented in figure 6.12(b), results for two quad sensors irradiated at $5 \times 10^{15}\,\text{n}_{\text{eq}}/\text{cm}^2$ fluence (0006A and 0121C) and one diode irradiated at $2 \times 10^{15}\,\text{n}_{\text{eq}}/\text{cm}^2$ (0121TSB3) show that the instability is no longer visible. The fluctuations are low despite that the measurement of 0006A suffered from fluctuating chiller T, and the diode 0121TSB3 was biased at a high voltage (400 V).

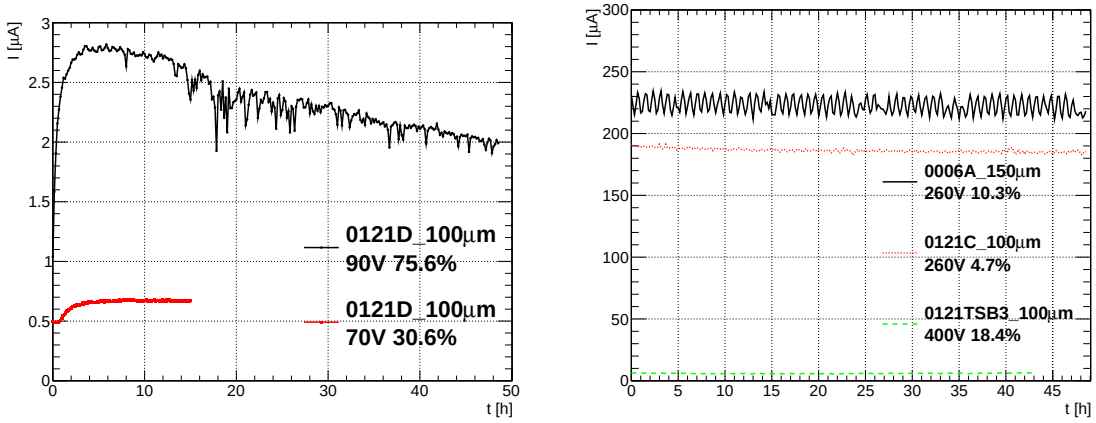

(a) Micron 100 µm, unirradiated.

(b) Micron 150 µm and 100 µm, irradiated.

Figure 6.12: *It* curves for unirradiated and irradiated Micron sensors. The wavy fluctuation in 0006A is due to temperature cycles of the chiller.

It is suspected that the change of leakage current in unirradiated sensors is due to a surface effect from oxidation. The suggested solution is to bake the sensors. The testing results are shown in the next subsection.

6.1.7. Baking Test for *It*

To investigate the unstable I_{leak} problem of the Micron 100 µm unirradiated planar sensors illustrated in figure 6.12, further baking tests were conducted. This is to test if baking could eliminated this effect, so that this type of sensors from the said vendor could still be purchased for production. Suggestions from the vendor is to bake the sensors at 125 °C for 16 hours, and flush the sensor for 2 to 3 h with dry N_2 if the sensor has been stored in an environment with relative humidity >50 % before baking. This suggestion is consistent with the practice in the strip detector community (150 °C for 15 hours with no special environment) [151]. This is because the instability of the leakage current could be from trapped charges in the oxide layer: electrons and holes have different mobility, holes could be trapped in the oxide layer, and affect I_{leak} when being biased for a period of time. Thermal excitation can lead to the trapped charges moving into the conductive part of the sensor, therefore mitigating the problem.

Due to unavailability of bare quad sensors, two fully assembled quad modules named CERN12 and CERN15 equipped with unirradiated Micron 100 µm sensors were used for this test. They were stored in a dry box with continuous dry air flushing[5]. CERN12 was baked at 150 °C for 16 h, and *It* curves were taken in a climate chamber at 20 °C with dry air flushing. See figure 6.13 for the temperature monitoring during baking.

Figure 6.14 shows all *It* curves taken for CERN12 and CERN15. The nominal reverse bias voltage is $V_{\text{dep}} + 50$ V, but a few different voltages were chosen for the tests. 120 V was chosen initially as it corresponds to the upper limit of the V_{dep} of pre-production

[5]The dry box is introduced in section 7.2.2

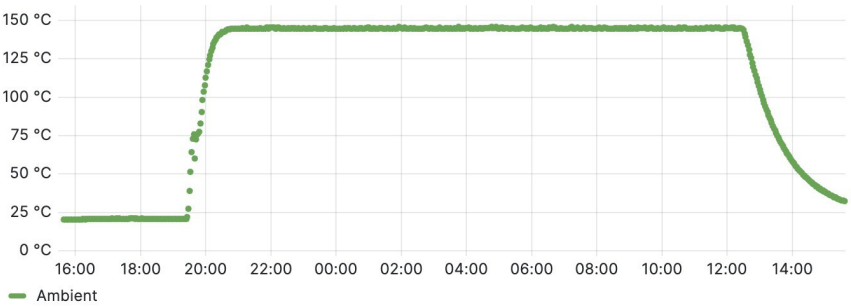

Figure 6.13: Environmental monitoring (temperature vs time) during baking.

sensors, and a higher bias voltage makes sure that the sensor is fully depleted. This was later changed to 70 V to test if an overall lower I_{leak} also results in less fluctuation. 90 V corresponds to the V_{dep} +50 V for 100 µm thickness sensors, as presented in section 6.1.5. Later, V_{dep} for CERN12 and CERN15 was obtained from the wafer information in the production database[6] uploaded by the vendor, being 22 V and 26 V, respectively, hence the last few *It* curves were taken at 80 V. It is unclear why the V_{dep} for these wafers are around 20 V lower than that determined through the QA measurements described in section 6.1.5.

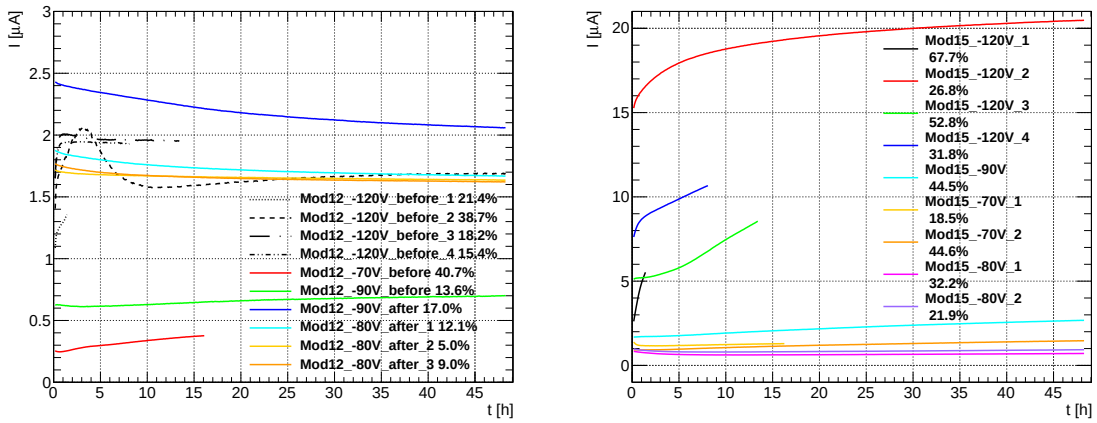

(a) CERN12 (b) CERN15

Figure 6.14: All *It* curves taken for CERN12 and CERN15.

A few shorter curves were taken first to get a first view of the fluctuation. For CERN12, the first measurement at 120 V for only 1.5 h already showed 21.4 % fluctuation. The following full 48 h *It* curve fluctuates 38.7 %. For repetitions 3 and 4, the shape of the curves in the first 10 h became completely different from the first two, the large fluctuation observed before seems to have been mitigated. After two weeks, a 16 h *It* curve taken at 70 V showed large fluctuation, but the following full 48 h measurement that was started on the same day after the previous measurement is within specification. The four curves taken after baking were measured consecutively within 8 days, the fluctuations are all within specification.

The leakage current of CERN15 when biased at 120 V varies drastically between different

[6]For more about the production database see section 7.3.

measurements. Repetition 3 was measured six days after rep 2, and the leakage current level is overall lower. Rep 4 was measured immediately after rep 3, and I_{leak} is very high. The fluctuation of all of these measurements are out of specification. After two weeks, the 48 h measurements at bias voltages 90, 70, and 80 taken within 11 days showed very different fluctuation results. After 70 V rep 2 was finished, 80 V rep 1 started three days afterwards, and 80 V rep 2 started the next day after the previous rep was finished. *IV* curves were taken for both modules, to get an overview of the expected I_{leak} and the breakdown status. The results are shown in figure 6.15(b), the measurement for CERN15 was taken around the same time as the first *It* curve. The *IV* of CERN15 is within specification, and there is no dramatic difference with that of CERN12. Due to time limit and the uncertain behaviour of the *It* curves, CERN15 was not baked.

Taking all results into consideration, it can be observed that I_{leak} stabilises after a few curves were taken. This effect weakens after a few days or weeks, and the fluctuation can become large again. The influence from the definition of fluctuation was investigated by calculating the fluctuation of CERN12 results differently, using the middle value between the maximum and minimum instead of the average. The resulting fluctuations only changed by −1.3–1.2 %, showing that the systematic uncertainty from the analysis method does not change the result. It was also suggested to define the fluctuation with respect to the minimum or maximum, instead of the average or middle point, but this is unlikely to change the whole picture.

Comparison of the *It* curves before and after baking for CERN12 at similar bias voltages 70 to 90 V is shown in figure 6.15(a).

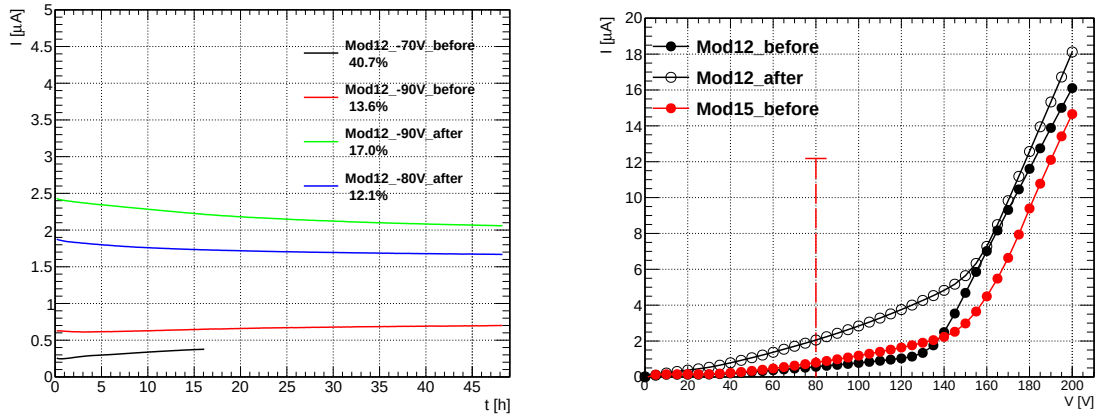

(a) *It* curves of CERN12 before and after baking at different bias voltages.

(b) *IV* for CERN12 before and after baking, and for CERN15 before baking.

Figure 6.15: *It* for CERN12, and *IV* for CERN12 and CERN15.

As shown before, the *It* curve at 70 V is out of specification, and the fluctuation of the curve at 90 V before baking is already decreased to be in spec. Comparing the curves before and after baking, it can be concluded that the leakage current increases over time before baking, and decreases over time after baking. However, after baking, the leakage current level is around three times that before. This is confirmed with *IV* curves: as shown in

figure 6.15(b), the *IV* curve for CERN12 elevated. This characteristics is not desirable. Therefore, baking is not deemed to be a reliable solution to the unstable *It* problem.

6.1.8. Inter-Pixel Resistance

On Strip TS

The wafer map and a photo of the strip TS from HPK is shown in figure 6.16.

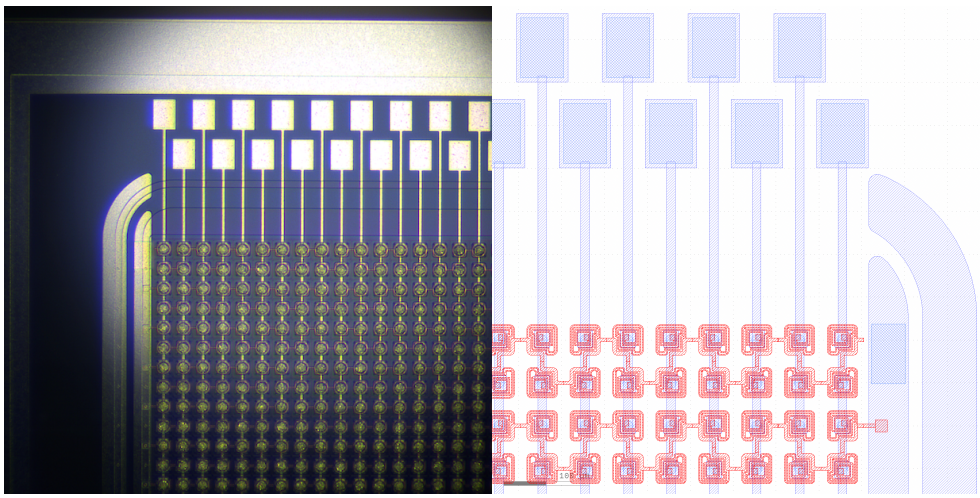

Figure 6.16: HPK strip TS photo and layout. The poly-Si bias rail (shown in red on the TS layout) connects half of the pixels on the neighbouring strips.

This TS was also used for charge collection efficiency measurements by sites with an Alibava setup [152]. It consists of connected pixels, forming strips. There are 40 connected pixels per strip, and 40 strips on one TS. For HPK strip TS, probing pads exist at both ends of each strip.

The measurements were performed by placing two probe needles on the neighbouring strips and applying voltage. Probing the pads on the same or different ends of two strips made no visible difference on the results.

The current vs voltage was measured for only a few volts around 0 V. When applying voltage across the two strips, the 40 pixels are connected in parallel, thus the total resistance R_{tot} and the resistance between each pair of pixels R_{n} (where $\text{n} = 1, 2, ..., 40$) follow the relation $\frac{1}{R_{\text{tot}}} = \sum_{\text{n}=1}^{40} \frac{1}{R_{\text{n}}}$. Since 20 of the pixels are connected by the poly-Si bias rail which result in much smaller resistance, the other pixels are considered to have $\frac{1}{R_{\text{n}}} \sim 0$. This gives $\frac{1}{R_{\text{tot}}} = 20 \times \frac{1}{R}$, where R is the inter-pixel resistance. Ohm's law $R_{\text{tot}} = \frac{V}{I}$ gives $\frac{I}{20} = \frac{V}{R}$, which means R can be obtained by dividing the measured current by 20 and plotting it against the voltage. After fitting a straight line to the linear part, R is inverse the slope. The results show that $R \sim 5\,\text{M}\Omega$ (figure 6.17), which meets the requirement. The TS were not biased in these measurements, giving a more conservative measurement of R [153].

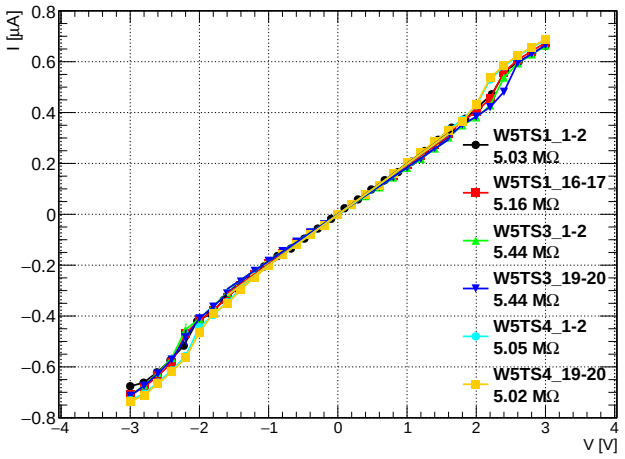

Figure 6.17: Inter-pixel R results, tested on HPK strip TS. Two pairs of strips on each of the three TS on wafer 5 were tested, the indices of the strips are indicated in the legend, e.g. 1-2 being the first two strips next to the edge of the TS. Results show that $R \sim 5\,\mathrm{M\Omega}$ independent of the location of the strip.

On Inter-Pixel TS

Each of the inter-pixel TS consists of six pairs of pads for probing. Local numberings were given to each pair of pads, see figure 6.18 for the numberings and the wafer map (without bias resistors and bias rail). Each pair of pads are connected to two strings of pixels in a double-layered ring shape, four of the six pairs have only one pixel on the inside.

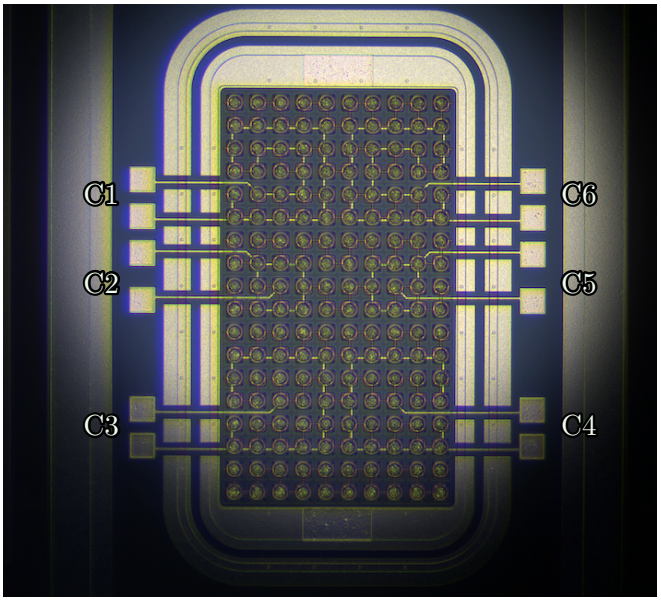

(a) Photo of inter-pixel TS, each pair of pads is given a numbering. The connection of the six pairs of pads are mirrored, i.e. there are three different configurations.

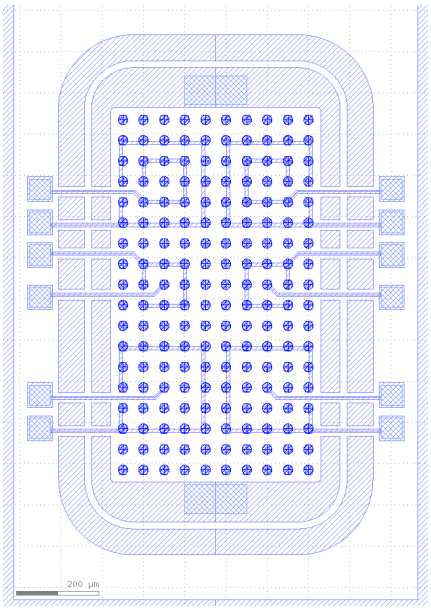

(b) The wafer map showing the rails clearly. The poly-Si bias resistors and bias rails are omitted.

Figure 6.18: HPK inter-pixel TS photo and layout.

Measurements were conducted by using two probe needles to apply a low voltage to the two pads, with the bias pads (at the top and bottom of the TS in figure 6.18) floating. The results are shown in figure 6.19.

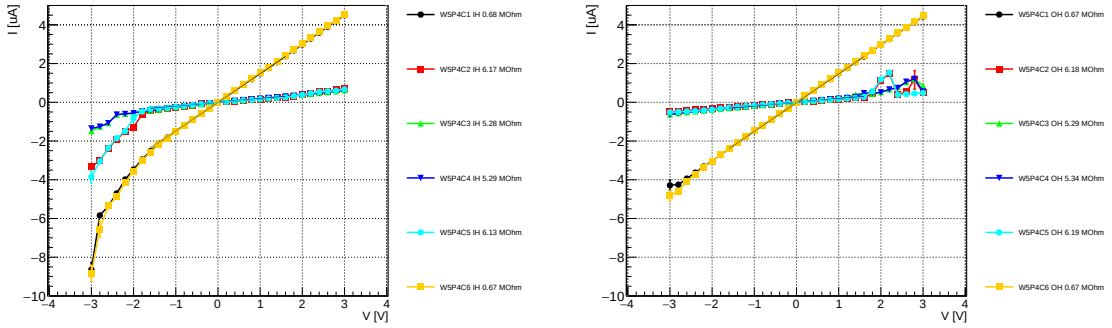

(a) Inner dot/circle connected to V_{out}, outer circle to ground.

(b) Outer circle connected to V_{out}, inner dot/circle to ground.

Figure 6.19: Inter-pixel R measured on the inter-pixel TS (without biasing) on HPK wafer 5, piece 4. Switching the polarity of the connection to the two pads (V_{out} or ground of the power supply) gives different curves, despite that the curves were taken from negative to positive voltage. However, fitting the straight part resulted in similar R between the two connections.

The polarity of the power supply connection to the inner/outer pixels gives different curves. The reason is unclear, since the voltage applied also switched polarity (curves were taken from negative voltage ramping to positive). A possible source of this asymmetric behaviour is the existence of impurities. R was obtained by fitting the straight part, and are almost identical between the two ways of connections. C1/6 have very low R ($\approx 0.67\,\mathrm{M\Omega}$), C2/5 $R \approx 6.17\,\mathrm{M\Omega}$, C3/4 $R \approx 5.3\,\mathrm{M\Omega}$. How to count the numbers of pixels/resistors connected in the circuit, or the source of the wobbles are unclear. A good explanation of the result is not yet found, and requires further studies.

6.1.9. Poly-Silicon Resistance

On the HPK TS dies there are five poly-Si TS that the vendor used for QC. Photo and layout are shown in figure 6.20. They are given local names: QC1 to QC5.

Results from wafer 5, piece 3 for QC1 to 4 are shown as an example in figure 6.21 (the curve for QC5 is not shown because the current is much larger and therefore out of scale). The other two pieces on W5 were also tested and give similar results. The R values are summarised in table 6.5, with the quoted uncertainty being the standard error of the mean of the results obtained from the three TS pieces, since the uncertainty from the fit is negligible. The results for structures QC2 and QC3 are grouped together since they have the same design.

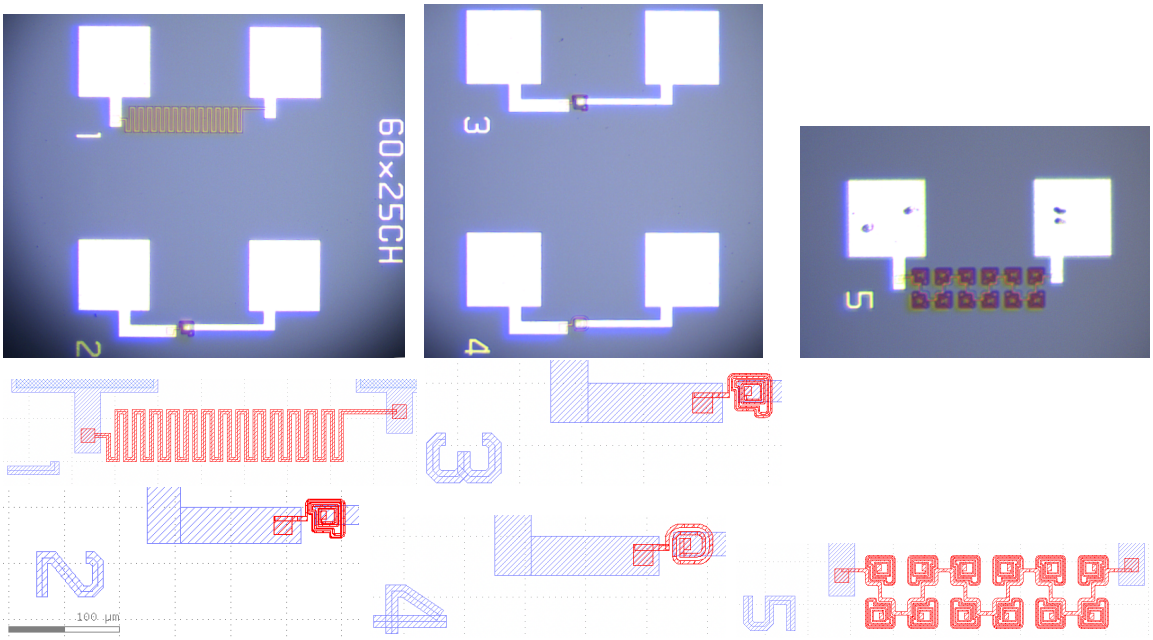

Figure 6.20: The vendor QC TS.

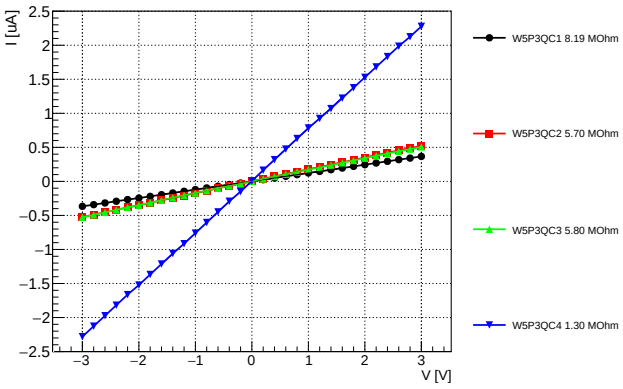

Figure 6.21: Poly-Si resistance of vendor QC TS on wafer 5, piece 3. The structures QC2 and 3 have the same design.

TS	$R\,[\mathrm{M}\Omega]$
QC1	7.96 ± 0.14
QC2&3	5.69 ± 0.15
QC4	1.28 ± 0.03
QC5	0.07 ± 0.01

Table 6.5: Poly-Si resistance of vendor QC TS. The uncertainty shown is the standard error of the mean.

The design for QC2 and QC3 is the same as on the sensors, and the result $R = 5.69 \pm 0.15\,\mathrm{M}\Omega$ agrees with the results from the strip TS. The trace on QC4 is wider and shorter, and the R is considerably lower than that of QC2&3. As expected from the layout, QC1 has a much bigger resistance. The assumed reason is that the length of the rail is longer than that of QC2, 3 and 4. However, the result of QC5 shines doubt on this explanation: the resistance for QC5 is significantly smaller than the others, despite having a long rail. The rail directly connects the blue pads, with punch-through structures that have the same shape as QC2&3 branching off from the rail. The reason that leads to these results is yet unclear and needs further investigation.

6.1.10. Inter-Pixel Capacitance

The inter-pixel capacitance is expected to be at ∼fF level, which is difficult to measure, also considering the interference from stray capacitance. Attempts were made on the designated TS shown in figure 6.18 using the LCR meter that was used to measure bulk capacitance. The pairs of pads on the TS were probed while leaving the bias pads floating. The inner circle of the TS was connected to the higher potential side of the power supply.

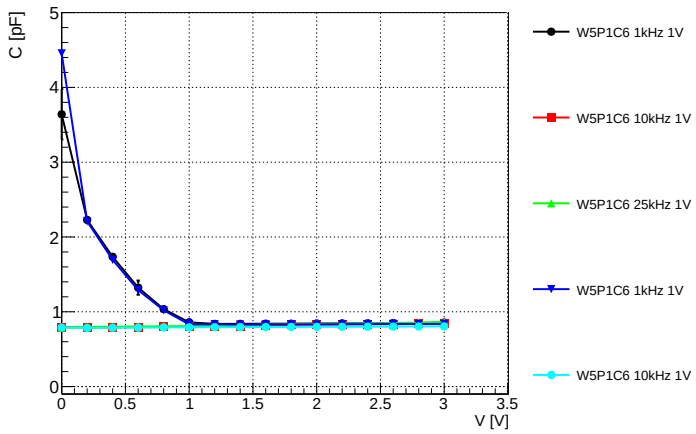

Figure 6.22: Inter-pixel capacitance measured at different frequencies. The 1 V in the legend refers to the amplitude of the measurement voltage from the LCR meter.

Figure 6.22 shows the results. An offset of 0.43 pF was subtracted. This value was obtained by taking a scan with the probe needles not in contact with the TS, and averaging the results. The capacitance is in pF range. The accuracy of the LCR meter is around 1.3% at 1 pF and 10 kHz.

It can be seen that repetitive measurements in the same frequency give similar results, and the curves are indistinguishable from each other at high voltage or frequencies. At 1 kHz, the measured capacitance decreases with voltage, and plateaus at 1 V.

Since multiple pixels are connected in this TS, it is unclear how the measured value should be processed to obtain the inter-pixel capacitance. The measured capacitance is nonetheless much larger than the expected fF range. Stray capacitance can be a possible reason for the higher values measured. However, since the correct usage of this TS is unclear, more studies are needed in order to draw meaningful conclusions.

6.1.11. Conclusions and Outlook

The sensor pre-production QA includes various tests on sensors and test structures (TS) from different vendors. This chapter showed electrical tests of planar sensors and TS from HPK (150 µm) and Micron (150 µm and 100 µm).

Leakage current vs bias voltage

IV curves on 30 unirradiated diodes from HPK were taken by various ITk sites, 29 out of 30 showed no breakdown, and the leakage current level is very well within the required limit. In terms of quad sensors, measurements on unirradiated HPK and Micron 100 µm sensors from ITk sites (KEK, MPP and Göttingen) and the vendors showed good agreement. There is hint of Micron 100 µm sensor leakage current increasing after being biased for a long time, which is consistent with the leakage current stability results.

Three HPK, two Micron 150 µm, and two Micron 100 µm sensors were irradiated and *IV* curves were taken. No breakdown was observed, and the leakage current levels are within specification.

Bulk capacitance vs voltage

CV curves of 33 diodes from HPK, eight 150 µm quad sensors and five 100 µm quad sensors from Micron were obtained (unirradiated), the depletion voltages (V_{dep}) are within specification. Diodes showed two-stage depletion due to p^+-doped rings surrounding the active areas of the diodes, causing lateral depletion. It was observed that the $\frac{1}{C^2}$ curves for a particular region of the wafers are consistently different from the others, indicating manufacturing differences across different area of the round wafer. This can be further investigated by plotting V_{dep} from TS at different regions of the wafer.

The *CV* curves for two 150 µm and two 100 µm irradiated at around $5 \times 10^{15}\,\text{n}_{\text{eq}}/\text{cm}^2$ were taken at 10 kHz. Lower frequencies could be tried in the future.

After the sensors are irradiated, both the *IV* and the $\frac{1}{C^2}$ curves are no longer in the typical shape. Further analysis could be done to investigate the cause within the Si lattice in detail, with assistance from simulation softwares for Si detectors like Allpix^2 [154].

Leakage current stability

It curves for HPK diodes showed fluctuation within specification. However, unirradiated Micron 100 µm sensors were found to have unstable leakage current.

Baking

Two fully assembled modules equipped with Micron 100 µm sensor were tested to investigate the unstable leakage current problem, one was baked. Before baking, the fluctuation of the *It* curves already decreased to within specification after having been biased for a long time for taking *It* curves. However, this is not sustainable. After baking, the leakage current switched from increasing over time to decreasing over time. However, the overall level increased significantly. Therefore, baking was not decided as a suitable solution. Large effect on the leakage current was observed after either doing consecutive long *It* measurements, or leaving the module without bias in storage for a few days to weeks. Further studies can be done on the effect of annealing at room temperature. It was also

suggested to measure *It* at higher humidity, to investigate if the higher conductivity result from the humidity mitigates the effect of the trapped charges. It is also uncertain why the depletion voltage of these sensor wafers is around 20 V lower than the pre-production QA results, which should be communicated with the vendor.

Inter-pixel resistance

Inter-pixel R was tested on two types of TS. The results from the strip TS are within specification, showing good pixel isolation from p-stop. Further investigation is needed on the results from the inter-pixel TS. The measurements were conducted without biasing, giving a conservative result. Further studies can be done with bias voltages.

Poly-Silicon resistance

Results from the vendor QC TS with the same design as the sensors shows good agreement with that from the strip TS. However, results for the other designs are not fully understood. This should be consulted with the vendor, to understand what the material and the structure is, in order to analyse and fully understand the results.

Inter-Pixel capacitance

Capacitance measurements were performed on the inter-pixel TS, tolerating the limited precision brought by the setup, which is mainly used to measure the bulk capacitance. Results show that the capacitance decreases with voltage until up to 1 V when measured at 1 kHz frequency, but keeps constant within the reachable precision at high frequency or voltage. Similar to the measurements for inter-pixel R performed on the same TS, it is unclear how to extract the inter-pixel capacitance from the results.

The report for the sensor production readiness review came out positive in 2023, except for the Micron 100 µm unirradiated planar sensors, due to the unstable leakage current problem. Because further baking tests gave undesirable results, the sensor community is following closely the *It* curves on module level, and is investigating the option of purchasing the corresponding share of 100 µm quad sensors from other vendors instead, which could cause delay due to limitation in the production rate. The rest of the purchase can be made. Overall, the ITk Pixel sensor status shows good prospect and can proceed to production.

6.2. Test-beam

Multiple test-beam campaigns were conducted during 2022 and 2023 at CERN PS and SPS to test the sensors on module level in beam. Various RD53A, ITkPix modules with planar or 3D sensors were tested. The following section focuses on testing of unirradiated HPK 150 µm sensors in quad modules equipped with ITkPixV1.1 FE chips, with data acquired in the 11.2022 SPS test-beam campaign. For 3D FBK sensors with $50 \times 50\,\mu m^2$ pixel pitch as ITkPixV1.1 FE single chip modules please refer to [155].

6.2.1. Setup

Figure 6.23 shows the setup with example of the measured distances between each plane. The modules to be tested, normally referred to as the Device Under Test (DUT), were put in a cooling box between six EUDET telescope planes. Two pairs of scintillators are at the left side of telescope plane 1 and right of plane 6, but are not visible in the photo. A single chip module equipped with an FEI4 readout chip was mounted on telescope plane 2. The centre of every device was aligned with the beam line for data-taking.

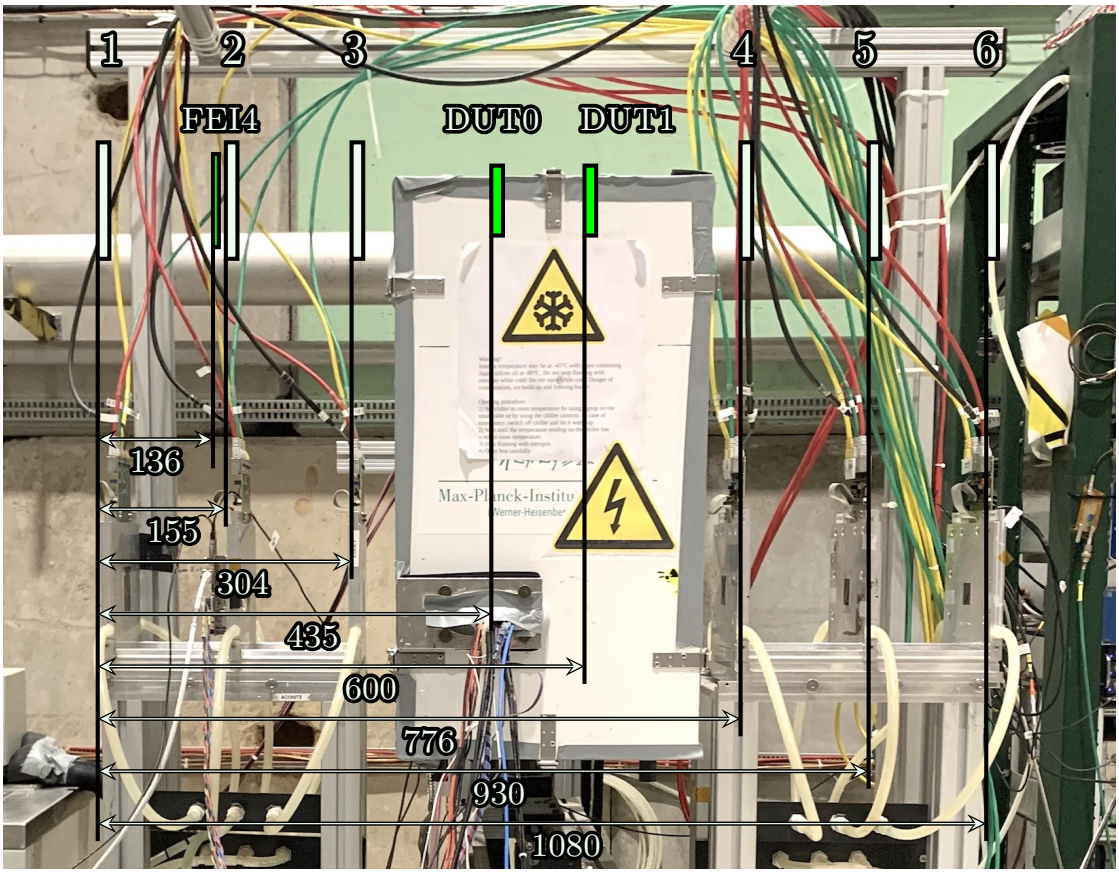

Figure 6.23: Test-beam setup and the distances ([mm]) between planes in 11.2022 SPS test-beam campaign.

The telescope planes were used for tracking, the four scintillators were used for triggering during data-taking, and the FEI4 module was used as the reference[7] in offline analysis. A Trigger Logic Unit (TLU) was used to issue triggers and synchronise the telescope planes, scintillators, FEI4, and DUTs.

HV and LV power supplies are used to bias the sensors and power the modules, including the telescope. The DUTs were connected to different channels of the power supply output, since serial powering is not the goal of the test. They were set in Shunt-LDO mode, which makes sure that the modules consume the same current. The FEI4 was reverse biased at 60 V, the reverse bias voltage on DUTs varies with the data-taking plan according to the goal of the investigation. Multiple chillers were used to control the temperature of the telescope and the cold box. The cold box also has dry air inlet to decrease the humidity, therefore the dew point. Several PCs were used for control and data-taking. A run control PC was put in the hut outside the beam areas, which has full remote control of the setup, allowing shifters to take data safely away from beam or even remotely.

DUTs for the Presented Analysis

The data for the analysis presented in this chapter was taken during the 11.2022 test-beam campaign. Details on the related DUTs (one of them only used as reference) can be found in table 6.6. The temperature of Q9 was kept between −11 and −14 °C during data taking. SCC4, which was measured to be with good efficiency [155], was also included in the cold box. It is – as for Q9 – equipped with pre-production sensor and chip, and was used as reference in the analysis, in addition to the FEI4 module.

Module	Q9	SCC4
Role	DUT	Reference
FE	ITkPixV1.1	ITkPixV1.1
Module Type	Quad	Single Chip Card
Sensor Type	Planar HPK	3D FBK
Active Thickness [µm]	150	150
Pixel Pitch [µm^2]	50×50	50×50
Irradiation	Unirradiated	Unirradiated
Reverse Bias Voltage [V]	20, 40, 60, 80, 100, 120	30
Threshold	2000e	1000e

Table 6.6: Information on the DUTs and test-beam measurements. The threshold is in units of electric charge e.

[7] A module like the FEI4 used as the reference in reconstruction and analysis is sometimes referred to as the "reference DUT", since it is not part of the telescope system but DUT-like, but the goal is not to test this device. When a telescope plane is used as reference, e.g. for monitoring correlation as in figure 6.26, it can be referred to as a reference plane.

6.2.2. Beam

The 11.2022 test-beam campaign was conducted at the CERN SPS north area [156] in the largest hall EHN1 at beam line H6 with 120 GeV pion beams.

The SPS accelerate proton beams to 450 GeV for the LHC, and the north area is a facility that provides beam lines to various test-beam and experiments for research and development. Figure 6.24 shows the facilities in the SPS north area, where there are three halls: EHN1, 2 and 3, and each hall can contain several beam lines. EHN1 houses four beam lines: H2, H4, H6 and H8. H6 is a general purpose test beam with beam momentum lower than the other lines in the same hall, with the maximum at 205 GeV.

Figure 6.24: Aerial view of the CERN SPS north area, showing the layout of the halls, primary targets, and beam lines. The transfer lines transfer the primary beam to the prinary targets. Image from [157].

The protons from SPS, as the primary beam, impinge on one of the primary target stations T2, T4 or T6[8] that are located about 1 km away from the beam extraction point at the SPS, producing secondary beams, and are splitted to different halls. The rate and composition of the secondary beam particles is determined by the length and material of the target [157]. The beam is controlled by the beam control program CESAR [158], which can identify and separate different types of beams – in the case of the EHN1 hall, pions and kaons. The particles are de-bunched by turning the RF off during extraction, and are served in "spills". There are 10^6 to 10^7 particles per 15 s in each spill, and the spill itself lasts for around 5 s.

[8] T2 is used for beam line H2 and H4, T4 for H6 and H8.

6.2.3. EUDET-type Beam Telescopes

The first EUDET-type beam telescope [159] was developed in the EUDET project (2006–2010), the original goal was detector research and development for the International Linear Collider. The Joint Research Activity 1 (JRA 1) is part of the EUDET project, and focused on test-beam infrastructures. Then came the AIDA project (2011–2014), with the goal of studying the required infrastructures for future particle physics experiments. The original EUDET beam telescope was later modified into the AIDA telescope, and more replicas were made. All the replicas are collectively referred to as the EUDET-type beam telescopes. The one that was used for ATLAS during the test-beam campaigns in the thesis work is the ACONITE. Other examples are DATURA and DURANTA at DESY [160]. These telescopes are stable and widely used. There is also continuous development on other telescopes, like ALPIDE [161] and Lycoris [162].

The EUDET-type beam telescopes consist of six pixel detector planes equipped with Mimosa 26 sensors [163], four scintillators to generate signals for triggers, a TLU to provide triggers, a DAQ system, and the mechanics for precise positioning of the telescope planes and the DUTs. In the beam area, alignment of the telescope planes with the beam line is made using lasers.

Mimosa26 Sensors

The six telescope planes are equipped with Mimosa26 sensors, which use monolithic active pixel sensor (MAPS) technology[9]. They are highly granular and thin (50 µm) CMOS sensors. The basic information about the Mimosa26 and other DUTs is summarised in table 6.7. During reconstruction and analysis, this information is specified in a file to provide geometry configuration to Corryvreckan.

	Mimosa26	FEI4	ITkPix Quad	ITkPix Single Chip Card
Number of pixels	1152×576	80×336	768×800	400×384
Pixel pitch [µm^2]	18.4×18.4	250×50	50×50	50×50 or 100×25
Spatial resolution [µm]	5.3, 5.3	72.2, 14.4	14.4, 14.4	14.4, 14.4
Time resolution	230.4 µs	25 ns	200 ns	200 ns
Material budget	0.00075	0.008	0.01	0.01

Table 6.7: Geometry of Mimosa26, FEI4, and ITkPix modules, as specified in analysis. The spatial resolution is the standard deviation of the uniform distribution $\frac{\text{pixel pitch}}{\sqrt{12}}$. Telescopes can reach better resolution (3.24 µm instead of 5.2 µm) due to charge sharing [100].

The resolution 5.3 um comes from the standard deviation of the uniform distribution, which is $\frac{\text{pixel pitch}}{\sqrt{12}}$. However, due to charge sharing, the mean intrinsic resolution was measured to be 3.24 µm [100].

The Mimosa26 telescopes operate in rolling shutter mode, which means that they read out row by row. One row is powered at a time, reducing power consumption, and all columns

[9] A type of CMOS technology.

are read out at the same time. The whole readout takes 115.2 µs, which means readout of 8680 frames/s.

It is worth pointing out that the time resolution for Mimosa26 is 230.4 µs rather than the readout time of 115.2 µs. This is because the readout FPGA raises a busy after a trigger, which is not synchronised with the rolling shutter readout. As a result, the subsequent frame needs to be read out too. The busy state can last for 115.2 to 230.4 µs. This causes a waste of events: with a busy signal being sent at the handshake with the TLU, the TLU will not continue to send triggers. Even though the read-out of FEI4 and ITkPix modules is much faster, they cannot continue to take data without triggers. Consequently, most reconstructed tracks only contain hits from the telescope planes, as those hits are not recorded by the FEI4 or ITkPix modules due to their shorter readout times. This can be improved in future campaigns by using the EUDAQ2 framework and the AIDA-TLU [164].

Scintillators

The scintillators consist of photomultiplier tubes. There are four scintillators in the beam line, two upstream of the telescope and two downstream. For each pair of scintillators, one is placed vertically and the other horizontally, providing an overlap area of around 2 cm × 1 cm. The signals from these scintillators are sent to the TLU to issue triggers.

Trigger Logic Unit

The EUDET-TLU [165] was used, which is based on a FPGA[10] board (Spartan 3) and interfaces via various connectors. The TLU receives four signals from the four scintillators, which can be combined logically with AND, OR, or VETO logics, and then the TLU generates the trigger. Each trigger increments an internal counter and the timestamp of the trigger is saved in a buffer, to be read out via USB2.0 by a PC.

In practice, the TLU was connected to the scintillators via LEMO connectors, and interfaces with the data reduction box of the telescope and the DAQ FPGA board of the DUTs (including FEI4 – the reference DUT) via RJ45 connectors. The TLU generates and distributes the triggers, therefore synchronising the readout systems of all these devices. It can also do handshakes with the DUTs, which could respond with a busy signal, and only sends the next triggers when the busy is dropped.

6.2.4. Data-taking

EUDAQ

EUDAQ [166] is a DAQ framework for the global operation and synchronised data-taking of beam telescopes and other devices such as DUTs. Its independent modules, which communicate via TCP/IP, can be run on different PCs, and it is easy to integrate new devices via their producers. See figure 6.25 for the different framework modules of EUDAQ.

[10] FPGA: field-programmable gate array.

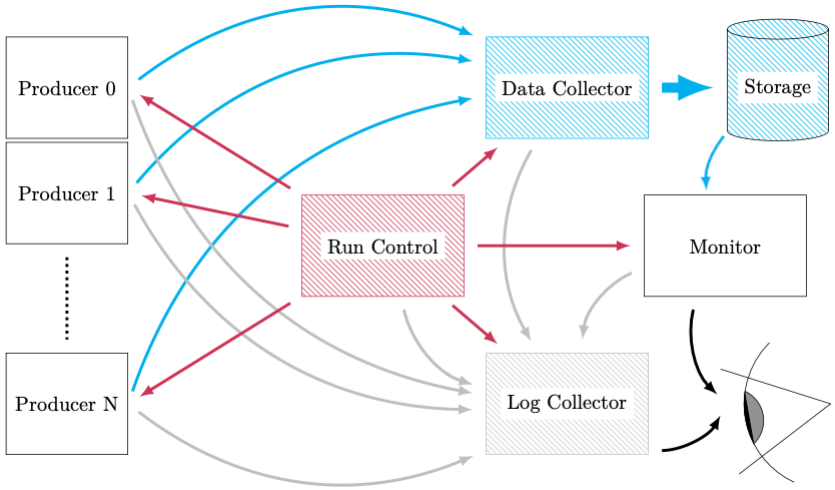

Figure 6.25: Components of the EUDAQ framework. Run Control centrally controls the rest of the framework modules and has a GUI. Producers are individual to different DAQ systems of the devices. Data Collector builds events and saves them into a data file per run. Log Collector gathers and shows the log messages. Monitor can be used during data-taking to judge data quality. Image modified from [167].

1. The Run Control has a GUI for controlling the other modules, like commanding initialise, configure, and start of data-taking.

2. Each EUDAQ producer is a software that controls and reads out the DUTs or other detector hardwares. They are provided by the user specifically for the readout of each type of device. The producers and DAQ systems for different devices are summarised in table 6.8. For the beam telescopes, the NI producer and Anemone used for reading out Mimosa 26 sensors run on a machine from National Instrument (NI) with Windows OS.

3. The Data Collector receives, for the same trigger, one event per device from the producers, and merges them into a global event. It also merges all data from one data-taking run into one file, adds a run header and trailer: beginning-of-run-event (BORE) and end-of-run-event (EORE), and puts the file into disk storage. BORE stores the config file and the EORE signals to the DAQ that the Producer has ended the run.

4. Log Collector receives log files from all framework modules, combine them, show them to the user, and save them to storage. This centralised approach facilitates debugging.

5. Monitor is crucial during data-taking The online monitor reads data from the disk, and provides plots for the shifters to judge the data quality, so that immediate actions are taken if problems such as loss of correlation (as introduced in the following) is spotted.

DAQ for DUTs

The DAQ systems for FEI4 and ITkPixV1.1 modules are summarised in table 6.8. A DAQ system includes a DAQ board that interfaces between the modules and the PC where the

Device	Producer	DAQ System	DAQ board	DAQ SW
EUDET	NI Producer	NI COTS [168]	Virtex 5	Anemome 1.3 LabView [169]
FEI4	STcontrol	USBpix [170]	MMC3	STcontrol
ITkPix	YarrProducer†	YARR [171]	XpressK7 / Trenz	YARR

Table 6.8: EUDAQ producer, DAQ system, FPGA boards, and the DAQ software used for different devices in test-beam. The EUDAQ DAQ framework in addition is used for operation and data-taking with all devices. †YarrProducer: https://gitlab.cern.ch/-YARR/YarrEudaqProducer.git.

DAQ software is run. The DAQ board carries an FPGA that hosts the firmware, and is often referred to as the FPGA board, or by the name of the DAQ system, like "USBpix board" for FEI4 readout or "YARR board" for ITkPix[11] module readout.

For FEI4, the STcontrol software used for DAQ has full EUDAQ integration and therefore includes an STcontrol producer. The FPGA board used for the USBPix system in the test-beam is MMC3: Multi-chip Module Card 3.0, which is a multi-Input/Output board with multi-chip functionality [172].

For ITkPixV1.1 modules, the FPGAs on the YARR boards used during test-beam are XpressK7 and Trenz. The YARR board, as it interfaces via PCIe[12], are sometimes also loosely referred to as the SPEC (Simple PCIe Carrier) board or PCIe card.

In test-beam, up to three ITkPix quad modules can be connected to one YARR board with DisplayPort cables via an Ohio adapter board[13]. Each adapter has four ports: A, B, C, and D. Port D is reserved for the TLU, and port A, B and C are for modules. Each port has 5 lanes: one reserved for sending commands, and the other four for receiving data. Therefore, each port can read four chips – one receiving lane per chip. 12 lanes are available from the three ports, allowing simultaneous read out of 12 chips[14] (three quad modules). Aurora protocol is used to coordinate and assemble the data from different chips. Each lane has two wires: positive and negative, which enables transmitting data via differential signalling.

Prior to data-taking, the DUTs are tuned and the standard masking procedure is performed, with the same principles as for the module quality control tests, as introduced in section 9.2.5. When data is collected at different conditions such as bias voltages, tuning and masking are often repeated to keep the threshold distributions good and the faulty pixels appropriately masked. The tuning results and masks are saved in the chip configuration files, and the masked pixels do not record any hits during data-taking. It is important to note that this mask is independent of the offline masking step introduced in section 6.2.5, which is performed during reconstruction and analysis.

[11] YARR is used for both RD53A and RD53B (ITkPix).
[12] PCIe: Peripheral Component Interconnect Express.
[13] Ohio adapter board: an FPGA Mezzanine Card (FMC).
[14] During lab module electrical tests, all 16 lanes can be used for module readout, as no places need to be reserved for TLU. This also allows using all four lanes on one port to transfer data for one FE, and all four ports for the four FE chips on only one module. In this case, the readout is faster.

Correlation

If a particle from the beam traverses the telescope planes and the DUTs, the corresponding x- and y-coordinates of the hit in one plane (be it a DUT or telescope plane) should be correlated with that on the other planes. During data-taking, correlation between all devices is checked using the online monitor in EUDAQ. This is an important tool to ensure basic validity of the data. Correlation can also be checked offline via the reconstruction and analysis software Corryvreckan [173].

Figure 6.26 shows the coordinates of the hits registered by one of the DUTs (denoted x and y) and the reference plane (denoted x_{ref} and y_{ref}). The reference plane is user-specified in Corryvreckan. In this case, it is the telescope plane 3. The numbers of hits peak at the

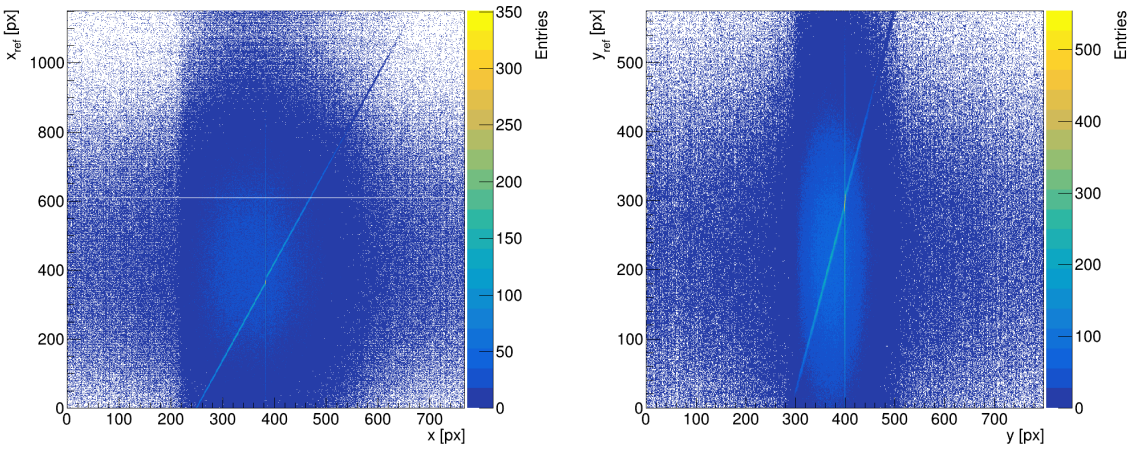

(a) x (b) y

Figure 6.26: Correlation plot between Q9 and telescope plane 3 (reference plane) produced by Corryvreckan. The area where hits are shown depends on the overlapped area of the scintillators, or the functioning area and pixels on the telescope. The faint vertical lines at 384, 400 pixels are due to the inter-pix region of the sensor.

diagonal line, showing the existence of correlation between the coordinates of the hits on the two planes. Depending on the orientation of the DUTs, correlation can show up on plots for either x_{ref} vs x and y_{ref} vs y, or x_{ref} vs y and y_{ref} vs x. In this case, the two devices have the same x- and y- orientation. If correlation is seen in the x vs y and y vs x plots, it means one of them (the DUT) is rotated 90° around the z-axis. The diagonal line can be either from lower left to upper right, as in the figure, showing positive correlation, or the other way around, showing negative correlation, in which case, one of the coordinates between the planes are pointing at the opposite direction.

The data-taking in test-beam campaigns has been suffering from desynchronisation, which refers to sudden correlation loss after an undefined numbers of events are taken. This is checked by plotting the difference of the cluster positions between the DUT and the reference plane (e.g. in the x-direction, $x_{\text{ref}} - x$) vs time (which is shown via the number of events). See figure 6.27 for such a plot.

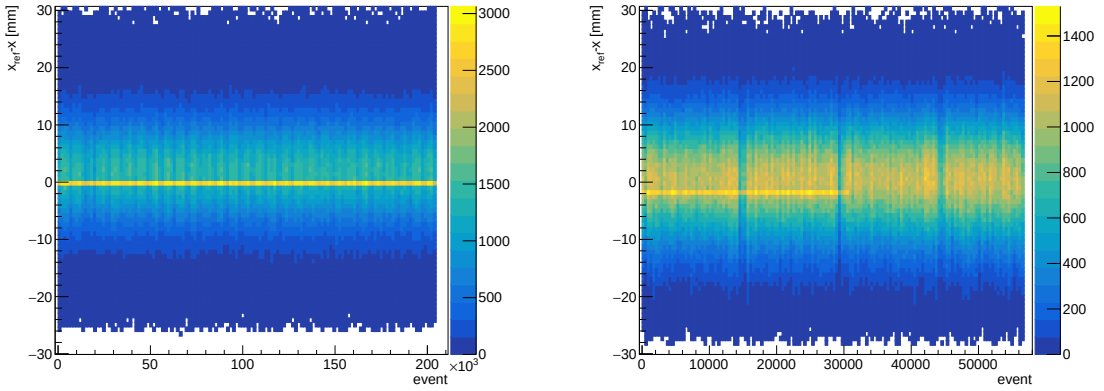

(a) A good run with correlation of data between the DUT and the reference plane.

(b) A run with desynchronisation after approximately 30000 events.

Figure 6.27: $x_{\text{ref}} - x$ vs number of events for two runs: one good run with correlation from the beginning to the end, one with desynchronisation. The periodic change is due to beam intensity cycles. The DUT is an ITkPixV1.1 quad module, and the reference plane is telescope plane 3.

After debugging, the problem was found in 2023 to be due to losing trigger. A tool[15] is being developed to resynchronise the data, in case previously un-useable desyncronised data need to be recovered and included in the analysis, to increase the statistics.

6.2.5. Reconstruction and Analysis

In the past, reconstruction and analysis has been routinely done with EUTelescope [174], for example, during the sensor market survey [3]. However, since the start of testing DUTs equipped with ITkPix chips, Corryvreckan [173] has been used. It was shown that the results obtained with EUTelescope and Corryvreckan are compatible, and in addition, a software module in Corryreckan – `[AnalysisITkPixQuad]` – was developed, to accommodate the special geometry of the inter-chip region on the quad sensors[16]. For details about this software module please refer to the thesis referenced in [2].

The offline reconstruction and analysis procedure consists of these steps:

1. Selection of good runs
2. Masking of noisy or dead pixels
3. Alignment of telescopes and DUTs
4. Analysis

[15] Data resynchronising tool: https://github.com/tbisanz/eudaq/tree/v1.x-desyncmon
[16] As introduced in section 4.3.1.

Good Run Selection

This step checks the data for the presence of correlation until the end of the run. In the case of the 11.2022 test-beam campaign, the runs are also screened for misalignment: using the same alignment geometry, the residual distribution of DUTs do not centre at zero for all the good runs. This could be from physically opening the box and moving the DUTs when switching them. For the results presented here, runs with misalignment within 15 µm were selected. The impact is expected to be small, as all clusters in the vicinity of 100 µm, 100 µm with the track is associated to the track, therefore a 15 µm shift is tolerated. This is also a compromise to get larger statistics.

Masking

Masking was performed using runs in the same condition (bias voltage and threshold). The generated mask was then applied to exclude certain pixels from reconstruction and analysis. Two types of masking criteria were used:

1. Noisy pixel masking via frequency cut: the cut value, e.g. 20, means pixels exhibiting 20 times the average hit of all pixels on the sensor are considered noisy and are masked.
2. Dead pixel masking: pixels that has not fired any hits are considered "dead" and are masked. Possible reasons include faulty pixels being masked in pre-beam tests and pixels that simply have not been hit by the beam.

Alignment

During offline software alignment, Corryvreckan adjusts the x, y values, and rotate the devices, to find a position where the tracks are aligned on all devices. The z values are the distances between the devices, and are measured physically with a regular ruler.

Each incoming particle can generate signals in multiple pixels. Therefore, the connected pixel hits are grouped into clusters, and the x- and y-coordinate of the cluster is that of the cluster centre, which is defined by either the arithmetic mean, or is weighted by charge. Tracks are found using the General Broken Lines algorithm [175]. It starts with finding a straight line to connect the clusters on the first and the last planes, then defines an ellipse in the xy-plane with user-specified spatial cut values in x and y directions. For the devices in between, clusters that are within the spatial cut are associated to the track.

For the alignment of telescope planes, Corryvreckan fits for the tracks, minimises the track χ^2, and adjust the geometry setting of the planes. This is done in an iterative process by gradually decreasing the specified spatial cut values. DUT alignment is done by minimising the distance between the clusters on the DUT and the track.

The alignment is done iteratively, each iteration gradually reducing the spatial cut values, until they are approximately the resolution of the device. Alignment iterations are monitored by the residual distribution, as shown in figure 6.28. For each cluster, the residual is the x or y of the cluster on the reference plane subtracting that on the DUT plane. The goal is

to get the clusters aligned, which means the residual distribution would centre around 0, and be as narrow as possible. Typically, the standard deviation of the distribution should be reduced to around the resolution of the device.

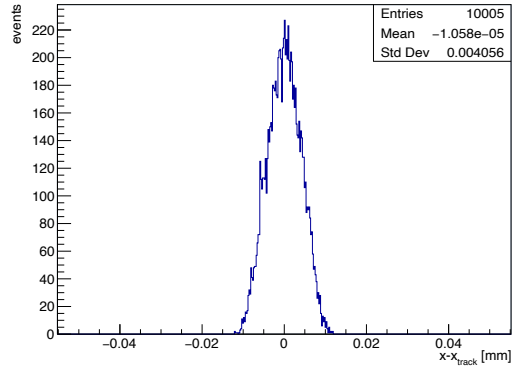

(a) Telescope plane 3 residuals x.

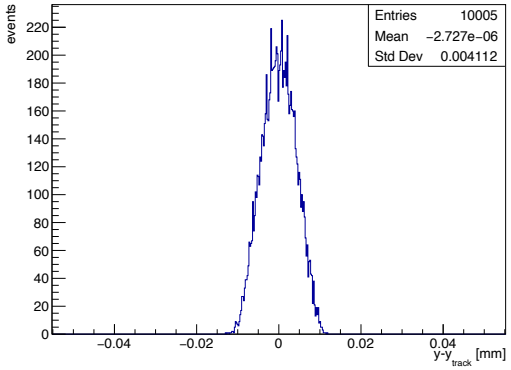

(b) Telescope plane 3 residuals y.

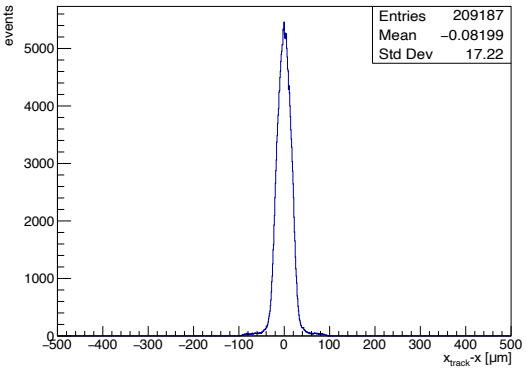

(c) Q9 residuals x.

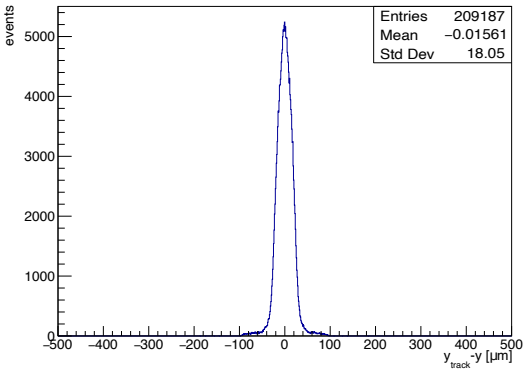

(d) Q9 residuals y.

Figure 6.28: Example of telescope and DUT alignment results. The peak is centred at 0, and the standard deviation is around the value of the spatial resolution.

Analysis

For the analysis, tracks with 7 hits on 6 telescope planes and 1 reference DUT were accepted. When associating a cluster on the DUT with a track, spatial cut of $x, y = 100\,\mu\text{m}, 100\,\mu\text{m}$ was applied. The primary hit position can be difficult to determine if a delta electron is produced in the Si by the initial particle. Delta electrons are energetic, which cause a secondary track, therefore showing up as a bigger and longer cluster. Because of this, the spatial requirement is set on the hit in the cluster that is the closest to the track, instead of the cluster centre.

The hit detection efficiency of the DUT is defined as:

$$\varepsilon = \frac{N_{\text{DUT}}}{N_{\text{reference}}}, \tag{6.1}$$

where N_{DUT} is the number of tracks found on the DUT and $N_{\text{reference}}$ is the number of tracks found on the reference. A "track" found on the DUT means there is an associated cluster on the DUT to the track defined by the telescope and reference DUT. Corryvreckan also gives an uncertainty, which is one standard deviation from applying the Clopper-Pearson confidence interval.

Analyses were repeated using different modules – FEI4 and SCC4 – as references, and investigations on different offline masking strategies were also conducted: two masking strategies were used, one completely without offline mask, and the other applying noise mask with frequency cut = 20 and dead pixel mask. Masking was done using all the good runs in the same condition (bias voltage and threshold).

6.2.6. Results

Results for the hit detection efficiency of the ITkPixV1.1 quad module Q9 with different bias voltages at 2000e threshold are shown in figure 6.29, and the exact values for the efficiencies are listed in table 6.9.

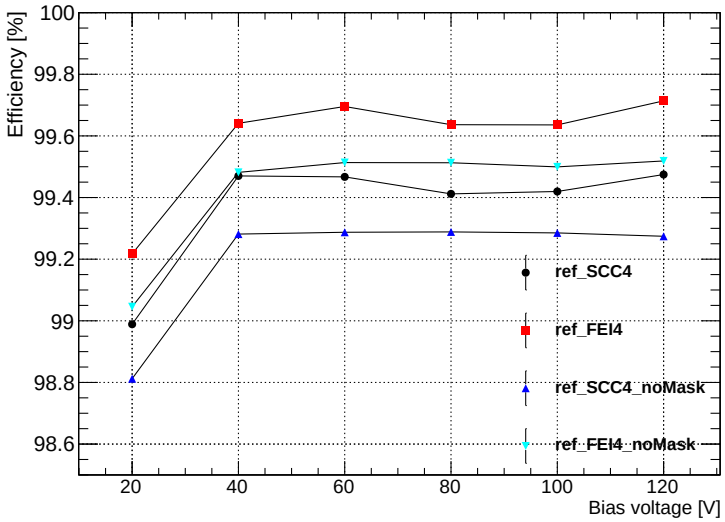

Figure 6.29: Hit detection efficiency vs reverse bias voltage of ITkPixV1.1 quad module Q9 analysed using different references (SCC4 or FEI4) and masking strategies (masking noisy and dead pixels vs without offline masking). The uncertainties given by Corryvreckan are plotted, but the error bars are too small to be visible.

In general, Q9 shows good efficiency: the specification requires 98.5 % at the operation voltage (50 V higher than the depletion voltage V_{dep}) for un-irradiated sensors, which is already reached at the lowest bias voltage of 20 V, at which the efficiency is only lower by approximately 0.4 % than with higher bias voltages at which the sensor can be fully depleted. As presented in section 6.1.5, the depletion voltage for HPK sensors is around 60 V. The results at 20 V show that at lower voltage, the depletion zone created by the bias voltage and intrinsic depletion is still enough for the sensor to generate signals and detect

Reference	Masking	20 V	40 V	60 V	80 V	100 V	120 V
SCC4	mask	98.99	99.47	99.47	99.41	99.42	99.47
FEI4	mask	99.22	99.64	99.70	99.64	99.64	99.71
SCC4	without mask	98.81	99.28	99.29	99.29	99.29	99.27
FEI4	without mask	99.05	99.48	99.51	99.51	99.50	99.52

Table 6.9: Efficiency of ITkPixV1.1 quad module Q9 [%] under different reverse bias voltages. The statistical uncertainty is 0.01 % for all measurements.

particles with good efficiency. Moreover, the threshold of 2000 electron charges is higher than that recommended for module quality control (as introduced in section 9.2.5), making the results more conservative.

The efficiencies measured is higher when using FEI4 as the reference than using SCC4, independent of the masking strategy. The choice of reference was thought to have no effect on the results: it only affects which tracks are included in the denominator, if there is no bias toward the types of track that can be detected, this should not influence the fraction of the tracks that another DUT could detect. The only factor that affects how many tracks (among the tracks detected by the reference) that the measured DUT could see should be the efficiency of the DUT itself. However, the results show that this is not the case. Another independent analysis was done on the same data, as shown in ref. [2], which used FEI4 as reference, noise mask with frequency cut 50, and dead pixel masking. The results between these two analyses are compatible. A possible reason for this observation is the pixel pitch of the FEI4 (250 µm, 50 µm) exceeding the spatial cut (100 µm, 100 µm). It is also possible to be due to FEI4 having difficulty detecting certain types of tracks that both SCC4 and Q9 can detect as they have novel sensors and ITkPixV1.1 FEs. More studies are required for a conclusion to be drawn.

The efficiencies measured after masking noisy and dead pixels are higher than that without masking, independent of the choice of reference. This is expected: some malfunctioning (noisy or dead) pixels are masked by YARR before data-taking, which do not record hits. If they are not masked in the offline analysis by Corryvreckan, these inefficient areas are still taken into account in the analysis, resulting in a lower hit detection efficiency result. Whereas with offline masking, faulty pixels are excluded in the analysis and do not affect the measured efficiency results.

After masking noisy and dead pixels, an efficiency dip of approximately 0.05% was observed at 80 and 100 V. The cause is not yet clear and requires further investigations, particularly regarding the masking, such as the specific areas of the sensor that were masked.

As mentioned in table 6.3, bias structures could cause efficiency decrease around the affected area. The in-pixel efficiency map can be used to investigate this. It is obtained by overlaying the tracks of all pixels into the size of one pixel, resulting in a plot that shows the efficiency distribution within the pixel. Figure 6.30 shows the results for Q9 (HPK sensors with poly-Si bias structures) when biased at 100 V. The efficiency distribution is relatively uniform,

without obvious low efficiency regions from bias structures.

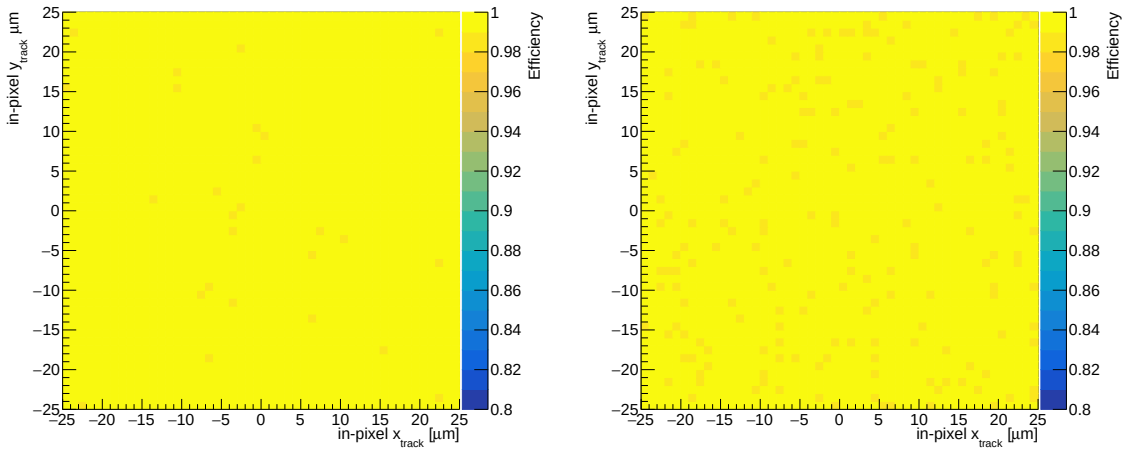

(a) FEI4 as reference.

(b) SCC4 as reference.

Figure 6.30: In-pixel efficiency map for ITkPixV1.1 quad module Q9 with reverse bias at 100V.

6.2.7. Conclusions and Outlook

An unirradiated ITkPixV1.1 quad module Q9 equipped with a HPK 150 µm planar sensor was tested in beam, reconstruction and analysis was conducted on data taken with the module tuned at 2000 electron charge threshold, and biased at different voltages from 20 to 120 V. Using a FEI4 module as reference, and after masking dead pixel that has fired no hits or noisy pixels that have recorded 20 times the average hits of the sensor, the hit detection efficiency of Q9 was measured to be 98.99 % at 20 V, and 99.47 % at higher bias voltages, with exception of 80 and 100 V, at approximately 99.42 %. The statistical uncertainty is 0.01 %. The efficiency at 20 V is about 0.4 % lower than at higher bias voltages, possibly due to not reaching full depletion. In-pixel efficiency map showed even efficiency across the whole pixel, no bias structure-caused low efficiency region was observed.

It was found that using different reference DUT can affect the result: using FEI4 gives around 0.2 % higher efficiency value than using a single chip module with the same flavour of front-end chip. The inferred reason is that the ITkPixV1.1 module is capable of detecting more hits than the FEI4. This can be further investigated by using a different FEI4 module as the reference to check if this is a consistent observation, and measuring the efficiency of FEI4 modules using ITkPixV1.1 and FEI4 respectively, to check if the efficiency of the FEI4 is lower when using an ITkPixV1.1 module as reference. Another possible reason is the spatial cut applied in the offline analysis being smaller than the pixel pitch of the FEI4.

Masking noisy or dead pixels result in a higher measured efficiency by approximately 0.2 %, as expected. However, it is unclear why masking caused a small yet observable efficiency decrease at 80 and 100 V. More investigations could be done on the masked pixels, to check if there is any differences in the number of masked pixels, and their position on the sensor.

There is also a new proposed masking strategy of masking only pixels that were disabled by YARR. This information is retrievable from the beginning-of-run-event of each run.

More studies can be conducted, such on the different-sized pixels at the inter-chip region. There is also a plan to switch from EUDAQ1 to EUDAQ2 [176], which implements the AIDA-TLU. It can configure each device individually with an individual busy. During the dead time of the slower devices, the faster devices can still receive triggers and take data. Therefore, the trigger rate will no longer be limited by the device with the longest read-out time. This could lead to improvements of data-taking rate by a factor of around 28 [164].

CHAPTER 7

Site Qualification

More than 20 ITk sites constitute the main workforce for ITk pixel module production. All sites are required to show their capabilities in performing the relevant procedures for which they are responsible. For this purpose, teams of experts wrote site qualification (SQ) documentations for various activities, each block detailing one procedure and the criteria to be met. After the sites submit their SQ material, the experts review the material, and comment on or pass the qualification accordingly. As Göttingen is an outer barrel (OB) site, this chapter concentrates on the parts relevant to OB activities. This chapter gives an overview of the SQ, introducing the lab infrastructure, database, as well as coating and wire-bond protection blocks. The other blocks related to module assembly and testing are detailed in chapter 8 and chapter 9.

7.1. Site Qualification Overview

7.1.1. Production Flow

Figure 7.1 shows the production flow of OB modules. After receiving the module components, the ITk sites conduct reception tests, assembly (flex to BM attach), and post-assembly tests similar to the reception tests. Then comes wire-bonding and electrical quality control (QC) test. The modules are then processed, packaged and sent to external companies for parylene coating. After receiving the modules back, the sites conduct a second round of electrical QC to check for damages in the process, then add mechanical wire-bond protection. The final tests are thermal cycling, stability test, and a final round of electrical QC.

During pre-production, modules that exhibit sufficient quality will be used for Loaded Local Support (LLS) pre-production, which includes cell loading, cell integration, and LLS QC. Cell loading means gluing a module to a flat carbon structure with good thermal

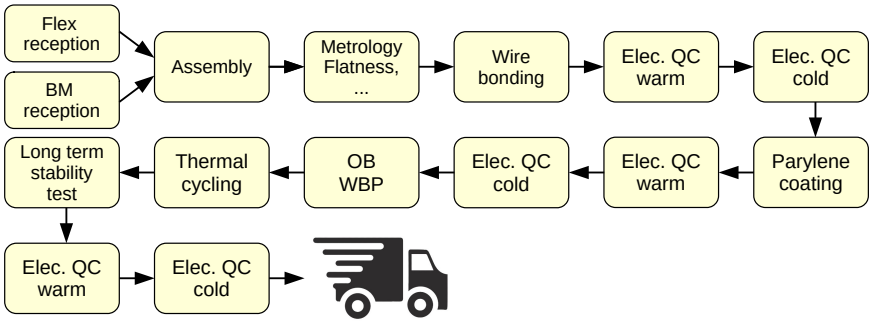

Figure 7.1: Production flow of outer barrel modules [177]. The assembly step after the module components (flex and BM) reception tests refers to the flex to BM attach. Three rounds of electrical QC are performed: initial warm&cold, post-parylene warm&cold, and final warm&cold.

conductivity that is referred to as a "cell". Before and after this process, basic tests are performed on the module. Loaded cells are then integrated to a local support, forming a "loaded local support", and this process is called cell integration. An LLS has functioning serial powering chains and is a fully functioning unit of the pixel detector. It also goes through specific QC tests. There are two types of LLS for OB: Longerons and Inclined Half Rings. Subsequently, a demonstrator will be built for integration and system test. In production, the modules that passed all the tests in the chain will go into the final ATLAS ITk pixel detector.

7.1.2. Site Qualification Blocks and Progress

The ongoing SQ started November 2022 when the first sub-block of the SQ documentation was approved. The SQ blocks are listed in table 7.1, including requirements on basic facilities like lab and software infrastructures, and relevant assembly and test procedures. Each ITk site need to qualify for the blocks relevant to the activities in which they are involved. For example, Göttingen is only involved in OB modules, all of which are quad modules, and thus do not need to qualify for the triplet related blocks, which are omitted from this thesis. Also note that for the testing blocks, the electrical tests are divided between block 11 (Digital Module Tests) and block 12 (Stage 2 Full QC), instead of only in block 11.

Figure 7.2 shows the SQ progress: "test" refers to when one site upload or pass the SQ material for one sub-block. This figure shows the percentage of tests that was uploaded or passed. The names of the SQ blocks in the legend correspond to the code beside the titles in table 7.1. The first few blocks for which sites were qualified are the lab infrastructure, quad reception and assembly, and digital module test blocks. The speed of growth for these blocks is different: qualification for the quad module reception test continued to grow and is the first block that reached the 100 % target, meaning every site is fully qualified for every sub-block, whereas quad assembly grew much slower. SQ for database did not start early,

1	Lab Infrastructure (LAB) Requirements on lab room environment and monitoring, compliance and handling of the dual use components (ASIC), storage and shipping of modules and components, production rate planning.
2	Database (DB) Make sure of necessary software and computing resources, so that the testing data can be stored, analysed, and uploaded to the ITk production database (PDB).
3&4	Flex & Flex Quality Assurance (FLEX) Various tests for the flex before and after population†, to ensure that the specifications are met, and that defects can be spotted and tracked early in the production chain.
5	Coating (COAT) The parylene coating (for HV isolation) will be conducted by external companies or specific institutes. This SQ step is to qualify sites for pre- and post-coating procedures: masking, shipping, thickness and adhesion test, de-masking, visual inspection (VI), and electrical tests.
6	Metrology and Reception of Quad Components (QREC) VI, metrology, and mass measurement of flex, Si dummy, and BMs, as well as electrical test (BM *IV*), and uploading of results to PDB.
7	Quad Assembly (QASS) Assembling flex with glass dummy to test glue coverage, with Si dummy to test xy-alignment and thickness, and with real BM for module production. For the assembled real modules, conduct VI, metrology, mass, backside flatness measurements, and upload results to PDB.
8&9	Metrology and Reception for Triplet Components (TREC), Triplet Assembly (TASS) Correspond to block 6 and 7, but are for triplets.
10	Testing Set-up (TEST) Building a testing setup with detector control system (DCS), software interlock, and hardware interlock for room temperature and cold test, thermal cycling, source or x-ray test, and stability test. Parallelisation of the setups to test multiple modules.
11	Digital Module Tests (DIG) First power-up, minimal tests, simple scans, advanced scans.
12	Stage 2 Full QC (FULL) Reception test, temperature controlled testing, disconnected bump tests, under-shunt protection, thermal cycling, long-term stability test, full QC with parallel setups and data transmission, swapping modules between sites for cross-validation.
13	Outer Barrel Wire-bonding Protection item and attachment (OBWBP) Reception test of OB WBP components, attachment, metrology, strain relief.

Table 7.1: All site qualification blocks [178]. The code in the bracket after the block titles are used in the database. †Bare, unpopulated, or unloaded flex refers to flex without SMD components.

but grew strong once started. The growth of lab infrastructure, digital module test, and database slowed down significantly since August 2023. The other blocks grew slowly and steadily. Full QC, triplet assembly, triplet reception and testing setup SQ either started way later than the other blocks, or increased slowly.

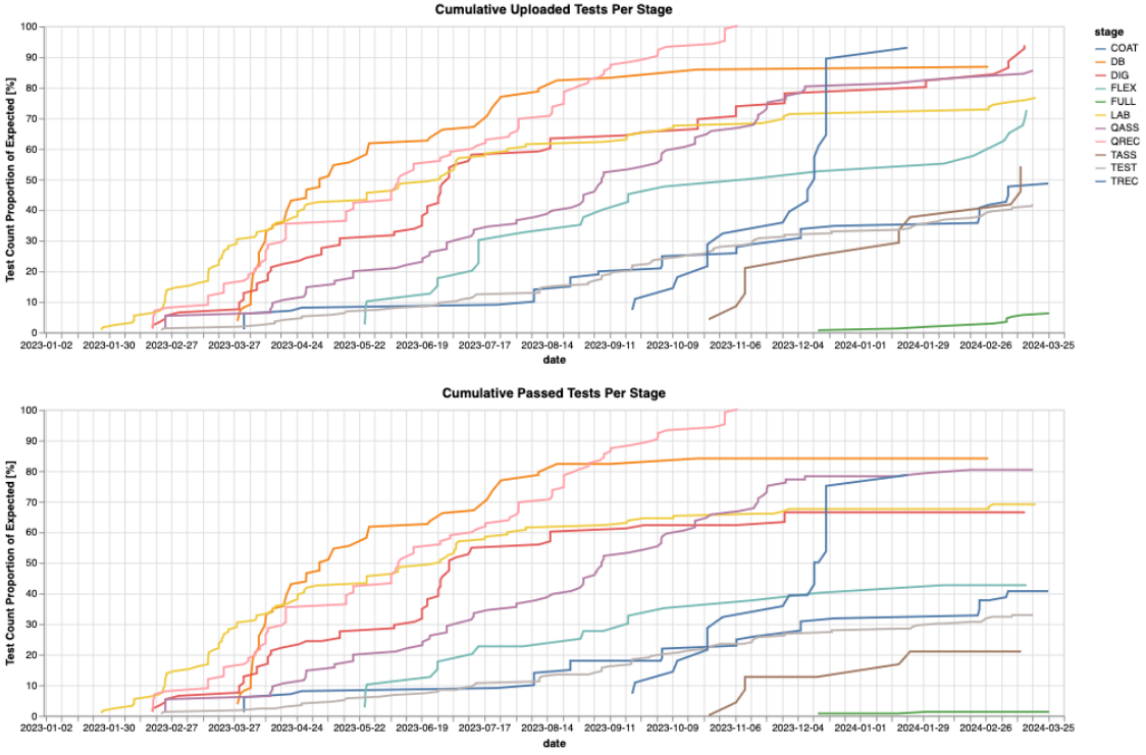

Figure 7.2: Percentage of tests (one sub-block from one site) that was submitted (above) or passed for different SQ blocks, the legend is as labeled in table 7.1. The two lines with similar blue are coating and triplet reception. The one that started earlier is coating. Figure from [179].

7.1.3. Module Production Target

The whole ITk pixel detector is divided into different regions: Inner System (IS), Outer Endcap (OE), and Outer Barrel (OB), as illustrated in figure 3.14(a). OE and OB consists of quad modules, while the IS consists of both quad and triplet modules. The number of production modules that will be used on-detector and the numbers to be produced are summarised in table 7.2. The reason that a larger number of modules will be produced is that a yield of around 75 % needs to be taken into account.

Location (Quad)	On-detector	Produce	Location (Triplet)	On-detector	Produce
IS Quad	1160	1609	IS R0.5-ring Triplet	120	166
OB	4472	6134	IS Linear Triplet	96	133
OE	2344	3112	IS Coupled-ring Triplet	180	250
Sum (Quad)	7976	10855	Sum (Triplet)	396	549

Table 7.2: Numbers of modules to be produced and to be installed on the detector in the Outer Barrel (OB), Outer Endcap (OE), and different locations of the Inner System (IS).

ITk module production sites in the same country[1] form clusters. The German cluster to

[1]Except for CERN, which is a category on its own.

which Göttingen belongs has 3 assembly and testing sites, and will produce 29% (1779) of the OB modules. The share of production modules is $5 : 3 : 1 = 988$, 593, and 198 for Bonn, Göttingen and Siegen, respectively.

In the next few sub-sections, the blocks relevant to OB sites are introduced, and the setup in Göttingen is shown as example. Block 6 and 7 are quad module assembly blocks (triplet SQ blocks have similar structure and items), and are introduced in chapter 8. Block 10, 11 and 12 are on module testing and are introduced in chapter 9.

7.2. Lab Infrastructure

Module assembly and testing require certain environment and facilities. This SQ block includes requirements on lab rooms and services, storage of module components and modules, shipping, compliance of ASIC related regulations, and a spreadsheet is provided for production rate planning, so that the production is practically estimated and well-planned.

7.2.1. Lab Rooms and Services

The responsibility of an assembly site includes the procedures in figure 7.1 before parylene coating, and the responsibility of a testing site is the procedures post parylene coating. Different activities bring different requirements for assembly and testing lab rooms. For flex QC sites, the requirement is the same as that for testing, excluding ESD safety.

Low dust level is needed to avoid contamination of the module components, and the temperature T and relative humidity RH affects the behaviour of the sensor, as shown in section 6.1. Especially, if the contamination on the components is conductive, the electrical functionality of the component can be impaired. Therefore, it is important to follow the requirements on lab environment.

The local setup at Göttingen involves two lab rooms: a grey room (D.01.132) where both assembly and testing take place, and the thermal lab (D.01.134) equipped with a shock chamber and a climate chamber for thermal cycling and stability test. The lab environment specifications [180] and the condition of the local setup are listed below in table 7.3:

Lab Particle Count
Assembly: particle concentration class 7 ISO 14644-1 or better (no requirement on airflow).
Lab garments: ISO7 compatible lab coat, hairnet, shoes / shoe covers (all of the above must be put on before entering the assembly area), gloves, face mask. Minimise contamination via limiting behaviours like touching skin/hair with gloves on, or fast movements. Sticky mats or equivalent at entrance. Avoid material like regular paper that increases particle levels.
Testing: class 9 ISO 14644-1, except for at least ISO7 for triplets VI.
Lab garments: ISO9 compatible lab coat, hairnet, shoes / shoe covers. Also gloves and face mask when handling modules with module carrier open.

Göttingen SQ: lab room D.01.132 has ISO6-level air in semi-enclosed probe station area (for probe station see figure 6.4(a)) and ISO7-level dust level for the entire room ensured by flow box above probe station. See figure 7.3 for 14 days particle level within spec. There is a sticky mat at the entrance. Lab attire: ESD-safe overcoat, ESD-safe overshoes or ESD-safe safety shoes. Gloves, face mask and hair net worn during components handling.
The particle level in D.01.134 in within ISO9 over a 14-day period.

Temperature and Humidity
Assembly: T from 16 to 24 °C with ±2 °C variation in one day, RH from 30 to 60 %.
Testing: dew point below module temperature.
Göttingen SQ: over 14 days, T 21 to 24 °C, RH 29 to 41 %.

Monitoring system
Assembly and Testing: particle count, T, and RH must be monitored, with a mechanism to alert the operator before commencing the assembly/testing, if any conditions go out of spec.
Göttingen SQ: two particle counters† read through either USB or a microcontroller unit. T and RH measured at two places by digital sensors†† with an Arduino or a microcontroller. Dew point calculated from T and RH. When RH=0% (meaning below smallest measurable value) at room T, dew point < -80 °C. Data written to influxDB and visualised through Grafana†††, where limits are set and alert is emailed and notification shown on slack. Nightly checks are run via Cron job to ensure that labRemote command line tools are running and would restart in case of failure.
†SPS30 particle counter; ††SHT85 or SHT35; †††Grafana: https://grafana.com/.

ESD Safety
Assembly and Testing: e.g. ESD-safe floor, work surfaces, shoes, wrist straps, pick up tools.
Göttingen SQ: ESD-safe attires. ESD bracelets also available. ESD mats on the assembly and testing tables, ESD-safe floor in lab rooms. Toolings are grounded.

Compressed Air and Vacuum Services
Assembly: dry compressed air supply and vacuum supply required. Dew point of dry air must be 10 °C lower than minimum room T, oil-free dry air (class 1 of ISO 8573-1) with enough flow rate. Vacuum system must have pressure ≥ 500mbar and is oil free.
Testing: in addition, dry air dew point must be at least −60 °C for the test system.
Göttingen SQ: general pressurised air supply in the building, oil free and reduced to pressure of 2.8 bar, then filtered through a 3-stage-system† to remove humidity.
The vacuum pumps†† provide contamination-free pumping at 2.2 m^3/h down to 7 mbar.
†BEKO DRYPOINT; ††Vacuubrand ME 2 NT.

Internal transport
When transporting components between different lab rooms, they must be put in a hard casing (e.g. module carrier) and an ESD-safe and airtight packaging that can be filled with dry air.
Göttingen SQ: the two lab rooms are only one room away from each other in the corridor (transportation time within 1 min). The components are put in ESD-safe bags, which is then put in hard plastic boxes filled with dry air via an inlet on the box (see figure 7.4(a)).

Handling Tools
The module and component handling tools, (e.g. vacuum pickup tools, tweezers, spatulas) must be ESD safe and leave no marking on the components.
Göttingen SQ: handling tools include ESD safe vacuum pen with rubber nozzle, chuck for gel-pak handling, and dry air gun, as shown in figure 7.4(c).

Table 7.3: Requirements of lab rooms and services [180].

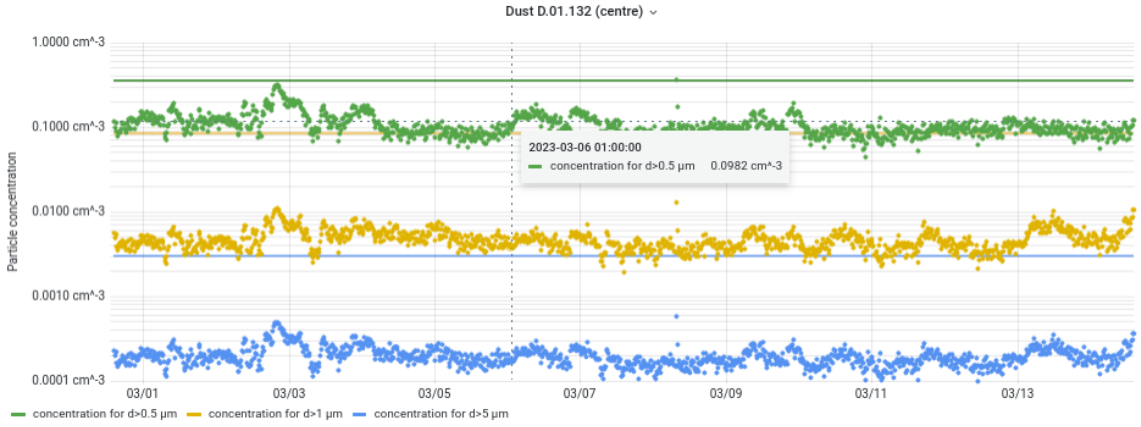

Figure 7.3: Dust level in lab room D01.132 for three different particle sizes, defined by their diameter d.

(a) To transport components between lab rooms, use ESD-safe bag and case with dry air inlet.

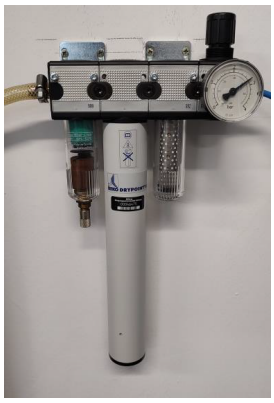

(b) Filter for dry and oil-free air.

(c) Vacuum pen, dry air gun, and gel-pak chuck.

Figure 7.4: Internal transport of components, dry air filter and outlet, handling tool, and gel-pak chuck.

7.2.2. Storage

Flex must be kept dry, clean and scratch-free: they are made from hygroscopic polyimide, the wire-bonding pads need to be clean and scratch-free for wire-bonding, the back side must be clean for good glue adhesion to BM, and the main body must be scratch and puncture-free to avoid HV discharge. BMs need to be free from humidity because of the sensor, and ESD-safe because of the FE chips. Assembled modules must be protected in addition to avoid damaging to the wire-bonds.

The requirement for storage of components (flex, BM) and assembled modules is tighter than the general environment requirement specified in the previous sub-section: all components and modules must be stored safely in desiccator cabinets and in clean containers (e.g. gel-paks, module carriers) in a stable environment with T range from 18 to 24 °C and RH

between 0 and 30 %, with ISO7-level particle count (reduced to ISO9 after parylene coating). The storage desiccator cabinets should be monitored and the operator should be alerted when the environment goes out of spec. There must be enough space to store four weeks of components and modules.

In Göttingen, a dry cabinet was designed and made in the fine mechanics workshop to store the components and modules. The cabinet is of size $40 \times 29 \times 20\,\mathrm{cm}^3$ and has grounded Al frame and ESD-safe trays. It also has a dry air inlet with a valve for flow regulation. The environment (T&RH) inside the cabinet is monitored by a setup with SHT85, Arduino and InfluxDB, with alerts through email. When the door is opened, it is observed that the RH spikes to 28%, but recovers to $< 5\%$ within 20 min.

7.2.3. Shipping

A large amount of components and modules will be shipped to and from sites for assembly, coating, testing, and in the end to loading sites. To prevent damage, requirements and recommendations are put and standard solution is provided on the packing and the monitoring of the shipping.

Packing

The modules are packed in several steps:

- Module carrier: after flex attach, the module should always be kept in its carrier and only taken out when necessary.
- Transport loop: if cables are shipped together with the module, strain relief measures must be taken to avoid damaging to the cable, and movement must be restricted, to avoid strain on the connectors. For this, transport loops were centrally produced. Custom-cut foam is used to prevent movement.
- ESD-safe bag: the module (including carrier and cable strain relief structures) need to be put in ESD-safe bags, vacuum sealed or filled with dry air while in the clean lab rooms, for a dry and dust-free environment during shipping.
- PeliCase: the packages are then put with custom-cut foam in a standard case centrally procured and tested by the ATLAS ITk collaboration. They are PeliCase flight cases: PeliAir 1525 or PeliAir 1606. The two differ in sizes, and a carousel for parylene coating (for detail see section 7.4.1) can be put in a 1606 case. This solution meets the ASTM D4169-16 transport standard in terms of vibration and shock. If a site use an alternative solution (including alternative foam design), it must be proved that the alternative meets the same standard.

The module carrier, transport loop, and a Peli case with custom-cut foam are shown in figure 7.5. The case is holding a carousel used to house modules for parylene coating, for details see section 7.4. An ESD-safe bag is shown in figure 7.4(a).

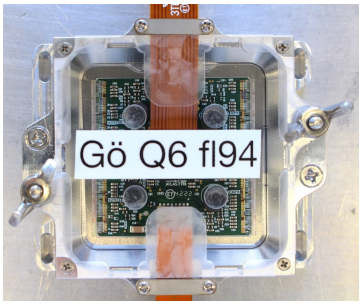

(a) A module in its carrier.

(b) Transport loop for shipping modules safely without strain on the pigtails. Photo from [181].

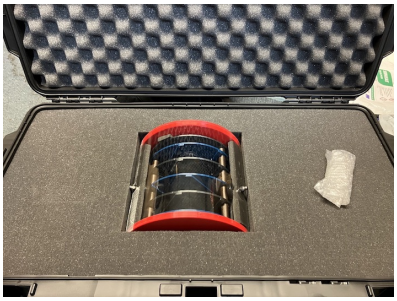

(c) A carousel packed safely in the centrally designated case and foam. Photo from [182].

Figure 7.5: Equipment for safe packing of modules: module carrier, transport loop, and case with custom-cut foam.

Monitoring

During shipping, it is recommended to monitor the T, RH, and shock/vibration in the case. A data logger[2] can be used for T&RH. For shock/vibration, it is believed that the limit of a module is more than 120 G. Because of cost reason, an external shock sticker of 100G sensitivity (or even lower) is recommended.

7.2.4. ASIC Compliance and Handling

The ASICs used on the modules are deep-submicron technology circuits fabricated by TSMC[3] and are dual-use[4] by nature. Therefore, all sites need to agree to follow the rules to properly handle, track and dispose of them, including the assembled or damaged detector components with ASICs attached to them. When the relevant components are shipped out of a country or union, an export license could be required. The sites are therefore responsible for preparing the proper paperwork. The shipment must be done both in reality and virtually in ITk PDB, and tracking information must be provided. The sites are not to reverse-engineer or transfer the ASICs for use. All detector components must eventually be returned to CERN: the sites must prevent the situation of losing or not being able to retrieve the components; if a component broke, the pieces must be collected and returned. A Letter of Compliance must be signed by the sites.

7.3. Database

This SQ block aims at ensuring that software tools developed for ITk pixel module data are installed and used properly by sites, so that assembly and testing can be conducted, and test results can be stored, analysed, and tracked properly. There must be an administrator in

[2]Example data logger: EL-USB-2-LCD+.
[3]Taiwan Semiconductor Manufacturing Company Limited.
[4]Could be for both civilian and military use.

each site responsible for the data and software tools, and make sure that adequate personnel, skillset, and workflow exist, therefore ensuring smooth production.

- **ITk Production Database** (ITkPD, or often PDB)[5] is where all components are tracked, and test results are stored. Each component has a serial number. After tests are done, the test results will be uploaded to the corresponding component. If the components are assembled or shipped, they should also be assembled and shipped virtually. In other SQ blocks, it is also required that the corresponding test results are uploaded to the PDB.
- **LocalDB**[6] is based on MongoDB (the backend database service), and is the local database where the sites store all their components and testing results. It can also generate analysis plots of electrical QC scan results. If a component is at a site, the site can both pull existing data from PDB, and select appropriate test results done locally in the lab to submit to PDB. A dedicated developer team from the ITk Pixel working group ensures smooth synchronisation.
- **InfluxDB** is used to store DCS data and can be configured to be viewed from Grafana.
- **Uploading of data** is performed using different tools: in module assembly and testing, there are two types of data – module electrical QC DAQ data from YARR[7], and non-QC data such as VI, metrology, mass, and BM *IV*. YARR comes with tools to upload DAQ data, and therefore the scan results can be uploaded directly. The rest of the data may have different formats specific to each site, therefore the test results need to be properly formatted and uploaded to LocalDB. This is done by a central GUI called the QCHelper, also known as the `module-qc-nonelec-gui`[8].
- `module-qc-database-tools`[9] can generate or pull chip config files from PDB.
- `module-qc-tools` [10] takes measurements.
- `module-qc-analysis-tools`[11] analyse the data taken by the measurement tools, generate plots, and determine if the results pass the corresponding QC requirements, and format the results to be uploaded to PDB.

In this SQ block, it is required to login to LocalDB and, via two access code authentication, to PDB, set up LocalDB by pulling metadata from PDB, download example module data, and submit information related to the server machine (OS, CPU, memory, disk profile) and the databases installed (LocalDB, MongoDB, InfluxDB). The administrator needs to provide reasonable answers to an awareness questionnaire regarding:

[5] PDB: https://itkpd-test.unicorncollege.cz, or the webapp https://uk-itk-pdb-webapp-pixels.web.cern.ch
[6] LocalDB Doc: https://atlas-itk-pixel-localdb.web.cern.ch/
[7] Yet Another Rapid Readout: https://gitlab.cern.ch/YARR/YARR. For detail about using YARR for DAQ see chapter 9. Documentation: https://yarr.web.cern.ch/yarr/
[8] Module QC nonelectric GUI: https://gitlab.cern.ch/atlas-itk/pixel/module/module-qc-nonelec-gui
[9] Module QC database tools: https://gitlab.cern.ch/atlas-itk/pixel/module/module-qc-database-tools
[10] Module QC measurement tools: https://gitlab.cern.ch/atlas-itk/pixel/module/module-qc-tools
[11] Module QC analysis tools: https://gitlab.cern.ch/atlas-itk/pixel/module/module-qc-analysis-tools

1. ITkPD account and privileges: cluster name and SQ serial number; list of cluster administrators, component managers, and server administrator.

2. Setting up InfluxDB&Grafana and LocalDB&viewer: depend on the numbers of modules to be produced, the allocated disk space and LocalDB host server PC, schematics of the server and intra/outside-lab network design, data backup, versions of all database tools and module QC analysis tools, and the installed modules of Python3.

3. Setting up QC Helper for non-DAQ data: install QCHelper and ensure the accessibility of the data to MongoDB.

4. Ensure that the format of non-QC data is suitable for the QCHelper, and the installed QCHelper version. Python3.7 or higher is required.

Göttingen is qualified for this block, and the schematics of the setup is shown in figure 7.6.

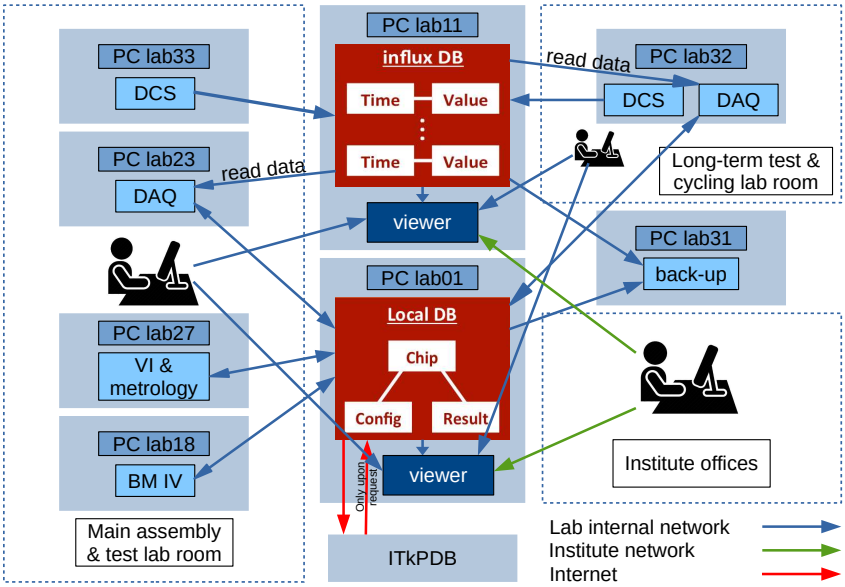

Figure 7.6: Servers, network design, software tools, and lab PC arrangements in Göttingen.

The relevant privileges and personnel for the PDB is ensured. To store data of around 600 modules in production, sufficient computing facility is allocated. Info on the server PCs and the versions of the installed software tools are as detailed in table 7.4. For data backup of LocalDB and InfluxDB, a separate PC (lab31) is used. Outside the lab network, access to the viewers is possible from the network inside the institute. There is no direct access to lab PCs from outside the institute. All lab PCs have the possibility to access the Internet (which is necessary for PDB). QCHelper is installed, with accessibility of MongoDB. It is noted that all module QC results should be pushed from the QCHelper to LocalDB, instead of to the ITkPD web interface or web app. The non-DAQ data has appropriate formats.

	Version	Host server PC information		
InfluxDB	1.8.10	lab11	Intel® Core™ 2 Duo CPU E7500, 2.93 GHz	1.5 TB HDD
MongoDB LocalDB	4.2.24 2.0.3	lab01	Intel® Xeon™ CPU E3-1220 V2, 3.10GHz	8 GB RAM, 4 TB HDD
PDB	0.4.0	—		
module-qc-analysis-tools	1.2.0	—		
Python	3.7.3	—		
QCHelper	4.0.dev1 git tag 0.0.2	—		

Table 7.4: Database and software tool versions, and information on the host server PCs.

7.4. Coating and Wire-bond Protection

During module operation, high bias voltage – especially after irradiation – is applied to the sensor, creating high voltage difference between the sensor and the chips, which are separated by bump-bonds only $25 \pm 15\,\mu m$ thick [183]. To avoid sparks from the high voltage between the sensor and FE chips destroying the BM, parylene coating is needed.

Parylene is a dielectric material. It must coat the edges where the sensor and FEs are facing each other, and fill the gap between the sensor and the FEs. In addition, the parylene also provides HV isolation and mechanical protection to the wire-bonds, and protects the module from humidity. Because of the better mechanical strength, parylene coating even decreases bump disconnections in thermal cycling tests. ITk Pixel modules use parylene type N with target thickness $7^{+3}_{-2}\,\mu m$ [184].

However, the mechanical protection provided by parylene is not enough for the wire-bonds. The majority of the wire-bond protection is provided by the canopies glued on top of the modules, as introduced in section 7.4.2.

Within the time scale of this thesis, Göttingen has not performed coating or wire-bond protection. The following sub-sections therefore describe the SQ requirements and plan.

7.4.1. Coating

The parylene coating procedure itself will be done by external companies or specific institutes[12]. The responsibility of the assembly sites is to mask certain areas of the modules, package the modules safely and ship them to the company, de-mask them after the modules are coated, and perform testing to check for damage or change in functionality. In the SQ coating block, the assembly sites need to show their capability of performing the procedures without damaging the modules. Figure 7.7 shows the tools.

[12]For the German cluster: the APS Coating Solutions in Paris, or MPP Munich.

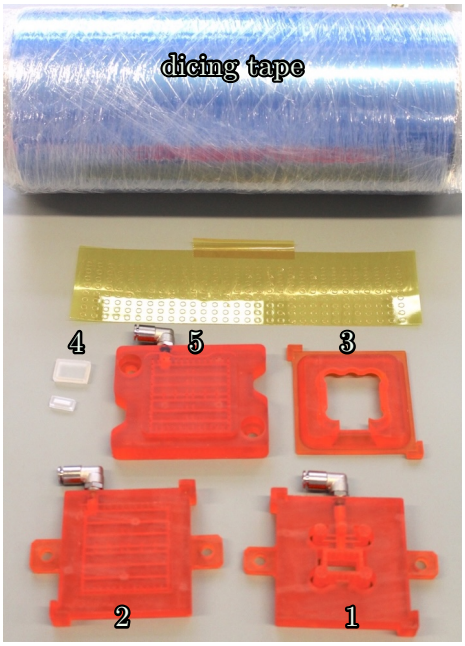

Figure 7.7: Tools for masking in parylene coating. Most parts are 3D printed with ABS resin. Parts 1 and 2 are used to press dicing tape to the surface of the flex at the masked areas. 3 protects the wire-bonds when putting the caps for connectors (4) on.

Masking: to prepare for parylene coating, some area on the module that are not to be coated should be masked with dicing tapes. These include the pick-up areas, around the data and power connectors, the strain relief area[13], and the back of the FEs. These areas are to be glued in later stages, and should therefore not be coated. For cutting the dicing tape masks, one site of each cluster should have a 2D cutter[14]. For the German cluster, the work on coating SQ is ongoing. Every site has purchased a 2D cutter, to minimise time cost from transporting material. Protecting caps should be attached onto the power and data connectors with silicone[15] using a syringe.

Shipping: to ship the modules to the company, a commonly designed carousel[16] of four layers is used. A photo is shown in figure 7.5(c). Eight modules (two on each layer) can be fixed in the carousel without the lid and the bottom of the carrier, and this assembly is suitable to be used by the company directly for parylene deposition, without taking the modules out. The carousel will be put in a PELI case, and surrounded by foam with suitable cut-outs during shipping. The German sites ship the modules to one central location (Bonn), where the modules will then be shipped to the coating company or institute.

Parylene Coating QC: after the modules are coated, QC tests of thickness and adhesion will be performed on test-coupons. The test-coupons are made from Si, release film or glass,

[13]The strain relief area is introduced in the next sub-section.
[14]The recommended one is Silhoutte Cameo.
[15]Stannol AK100 Coating mask is used to attach the protection caps to the connectors.
[16]It is allowed for sites to use alternatives, provided that the effectiveness of the alternative solution is demonstrated in SQ.

and are put close to the modules in the carousel. One site in each cluster should be able to produce test-coupons. The thickness measurement can be done with a micrometer screw gauge. Adhesion test is done by cutting lines around 2 cm long on the coating with 1 mm separation, to form a 6×6 grid. After peeling the pattern off with transparent Scotch tape, inspect and grade the pattern based on the detachment (flaking) of the coating. The adhesion is of high grade if the edges of the cuts are smooth and without detachment. This could be done by the vendor, and Göttingen has a cutter for the German cluster to cross-check the results.

De-masking: to de-mask the modules, remove the dicing tapes with ESD-safe tweezers or scalpels, and remove the masking caps on the connectors.

Visual Inspection and Minimum Health Test: finally, perform VI and Minimum Health Test on the module (if the site is using digital modules to qualify, disconnected bump scan is omitted)[17] to test for damage.

7.4.2. Wire-bond Protection

The wire-bonds on the modules are fragile and must be protected from external force, for example, from contact with pigtails during subsequent processes like cell loading and cell integration[18]. The protection structure must be tolerant to radiation and thermal cycling. Various types of material for encapsulation were investigated, and were excluded as suitable solutions. Parylene coating is radiation and thermal cycle tolerant, but does not provide enough mechanical protection. Therefore, wire-bond mechanical protection (WBMP) is selected as a solution.

Due to the different geometry and corresponding cabling of different systems, the WBMP is different for Inner System, Outer Endcap and Outer Barrel (OB). For OB, a canopy made from Carbon Fibre Reinforced Polymer[19] was designed. See figure 7.8.

The canopies are glued on top of the flex along the wire-bonding edge with Araldite 2011 adhesive [186] at the pick-up areas, to protect the wire-bonds from the pigtails that may pass directly above. As the whole assembly must be within the module envelope[20], the dimension of the canopies and their alignment with the module is such that the canopies are within the FE and sensor edges. The canopies also rise enough above, leaving space to not touch the wire-bonds. The spacing is kept by the thicker part where the canopies are glued with the flex. For more detail please refer to [187].

The attachment procedure is done with a dedicated and centrally distributed tooling via the stencil method. See figure 7.9 for the tools and the stencil[21]. After applying glue on

[17] All the module QC tests, including Minimum Health Test are introduced in chapter 9.
[18] Cell loading and integration are briefly introduced in section 7.1.1.
[19] CFRP XN-90.
[20] Details in chapter 8.
[21] At two sites, the module assembly and cell loading are done as one step, therefore they are using a different version of tooling with similar principle.

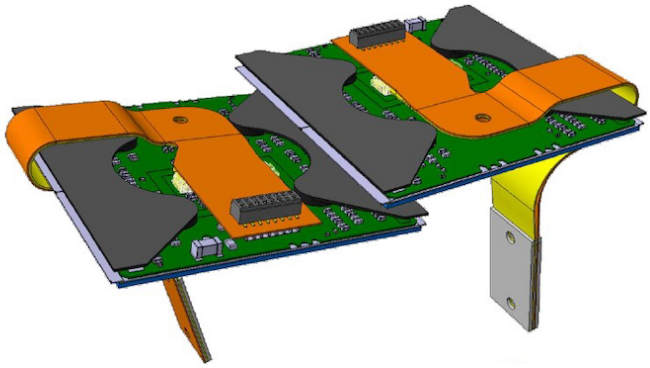

(a) Pigtail configurations for Longerons. The pigtails go directly above the wire-bonds.

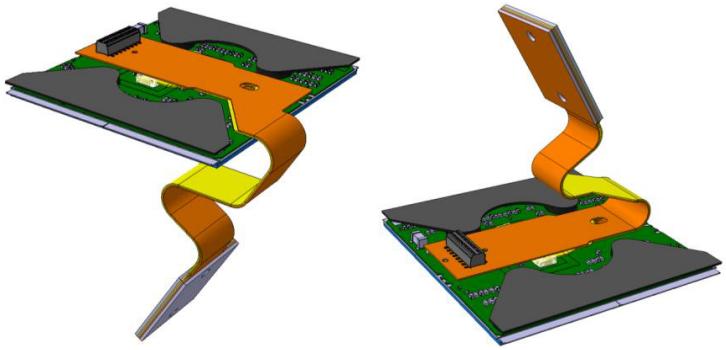

(b) Pigtail configurations for Inclined Half Rings.

Figure 7.8: OB module cells with wire-bond mechanical protection (black canopies) and different pigtail configurations for Longerons and Inclined Half Rings. The pigtails are power and data pigtails overlayed together. Images from [185].

the canopies by swiping the spatula across the stencil, silver epoxy[22] is added using a Q-tip swab on the golden grounding pads at the pick-up areas of the flex, so that the canopies, which are made from carbon fibre – thus conductive – are connected to the flex grounding across the glue layer instead of electrically floating. Then the jig is flipped to glue the canopies to the flex.

In addition to the canopies, a strain relief washer[23] is glued to the module at the same time using the same tooling. The washer is between pick-up area 1 and 4, the position is aligned with the hole on the pigtails, which is visible in figure 7.8. After the pigtails are inserted, Araldite 2011 adhesive is put through the hole, gluing the pigtails to the washer, relieving the strain on the connectors, and prevent the pigtails from coming off during handling and detector operation.

The SQ includes VI, mass measurements, as well as testing of the glue pattern using glass dummies and Test-PCB dummies. On real modules, the required tests are VI, mass, conductivity measurements, geometrical alignment measurements, and electrical tests (sensor *IV*, Minimal Health Test, Pixel Failure Analysis).

[22] AA-DUCT 902.

[23] Washer: a disc plate, normally thin and small, made of certain material, with a hole at the centre. The one used here is of 4 mm outer diameter and 2 mm inner hole diameter and thickness 0.9 mm.

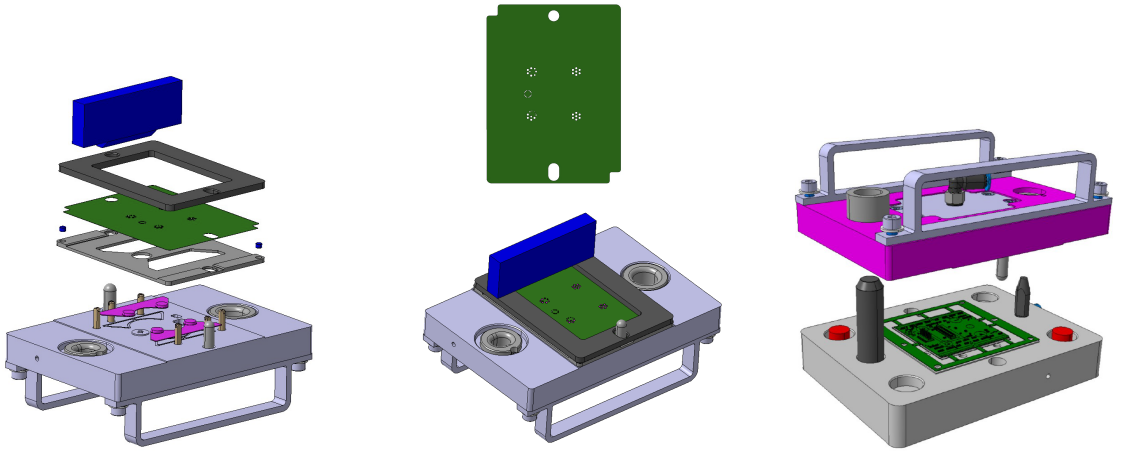

(a) The jig that holds the canopy and strain relief washer, and the additional components to apply glue.

(b) Stencil and glue application.

(c) The canopies and the strain relief washer are held by the jig on top.

Figure 7.9: The common pre-production tooling for outer barrel wire-bond protection. After applying glue on the canopies and the strain relief washer, the jigs are put together to glue the canopies and the washer to the module. Drawings from [188, 189].

CHAPTER 8

Quad Module Assembly

During production, 10855 ITk Pixel quad modules will be assembled at 14 assembly sites. In order to keep a consistent assembly quality that can withstand ten years of operation, a common tooling – the ITk Pixel Quad Assembly Tooling V2, was developed at Göttingen for the step of attaching bare modules (BM) to the printed circuit boards (flex).

The initial idea of an assembly tooling came from the IBL module production for FEI4 module assembly [80, 103]. The ITk Pixel Tooling V1, as described in ref. [3], was then designed and used centrally for RD53A module assembly. Based on the experience, Tooling V2 was developed and tested. Assembly sites receive BMs, flexes, as well as multiple sets of Tooling V2, to assemble modules for pre-production and production. This chapter introduces the assembly specifications, the tooling, its performance, the assembly site qualification, and the module assembly conducted in Göttingen for pre-production.

8.1. Module Assembly Goal

As introduced in section 4.3, an ITk Pixel module consists of a flex and a BM, which, for a quad module, consists of one sensor bump-bonded to four front-end chips (FE), as shown in figure 4.13. The flex must be assembled to the BM with a homogeneous glue layer, so that the flex does not detach easily from the BM. Various specifications must be met.

After the BM to flex attachment, the flex will be wire-bonded to the FEs, making it a fully functioning module. The fully assembled module then goes through parylene coating and mechanical wire-bond protection[1], to lower the risk of damage from the high bias voltage and other mechanical structures and forces.

[1] As introduced in section 7.4.

The word "assembly" is used for both steps: BM to flex attachment and full assembly. In this chapter, it is used in most cases to refer to the BM to flex attachment step. This section introduces the module components and the assembly related specifications, focusing on modules with 150 µm sensors, whose dimensions differ slightly from BMs with 100 µm sensors[2].

8.1.1. ITk Pixel Quad Module Assembly Specifications

The dimension and functionality of the module components determine the specifications. Figure 8.1 shows a front view drawing of an assembled ITk Pixel quad module with 150 µm sensors [190]. The dimensions and thicknesses are summarised in table 8.1.

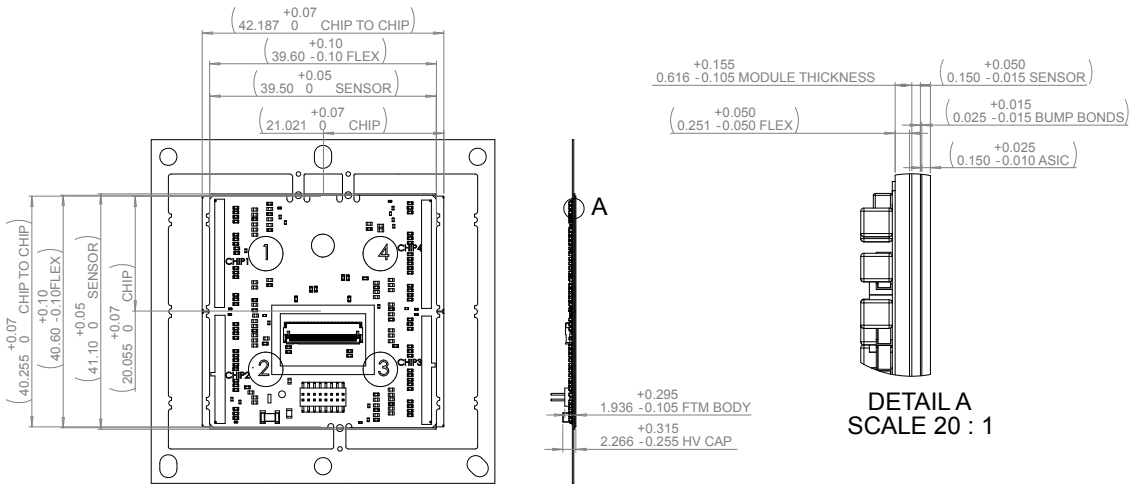

Figure 8.1: Assembled module drawing (v11 26.1.2023) for modules with 150 µm sensors and flex v3.2, showing specifications in xy-dimensions and thicknesses in mm. Image from [190].

After receiving the components, the assembly sites perform reception tests, to decide if the quality of a component is good for assembly. These tests include metrology for measuring the X (width), Y (length), and Z (thickness) dimensions, mass, visual inspection (VI), and electrical tests. In production, the results for reception tests will be used to veto the assembly of failed components.

After assembly, the mass and thickness of the assembled module will be measured, which allows monitoring the amount of glue deposited, estimating the glue thickness, and calculating the glued module flatness. The glue mass and thickness provides an estimation of the glue coverage. In addition, xy-alignment is measured via the relative position in the x and y-direction of the fiducial marks[3] on the glued module.

[2] A 100 µm thick sensor is smaller in X and Y by 0.4 mm, and the flex used for a BM with 100 µm sensor is 0.2 mm narrower in X. As the sensor is thinner by 50 µm, the thicknesses of the assembled module differ accordingly.

[3] As introduced in section 8.1.2.

	X [mm]	Y [mm]	Z [mm]
Sensor (150 µm)	$39.50^{+0.05}_{0}$	$41.10^{+0.05}_{0}$	$0.15^{+0.05}_{-0.015}$
FE	$42.187^{+0.07}_{0}$	$40.255^{+0.07}_{0}$	$0.15^{+0.025}_{-0.01}$
Bump Bonding	–	–	0.025 ± 0.015
Flex Body (for 150 µm sensor)	$39.60^{+0.10}_{-0.10}$	$40.60^{+0.10}_{-0.10}$	$0.251^{+0.050}_{-0.050}$
BM (with 150 µm sensor)	–	–	$0.325^{+0.09}_{-0.04}$
Module Pick-up Area	–	–	$0.616^{+0.155}_{-0.105}$
Module Power Connector Body	–	–	$1.936^{+0.295}_{-0.105}$
Module HV Capacitor	–	–	$2.266^{+0.315}_{-0.255}$

Table 8.1: The specifications of module components and assembled modules with 150 µm thickness sensors [183, 190].

After assembly, the following specifications must be met [191]. Overall, the xy-alignment and the dimension of the assembled module must guarantee that after going through follow-up procedures, the whole module fits the required size referred to as the module envelope, and can therefore later fit into the local support.

1. xy-alignment: the flex and the BM centre should be within ±100 µm in both x- and y-direction. In practice, this is defined by the nominal distance in x and y between the fiducial marks on the BM and the flex. This is to guarantee the module envelope, as well as to ensure that the angle between the wire-bonding edges (the left and right vertical edges) of the flex and BM are not too large to hinder wire-bonding.

2. Glued module thickness: the glued module must conform to the module envelope. This depends on the thickest parts – the body of the power connector, and the HV capacitor.

3. Flatness: when the module is held flat from the FE side, the pick-up area (the circles marked 1, 2, 3, and 4 in figure 8.1) thicknesses on the copper probe pads must differ no more than 15 µm. This is important for ensuring successful pick-up by the cell loading tooling in the subsequent cell loading procedure.

4. Glue thickness: must be > 10 µm to provide enough strength for wire-bonding, and guarantee the structural integrity to endure thermal cycling (see chapter 9) and future radiation fluence without delamination.

5. Glue coverage: the glue should cover 80 % of the flex main body, and be present under wire-bond pads and pick-up areas. This is to ensure that the continuous glue coverage puts minimum stress on the glue layer, and to avoid delamination. The presence of glue provides a stiff base for semi-/automatic wire-bonding mode and pick-up. The glue should also not protrude from the flex edges so much that it reaches the sensor edge, cover the wire-bond pads on the FEs, or cover the hole for HV wire-bond connection.

8.1.2. Module Components

For BMs, different FE versions such as ITkPixV1.0 and V1.1 have different circuits and electrical functionalities. However, the relevant aspect for assembly is the change in dimensions. These modifications can be accommodated due to the flexibility of the tooling via calibration or replacing the BM chuck.

Different types of flex with modifications that impact the assembly have been used: Flex v2.4 is a prototype ITkPix flex, and was used for most tests for the tooling review. V3.2 is the pre-production design. RD53A flexes have been used on testing of the stencil tool, before ITkPix flex v2.4 became available. Within the same version, different sub-versions can be distinguished via the serial numbers (SN). Examples of different ITkPix flexes are shown in figure 8.2. The tabs on the left and right side that connect the flex body with the frame must be cut before assembly to not hinder wire-bonding, as in figure 8.2(c).

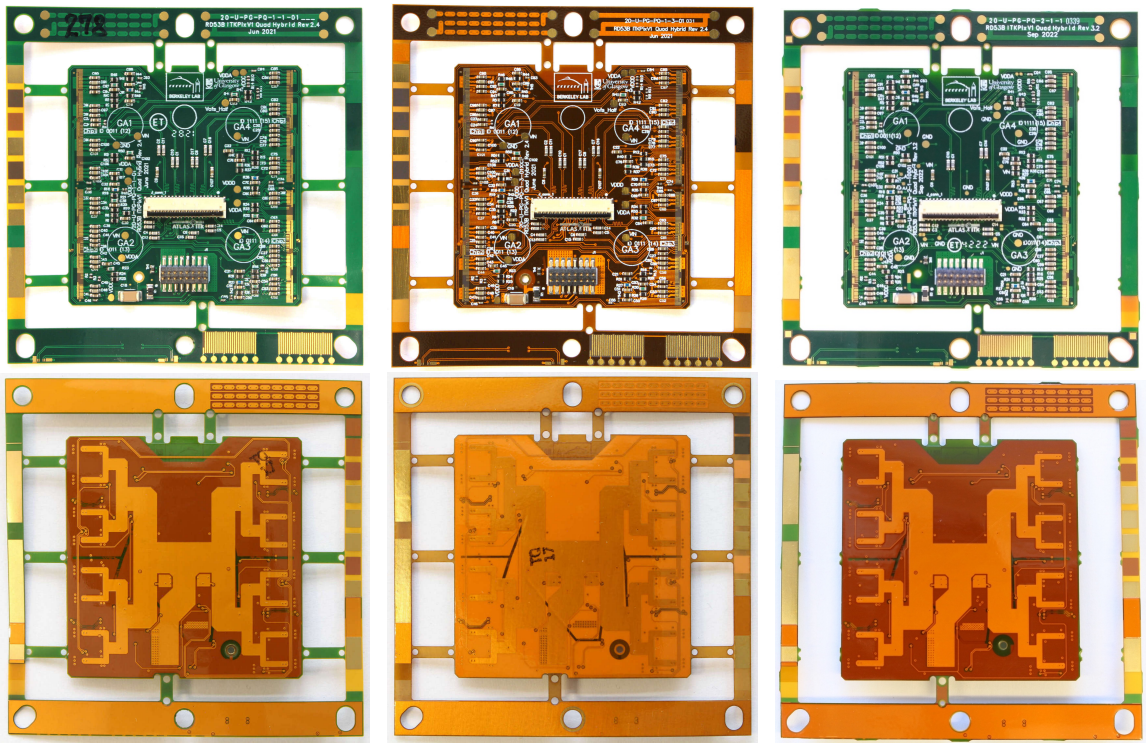

(a) Flex v2.4 with serial number `20-U-PG-PQ-1-1-01___`.

(b) Flex v2.4 with serial number `20-U-PG-PQ-1-3-01___`.

(c) Flex v3.2 with serial number `20-U-PG-PQ-2-1-1____`.

Figure 8.2: Two types of flex v2.4 with different serial numbers, and a flex v3.2. Both v2.4 types had no impact on assembly. V3.2 is used later for site qualification and pre-production. The empty spaces in the serial numbers are different for each individual flex.

Two more types of flex are shown in appendix B.1, including bare[4] flex and another flavour of v2.4 produced by a different vendor with larger tolerances at the holes and slots on the flex frame, and more obscured fiducial marks, as introduced below. The bare flexes were used for glue thickness and coverage tests, after a clash between the SMD components and

[4]Bare, un-populated, or un-loaded flex refers to those with no SMD components.

the flex jig[5] was found. The v2.4 flexes with large tolerances and bad fiducial mark quality are not ideal for xy-alignment tests, but was used for thickness and glue coverage tests.

Designated structures referred to as fiducial marks were used for xy-alignment measurements, as the edges of the flex body are not well-defined. The fiducial marks also provide pattern recognition possibility for wire-bonding programs. The top-left and the bottom-right fiducial marks provide two pairs of xy-alignment measurements. If both the top-left and bottom-right results indicate shifts within specification, the centre of the BM and flex is within specification, and the rotation between the components is also controlled.

Flex v2.4

For assembled modules that use flex v2.4, the nominal distances between the flex fiducial marks and the BM edges are shown in figure 8.3. The quality of fiducial marks also differs, as shown in figure 8.4. Those with better quality (with SN ending with `1-1-01___` and `1-3-01___`) were selected for the xy-alignment tests.

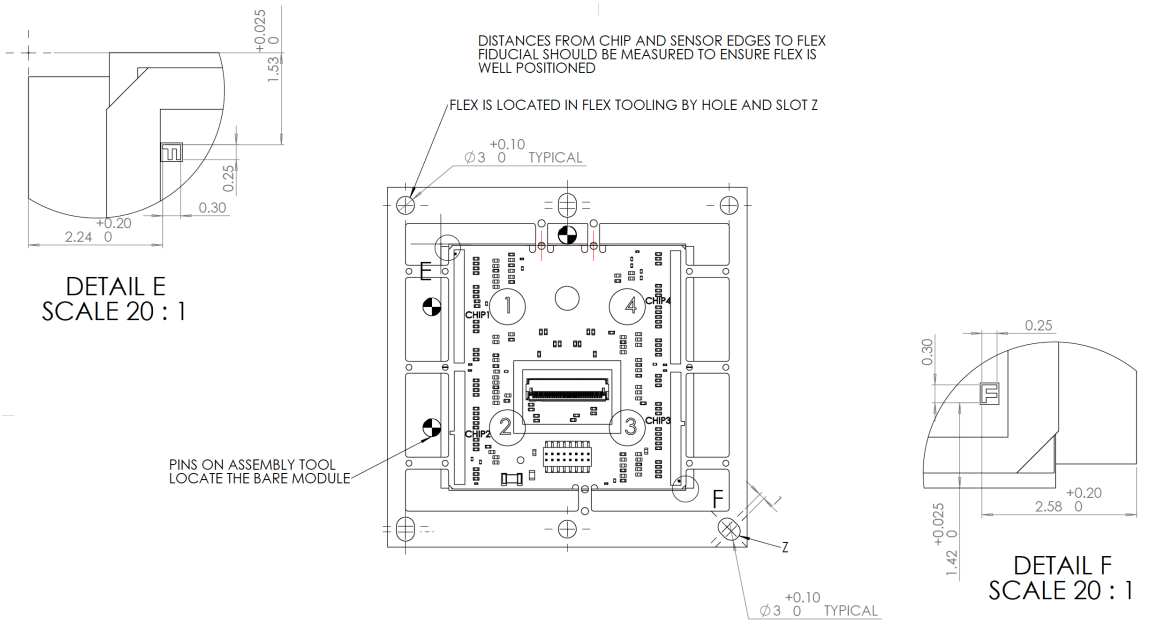

Figure 8.3: Position of fiducial marks for flex v2.4 relative to BM edges. Image from [192].

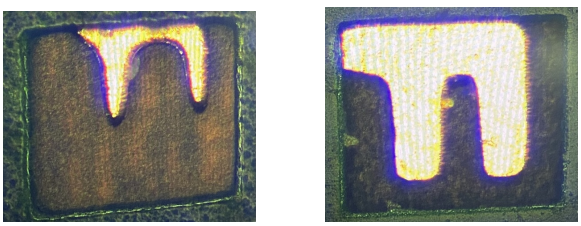

Figure 8.4: Fiducial mark quality on flex v2.4 from different vendors.

[5]The flex jig is introduced in section 8.2.2, and the glue pattern test with bare flex is in section 8.4.4.

Flex v3.2

The pre-production flex v3.2 has a different fiducial mark design, and the nominal xy-alignment measurement is defined by the distances between the fiducial marks on both the flex and the BM or Si dummy. The nominal distances are shown in figure 8.5.

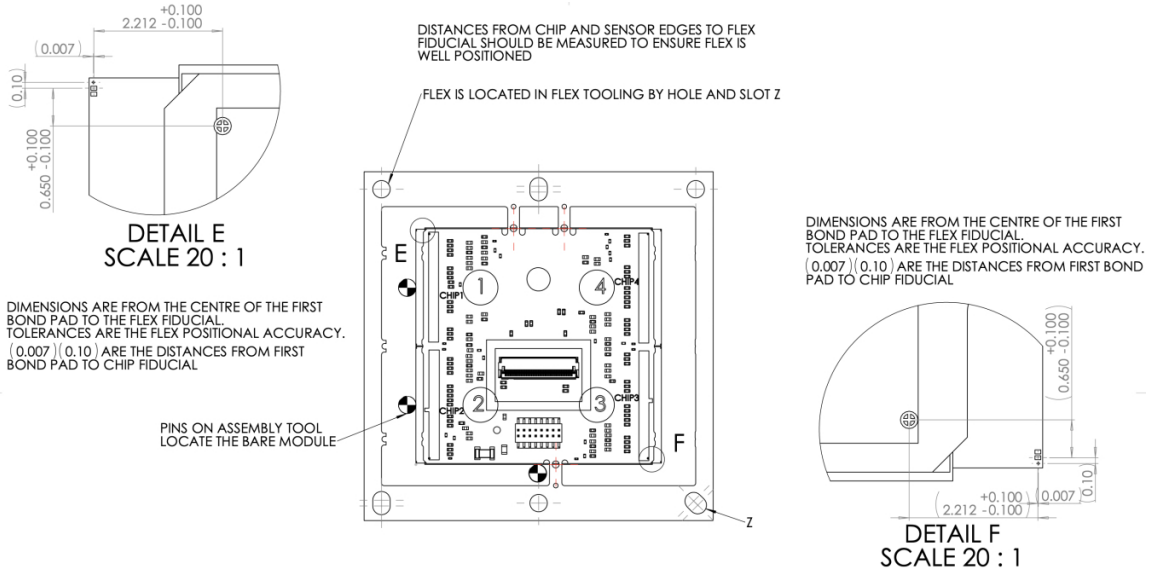

Figure 8.5: Positions of fiducial marks on flex v3.2 relative to that on BM. Image from [190].

8.2. ITk Pixel Quad Assembly Tooling V2

The Tooling V2 consists of a few parts: BM jig, flex jig, stencil tool, and spatula, as shown in figure 8.6.

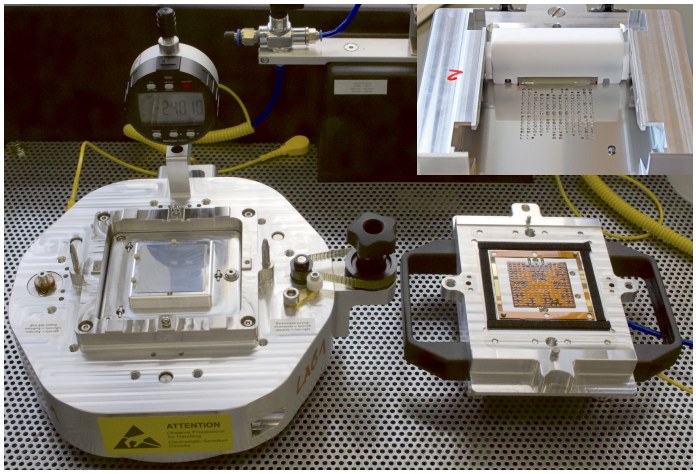

Figure 8.6: ITk Pixel Quad Assembly Tooling V2: BM jig (left) and flex jig (right) with BM and flex on top, glue dots are already distributed on the back of the flex. Top-right photo: stencil tool and spatula on the stencil and flex jig, ready for glue distribution.

For layered views of glue distribution process and the matching of the two jigs afterwards, see figure 8.7. The structures and their functionalities are detailed below.

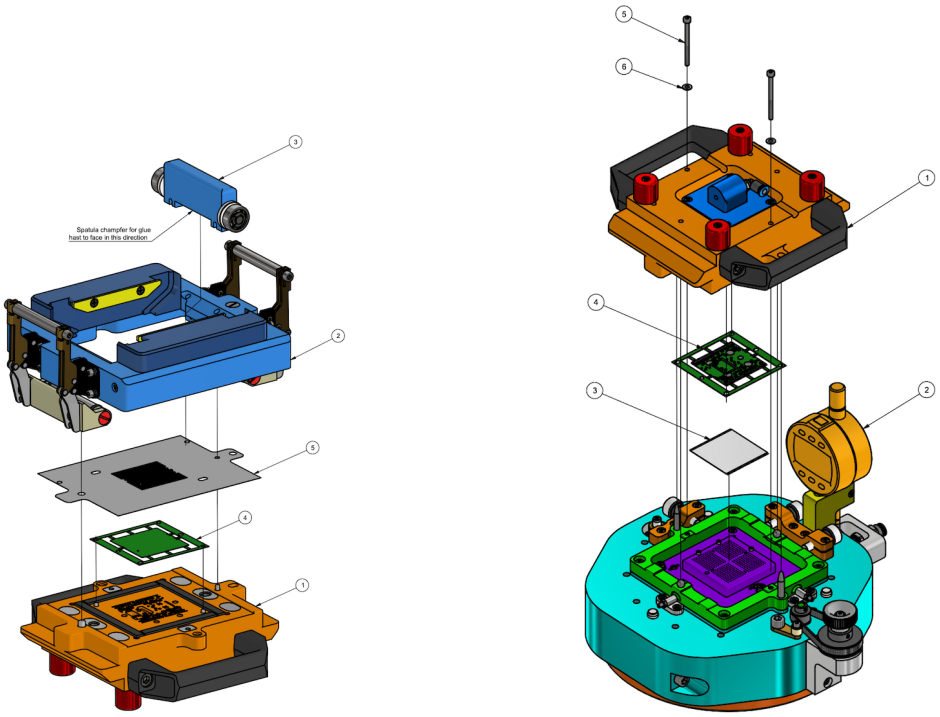

(a) Matching of stencil tool with flex jig for glue distribution. ① Flex jig, ② Stencil tool, ③ Spatula, ④ Flex, ⑤ Stencil.

(b) Matching of flex jig with BM jig after glue distribution. ① Flex jig, ② BM jig, ③ BM (with 150 µm sensor), ④ Flex, ⑤ Fixing screw (hex socket bolt), ⑥ Washer.

Figure 8.7: Layered view of two processes in the assembly procedure. Images from [193].

8.2.1. Bare Module Jig

Figure 8.8(a) shows the BM jig with different parts and features labelled. The pivot plate contains a top surface (which is the BM chuck) and a surrounding surface. The BM chuck is the BM contact surface, and comes with vacuum holes to fix and flatten the BM. The pivot plate is a whole and moves up and down together.

The BM chuck contains four holes, but only three dowel pins should be inserted, as described in section 8.3.2, to align the BM. The xy-alignment is made sure by the precise location of the dowel pins, the spheres, and the calibration between the notches on the adjustment frame and the BM chuck.

At the z-direction, the whole pivot plate is constantly being pushed up by an internal spring, and can be pushed down or released up using two screws: the knob on the right hand side, and the inner fine thread screw on the left. Benefiting from the three vertical linear bearings (figure 8.9), the pivot plate maintains its parallelism while moving. A dial gauge is installed to monitor the height. The tooling has an operational thickness range:

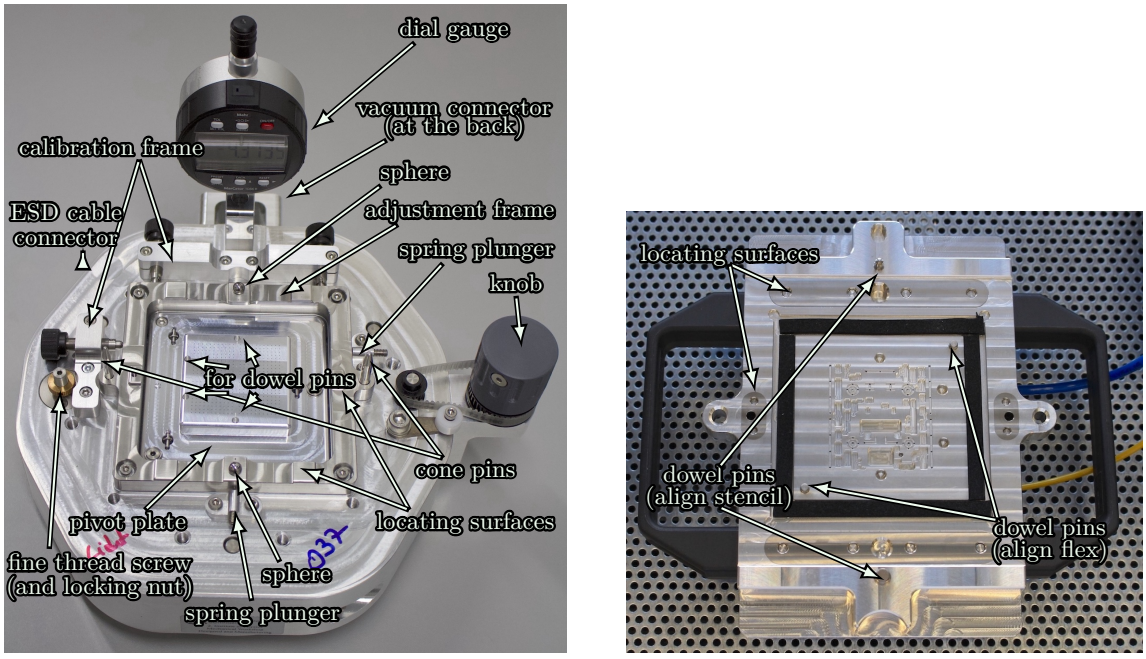

(a) BM jig

(b) Flex jig

Figure 8.8: Detailed structures on the BM jig and flex jig. The BM and flex chucks are the surface on the pivot plate of the BM jig and the surface at the centre of the flex jig.

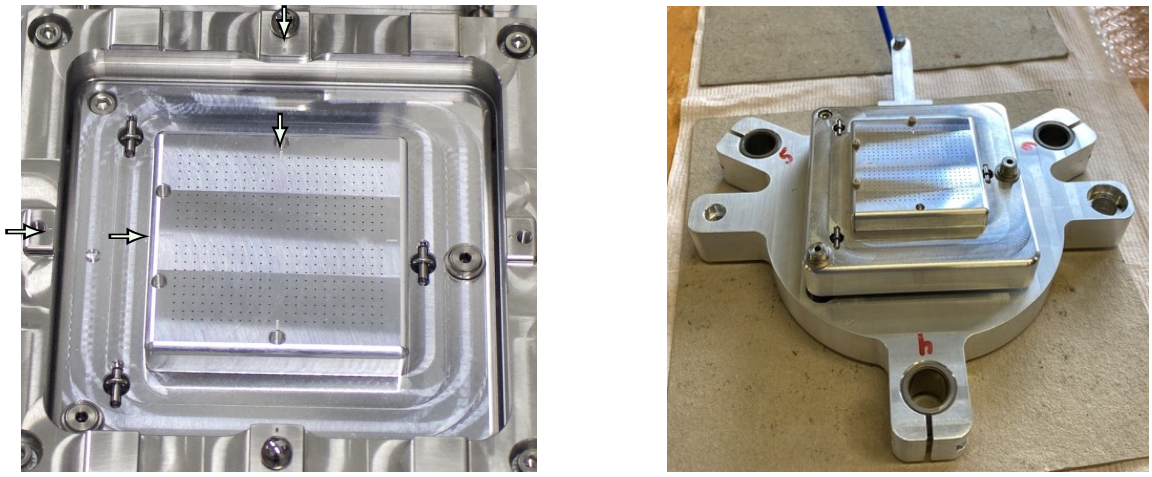

Figure 8.9: Left: notches on the pivot plate and adjustment frame. They are very small, four out of eight are pointed out by arrows, the rest are symmetrical. Right: internal structure below the pivot plate for three linear bearings to guarantee parallel movement of the pivot plate with respect to the xy-plane.

it is possible to glue modules with target total thickness of 390 to $790 \pm 25\,\mu\text{m}$, which is defined by the range of height movement of the pivot plate.

To ensure parallelism between the BM and the flex, the three screws on the pivot plate surrounding surface are used in calibration to ensure that the pivot plate is parallel to the plane formed by all locating surfaces – the flat surfaces on the BM jig adjustment frame.

The flex fig also has precisely manufactured and inserted locating surfaces. These surfaces on the two jigs are designed to be in contact, and the parallelism is propagated to the BM and flex chucks.

For xy-alignment between the BM and the flex, the flex jig with the BM jig must be aligned precisely during the mating process. The gross positioning is defined by two cone pins with different diameters, which ensure that the flex jig can only be put onto the BM jig in the correct orientation. The two spheres on the BM jig adjustment frame are in contact with the corresponding holes on the flex jig, ensuring fine xy-positioning between the jigs, and therefore the xy-alignment of the BM and flex.

The calibration frames are not necessary for the assembly procedure but are solely used for calibration. All assembly sites that use the Tooling V2 receive the toolings in an already calibrated state, and therefore do not need the calibration frames.

8.2.2. Flex Jig

The flex jig cutout, as shown in figure 8.8(b), fits the SMD components and connectors on the flex front surface. The flex is aligned by the two dowel pins that matches the hole and slot on the flex frame, and the vacuum holes on the jig fixes the flex. When placing the stencil and the stencil tool on the flex jig, the alignment is achieved via two dowel pins of two different diameters, to ensure the correct orientation. When mating the flex jig with the BM jig, the two holes on the locating surfaces (the steel inserts) match the spheres on the BM jig, ensuring precise xy-alignment.

8.2.3. Stencil Tool

The stencil tool fixes the stencil onto the flex jig with clamps. There are guiding rails for the spatula when it is being swiped across the stencil. This is designed to leave a stable amount of glue on the back of the flex, independent of the operator. The holes on the top and bottom have different diameters, and fit the corresponding dowel pins on the flex jig.

8.2.4. Stencil and Glue

In addition to the ITk Pixel Quad Assembly Tooling V2, the stencil[6] is also crucial for assembly. It controls the amount and pattern of glue that is distributed onto the back of the flex, and is important for the glue coverage after compressed to the desired thickness. The stencil patterns have gone through many rounds of trials. Different versions, including some from the RD53A era, are summarised in figure 8.10.

[6] To prevent damaging to the spatula, the stencil should be polished to get rid of the burrs around the hole edges. The polishing can be done via wrapping a sandpaper around a flat surface, and polishing the stencil with the aid of a few drops of water. Two rounds of polishing with e.g. 1500 and then 5000 grid sandpaper is recommended.

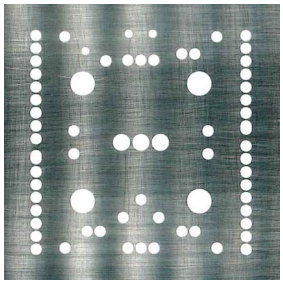

(a) RD53A v1.

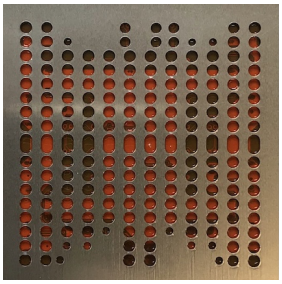

(b) RD53A v2. Image from [3].

(c) RD53A v3 – improved HV hole safety.

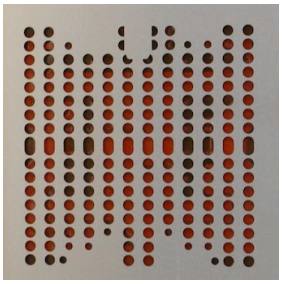

(d) RD53A v4 – used for stencil tool development.

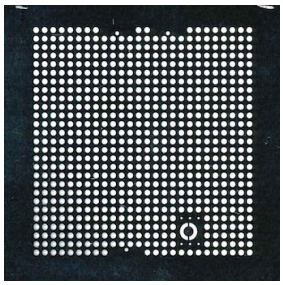

(e) ITk Pixel v5.

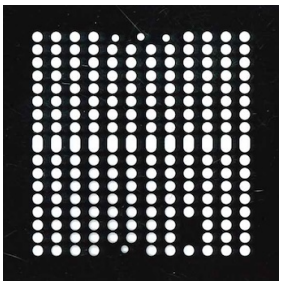

(f) ITk Pixel v6 – back to RD53A style as small holes performed badly.

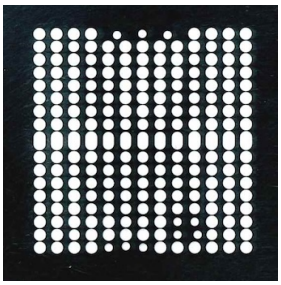

(g) ITk Pixel v7 – bigger holes for more glue.

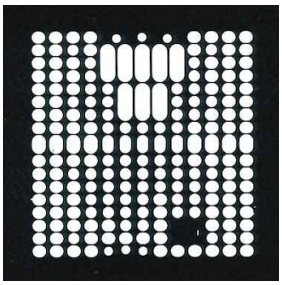

(h) ITk Pixel v8 – larger area at thin part of flex, dots away from HV hole.

Figure 8.10: Summary of stencil pattern designs and their features.

The glue selected for assembly is the epoxy-based adhesive Araldite2011, which contains two components, and only starts to cure when mixed. The pot life at room temperature is 100 min, and the curing time at room temperature is 7 h. During assembly, a glue gun is used to apply a strip of glue onto the stencil, to be distributed by the spatula, and the two components of the glue are mixed in the disposable nozzle when passing through.

8.3. Tooling V2 Gluing Procedure and Calibration

This section introduces the gluing procedure, the mechanism for alignment and parallelism, and highlights the new features of the Tooling V2.

8.3.1. Gluing Procedure

The procedure of assembling ITkPix quad modules using the Tooling V2 is described below. See figure 8.11 for the required equipment, including these auxiliary items: scalpel for cutting the horizontal tabs that connect the flex main body with the flex frame, tweezers for applying and removing kapton tape in case it is needed for HV hole protection from glue seepage that hinders wire-bonding, and pen for marking start and end of glue on the stencil. In addition, cleaning equipment includes lint-free wipes[7] and isopropanol.

1. Preparation

[7] E.g. ThermaSeal 60 TX2069.

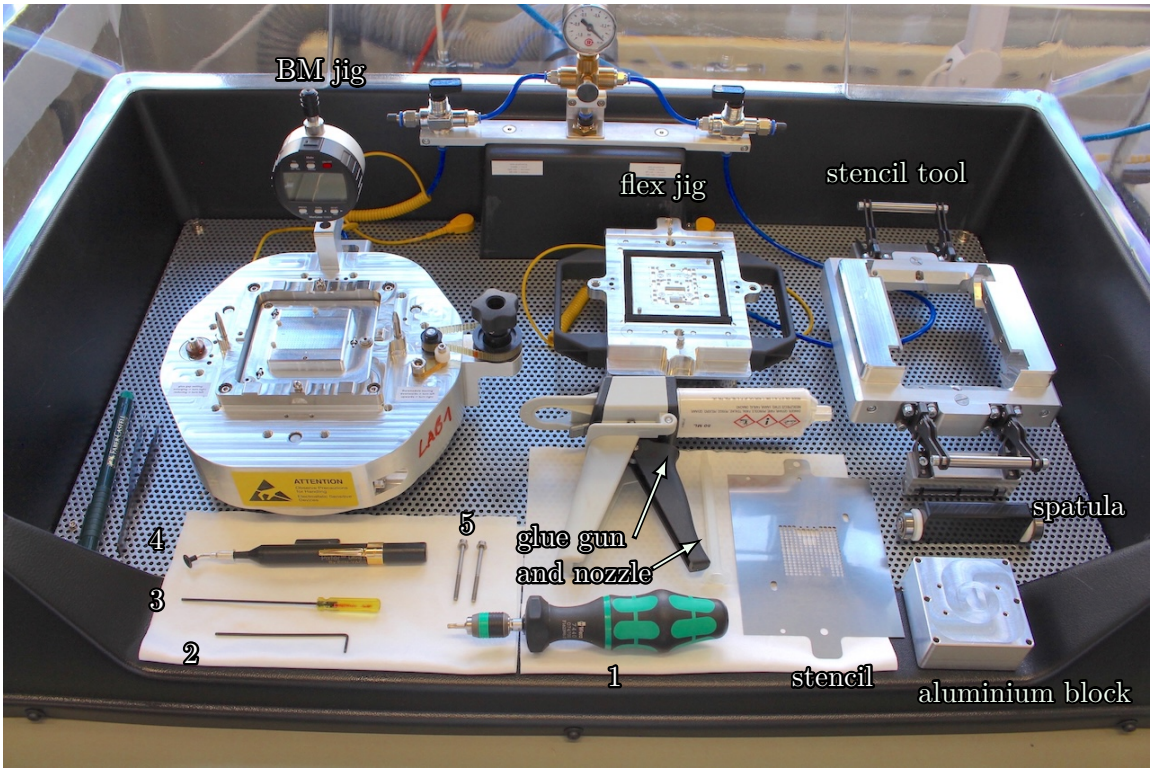

Figure 8.11: Equipment for gluing. 1: WERA 7440 x1/4"x0.3-1.2 Torque Screwdriver, 2.5 mm; 2: 1.5 mm Hex key; 3: 1/16" balldriver for fine adjustment thread; 4: vacuum pen EDSYN LP200; 5: fixing screws. The blue tubes are for vacuum, and the yellow wires are for ESD safety.

- Connect the ESD protection cables and vacuum.
- Clean all surfaces that will touch the module components, and the locating surfaces.

2. Placing of components

- Place the BM on the BM chuck with the edges touching the three alignment pins.
- Place the flex on the flex jig, and place the aluminium block on top to flatten it.
- Turn on vacuum for both jigs, and remove aluminium block.

3. Putting the flex and BM in contact with each other

- Turn on the dial gauge. Turn the knob on the right hand side clockwise, to move the pivot plate to the highest position. Turn the fine adjustment thread screw on the left hand side counter-clockwise to the top of its working range using the 1/16" balldriver, to move the pivot plate to the highest position possible. Note the dial gauge reading.
- Turn the knob to push the pivot plate down by ∼1 mm, flip the flex jig to put it onto the BM jig, fix the two fixing screws with the torque screw driver that is set to 0.3 Nm. Moving the pivot plate down beforehand avoids putting uneven pressure on the components when matching the flex jig upside-down on top of the BM jig.
- Turn the knob to release the pivot plate to the highest position so that the components

are in contact with each other. This can be checked via observing if the dial gauge now shows a lower value than before.
- Zero the dial gauge – at this point, there is no gap between the back of the flex and the sensor top of the BM.

4. Setting of the glue gap

   - Turn the fine adjustment screw to push the pivot plate down, creating the desired glue gap[8], which is reflected in the dial gauge reading[9]. To mitigate the effect of mechanical backlash, turn the fine adjustment screw until the gap is larger than the target glue gap, and then go backwards until the target is reached – e.g. if the target is 35 µm, adjust to ∼40 µm, and screw back carefully until 35 µm. Now, the highest possible position of the pivot plate is restricted by the fine adjustment screw.
   - Turn the knob to press down the pivot plate by ∼1 mm, remove the fixing screws, and take the flex jig off.

5. Glue distribution on the back of the flex

   - Fix the stencil onto the flex jig with the stencil tool – put the stencil and then the stencil tool on, close the clamps.
   - Mark glue position – insert the spatula to the guiding rails of the stencil tool, and mark the start and end point of the slanted edge of the spatula[10]. Remove spatula.
   - Add glue – use the glue gun to apply a line of glue[11] between the marks.
   - Distribute glue – insert spatula from top, pull it with even speed through the guiding rails and take it out at the other end to distribute the glue. The duration of the movement should be 10 to 20 s.
   - Un-clamp, take the stencil tool off, remove the stencil, check the glue pattern on the back of the flex.

6. Attaching

   - Put the flex jig back onto the BM jig, fix the screws. Use the knob to release the pivot plate to the top. At this point, the fine adjustment screw is still holding the possible topmost position of the pivot plate, which is lower than the back of the flex by the target glue gap.
   - Leave to cure for at least 8 h. It is normal for the dial gauge reading to differ from the original setting by 2 or 3 µm due to mechanical tolerances.

7. Cleanup

[8] In the past, 40 µm has been used. In pre-production, many sites use 35 µm. The exact value needs to be adjusted according to the individual unit of tooling, since there is a tolerance of ±15 µm, and the resolution of the dial gauge is 0.1 µm.

[9] The dial gauge reading is negative since the pivot plate is moved down from the original zeroed position to separate the components, creating the gap. But we will omit the minus sign in the following descriptions to refer to the width of the glue gap intuitively.

[10] This can either be done with a thin marker, or a sharp object to put permanent scratch on the stencil.

[11] The glue used is Araldite 2011, same as for wire-bond protection, as mentioned in section 7.4.2.

- Clean the spatula and stencil with isopropanol and lint-free wipes.

8. Taking the glued module out
   - Turn off the vacuum supply to the flex jig, and make sure there is no residual vacuum pressure[12]. Keep the vacuum of the BM jig so that it holds the glued module.
   - Push the pivot plate down using the knob to detach the module from the flex jig. The knob provides parallel and stable movement, which minimises the stress on the tabs between the flex body and the frame.
   - Take off flex jig, turn off vacuum, put the glued module in a module carrier.

When taking the flex jig off to take out the glued module, in principle, there are two options:

- Turn off the vacuum on the BM jig and keep the module fixed on the flex jig before it is put in a stable position to be taken out.
- Turn off the flex jig vacuum, and keep the module on the BM jig.

The default is the latter, as it avoids the BM edge scratching the dowel pins on the BM jig, which should be kept intact to provide good xy-alignment. The downside is that since the dowel pin on the flex jig is in the hole of the flex frame, the small tolerance of the hole (which benefits xy-alignment) makes it too tight to be easily taken off. Since the flex does not detach easily from the dowel pin on the flex jig, keeping the module on the BM jig while taking out the flex jig causes pressure in particular on one of the tabs that attach the flex body from the frame. However, moving the pivot plate down first with the knob mitigates the stress and makes the default option possible.

The whole procedure except for curing and cleaning takes roughly 15 min.

8.3.2. Before First Use

Choose Type of Module

When using the tooling for the first time, choose the correct dowel pin configuration for the module type. Three dowel pins should be inserted to the four holes on the BM chuck: two on the left, and one on either the top or the bottom. To glue modules with 150 µm thickness sensors, put the third dowel pin in the top hole. For modules with 100 µm thickness sensors, use the bottom hole. In case of switching configuration, do not re-use the dowel pins, since they deform when being pulled out, and may no longer meet the required specification.

Adjust the Fine Adjustment Screw

This step is not needed for the assembly sites, as it is done at Göttingen as part of the calibration procedure. However, in case the sites need to glue modules using e.g. dummies with thicknesses that differ largely from that of the BM or flex, the fine adjustment screw may need to be adjusted to allow a different working range.

[12] By e.g. un-plugging the vacuum tube.

To turn the fine adjustment screw, put a hex key through the hole on the top of the screw. There are two different levels inside, each fits a different-sized hex key, and they control the different types of threads: the inner fine thread (can be turned using the 1/16" balldriver[13] supplied with the tooling) and an outer coarse thread (1.5 mm hex key).

The movement range of the fine thread is 450 µm – it can be turned 18 rounds, each 25 µm. With the movement, the sphere tip (see figure 8.12) pushes the pivot plate down or releases it back up. For initial adjustment, set it to the middle position, and then insert the whole screw into the BM jig to a position suitable for gluing the components.

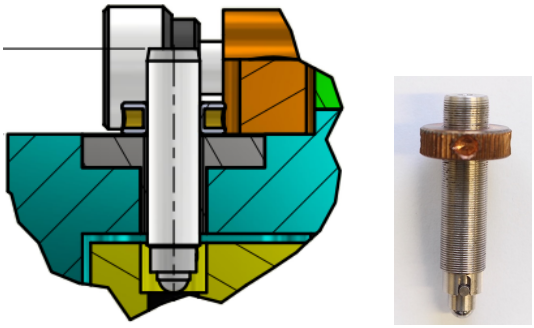

Figure 8.12: The fine adjustment screw on the BM jig [193]. Inside the screw is the inner fine threads, and the outside are the coarse threads. The bottom is a sphere tip, which moves up and down when the inner fine thread is turned.

To set the fine thread to middle range, the user can take out the screw completely, turn the fine thread until it reaches either end, and turn back nine rounds, which sets the fine thread to the middle position. This is because the middle position is the more accurate range, and gives freedom to move both up and down.

Then, to insert the screw into the BM jig to a suitable position: first put the BM and the flex on their respective jigs, and match the flex jig on the BM jig. Adjust the knob so that the components are in contact with each other, zero the dial gauge. Then, put the screw back into the BM jig, turn the whole screw either using the 1.5 mm hex key or by hand, until the dial gauge shows around −10 µm, tighten the locking nut to secure the position. Now, the location of the fine thread has enough freedom to move up and down for glue gap adjustment, and to account for the deviations in the thicknesses of module components.

8.3.3. Calibration

Calibration is performed at Göttingen and is not required at the assembly sites. The principle is introduced here for reference.

To calibrate the BM chuck so that it is parallel to the locating surfaces on the adjustment frame, first, adjust the fine adjustment screw as described in section 8.3.2, but without

[13] A balldriver is a hex key with a ball end so that the key can be inserted with an angle instead of completely perpendicular.

module components. Next, adjust the incline of the pivot plate using the two screws (fine thread) on the pivot plate surrounding surfaces.

For the alignment in the xy-direction, the position of the adjustment frame should be adjusted in the xy-plane so that the four notches on it are aligned with the four notches on the BM chuck. This is done via the three fine adjustment screws on the calibration frames at the left and top of the adjustment frame, and the two corresponding spring plungers[14] on the opposite sides provide counter-force. To enable movement of the adjustment frame and the calibration frames, loosen the screws that fix them onto the BM jig, which for the adjustment frame are the four screws at the corners. The coarse thread of the three fine adjustment screws should be set so that they are just touching the adjustment frame while the fine thread is set to the middle position, to allow room for later adjustments. The spring loaded screws on the other side should also be adjusted so that they are just in contact with the adjustment frame.

Calibration is an iterative process of doing the adjustments mentioned above, and measuring the status of the xy-alignment and parallelism, until the desired values within specification are reached. For mechanical details, please refer to the drawings in ref. [193].

8.3.4. Changes Based on Tooling V1 Experience

The assembly of RD53A modules with Tooling V1 provided valuable experience for identifying potential improvements. The basic principle of the Tooling V1 is briefly introduced here, for details and performance please refer to ref. [3].

For Tooling V1, the glue gap and parallelism is adjusted using a spacer (thin film) with a thickness that corresponds to the target glue gap. The spacer is put between the BM and flex, and heavy weights are put on top of the flex jig to ensure firm contact. Parallel movement between BM chuck and flex chuck is ensured via vertical guiding rods. The gap and parallelism is set via three screws fixed by locking nuts on the flex jig, and the corresponding contact surfaces on the BM jig. The calibration is performed via carefully adjusting the screws and fixing them with locking nuts when the operator just feels resistance or movement (monitored via a dial gauge).

Since the adjustment of the screws and locking nuts must be done slowly and precisely with steady hands, this requires high technical abilities and is subject to larger uncertainties. When mating the two jigs and putting heavy weights on top of the flex jig, there is the risk of putting stress on the components. A large deviation in the amount of glue was also observed.

The design of V2 has taken several possible improvements into consideration.

1. The stencil tool provides reproducibility of glue mass independent of the operator, and the clamps on the stencil tool fix the stencil onto the flex jig quickly and without excessive stress or rotation on the stencil.

[14] A screw with a spring tip.

2. For glue gap:

   a) The reference point is where the BM sensor side contacts the flex backside, therefore, the glue gap is not affected by the deviation of component thicknesses.
   b) Dial gauge provides precise monitoring of the glue gap.
   c) It is easy to set different target glue gap, without needing re-calibration of the tool, or finding spacers with the correct thicknesses.

3. The parallelism calibration is conducted only once during calibration, and the new method provides higher precision and repeatability. This benefits the glued module thickness and flatness, as well as homogeneous glue thickness and coverage.

4. For xy-alignment:

   a) Better precision of positioning the flex jig and BM jig achieved via the two spheres.
   b) The calibration is also performed only once, and the design even makes it possible to be calibrated with an offset, to compensate for systematic uncertainty from manufacturing tolerances of the module components.

5. To avoid the uneven weight distribution from the weights on top of the flex jig damaging the module components, especially the BMs:

   a) No extra weight required – even and adjustable pressure is provided via a spring.
   b) The BM chuck is easily moved down using the knob while keeping the parallelism, to get a clearance of $\sim$1 mm between the BM and the flex. This avoids uncontrolled direct contact between the module components. After curing, this also facilitates taking the glued module out with less pressure on the tabs that connects the flex body with its frame.

6. Added ESD-safe cable attachment points.

7. The vacuum hole patterns put less stress on the BM.

8. Flexibility and replaceability: the BM chuck is replaceable in case of damage or the need of fitting different BM geometries for xy-alignment.

8.4. Tooling V2 Review and Performance

A tooling review was conducted in 2022, where the performance of Tooling V2, as well as the Japan assembly and cell loading combined tooling was demonstrated. The tools were evaluated in four criteria: technical specifications, cost, schedule, and risk. After the review, feedback and instructions were provided (see ref. [193]), and Tooling V2 was set as the baseline tooling. This chapter presents the performance of Tooling V2, mainly based on the results obtained at the time of the review. The tests were conducted using real flex, brass flex dummy, glass BM dummy, and Si BM dummy. Later developments are also included.

8.4.1. Equipment and Measurements

Equipment for Measurements

Equipment used to perform measurements is shown in figure 8.13. Metrology is performed with the microscope. Thicknesses can in addition also be measured using the micrometer screw gauge. VI is conducted using both the DSLR camera and the microscope. The scale provides straightforward mass measurements.

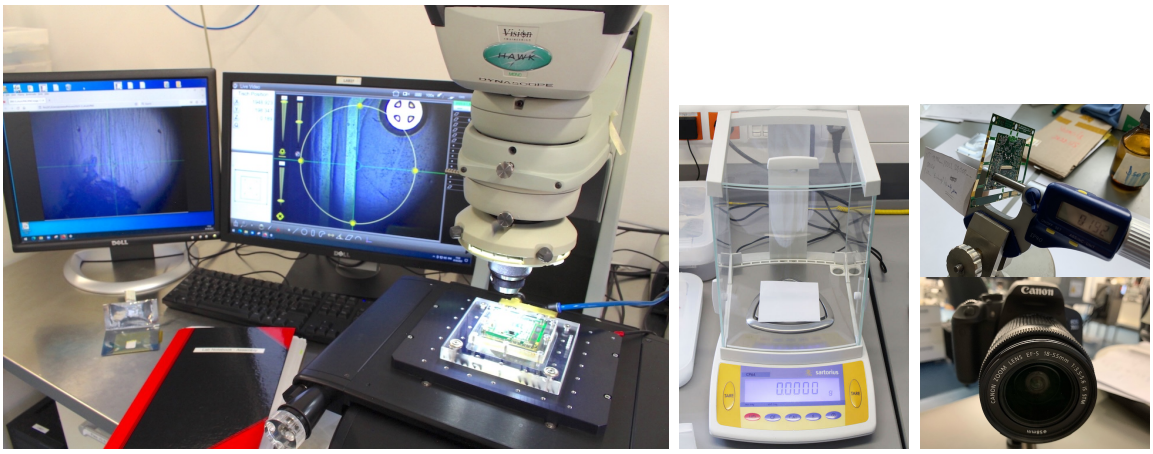

Figure 8.13: Equipment for measurements. Metrology and VI: Vision Engineering Hawk Mono Dynascope, xy-precision 2 µm (certified at calibration on 29.9.2021). VI: Canon EOS 700, EFS 18-55 mm lens. Thickness: Micrometer screw gauge. Mass: Sartorius CP64, nominal precision: standard deviation 0.1 mg.

Metrology Using a Microscope

Using a microscope, 3D positions of points on the components can be measured. With the component fixed onto the chuck by vacuum, the x- and y-coordinates are determined through the movement of the chuck, and the z-coordinate is obtained by the focus.

The 3M software is used to fit lines to find the edge locations, fit circles for the holes and slots, and fit planes for flatness measurements. The coordinate system can also be defined based on the measured edges and planes.

Flatness and parallelism are defined as follows:

- Flatness: after fitting a plane to the measured points on a surface, the flatness is defined as the difference between the maximum and minimum distances of the points relative to the fitted plane.
- Parallelism between two surfaces: measure one surface and fit a plane, which is defined as the reference plane. Parallelism is then defined as the difference between the maximum and minimum distances of the measured points on the second surface, relative to the reference plane.

Before conducting measurements, an initial cleaning of the microscope chuck with iso-

propanol is required, if there is a long time before the last measurement was made. Afterwards, the chuck is cleaned only via blowing with dry air.

The chuck is measured first to define the xy-plane with $z = 0$. Points were measured via focusing on the scratches on the surface of the chuck, which are not obvious to the naked eye but clearly visible under the microscope. The precision of the focus depends on the operator, the surface to be measured, and the metrology machine. For the measurements presented in this thesis, the standard deviation (std dev) of re-focusing repeatedly at one location of the chuck is 5 µm, and the difference between the maximum and minimum is 22 µm. In combination with uncertainties from further measurements on the components, this leads to a large uncertainty on the thickness measurements, especially for the flatness, since the specification requires a flatness of only 15 µm. Therefore, an automatic machine from Micro·Vu was acquired later for the tooling calibration, pre-production, and production in Göttingen. A photo of the automatic machine can be found in figure 8.28.

For an estimation of the precision, the chuck was measured 11 times, the distribution of the difference in z is shown in figure 8.14. The mean value is 1 µm, with a std dev of 3 µm.

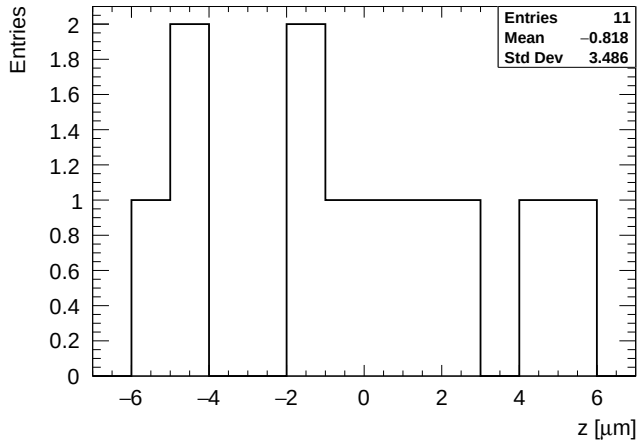

Figure 8.14: Difference in z of 11 repeated measurements of the microscope chuck.

8.4.2. Calibration Performance

After tooling calibration, the flatnesses of the BM chuck, adjustment frame locating surfaces, and flex chuck were measured, as well as the parallelism between the locating surfaces and the chuck surfaces.

All toolings are calibrated with parallelism within 4 µm at Göttingen before being sent out to other assembly sites. The calibration results for the prototype tooling unit at Göttingen are shown in table 8.2.

Parallelism and alignment measurements of the BM jig were performed twice at the time of calibration for estimation of repeatability, and the BM jig parallelism measurement was repeated after 1.5 years. The parallelism between the BM chuck and the adjustment frame

	Dec 2021		Jul 2023	
Repetition	1	2	1	2
BM chuck flatness	4	–	–	–
Adjustment frame locating surfaces flatness	4	4	–	–
Parallelism of BM jig	2	2	11	8
Parallelism of BM jig (lower pivot plate position)	–	–	7	5
xy-alignment	-2, -4	-3, 0	–	–
Angle between vertical notches	0°40'90"	0°00'26"	–	–
Angle between horizontal notches	0°00'10"	0°01'29"	–	–
Flex chuck flatness	4	–	–	–
Parallelism of flex jig	10	–	–	–

Table 8.2: Calibration measurements of the Göttingen prototype tooling. All the flatness, parallelism, and alignment results are in unit of µm.

locating surfaces was measured both for the pivot plate being on the topmost position (the location at which the calibration was done) and a lower position, being 0.6 mm and 1 mm lower from the locating surfaces, respectively. The xy-alignment is the difference between the (x, y) coordinates of the adjustment frame centre (marked by the notches) and the BM nominal centre. In addition, the angle between the lines connecting the notches at the vertical and horizontal directions should be close to 0. The results show good calibration performance.

To estimate the precision of the measurements, the calibration operator also measured the height of the same point on the tooling surface repeatedly 30 times, and the std dev is 3 µm. Therefore, the parallelism seem to have degraded by a few microns over the 1.5 years of use, however, this conclusion is undermined by the limitation from the precision of the thickness measurement using the microscope.

8.4.3. Glue Mass Stability

The theoretical amount of glue deposition is defined by the area of the cutout and the thickness of the stencil:

$$m_{\text{glue}} = A \times d \times \rho, \tag{8.1}$$

where:

A is the area of the cutouts on the stencil
d is the stencil thickness
ρ is the glue density, $\rho = 1.05\,\text{mg/mm}^3$ for Araldite 2011

In practice, the amount of glue deposited is also related to the dimension of the spatula (the distance between the bottom and the axis of the bearings) since firmer pressing leads to less glue deposition. Tests were conducted to determine the stability of the glue mass m_{glue}. The results using different versions of flexes and stencils are summarised in table 8.3, showing a stable glue mass with a std dev within 4 % of the average.

	RD53A flex, stencil v4	ITkPix v2.4 flex, stencil v6
Cutout Area [mm^2]	502.79	544.74
Theoretical m_{glue} [mg]	52.8	57.2
Avg m_{glue} [mg]	44.8	52.14
Std Dev [mg]	1.7	1.9
Std Dev/Avg [%]	3.8	3.7

Table 8.3: Glue mass stability. Five repetitions were done for both configurations: RD53A flex using stencil v4, and ITkPix flex using stencil v6. The stencil thicknesses are both 0.1 mm. The RD53A tests were performed by different operators.

During stencil tool testing, it was found that the duration taken to pull the spatula across the guiding rail influences the glue mass and the stability, see figure 8.15 for the results obtained using stencil v4 and RD53A flex. A duration of larger than 10 s is therefore recommended.

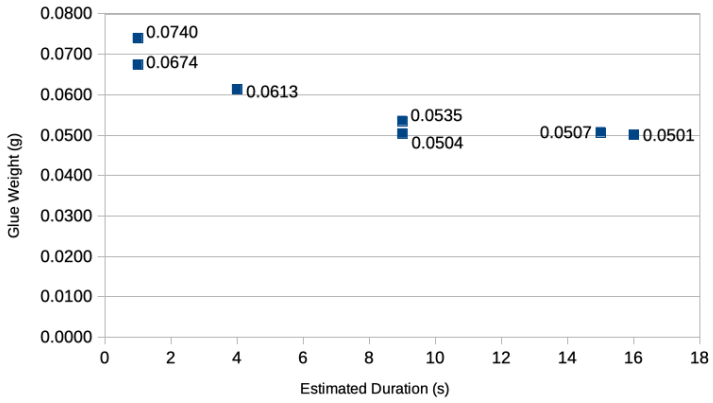

Figure 8.15: Amount of glue distributed to the flex vs duration of pulling the spatula across the flex.

8.4.4. Glue Coverage

Gluing a flex or its dummy to a glass BM dummy allows direct observation of the glue pattern. An image processing code was developed, together with a procedure of photo taking, to calculate the coverage[15] with respect to the size of the flex main body. It goes through user defined cut values to make the photo a binary black and white picture, and calculates the percentage of the black pixels over the number of pixels on the whole picture, which is corrected for the size of the flex body.

Several steel flex dummy + glass and real flex + glass samples were glued. The results are summarised in table 8.4, and explained below. Results include the amount of glue that was distributed onto the steel or flex, the average glue thickness calculated from micrometer screw gauge measurements on four pick-up areas, with the upper and lower values relative to

[15]Image processing code: https://gitlab.cern.ch/tiany/image_analysis.git

Sample name	Target [µm]	Measured [µm]	m_{glue} [mg]	Coverage	Theoretical coverage	Note
Steel 30	30	38^{+2}_{-1}	41.2	65 %	64 %	–
Steel 25 rep1	25	33^{+1}_{-2}	44.8	80 %	81 %	–
Steel 25 rep2	25	32^{+1}_{-2}	43.2	82 %	81 %	–
Flex 20	20	32^{+1}_{-2}	49.1	64 %	91 %	–
Flex 30	30	40^{+1}_{-0}	51.6	56 %	76 %	76 % at thick part
Flex 40	40	49^{+3}_{-3}	54.1	52 %	66 %	Cured for only 4 h
Bare flex 30	30	–	77.9	80 %	–	Stencil v8

Table 8.4: Summary of glue coverage results: sample name, target thickness set with the Tooling V2, measured thickness by screw gauge, coverage obtained using image analysis code, and the theoretical coverage calculated via the amount of glue and measured thickness. Most tests were performed using stencil v6, except for the last sample (bare flex 30), where v8 was used.

the average noted in the superscripts and subscripts. The theoretical coverage is calculated based on the measured thickness and the volume of glue applied, which is obtained from the glue mass and density. The samples are named after the material on which glue is distributed (flex or its dummy) and their important features (such as target thickness) for convenience.

Steel + Glass

To test the glue coverage performance from Tooling V2 and the stencil while controlling other variables like the uneven backside of the flex, steel and glass dummies were used. Three samples were glued, the results are summarised in table 8.4, and photos of the glued samples as well as the binary picture for Steel 30 are shown in figure 8.16.

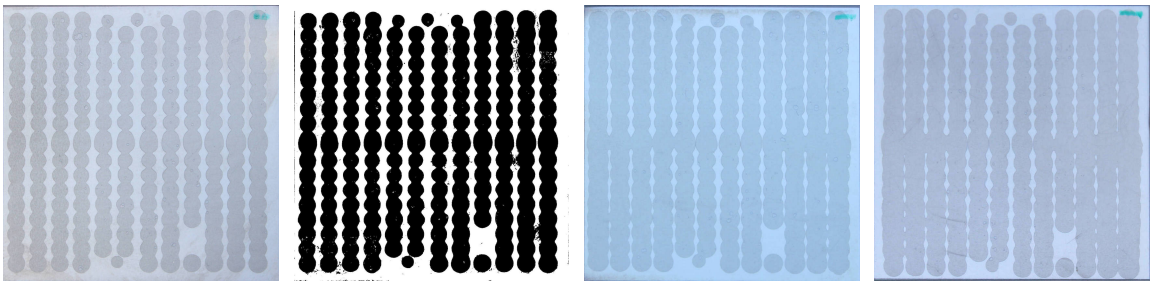

(a) 30 µm (b) Coverage 65% (c) 25 µm rep 1, 80% (d) 25 µm rep 2, 82%

Figure 8.16: Steel flex dummy and glass BM dummy glue patterns with calculated coverage, and the binary picture for the 30 µm photo.

The coverages extracted from image analysis are consistent with the theoretical calculations, confirming reasonable glue thickness measurements from the screw gauge, despite a 10 µm offset with the target. Comparing Steel 30 and the two repetitions of Steel 25, the 5 µm change in target thickness is also reflected in the measured thicknesses.

Real Flex v2.4 + Glass

Three flexes were glued with glass dummies using different dial gauge settings: 20, 30 and 40 µm. See figure 8.17 for the glue patterns with the results written in subfigure captions for convenience. The results are also summarised in table 8.4.

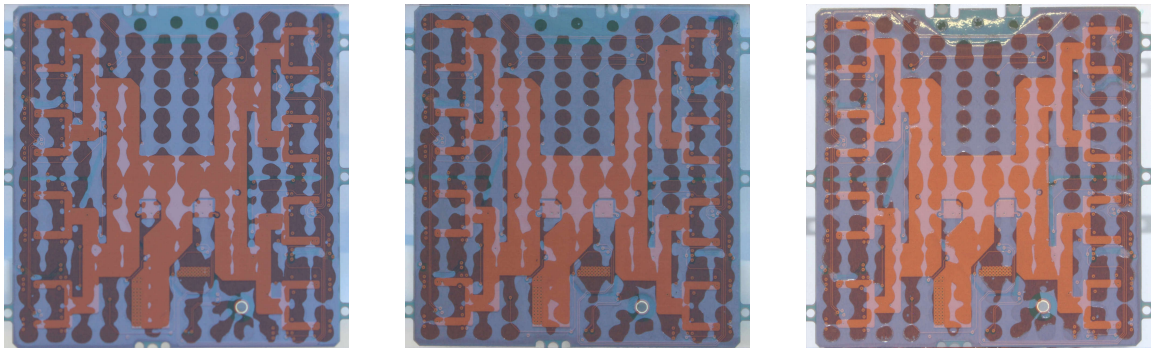

(a) 20 µm, 49.1 mg, measured 32^{+1}_{-2} µm, 64%, theor. 91 %.

(b) 30 µm, 51.6 mg, measured 40^{+1}_{-0} µm, 56%, theor. 76 %.

(c) 40 µm, 54.1 mg, measured 49^{+3}_{-3} µm, 52%, theor. 66 %.

Figure 8.17: Glue pattern of three flex-glass dummy assemblies, with the target thicknesses, glue mass, measured glue thickness, measured coverage, and theoretical coverage.

The coverage is lower than the desired 80 %. This is because the target glue thickness is w.r.t. when the flex and BM dummy touch each other, which means that the zero gap is defined by the thickest parts of the stacked components, and the glue gap setting on the dial gauge shows the glue gap at this position. As the flex back surface is very uneven – the darker part is approximately 20 µm thinner than the orange coloured area with copper layer – the actual glue thickness at these areas are around 20 µm larger.

It can be seen that the glue compression is even within the respective flex areas with similar thicknesses. Glue is compressed more at the thicker area with the copper layer. The average glue thickness in the pick-up areas (which belong to the thicker part that is with copper layer) is consistent with the previous results of 10 µm offset with respect to the target.

To validate the hypothesis that the unevenness of the flex backside is the reason for lower coverage and quantitatively estimate the effect, analysis was performed only taking into account the thick part. This is done by manually masking the thinner part using image editing software[16] with a distinctive colour (green, similar to a green screen background for visual effects in movies), and a functionality was added to the code to only take into consideration the part without green screen mask. Figure 8.18 shows the result for the 30 µm trial. The resulting coverage is close to the specification and expected theoretical coverage, confirming that not reaching the desired coverage is caused by the uneven surface of the flex.

It is worth noticing that the glue invades the HV hole, and the glue pattern around the HV hole area indicates that the glue dots are sucked into it. Investigations in the assembly community indicate that this is due to the thinner part around the HV hole creating a gap

[16] E.g. GIMP.

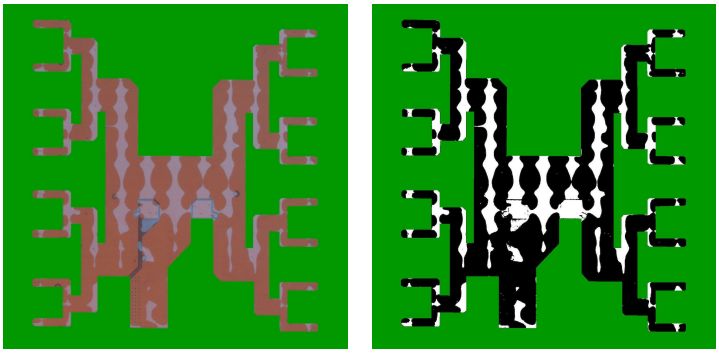

(a) Masked thinner part. (b) 76% coverage.

Figure 8.18: Coverage of the thick part on the flex.

between the flex and the jig, which causes the vacuum pressure to be leaked through the hole, sucking the glue dots inward. This would cause the HV hole to be covered with glue, leaving no place for wire-bonds, making the module non-functional.

Due to the issues with the below-specification coverage and HV hole safety, after the tooling review, more stencil tests were conducted to optimise the stencil pattern. The stencil evolution is shown in figure 8.10. 80 % target coverage was shown to be reached using a bare flex and stencil v8 with 30 µm target glue gap. The glue mass is 77.9 mg, significantly larger than the previous stencil versions. This sample was not cured, and thus the glue thickness was not measured.

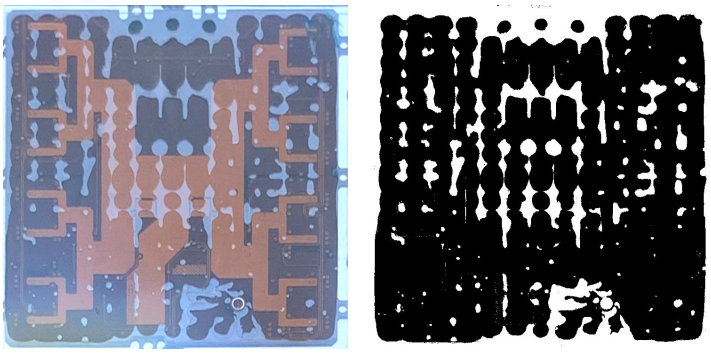

Figure 8.19: 80 % coverage reached with stencil v8 and 30 µm target glue gap, glue mass 77.9 mg.

During testing, it was also observed that certain SMD components clash with the flex jig cutout. This lead to a change of the flex jig cutout design, to allow higher tolerances of the flex SMD component alignment.

However, solely varying the stencil design did not guarantee HV hole safety. At pre-production, as shown in section 8.5.2, kapton tape pieces were provided to assembly sites, to seal the HV hole and block the vacuum pressure, and prevent glue seepage.

8.4.5. *xy*-alignment

Brass Flex Dummy + BM Dummy

The tooling was designed and calibrated assuming nominal flex and BM dimensions. However, the xy-alignment also depends on deviations between individual components regarding, for instance, the fiducial mark position relative to the hole and slot on the flex frame, the tolerances of the flex frame hole and slot, and the size of the BM.

Therefore, to test the performance of the tooling itself independent of the components, a brass flex dummy was designed according to the nominal hole and slot dimensions of the flex, and was manufactured with much smaller tolerances. Si dummies or steel sheets of the same xy-dimensions were used as BM dummies. Photos can be found in appendix B.2.

Three Si dummies and one steel sheet were assembled to brass flex dummies with a fast cure glue[17]. The type of glue does not affect the alignment, since both components are fixed with vacuum. The glued samples are shown in figure 8.20.

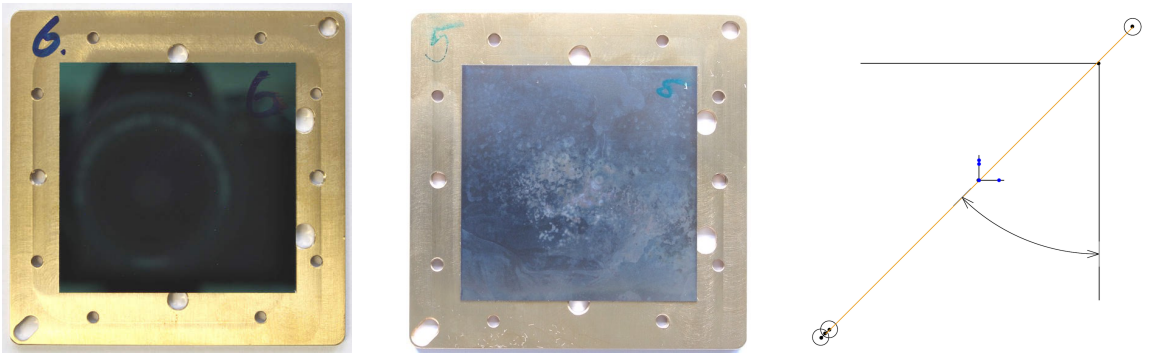

(a) Brass flex dummy glued with Si dummy.

(b) Brass flex dummy glued with steel dummy.

(c) The defined lines, hole, slot, and angle for analysis.

Figure 8.20: Glued samples for xy-alignment test, and the measurements for analysis.

Metrology was done with the microscope to measure the edges and circles for the holes and slots. The orientation of the samples during metrology is as in figure 8.20. The Si top and right edges were measured: when flipped, they are the top and left edges, whose positions are defined by the dowel pins.

The analysis of the results attempts to correct for the influence of tolerances: the Si right edge was set as the reference edge and is defined as 90° (vertical, as the y-axis), since it is controlled by two dowel pins. The centre of the flex dummy is defined by the middle of the diagonal line that connects the top right hole and bottom left slot (when viewing the flex from the back side). In the analysis, the nominal value of the distance between the hole and slot centre (76.368 mm) is used to correct for component deviations. The centre is defined on the measured line between the hole and the slot, with a distance of half the nominal mentioned above from the centre of the hole. This nominal-corrected flex centre is set as the origin of the coordinate system. The centre of the BM is defined according

[17] UHU Plus Schnellfest 2-K-Epoxidharzklebstoff.

to the nominal value (-21.100, -20.550) mm w.r.t. the Si top right corner. Then the xy-misalignment is defined as the (x, y) coordinates of the BM centre w.r.t. the coordinates of the flex centre. The angle between the line from the flex hole and slot and the Si reference edge θ is also measured, which should be $\theta = 45\,^\circ$ in the norminal case. See figure 8.20(c) for an illustration of the analysis, and the results are shown in table 8.5. The real measured centre between the hole and slot of the brass flex dummy is also shown.

	BM x, y [µm]	θ	Hole&Slot Measured Centre
Si6	-23, 1	45°01'37"	-1, -1
Si7	2, 4	45°00'34"	6, 6
Si8	-6, 6	45°00'24"	2, 2
Steel	-33, 2	45°00'10"	0, 1

Table 8.5: xy-alignment results with brass flex dummy and Si or steel BM dummy.

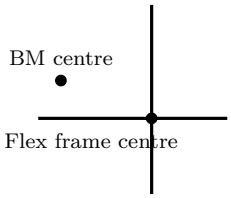

Figure 8.21: Result: Si centre mostly at 2nd quadrant of flex nominal centre.

The specification v3.5 [191] requires the centres of the flex and BM to be within 100 µm in both x- and y-direction, and the results show that the dummy assemblies meet this specification. The Si centre is mostly at the 2nd quadrant, relative to the flex centre, as visualised in figure 8.21. The angle is very close to nominal. The dimensions of the manufactured flex dummies are very close to nominal, since the centre between the hole and slot is very close to the nominal centre. Therefore, the tooling is shown to be able to glue flex and BM with very good xy-alignment and very small rotation within specifications for module components with close to nominal dimensions.

Real Flex v2.4 + Si Dummy

Two populated flexes v2.4 named flex207 and 208[18] were glued with the nominal glue – Araldite 2011. Two lines were measured on the two outer edges of the "F"-shaped fiducial marks, and the locations of the intersection points are compared to the nominal.

Firstly, to estimate how much the components deviate from nominal, the distances between the two fiducial marks were measured. For both samples, the distance was measured to be 52.962 mm, which is 24 µm shorter than the nominal: 52.986 mm. When distributed to x- and y-direction, this means 17 µm of shifting from the deviation of the fiducial marks w.r.t. nominal.

When analysing the results, the BM left edge was again set as the y-axis. With the top left corner set as (0,0), the misalignment of the centres is defined as the difference between the coordinates of the fiducial marks and the nominal coordinates of the fiducial marks. The results are shown in table 8.6, and the shift of the centres is qualitatively illustrated in figure 8.22.

[18] Defined by their SN.

	Flex207	Flex208
x, y top left [µm]	-33, -20	-24, 21
x, y bottom right [µm]	-2, 44	-33, 46

Table 8.6: xy-alignment of the glued flex207 and 208.

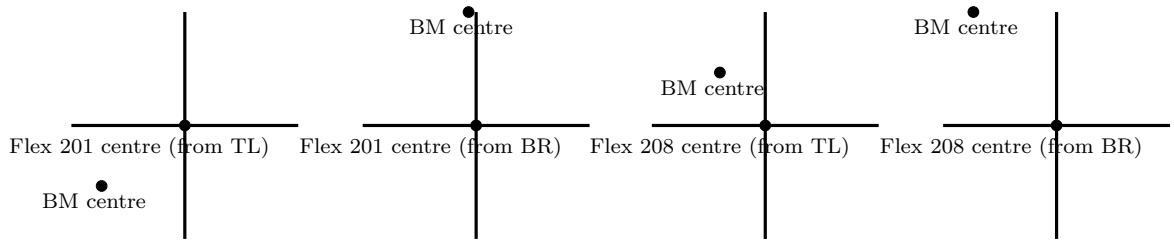

Figure 8.22: Shift of the BM centre w.r.t. the flex centre.

For the same flex-Si assembly, the shifts measured from the top left and bottom right fiducial marks are different, but both are within specification. Therefore, the misalignment between the centres of the components is in specification. However, these samples were glued without cutting the side tabs. Extra shift from the instability after cutting the tabs is estimated to be around 20 µm.

8.4.6. Thickness and Flatness

Two flex-Si dummies were assembled, flex282 was assembled with 30 µm target glue gap, and flex281 with 20 µm. Four points and two points were measured for the thickness on the body of the connector and the HV capacitor respectively, and the maximum value is taken. The flatness was measured by measuring 3 points per pick-up area on the copper traces[19], and after fitting a plane, the maximum and minimum distances between the measured points and the plane are determined. Table 8.7 shows the results.

	Flex282 (30 µm)	Flex281 (20 µm)
Pick-up Thickness Avg [µm]	569	561
Flatness [µm]	17	12
Connector Max [µm]	1951	1891
Capacitor Max [µm]	2228	2314

Table 8.7: Flex + Si dummy module thickness and flatness. The two samples are glued with different target glue gaps, as labeled.

The flatness is around the required 15 µm. However, as mentioned before, this is subject to large uncertainty due to the instrument limitation. The measured maximum thicknesses of the power connector body and the HV capacitor are within the requirements.

[19]The copper traces show up as lines with lighter colour on the flex top surface.

8.4.7. Conclusions and Outlook

The ITk Pixel Quad Assembly Tooling V2 was developed and tested to facilitate the assembly the large number of modules needed for the ITk Pixel detector. The performance was tested via metrology, VI, and mass measurements. The prototype unit at Göttingen was measured, showing a flatness of 2 to 4 µm for the BM chuck, BM jig adjustment frame locating surfaces, and flex chuck. The calibration resulted in a parallelism of 2 µm between the BM chuck and the adjustment frame locating surfaces, and 10 µm between the flex jig flex contact surface and locating surfaces. Precision was estimated based on the spread of measurements at a single point of the tooling surface, which is 3 µm. After 1.5 years of use, the degradation in parallelism is in the order of a few microns between the BM chuck and the BM jig locating surfaces. More precise measurements and calibration can be done with more precise equipment.

The stencil tool, in combination with the stencil, can provide stable glue mass with std dev within 5 % of the average. The duration it takes to pull the spatula across the stencil stabilises at longer than around 10 s, which is the standard practice set for further quad module assembly activities. However, this test was done on an RD53A flex with RD53A stencil v4, while the version used in pre-production is ITkPix flex v3.2 and stencil v8. Further tests can be done with the latest versions of component, stencil and tooling.

Measurements on four brass flex dummy + Si/steel BM dummy assemblies and two real flex + Si dummies showed that the xy-alignments are within specification. The module thickness and flatness was tested on two flex + Si dummy assemblies, the overall thickness is within specification, and the flatness is around the specification. However, the std dev of focusing is at the level of a few micron, therefore the precision is restricted by the equipment. An automatic microscope with higher precision was purchased later for production.

In terms of glue coverage, tests on three steel + glass dummies showed good coverages and consistency with theoretical calculations based on measured glue mass and thickness, with a 10 µm offset from the target thickness. The compressed pattern is even, showing good parallelism of the tooling. Three flex + glass dummy samples confirmed 10 µm offset, however, the glue coverage is not ideal at the part of the flex that is much thinner than the rest. These tests, as well as the finding of a flex SMD component location clash, has lead to later developments of stencil patterns and modification of the flex jig cutout. Stencil v8 tested with bare flex + glass assembly managed to reach 80 % coverage with 30 µm glue gap. To prevent glue from seeping into the HV hole and preventing wire-bonding, using kapton tape circles to seal the HV hole was established as a solution.

Following a tooling review in March 2022, Tooling V2 was established as the baseline tooling for ITk Pixel quad module assembly. To date, a total of 85 sets of Tooling V2 and two prototypes were produced. 75 of them were distributed to the assembly sites, with the rest being spares.

8.5. Assembly Site Qualification

As mentioned in chapter 7, there are two SQ blocks regarding assembly: reception tests and assembly. This section introduces the assembly SQ requirements and the local setup at Göttingen, and the results will be shown in the next section.

8.5.1. Reception of Quad Components

To qualify for the metrology and reception of quad module components, the following information and measurements are required[20]:

- The instrument used for the measurements, including information on precision.
- For instrument precision, it is in addition required to measure the X, Y, Z (thickness) and weight of a reference sample 10 times, each time removing and re-placing the component, and show the histogram and deviation with respect to nominal.
- Results on metrology, mass, VI, and BM electrical test. Measure 2 flexes, 3 Si dummies and 3 BMs.
- The duration of each measurement, to provide an estimation of the production rate.
- SN of the flexes and BMs.
- Upload test results to the production database (PDB) under each component.

The Göttingen setup for metrology, mass and VI is as introduced in section 8.4.1, and the setup for BM electrical test is as described in section 6.1.3. With these setups, Si dummy or BM metrology and mass measurements take around 15 to 20 min. VI of flex takes around 15 min, including taking photos, inspecting them, and uploading results to the PDB. VI for Si dummy takes around 20 min, including detailed checks under the microscope. For the BM, VI takes around 30 min. For BM electrical tests, after setting up the probe station and chiller, each IV curve takes ~ 15 min.

Metrology and Mass

The mass measurement is straightforward. For metrology, the detailed SQ requirements and the practice at Göttingen is detailed below.

Metrology is performed to provide the dimensions (width X and length Y) of the flex main body and the BM or its dummy. For the BM, two sets of measurements are made: on the sensor and on the four FEs, which are measured as a whole.

Requiring only one pair of width and length result has its limitations: even if the specifications are met, it is still possible that the BM or flex is shaped like a parallelogram or other irregular quadrilateral. Also, as the relative position between the sensor and the four FEs is not required, a shift differ from nominal is possible, which could lead to the BM exceeding envelope despite both sensor and FE being in specification. But in practice, no problem has been observed, and therefore no additional measurements are required.

[20] A component should be exchanged with another site to cross-check the measurements, but this is not yet a qualification requirement due to the current constraints in time and effort.

In the z-direction (thicknesses), the required measurements are:

- Flex:
  - Thickness on black body of power connector for envelope check, either via microscope or probe – average of minimum 3 points.
  - Thickness of the HV capacitor for envelope check – average of 2 points.
  - Thickness of the four pick-up areas with the flex facing either up or down, the probe pads can be used for precise measurements – report average and std dev.
- Si dummy:
  - Thickness – average of 9 points.
- BM:
  - FE thickness – average and std dev of four points: one per FE.
  - Module thickness – average and std dev of 9 points, this is measured on the sensor.
  - Measurements are required only with sensor facing up, therefore sensor thickness measurement is not required.

The metrology plan used in Göttingen for pre-production measurements is shown in figure 8.23(c). The width and length of the flex body are defined by measuring two points per

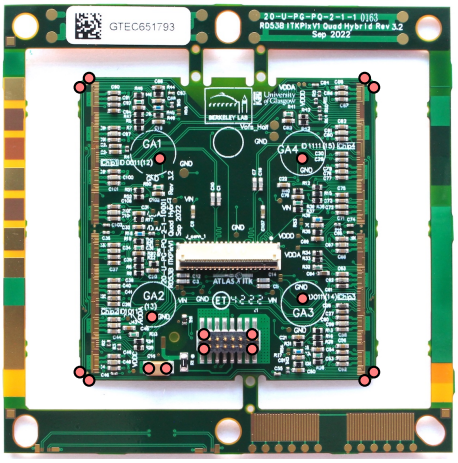

(a) Two points per edge for X and Y dimensions, the others for thickness.

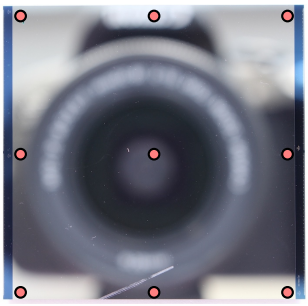

(b) 9 evenly distributed points used for thickness.

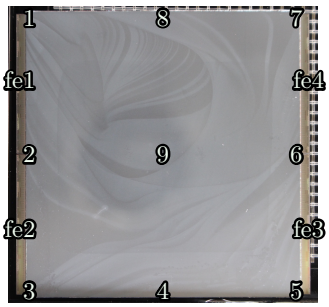

(c) Points 1-9 for sensor thickness, fe1-4 for FE thicknesses.

Figure 8.23: Metrology points for flex, Si dummy and BM. The points for X and Y dimensions for Si dummy and BM are the same as that on the flex. The flex thickness is measured on the power connector body (black part), HV capacitor, and the golden probing pads in the pick-up areas.

edge[21]. The location of one of the points for X and Y is shown in figure 8.24. The lines for the four edges are fitted through the measured points, and the 4 corners are defined by the intersection points. Then, the four edges are found by connecting the corners. The average of the two horizontal or vertical edges are the width and length of the flex body, respectively.

[21] It was also tested if lines fit from four points make a visible difference, but the difference between the lengths measured using two or four points is only ∼2 µm, therefore the two points plan is sufficient.

Figure 8.24 also shows that the edge of the flex is not very well defined: the different flex layers make a visible difference. Measuring on the edge of the top green layer results in the flex dimensions being lower than the actual dimensions. Therefore, it was decided that the outer edges should be measured.

The X and Y dimensions for Si dummy and BM are measured in the same way as the flex, except that there are two sets of measurements for each BM on sensor and FEs.

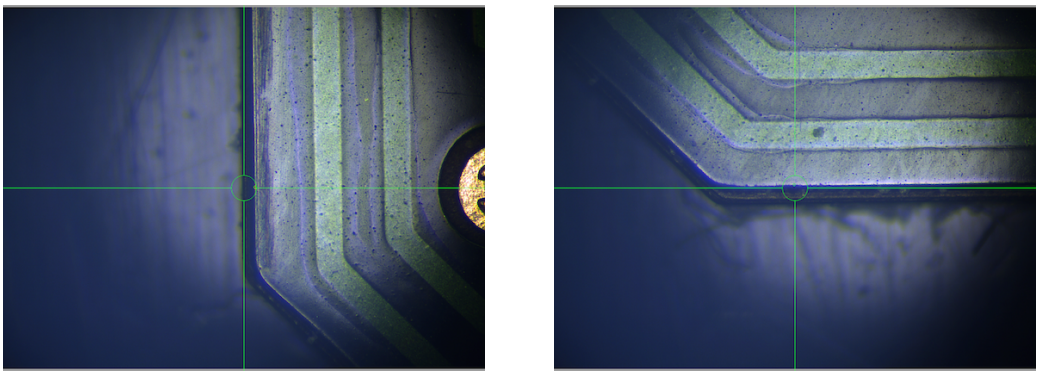

Figure 8.24: Measure on the flex edges for X and Y.

The z-thickness is measured for the flex on the golden probe pads on the pick-up areas, the power connector body (the black part), and the HV capacitor. Two points per pick-up area are measured. Only for these points, two points are only illustrated as one point in figure 8.23(c) due to lack of space, and the golden pads are covered by the marks. The thickness for the Si dummy is measured from 9 evenly distributed points, this is the same for BM thickness (on the sensor with FE facing down). The thickness of the FEs is measured at the edge where the FEs are exposed by measuring one point per FE.

Visual Inspection

VI is required to spot any possible defects early on, and is in particular important for flex and BM. It is required to upload HD photos[22] for the components and the defects to the PDB, which provides justification of a final grading of the component. The template for grading the flex can be found in [194]. For BMs, the categories of possible defects are listed in table 8.8. Some examples are provided in section 8.6.2.

Bare Module Electrical Test (BM *IV*)

The BM electrical test requires measuring the leakage current vs bias voltage (IV) curve, to test the electrical functionality of the sensor, as introduced in section 4.2.2 and chapter 6. The SQ requires description of all devices[23], including probe station details such as the number of available needles.

[22] Each photo max. 30 MB.
[23] Probe station, HV sources, meters, and equipment for environmental control and monitoring.

	Sensor	FE
Front side	Systematic rough edge or dicing defect	Bond pad contamination
	Tooling marks	Irregular dicing
	Random scratch	Scratch on top side (pad side)
	Dot-like contamination	Excess material (not diced near FE border)
	Chipped corner	Chipped outer corner
Back side	–	Chipped inner corner
	–	Scratch on back side

Table 8.8: BM VI. Front side refers to the sensor side, and the back side refers to the side where all four FEs are visible.

The number of probe needles is relevant for testing BMs with sensors that have different bias structures: for probing, two methods can be used. Method 1 is with sensor facing up, and method 2 is with FEs facing up. For sensors without biasing structure, only method 1 is applicable. As introduced in section 6.1.2, this includes FBK 100 µm quad sensors, therefore one probe for each of the 4 FEs is needed.

There are multiple probe pads on the BM for the analog ground (GNDA): pads 9–13, 61–65 etc. Their functionalities are identical. Pad 11 is the nominal recommendation, since it is in the middle of a few consecutive pads and is therefore more tolerant to human error.

- Method 1: the connections are summarised in table 8.9, and an example of probing FE1 of a BM using two probe needles is illustrated in figure 8.25.

BM Type	GNDA	Number of Needles
Quad BM with bias structure	1 needle to pad 11 of one of the FEs	2
Quad BM without bias structure	4 needles to pad 11 of all 4 FEs	5
Single BM (3D, for triplet)	1 needle to pad 11	2

Table 8.9: Summary of connections for BM *IV*. Pad 11 is the nominal choice to ground the GNDA with probe needle. HV is applied through 1 needle to the back of the sensor, and the chuck should always be grounded.

- Method 2: place the BM with FE on top, connect the sensor back side via chuck to HV, and ground the bias rail on the sensor directly with a probe needle. The location of the probe pads depends on the vendor. Figure 8.26 shows examples of probe pad positions for HPK and Micron sensors. The probe pads for HPK are in the space between the FEs near the sensor edges, and Micron sensors have them at the corners of the sensor.

The probe needle(s) must be placed at the corner of the probe pad, in order to minimise the scratch on the pad that could hinder wire-bonding. When probing multiple times for e.g new measurements, it is recommended to use the same pad, to minimise the number of pads that are scratched. In the case of unexpected results, different pads of the same functionality can be probed.

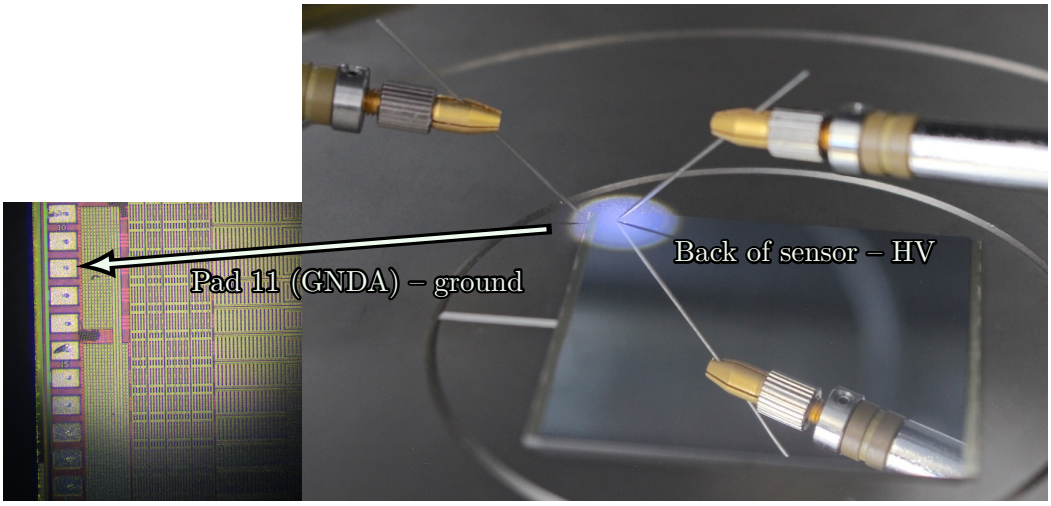

Figure 8.25: An example of BM probing with method 1 on a BM with biasing structure.

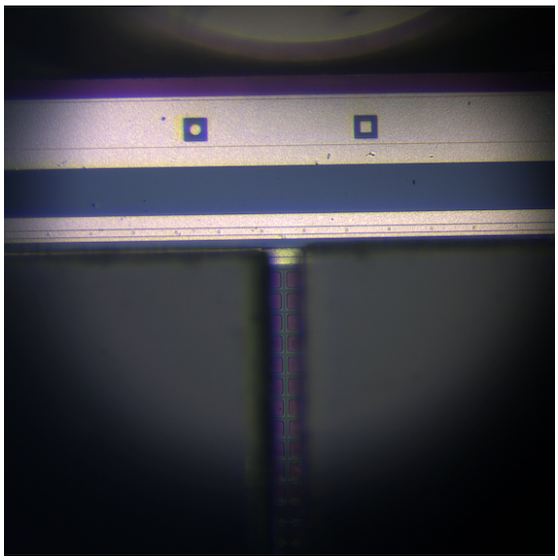

(a) Sensor with a pad between FE edges – HPK.

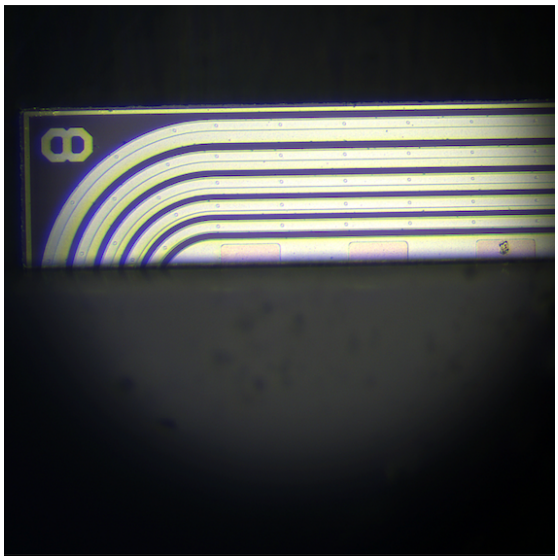

(b) Sensor with pads at the corners – Micron.

Figure 8.26: Position of probe pads used in method 2 for two vendors.

The required testing environment, measurement details such as waiting time, and acceptance criteria are consistent with those of un-irradiated sensor *IV*. For quad sensors, they are introduced in section 6.1. For single sensors used in triplet modules, *IV* scan should run from 0 to 100 V[24] or until compliance is reached, with maximum step size 1 V.

In addition to the *IV* curve, the breakdown voltage[25] as well as the leakage current at the depletion voltage are uploaded to the PDB, these results decide if a BM passes the BM electrical reception test. V_{dep} information can be obtained with different methods. In the order of preference:

[24]The leakage current and bias voltage are defined as positive, despite reverse bias.
[25]The default value to put in is -999 V in case of no breakdown observed.

1. Check V_{dep} information from the previous *CV* measurements of the sensor on this BM in the PDB.
2. If no *CV* measurement for the sensor is available, check the V_{dep} of the sensor wafer from the vendor quality control tests.
3. If no *CV* or V_{dep} information is available on either the sensor or the sensor wafer, use the default values as listed in table 8.10, which is from the experience of sensor QA. The results for planar sensors are as shown in chapter 6.
4. If the assembly site has a *CV* test setup, they can perform the measurement and upload the result to the PDB, then option 1 applies.

Sensor Type	V_{dep} [V]	V_{op} [V]
150 µm planar	60	60V + 50V = 110V
100 µm planar	40	40V + 50V = 90V
3D	5	5V + 20V = 25V

Table 8.10: Default depletion voltage and operation voltage for different types of sensors.

Göttingen uses method 1, with chuck T set to 20°C, and RH well below 50 % (normally 4-6 %) due to continuously flushing with dry air. The BMs to be assembled at Göttingen are equipped with HPK 150 µm sensors (poly-Si biasing).

8.5.2. Quad Assembly

For qualification of performing quad module assembly, the sites are required to assemble various samples in sequence, perform reception tests on the components prior to assembly, and conduct post assembly measurements on the glued samples. The samples to be glued and the required tests are summarised in table 8.11.

Number	BM or Dummy	Post Assembly Tests and Procedures
2	Glass	Photos and glue coverage, showing homogeneous glue layer without seepage.
3	Si	Metrology (including glue thickness), mass (including glue mass), VI. Wire-bonding, backside flatness.
1+4	BM	

Table 8.11: Quad assembly requirements. The BMs or its dummies are to be assembled to populated flex v3.2. Backside flatness is only required on the pickup tool itself, one Si dummy assembly and one real module.

For the assembly, in case the common tooling is used[26], the sites only need to state the spatula swiping duration and the glue gap. Additional information is required regarding masking of the HV hole, before-assembly cleaning of components, after-assembly cleaning of tooling and stencil, glue mixing method, time between glue mixing and deposition, curing time, and the temperature, RH, and vacuum pressure.

[26] Japan uses a designated tooling that has both assembly and cell loading functionality, and Oxford uses a setup with a machine with automated glue distribution functionality.

In Göttingen, the cleaning of components before assembly includes only blowing away dust using dry air. For example, for Si dummies that have only been handled with a clean vacuum pen. This is to avoid scratches from wiping with tissue+isopropanol. Some flexes were cleaned with isopropanol after trial gluing. The vacuum pressure to fix the components on the chucks is -0.9 bar. Glue is mixed in the glue gun nozzle, and takes only a few minutes before being distributed to the flex and glued. The duration used to pull the spatula for glue distribution is around 10 s, and the curing time is larger than 8 h. Cleaning of tooling parts and stencil after assembly: wipe repeatedly with isopropanol, until visibly no trace of glue left. The temperature in the lab is around 20 to 25 °C, and RH is 30 to 40 %.

HV Hole Masking

To prevent glue seepage into the HV hole, pre-cut circular kapton tape pieces were provided to mask the HV hole. When setting the glue gap, the dial gauge is zeroed without kapton tape, and then the flex is taken out to apply the kapton tape mask. This is to not let the thickness of the kapton tape affect the glue gap setting. The estimated uncertainty on the glue gap from removing and putting back the flex is $\sim 1\,\mu m$, which is smaller than the influence of kapton tape on the glue thickness.

Figure 8.27: Circular kapton tape for HV hole safety.

Post-assembly Metrology, Mass, and Visual Inspection

For the glued module ***xy*-alignment** measurement, there are three methods: one nominal method and two alternatives. In case an alternative method is used, the reason should be justified.

- Nominal method: measure the distances in the x- and y-directions between the fiducial marks on the flex and the Si dummy or BM, and compare to the nominal distances, which are shown in figure 8.5.
- Alternative 1: find the Si dummy centre and flex centre defined by the intersection point of the diagonals, and the xy-alignment is the difference between the centres.
- Alternative 2: measure the distances between the flex and Si edges on the top right and bottom left and compare with the nominal values.

The **thickness** measurement of the glued module is the same as that for the flex.

The **mass** of the assembled module is measured. Together with the mass from component reception measurement, the amount of glue can be extracted. The glue mass, in combination with the thickness, provides an estimation of the glue coverage, and therefore the structural integrity of the assembly.

VI includes checking for glue seepage at the HV hole and at edges that could hinder wire-bonding.

Wire Bonding

Wire bonding[27] is needed on the flex–Si dummy assemblies and real module assemblies, to obtain fully functioning modules. For SQ, the bonding machine, wedge tool, wire, and pull tester should be described. The required information related to the bonding machine includes stage range, accuracy, repeatability, autofocus ability, ultrasonic generator, and bonding head. Other required information is the cleaning method, wire-bonding program with detailed parameters on ultrasonic time and power, the bond and touchdown force, and the bonding strategy (workflow).

After wire-bonding, quality control tests like VI, loop heights for OB modules, and pull tests are done to ensure the quality. VI is for checking touching or crossing wires and the width and length of the wire bond foot. The width should be 1.2 to 2 times the diameter of the wire, and the length should be 1.5 to 3 times. For OB modules, metrology should be done to measure the wire loop height. The requirement is that the highest point of the wire-bonds should be 750 µm or less from the flex. For the recommended wires for this measurement, please refer to [178].

There are also recommended wires for the pull test. For flex-Si dummy assemblies, pull at least 32 wires. The required measurements are the break force and type (heel break, lift off, or wire break). The break force should be 8 g on average with std dev 15%, and minimum 5 g. For break type, heel breaks should account for minimum 90 %.

Göttingen has been doing joint assembly with Bonn while a new F&K Delvotec M17S wire-bonding machine and Nordson Stellar 4000 bond tester were pending arrival. The machines have arrived and personnels were trained, to carry out the work for the rest of the pre-production and production. See figure 8.28(b) for a photo of the bond tester.

(a) Micro·VU automatic metrology machine. (b) Nordson Test&Inspection Stellar 4000 bondtester.

Figure 8.28: New machines for pre-production and production.

[27] Bonding map: https://twiki.cern.ch/twiki/pub/Atlas/ITKPixelModuleAssemblyITkPixV1/ITkPix_v3-2_BondingMap_v2023-02-15a.pdf

Backside Flatness

Backside flatness is measured on the four FEs while the module is being held from the pick-up areas in the front. The peak-to-valley flatness[28] should be within 50 µm (±25 µm).

The backside flatness tool, also called the quad metrology handling tool [195], consists of a pickup base and a pickup body. The base fixes the sample under vacuum, and aligns it via three dowel pins. The pickup body consists of four suction cups to pick up the sample, and turns the sample upside down to show the back side (FE side in the case of a BM) for flatness measurement.

The surfaces on the pickup body that supports the sample need to be measured for flatness and parallelism, so that they can be used to measure the flatness of the samples with good accuracy. Then, measurements of a Si dummy and a real module are required.

Göttingen received the centrally distributed backside flatness tool, and is preparing for measurements.

8.6. Results for Site Qualification and Pre-production Module Assembly

8.6.1. Metrology and Mass

Precision – Repeated Measurements of Metrology and Mass

Repeated measurements of one flex were performed for precision estimation, the results are shown in figure 8.29.

The metrology points used to calculate the X and Y dimensions were measured on the top green layer of the flex, instead of the outer edges defined by the black lines, as shown in figure 8.24. As a result, the measured dimensions are smaller than the actual sizes: the measured flex width and length are, on average, 207 µm and 187 µm less than nominal, respectively, with a std dev of only 1–2 µm. Repetitions of pick-up area thickness show an average of 209 µm, with a larger std dev of 5 µm. The mass measurements are very precise, with a std dev of only 0.1 mg.

Metrology of Flex v3.2

16 flex v3.2 were measured, the X and Y dimensions are illustrated in figure 8.30. Compared to the specifications[29], seven flexes are too small in X, and six are small in Y.

[28] The "peak to valley" flatness refers to the maximum – minimum heights, and is a conservative measurement for the worst scenario.

[29] $X = 39.60^{+0.10}_{-0.10}$ and $Y = 40.60^{+0.10}_{-0.10}$, as summarised in table 8.1.

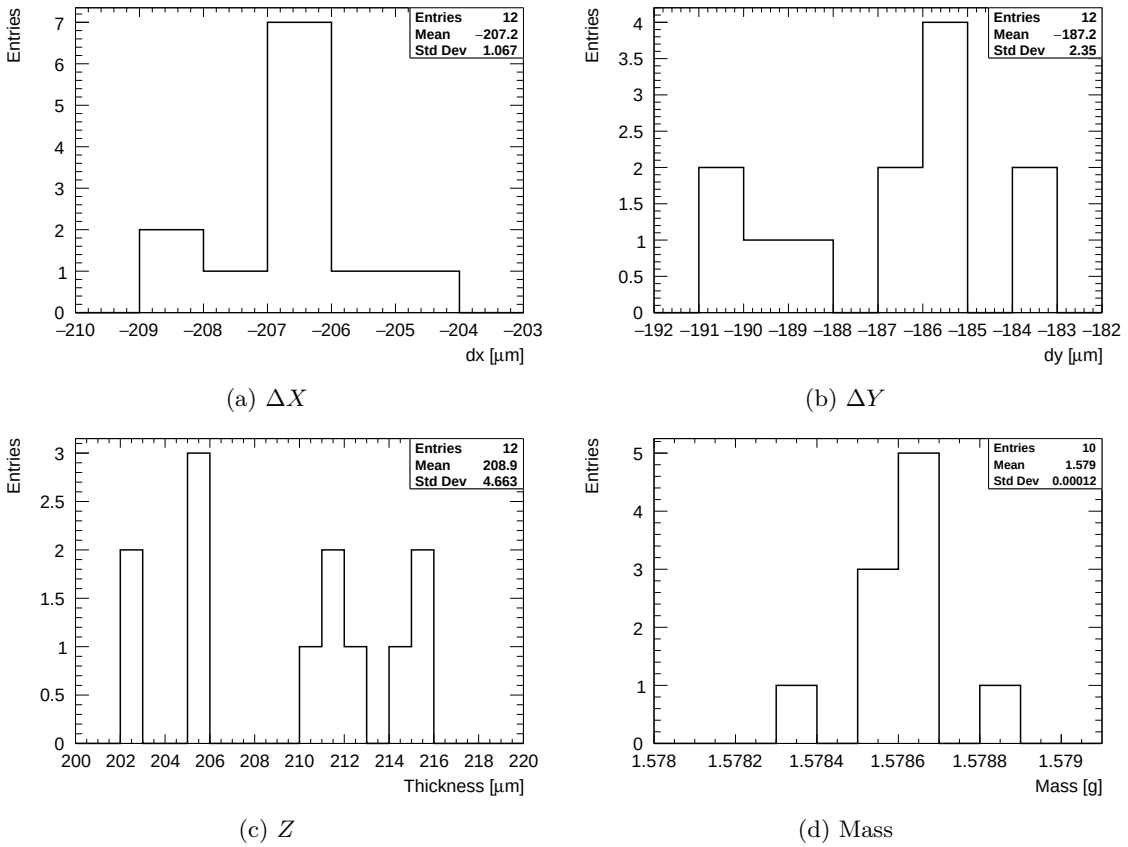

(a) ΔX (b) ΔY

(c) Z (d) Mass

Figure 8.29: Histograms of repeated measurements on flex0338. ΔX and ΔY are the differences between the measured X and Y dimensions and the nominal. Z is the pick-up area thickness.

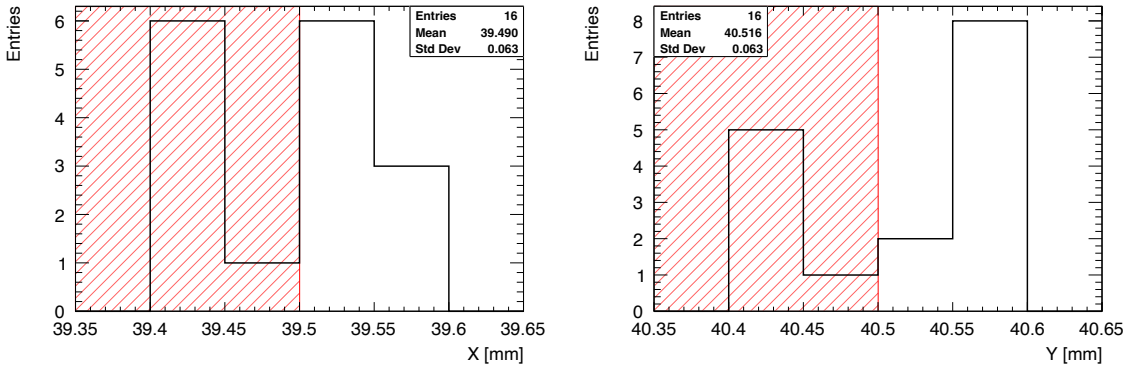

(a) X (b) Y

Figure 8.30: X and Y dimensions of 16 flexes. The areas marked in red are out of specification.

Metrology of Si Dummy

Three Si dummies were measured, the results and the corresponding specifications (which are the same as those for BMs) are presented in table 8.12. The specifications are met.

	Specification	Si1	Si2	Si3	Si4
Si X [mm]	$42.187^{+0.07}_{0}$	42.234	42.232	42.231	42.231
Si Y [mm]	$41.10^{+0.05}_{0}$	41.143	41.142	41.138	41.138
Si Z [µm]	325^{+90}_{-40}	315	309	311	309
Mass [mg]		1265.7	1254.4	1265.3	1252.6

Table 8.12: Metrology and mass for Si dummies. The specification values are the same as for FE X, sensor Y, and module Z. All Si dimensions are in specification.

Metrology of Bare Module

16 quad BMs named Q6 to Q22 were received, measured, and assembled. The numbering continued from previous assembly activities conducted before the SQ. Nine BMs (Q6–14) arrived in one batch, and the remaining arrived in a separate batch. All BMs are equipped with HPK 150 µm sensors, and their metrology and mass results are presented in table 8.13.

		Spec	Q9	Q10	Q8	Q7	Q6	Q11	Q12	Q13	Q14
Sensor X		$39.50^{+0.05}_{0}$	39.518	39.465	39.522	39.507	39.524	39.499	39.505	39.480	39.498
Sensor Y		$41.10^{+0.05}_{0}$	41.102	41.069	41.130	41.119	41.111	41.123	41.116	41.114	41.112
FE X		$42.187^{+0.07}_{0}$	42.190	42.187	42.198	42.194	42.195	42.208	42.198	42.200	42.208
FE Y		$40.255^{+0.07}_{0}$	40.284	40.271	40.283	40.286	40.283	40.301	40.302	40.288	40.284
BM Z	Avg	325^{+90}_{-40}	331	326	332	338	362	344	350	341	349
	Std		8	10	7	10	9	7	8	11	40
FE Z	Avg	150^{+25}_{-10}	162	155	154	159	188	173	175	163	161
	Std		12	13	10	11	11	6	13	12	13
Mass			1251.9	1250.9	1249.9	1252.0	1251.2	1263.3	1266.1	1266.0	1261.4

Table 8.13: Metrology and mass for BM 6 to 14. The order listed is the same as the order of gluing, except for Q14, which was not assembled due to problems with the top left corner. Units: X, Y dimensions in mm, thicknesses in µm, mass in mg. The out-of-specification parameters are marked with a different colour.

The sensor X is too small for four BMs, Q10 is too small in sensor Y, and the FEs of BM6 is thicker than required. In pre-production, due to the need for various investigations, all components are assembled, even if they are out of specifications. However, for Q14, the point measured at the top left corner of the sensor is about 100 µm higher than usual, which would hinder glue gap adjustment and was therefore not assembled.

8.6.2. Visual Inspection

VI photos were taken with a camera[30] and the defects were checked under the microscope. For all BMs, VI shows rough sensor edge, dot-like contamination, random scratches, FE bond pad contamination, and poor dicing on some edges. Example photos of the bad

[30] Camera parameters: manual focus, aperture=10, iso=400, exposure compensation 0 for flex, and -1 to -2 for the backsides of Si dummies and the FE side of BMs (not required for SQ), wait time 2 s.

		Q15	Q16	Q17	Q18	Q19	Q20	Q21	Q22
Sensor X		39.524	39.518	39.524	39.523	39.528	39.526	39.525	39.520
Sensor Y		41.133	41.136	41.124	41.132	41.136	41.135	41.135	41.134
FE X		42.220	42.218	42.217	42.216	42.217	42.217	42.217	42.218
FE Y		40.316	40.307	40.299	40.318	40.308	40.300	40.310	40.304
BM Z	Avg	330	324	326	317	327	332	328	328
	Std	5	5	3	5	5	8	4	3
FE Z	Avg	158	152	154	154	155	161	159	155
	Std	2	1	3	3	2	3	2	2
Mass [mg]		1269.9	1265.8	1263.8	1262.6	1262.0	1265.7	1263.5	1260.0

Table 8.14: Metrology and mass for BM 15-22. The X and Y dimensions are in mm and Z thicknesses in µm.

scenarios are shown in figure 8.31. For Si dummies, the defects are mainly scratches on surfaces and pads. An example photo of a Si dummy is shown in figure 8.23(b), and photos of defects are in appendix B.3.

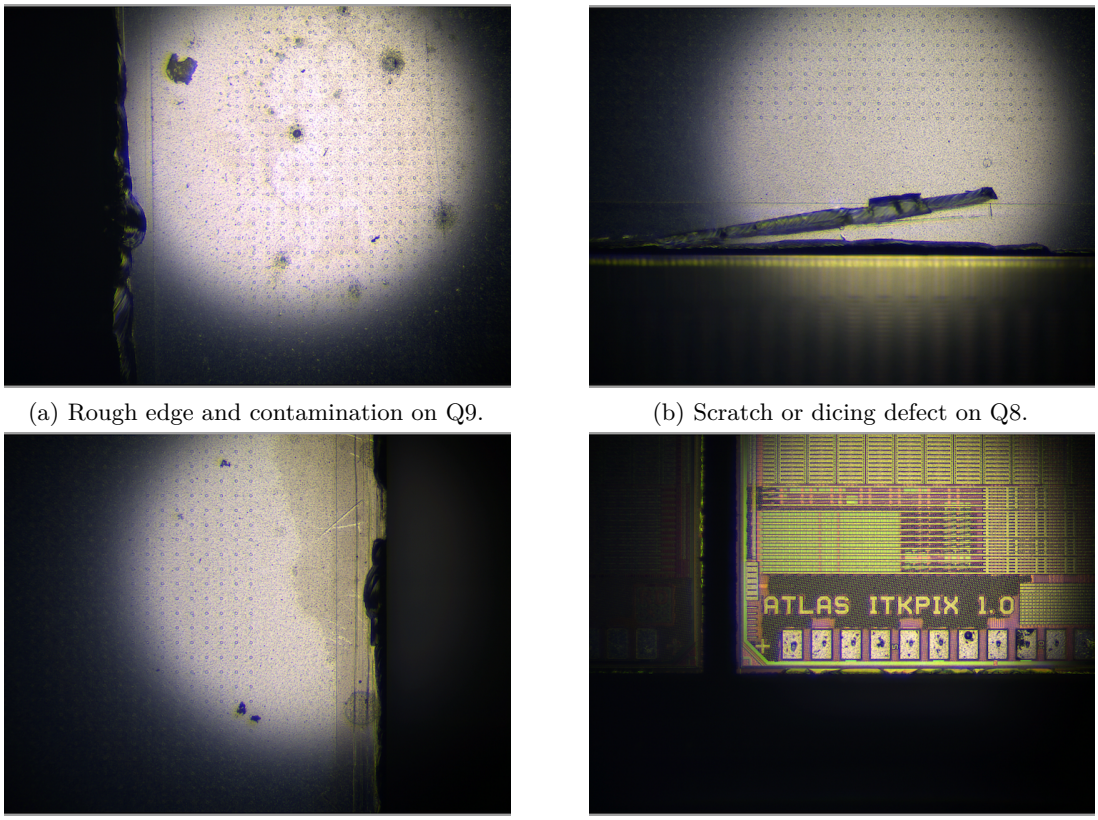

(a) Rough edge and contamination on Q9.

(b) Scratch or dicing defect on Q8.

(c) Contamination on Q7.

(d) Poor dicing and contaminated pad on Q10.

Figure 8.31: Example of defects found in BM VI.

8.6.3. BM *IV*

CV curves are not required for SQ, but were measured on a few BMs to check the V_{dep} level and compare to the values from the pre-production sensor QA results. See figure 8.32 for the $\frac{1}{C^2}$ vs reverse bias voltage curves, and the corresponding *CV* plot is in appendix B.4.

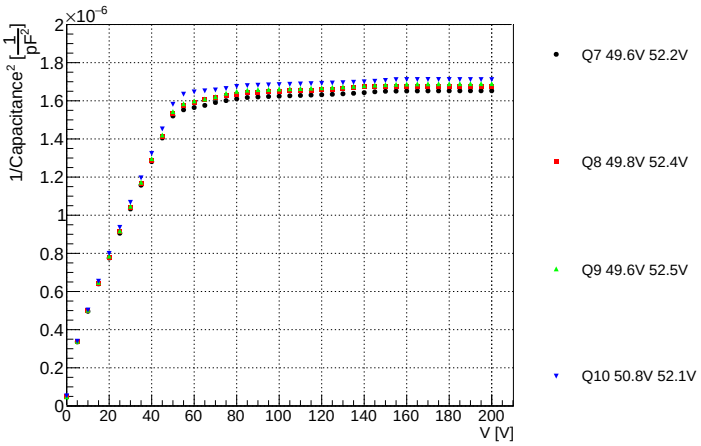

Figure 8.32: $\frac{1}{C^2}$ vs reverse bias voltage for BM 7 to 10.

The BMs are equipped with HPK sensors, but the results show no obvious edge effect as observed on the diodes, which is presented in section 6.1.5. The reason is attributed to the area of quad sensors being larger than that of diodes. The curves have a slightly larger slope close to the turning point, therefore, two fits were done for the regions close and further away from the turning point. The results are labeled in the legend. The average V_{dep} is 51 ± 0.5 V (both fits included), slightly lower than the diode results from section 6.1.5 (58 ± 5 V).

IV curves are shown in figure 8.33. The leakage current for Q12, 17, 18, and 19 is out of specification, and Q10 and 14 show soft breakdown. As Q17, 18, and 19 were already marked with sensor cut failure before being sent to Göttingen, their bad electrical performance is expected.

8.6.4. Glue Mass Stability

Using stencil v8, 12 glue distribution trials and assemblies (2 out of 12 were performed by a different operator) give an average glue mass of 65.3 mg, with std dev 1.8 mg (2.8% of the average). The average glue mass is much lower than that for a previous trial mentioned in figure 8.19, which is around 78 mg.

This is mainly due to a new spatula being used after the old one was damaged in an accident. As mentioned before, the spatula size, which is defined as the distance between bottom surface that touches the stencil and the ball bearing axis, affects the glue mass. Test results from RD53A flex and stencil RD53A v2 (a much simpler situation due to the even backside of the flex) showed that 0.1 mm difference in spatula sizes resulted in the glue

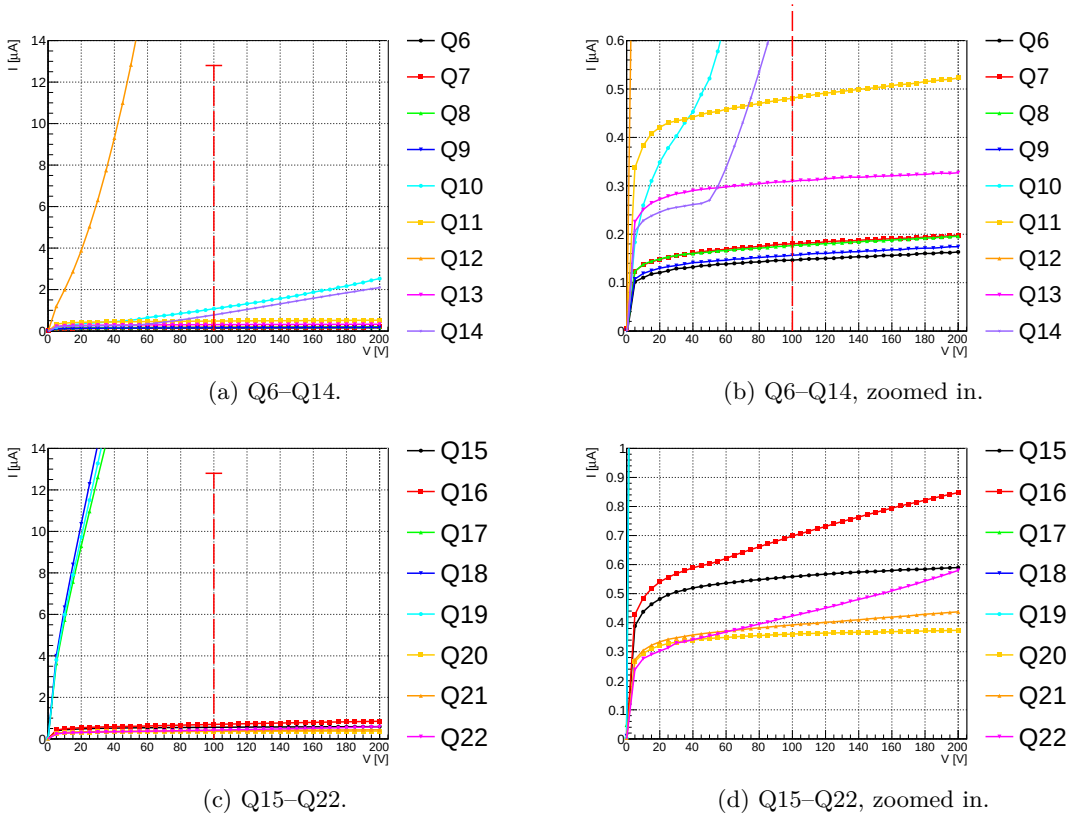

(a) Q6–Q14.

(b) Q6–Q14, zoomed in.

(c) Q15–Q22.

(d) Q15–Q22, zoomed in.

Figure 8.33: BM *IV* for Q6 to Q22 shown in two ranges.

mass changing from 45.5 mg (std dev 2.7 mg – 5.9 %) to 43.6 mg (std dev 0.2 mg – 0.5 %). The size of the new spatula was measured to be 11.85 mm, which is within the designed dimension of $11.8 + 0.05$ mm. Thus the new glue mass results are the expected value for a standard sized spatula. However, it is possible that the manufacturing tolerance of 0.05 mm is big enough to impact the glue mass. Therefore, in the rest of the pre-production, special attention will be paid on gluing tests with different spatulas from different sites. Another possible reason is the stencil: the previous stencil was produced by a different vendor with a different surface treatment.

8.6.5. Glue Coverage

Two flex + glass dummies were assembled, with target glue gaps 30 µm and 35 µm. The glue patterns and coverages are shown in figure 8.34.

Flex0308+glass 5 was glued before kapton tape became a common practice, and the operator wiped away two glue dots around the HV hole to prevent glue seepage (which still occurred). Therefore, this sample has a lower glue mass.

The coverage of the two samples is similar, despite the different target glue gaps. After comparing all thickness measurements (as presented in section 8.6.8), it became evident that the glue thickness of flex0308 + glass5 is comparable to that of the other samples with

(a) Flex0308+glass5, 30 µm target gap, 63.7 mg glue, 69% coverage.

(b) Flex0306+glass7, 35 µm target gap, 65.6 mg glue, 68% coverage.

Figure 8.34: Glue pattern and coverage for two flex+glass dummy samples.

a 35 µm target. This unintended outcome is likely due to mistake in the gluing procedure.

During trial gluing tests, a difference in glue patterns before and after complete curing was observed. The patterns from two trials cured for < 30 min, with glue gap set to 35 µm, are shown in figure 8.35. The un-cured glue dots have rounder edges, while the fully-cured

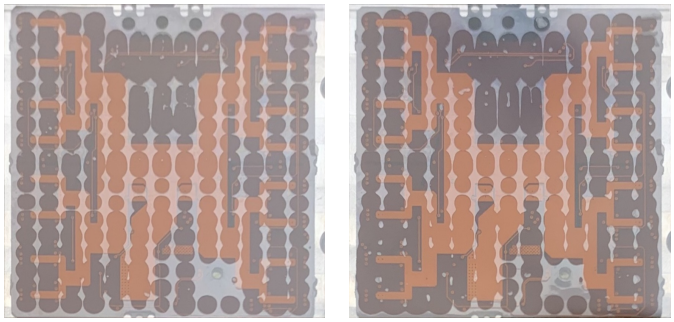

Figure 8.35: Glue pattern without curing. Two trials both show rounder glue dots compared to the glue pattern from cured samples.

patterns are deformed. The reason could be glue shrinkage after curing, which can be affected by surface tension, and therefore is dependent on the material of the components. For this reason, it is uncertain how well the glue coverage from glass dummies reflects the actual coverage of flex + BM assemblies. Further tests can be conducted using X-ray to investigate the glue pattern of flex + Si dummy and real modules.

The coverage is less than the 80% reached in the test shown in figure 8.19, which was obtained under different testing parameters: unloaded flex was used, the target thickness was smaller, the glue mass was larger, and the flex jig cutout was also smaller.

In the past, 30 µm target thickness have been used. In SQ, 35 µm was initially chosen for safety reason – avoiding glue seepage – and was kept for the rest of the assemblies to obtain more statistics on the consistency of the glue gap. The flex jig cutout change due to clashing SMD components on the flex resulted in larger cutouts to allow larger tolerances, which results in less compression around the bigger cutout areas, especially around the connectors. Therefore, the coverage from these tests is lower than before.

8.6.6. Post-assembly Visual Inspection

Example VI photos of flex + Si dummies and their defects are shown in figure 8.36. No

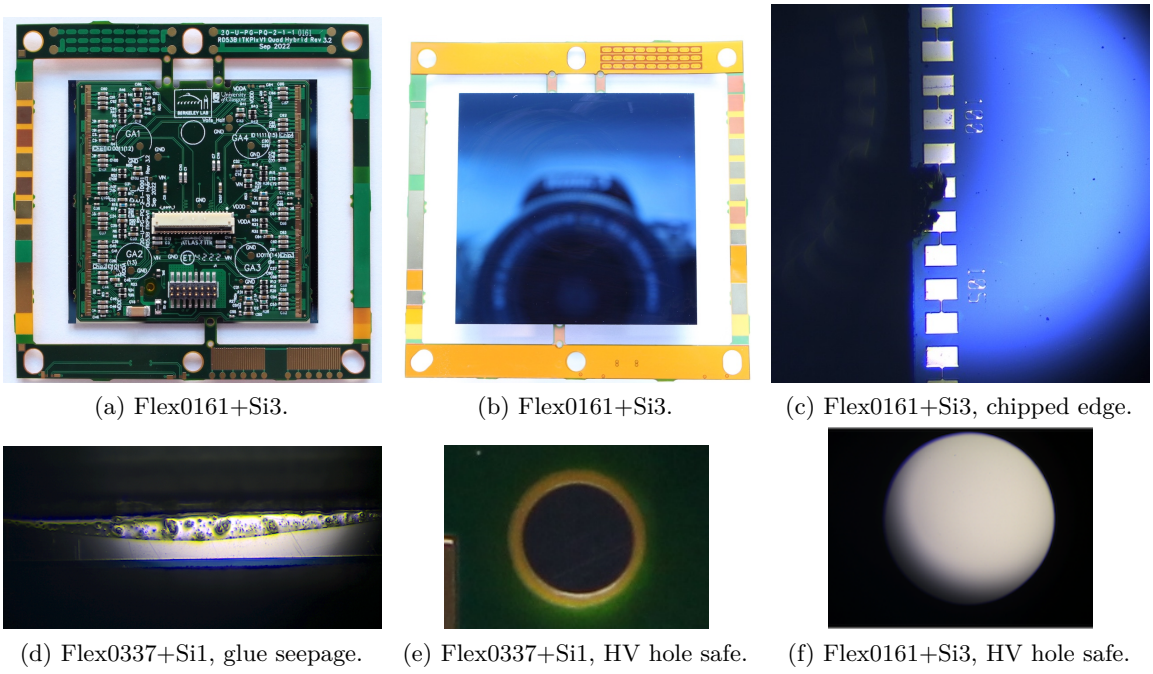

(a) Flex0161+Si3. (b) Flex0161+Si3. (c) Flex0161+Si3, chipped edge.

(d) Flex0337+Si1, glue seepage. (e) Flex0337+Si1, HV hole safe. (f) Flex0161+Si3, HV hole safe.

Figure 8.36: Photos showing both sides of the glued sample flex0161+Si3, chipped edge (can be prevented by more careful handling), glue seepage at the bottom of flex0337+Si1, and HV hole safety.

glue seepage was observed at the HV hole, but seepage at the bottom edge was observed for flex0337+Si1 due to a smaller glue gap. The seepage is not on wire-bonding edges and therefore does not hinder wire-bonding, and does not exceed the Si edge.

8.6.7. *xy*-alignment

xy-alignment was measured on four $flex + Si$ samples. Similar to the analysis performed in section 8.4.5, the Si left edge is defined as 90°, and the *xy*-alignment ΔX and ΔY are calculated by subtracting the nominal distance differences between fiducial marks from the measured values: $\Delta X = X_{\text{meas}} - X_{\text{nominal}}$. The nominal distances as mentioned in section 8.1.2 are $X_{\text{nominal}}, Y_{\text{nominal}} = 2212, 750$ [µm]. Results are summarised in table 8.15, and are within the required specification of 100 µm.

	Flex0337 + Si1	Flex0339 + Si2	Flex0161 + Si3	Flex0162 + Si4
Top left [µm]	-69, 17	58, -26	58, -84	23, -18
Bottom right [µm]	93, -28	-27, 4	-38, 58	-17, 14

Table 8.15: *xy*-alignment results ΔX, ΔY from two pairs of fiducial marks on the top left and bottom right.

8.6.8. Thickness

Four more flex+Si assemblies were glued, and the thickness and mass results are summarised in table 8.16.

	F308+G5	F306+G7	F337+Si1	F339+Si2	F161+Si3	F162+Si4
Target	30	35	32	35	35	35
Cured	28	32.5	29	32.5	32.5	31.5
Pick-up (screw gauge)	656	656	567	570	574	569
Glue (screw gauge)	45	45	36	42	43	42
Pick-up (microscope)	636	644	557	556	558	553
Glue (microscope)	38	47	33	45	49	42
SMD	–	–	2153	2319	2345	2224
Connector	–	–	1881	1954	1946	1960
Mass [g]	3.3298	3.3195	2.9083	2.9065	2.8969	2.8873
Glue [mg]	63.7	65.6	64.9	66.6	63.2	62.9

Table 8.16: Average thickness and mass results of all glued flex + glass or Si dummy samples. All thicknesses are in µm. "Target" and "Cured" are readings of the dial gauge on the Tooling V2: the adjusted target glue gap, and the number shown after curing.

Flex0337 + Si1 was glued without kapton, and 4 glue dots around the HV hole were wiped away before gluing, to avoid glue seepage into the HV hole. The other three Si samples were glued with kapton. As mentioned before, after curing, the dial gauge reading decreases by 2 to 3 µm. This is due to mechanical tolerances of the tooling.

Results show that the thicknesses measured using the screw gauge are higher than that using the microscope. The calculated glue thicknesses from microscope measurements vary more due to lower precision from focusing: as mentioned before, repeatedly measuring the thickness of one point on the chuck gives a std dev of 5 µm, with the difference between the maximum and the minimum values Δ being 22 µm. This measurement is repeated on glass, and the std dev is 7 µm with $\Delta = 21$ µm. Therefore, the precision of the thickness measurements with the micrometer screw gauge is better than that of the microscope.

Four of the samples (one glass, three Si) are glued with dial gauge target glue gap 35 µm, and the glue thickness results are consistent with each other. Flex0337 + Si1 was glued with 32 µm target, and the measured glue thickness is indeed smaller. However, flex308 + glass5, which was glued with a target thickness of 30 µm, has a similar glue thickness compared with the ones with 35 µm target, showing that this sample was subject to human error.

The thicknesses of power connector and HV capacitors are within specification. These thicknesses are, as required by SQ, defined as the average of all the measured points, instead of the maximum as defined in section 8.4.6.

8.6.9. Pre-production Module Assembly

In pre-production, up to the point of this thesis, Göttingen assembled 15 modules. The flex and BM reception test results are presented in the previous subsections, and the post assembly results are shown below.

The glued module pick-up area, power connector body, and HV capacitor thickness, as well as the xy-alignment, glue mass, and thickness results are shown in table 8.17. An example VI photo of Q11 + flex0096 after wire-bonding is shown in figure 4.10(a).

	Z_{avg}	Z_{std}	Z_{con}	Z_{SMD}	ΔX_{TL}	ΔY_{TL}	ΔX_{BR}	ΔY_{BR}	m_{glue}	Z_{glue}
Q9+F0513	599	8	1965	2352	13	22	-60	9	65.4	67
Q10+F0051	578	4	1927	2340	29	-29	-22	17	65.6	21
Q8+F0456	606	10	1980	2362	-56	-60	48	58	66.6	59
Q7+F0058	601	5	1950	2353	-45	2	66	-50	63.8	41
Q6+F0094	585	5	1902	2386	2	-125	-11	125	62.3	1
Q11+F0096	586	4	1920	2333	7	-75	46	15	62.4	-6
Q12+F0081	581	8	1948	2334	35	-31	-64	53	63.4	-1
Q13+F0169	587	7	1924	2351	-69	-49	89	16	61.3	25
Q15+F0171	581	3	1908	2335	28	-11	-59	43	62.3	52
Q16+F0168	569	1	1960	2229	-11	-32	36	-2	65.2	42
Q17+F0467	567	3	1913	2332	49	-218	309	-136	61.6	41
Q18+F0103	564	3	1961	2330	-74	-54	83	49	63.9	34
Q19+F0104	570	2	1976	2248	-50	-87	76	63	61.5	40
Q20+F0165	569	3	1954	2245	-45	-84	-1	105	63.3	32
Q21+F0166	570	3	1961	2226	39	-44	-54	45	63.9	36
Q22+F0167	572	1	1940	2204	-43	-64	43	49	66.3	41

Table 8.17: Assembled module metrology ([µm]), alignment ([µm]), glue mass ([mg]), and glue thickness ([µm]) results. The results that are out of specifications are coloured. Some glue gap values are unusually low or even negative due to residual glue from a sticker at the back of the flex not being cleaned before metrology, but cleaned right before assembly. The glue gaps for samples that are possibly subject to this are marked in grey.

The target glue gap is 35 µm, and the average measured glue mass is 63.7 µm with std dev 1.7 µm (2.7 % of the average). None of the samples had glue seepage. Some of the measured glue gaps are unphysical or deviate largely from the target, the reason is attributed to that some flexes came with a sticker at the backside, which must be peeled off before assembly. If the residual glue was not cleaned before flex metrology but was cleaned just before assembly, the measured flex thickness can be higher due to residual glue, and the calculated glue thickness is lower. If the residual glue is not cleaned, it could cause further contamination, leading to effectively a larger glue gap. This issue can be resolved by cleaning the residual glue before flex metrology. The sticker on the later batch of flexes is on the frame, and therefore no longer affect the thickness measurement, target glue gap setting, and the calculated glue thickness. These are flex 0103, 0104, 0165, 0166, 0167, and 0168, and the corresponding glue thickness results are 34, 40, 32, 36, 41, and 42, consistent with the target within the precision provided by the microscope. No screw gauge measurement was conducted, to avoid damages to the BM.

The xy-alignment of 3 out of 15 modules are out of specification, as marked in colour. The glued module thicknesses at the power connector body and HV capacitor are within the required limit.

8.7. Conclusions and Outlook

To assemble 10855 quad modules for the ITk pixel detector[31], the ITk Pixel Quad Assembly Tooling V2 was developed, and the performance was evaluated. The relevant conclusions and outlook are summarised in section 8.4.7.

For the ongoing Site Qualification, SQ documents regarding module assembly were released, and assembly sites are being qualified according to the requirements. Pre-production modules were assembled.

Reception tests for components include metrology, mass, VI, and BM *IV*. Post-assembly measurements include glue mass, glue coverage, xy-alignment, and various thicknesses. Assembly of glass, Si dummies and BMs were performed, and the reception and post-assembly results were presented. Göttingen passed all SQ sub-blocks until wire-bonding, the new wire-bonding machine and pull tester have arrived and will be used for the rest of pre-production and production. Precision of metrology was estimated via flex X, Y and Z measurements, with std dev of 1, 2, and 5 µm, respectively, indicating large spread for thickness measurements. Mass measurements have a very small spread of 0.1mg. A new automatic metrology machine was purchased and is being used for tooling calibration, and will be providing faster and more precise assembly for the rest of pre-production and production. Backside flatness measurement is in preparation.

16 flexes and 17 BMs were measured for SQ and module pre-production. BM Q10, 11, 13 and 14 have slightly smaller sensors, and the FE thickness of Q6 is larger than in the specification. Q14 has a sensor corner that is around 100 µm higher, and is therefore not assembled. The leakage currents for Q12, 17, 18 and 19 are out of specification, and Q10 and 14 have elevated *IV* curves indicating a soft breakdown.

In total, 16 modules were assembled. Stencil v8 used in pre-production, in combination with the stencil tool in Tooling V2, leaves on average 65.3 mg glue with 2.8% std dev. Results from different sites should be studied, to determine the glue mass stability with different units of tooling and operator. The glue mass combined with 35 µm target glue gap gave around 68 % glue coverage. Kapton tape was used to mask the HV hole to avoid glue seepage, and a procedure was decided to avoid this hindering the glue gap adjustment. However, the coverage from cured flex+glass dummy may differ from the real coverage of flex+BM. X-ray studies could be done to determine the real coverage of the assembled modules, and a collective decision can be made on a different target glue gap. The thicknesses of glued samples on the power connector body and HV capacitor are within specifications. The glue thickness precision is restricted by the metrology equipment, and the measurements for some

[31] Taking the yield into account.

samples were interfered due to stickers put on the flex backside. The glue thickness for the un-affected samples are consistent with the target within uncertainty. The xy-alignment for 13 out of 16 glued samples are within specifications. For the out-of-spec samples, metrology measurements can be done on the components to investigate the relative positions between fiducial marks and the reference points used by the tooling, to determine the exact reason.

Results from all assembly sites are required to be uploaded to the PDB, enabling further studies with higher statistics on all module assembly results obtained by different assembly sites, to support decisions for production. After assembly, modules go through full electrical tests to check their functionalities. Three of the assembled modules were tested at Göttingen, the tests and results are discussed in chapter 9.

CHAPTER 9

Module Testing

After full assembly, modules undergo quality control (QC) tests, to ensure that they meet the electrical specifications and therefore can perform the required functions in the detector. The QC tests check the functionality of both the analog and digital part of the FE chips, bump-bond quality, sensor, and wire-bonds.

Pre-production modules are with FE chip version ITkPixV1.1, and production modules with ITkPixV2, both are subject to the same module QC tests, but the exact values of the requirements are different. The specifications for production will be determined by the pre-production results[1]. The defects and noise of pre-production modules will also provide experience for re-defining the wafer-probing criterion for grading chips as good.

From the RD53A experience, as described in ref. [3], it was clear that uniform testing procedures, proper ordering of the tests, proper book-keeping, and systematical analysis of the testing results are crucial for avoiding influence from the operator and the setup, allowing comparability between modules and the same modules in different production stages, and to correctly judge and classify faulty pixels and modules. Therefore, software (SW) tools for performing tests, analysing the results, and databases for keeping and sharing results were developed, and common testing procedures were defined.

The testing sites also undergo site qualification (SQ) to show their capability and capability of performing QC tests with comparable setups and the central testing tools and procedures. As mentioned in chapter 7, regarding module testing there are three SQ blocks: Testing Setup, Digital Module Tests, and Stage 2 Full QC.

[1] For example, the effective resistance of the chips and the offset voltage are determined by components on the bare module (BM), and the optimal values for these components are investigated via simulation. Pre-production results can be used as inputs of the simulation, and help determining the values of the components on production modules.

This chapter describes the ITkPixV1.1 module QC procedure, testing setup, and the testing results for three modules assembled at Göttingen.

9.1. Module Quality Control Tests

Full QC includes electrical QC tests (warm and cold), thermal stress test (thermal cycling), and long term stability test. After full QC, modules go to cell loading and loaded local support production sites, as introduced in section 7.1.1.

Most electrical QC tests can be performed using digital modules, which are modules without a sensor. They are built faster than real modules, and thus can be used for qualifying set-ups and validating test procedures. But they cannot be used for tests related to bump-bond quality: disconnected bump scan, source scan, and thermal stress test.

Module QC includes a comprehensive set of electrical tests, which are performed twice at different temperatures. They are referred to as the "warm test" and the "cold test", being carried out at room temperature and $-15\,^{\circ}\mathrm{C}$[2], respectively.

Warm test is easier to execute, and therefore is performed first, to catch problems early. If a module fails the warm test, the testing of this module will not proceed to the following stages. In subsequent steps like cell loading, cell integration, and loaded local support reception tests, a selection of warm tests are also conducted. Performing all the warm tests at module QC allows checking and comparing of the results in the later steps.

Cold test then test the modules at the operation temperature.

9.1.1. Testing Flow

After a module is assembled, it needs to be registered and virtually assembled at the PDB from the BM, flex and carrier[3]. Each child component has a serial number (SN), and the SN of the newly assembled module is determined by the module type and the flex SN.

For electrical tests, various database and SW tools are developed and used, as mentioned in section 7.3. Before starting the tests, previous information of the module should be pulled to LocalDB, and the correct stage of the module should be set in DB, so that the test results are associated with the correct testing stage. After the procedures in the corresponding stage are finished, the stage is signed off, and incremented to the next stage for the next set of tests. The module stages reflect the production flow shown in figure 7.1:

- Assembly
- Wire-bonding
- Initial Warm, Initial Cold
- Parylene Coating

[2] $-15\,^{\circ}\mathrm{C}$ for quads, $-25\,^{\circ}\mathrm{C}$ for triplets.

[3] In the PDB, these are the sub-components of a module. And the sub-components of a BM are one sensor tile, and four FEs.

- Post-Parylene Warm, Post-Parylene Cold
- Wire-bond Protection
- Thermal Cycles
- Long Term Stability Test
- Final Warm, Final Cold

Majority of electrical tests are for FE chips. The functionalities of an FE – hence a large part of the module behaviour – is controlled by the configuration file. This section introduces the testing flow of the full QC, firstly introducing the config files for the FE chips.

9.1.2. FE Chip Config File

The FE chip config files are used throughout testing. They are generated or pulled from the PDB. The first electrical test stage is the initial warm stage. At this stage, if the module has not gone through electrical test before (e.g. from another site for cross-check), the starting point of the config file is from wafer probing results. After electrical tests are performed, some test results update the chip configs, and the new version of the config file is updated in the database.

There are three different sets of chip configs: warm, cold, and low power mode, each used for the corresponding tests. For example, the warm and cold test config files differ in ADC calibration and tuning.

The config files are in `json` format, and consist of three parts:

- `GlobalConfig`: contains 200 global parameters (or called registers).
- `Parameter`: these are external parameters like temperature calibration.
- `PixelConfig`: contains parameters for each individual pixel on the chip. Like pixel enable, hit bus, injection enable, and the trim value for tuning[4].

They are stored in PDB, LocalDB and the local data acquisition (DAQ) machine (DAQ host). At the DAQ host, the tester can generate or pull the chip configs by interacting with PDB. The tests and corresponding chip config changes are submitted to LocalDB, and the representative ones selected by the tester will be submitted to PDB, which can then be seen/used by other sites, to achieve consistent testing and proper book-keeping.

9.1.3. List of Tests

The non-electrical tests like metrology, VI, mass are performed in assembly, and is uploaded to LocalDB and PDB. The electrical tests are listed below.

- First Power-up
- Module *IV*
- E-fuses

[4]This register is referred to as TDAC – Threshold Digital to Analog Converter or Trimming Digital to Analog Converter. The global register for tuning is GDAC (Global DAC).

- Simple Electrical Tests:
  - **ADC Calibration**
  - **Analog Readback**
  - SLDO Qualification
  - **Vcal Calibration**
  - **Injection Capacitance**
  - Low Power Mode (LP Mode)
  - Overvoltage Protection (OVP)
  - Undershunt Protection (USP)
  - Data Transmission
- Pixel Performance Tests[5]:
  - Minimum Health Test
  - Tuning
  - Pixel Failure Analysis

Each pixel performance test includes a series of YARR scans. The simple electrical tests marked in bold are the calibration measurements, and – together with tuning – are used to update the chip config files. In addition, there are thermal cycling and long term stability test. The details of all the tests are introduced in section 9.2.

9.2. Tests and Scans

This section introduces all the tests in full QC, zooming into each simple electrical test, and various scans in the pixel performance tests. For more details about the criteria, please refer to [191, 196].

9.2.1. First Power-up

This is the first test, it checks if the module is powered correctly and has minimal functionality. For the first power-up, put the module in the setup, and power up the module with the low voltage (LV) power supply in constant current mode. The total input current I_{in} depends on the type of modules. This is because the modules in the inner layers are closer to the interaction point, where there is a larger number of hits in a smaller area compared to the outer layers. As a result, the inner layer modules require a larger bandwidth for the readout. More readout links result in larger current consumption, leading to the need of different nominal I_{in}. The nominal values are summarised in table 9.1, some values of relevance to later tests are also mentioned.

Measure the input voltage on the power adapter V_{in} with a multimeter, and check if the result is in specification. Normally, the output of the LV power supply should not exceed 2.2 V to provide sufficient V_{in} for the required constant current. This can be achieved even after accounting for voltage drop, if the recommended power cables of AWG 16 or better is

[5] Also sometimes referred to as Advanced Scans or Complex Electrical Tests.

Type of Module	I_{in} [A]	V_{in} [V]	$I_{\text{in}}^{\text{max}}$ [A]	$I_{\text{in}}^{\text{LP}}$ [A]
L0/triplets	5.55	1.642 ± 0.025	9.75	1.626
L1	6.6	1.791 ± 0.025	10.6	2.112
L2-L4	5.88	1.758 ± 0.025	9.48	2.012

Table 9.1: Nominal input current and voltage I_{in} and V_{in}, upper limit of the SLDO qualification measurement $I_{\text{in}}^{\text{max}}$, and nominal low power (LP) mode $I_{\text{in}}^{\text{LP}}$ for modules in different locations of the detector.

used. As for voltage drop resulting from a module, the resistance of the module itself plus a 15 cm power pigtail is 0.045 Ω for quads and 0.026 Ω for triplets. This results in e.g. a 265 mV voltage drop from L2 quads.

9.2.2. Sensor *IV*

This test verifies that the leakage current I_{leak} and breakdown voltage V_{bd} of the sensor are still within specifications after module assembly, and it also allows comparison with *IV* from earlier stages.

As bare sensors, *IV* curves are measured by sensor vendors. The sensors then go through hybridisation, forming BMs, and BM level measurements are conducted by assembly sites as part of the reception tests[6]. After full assembly, sensor *IV* is measured again at module level, as introduced here, during module QC. Differences between the *IV* curves at these three stages can therefore reflect effects or damages resulting from the hybridisation and assembly procedures.

The requirements on I_{leak} and V_{bd} is to ensure that no issues arise during operation. Moderate degradation compared to sensor level results can be tolerated. Therefore, the I_{leak} specification is set at twice the sensor specification shown in table 6.1[7]. The sensor specification on the minimum V_{bd} still holds[8], with an additional requirement on the maximum decrease of V_{bd} after assembly: the decrease should be less than 10 V, and for planar sensors, if V_{bd} is > 200 V at BM level, it must still be > 200 V after assembly.

9.2.3. E-fuses

An electronic fuse writes one bit of information irreversibly to the FE chip. Despite the E-fuses being not radiation tolerant and are not required for operation, they are important for identifying the FE chips. In this test, the E-fuse register should be read and compared to the correct value. This can simply be checked in the printout of YARR scans.

[6] As introduced in section 8.5.1.

[7] For 3D sensors, which is not included in the table, the specification for sensor *IV* after assembly is $< 5.0\,\mu\text{A/cm}^2$ at V_{dep} +50 V.

[8] For 3D sensors the specification is $V_{\text{bd}} > V_{\text{dep}}$ +20 V.

9.2.4. Simple Electrical Tests

A simple electrical test consists of three steps: measurement, analysis (processed by LocalDB), and, in case of a calibration measurement, updating of the chip config. Some tests rely on correct calibration from previous test results, making it important to carry out the tests in the correct order, so that the following tests are executed correctly.

After measurements[9], the results are saved as `RAW` files, which contain all the necessary information for QC analysis (hence the name "simple" electrical test). The DAQ host then submits the measurement to LocalDB, which analyses the measurement[10], produces analysis results in a `json` format that is ready for upload to the PDB, and determine whether the results pass QC requirements. Having this common analysis tool ensures consistent module grading across all the testing sites. Then, for calibration measurements (marked in bold in section 9.1.3), the chip config file is updated based on the results. In module QC, the calibration data is compared with wafer probing results.

All the simple electrical tests are introduced below, and the required QC criteria are presented in the figures with the results in section 9.4.

ADC Calibration

The ADC in the chip can be used to read out the monitoring multiplexer (mux). The mux can be configured such that various internal voltages and currents can be measured through the voltage monitoring multiplexer V_{mux} output and the current monitoring multiplexer I_{mux}. After the first power up, the ADC should be calibrated, so that the monitoring of various chip internal voltages and currents can be achieved through the ADC, instead of having to be measured through external multimeters. The calibration is performed by configuring the digital-to-analog converters (DACs) to be scanned from 500 to 2500 with 100 interval, measuring the lower injection voltage $V_{\text{cal}}^{\text{med}}$[11] through V_{mux}, and obtaining the ADC count for the injected calibration voltage by reading the corresponding register of the chip.

Module QC requires that the slope, offset, and linearity of the measured calibration curve, as well as the mean analog ground are within the required ranges.

Analog Readback

After ADC calibration, it is possible to perform analog readback, which is measurement of the analog signals via V_{mux} and I_{mux}, to read and check the internal voltages and currents. The mux values can be set to from 0 to 63[12], different V_{mux}, I_{mux} and ground values provide measurements to different internal values, e.g. V_{DDA} and V_{DDD} (analog and digital supply voltages) vs analog trim value (from 0 to 15), V_{refA} and V_{refD} (analog and digital reference

[9] The measurements are taken using `module-qc-tools`, as mentioned in section 7.3.
[10] The analysis is done by `module-qc-analysis-tools`.
[11] There are two injection voltages, $V_{\text{cal}}^{\text{med}}$ and $V_{\text{cal}}^{\text{high}}$.
[12] But not all values correspond to a parameter.

voltage), frequency of the ring oscillators, and temperature from chip NTC and two other internal sensors.

The measured values will be checked with the specification, including cross-checking of temperature measurements, criterion for various internal voltages and currents, and the frequency of ring oscillators being within 10 % of nominal. After the measurements and analysis, the chip configuration files should be updated before doing the power measurements like SLDO.

SLDO Qualification

The principle of SLDO is introduced in section 4.3.2. This test verifies that after the FE chips are configured, all internal currents, voltages, and other parameters that determine the SLDO behaviour are within specification.

This measurement scans the input current from the nominal current to the maximum current (the values are specified in table 9.1) with a 0.2 A step size, and measures the corresponding V_{mux} and I_{mux} channels for the parameters that need to be measured while recording the module NTC temperature.

The analog and digital parts in the FE are connected in parallel. Therefore, the analog and digital input voltages V_{inA} and V_{inD} should agree within the precision of the ADC of 0.01 V. To ensure an extra margin in analog and digital currents during operation, the shunt currents for either should be above a minimum. The margin to be kept is $\frac{I_{\text{shuntA}}}{I_{\text{inA}}-I_{\text{shuntA}}} \geq 1\,\%$ for analog, and 10% for digital.

To verify the Ohmic behaviour, the VI curve should be linear. The linearity is defined by the difference between the measured voltage at the input current and the theoretically expected voltage: $|V(I_{\text{in}}) - V_{\text{theory}}(I_{\text{in}})| < 0.035\,\text{V}$. The expected voltage $V_{\text{theory}}(I_{\text{in}}) = R_{\text{eff}} \times I_{\text{in}} + V_{\text{ofs}}$, where R_{eff} is the effective resistance and V_{ofs} is the offset voltage.

Vcal Calibration

V_{cal} is the injection voltage. The injection circuit, shown in the pixel unit cell diagram in figure 4.5, is controlled via a DAC[13] and a reference voltage applied to it, and the DAC needs to be calibrated. Since the injection voltage V_{cal} is the calibration voltage for chip tuning, V_{cal} calibration should be performed before tuning.

The lower and higher ranges of V_{cal} are referred to as $V_{\text{cal}}^{\text{med}}$ and $V_{\text{cal}}^{\text{high}}$, respectively. The calibration process measures the $V_{\text{cal}}^{\text{med}}$ and $V_{\text{cal}}^{\text{high}}$ in both small and large ranges by varying the DAC in steps within the selected range, making four sets of measurements. Then, measure the converted voltage through the ADC (therefore it is important that the ADC is calibrated), and fit a line of voltage vs DAC. After the calibration, the chip config file is updated with the slope and offset obtained from the large range measurements.

[13] DAC: digital to analogue converter.

Injection Capacitance

This is the measurement of the capacitance in the injection circuit shown in figure 4.5. The measurement must be precise, as it is used to determine the injected charge to the pixels in chip tuning: the capacitance is injected by injecting voltage, and V_{cal} is the amplitude of the pulse. After measuring both V_{cal} and injection capacitance, the amount of charge injected can be determined. The analysis will be used to update the chip config files. The injection capacitance should be within a range of $7.87 \pm 1.13\,\text{fF}$.

Low Power Mode (LP Mode)

After the modules are integrated into larger scale systems like loaded local support, the integration tests require CO_2 cooling. However, when testing basic functionalities, it is preferable if the modules can be tested for a short time without having to operate the cooling. Therefore, the modules should be able to perform basic functionalities with low power that induces lower heat dissipation.

The nominal lower current to be set is shown in table 9.1. For the LP mode test, configure the chips with the LP config file, and on the data adapter, the LP enable pins are connected with a jumper. Then measure V_{inA}, V_{inD}, V_{ofs}, I_{inA}, and I_{inD}. These internal voltages and currents are compared with the specification, and the shunt currents should be non-zero. Also perform a digital scan to check that the module functions and provides a meaningful output.

Overvoltage Protection (OVP)

Every chip has an OVP circuit. It limits V_{in} when it reaches 2 V, to decrease the V_{in} in the part of the circuit before SLDO. Therefore, the criterion is that the expected V_{in} should be larger than the measured V_{in} by 0.040 V, and that $I_{\text{inA}} + I_{\text{inD}} < I_{\text{in}}$.

In this test, $V_{\text{ref}}^{\text{OVP}}$[14], I_{inA}, and I_{inD} are measured and compared to the specifications. This test is performed in LP mode, and the powering scheme should be reverted to the nominal afterwards.

The FE chips are connected in parallel. Since there is no current regulation mechanism between the chips, if the effective OVP threshold is lower in one of them, this would result in this chip being powered with a higher current.

Undershunt Protection (USP)

If the current drawn by the chip is lower than I_{in}, the extra current can be shunted away. However, if the chip starts to consume more current, this cannot be solved by the shunt. This is when the USP circuit is needed. The USP is done by reducing the reference voltage V_{ref}, to reduce the power needed by the chip.

[14] Same as $V_{\text{ref}}^{\text{PRE}}$, the preregulator bandgap output voltage.

This is also a test in LP mode. All default voltages $V_{\mathrm{refA/D}}$, $V_{\mathrm{inA/D}}$, $V_{\mathrm{DDA/D}}$, and currents $I_{\mathrm{inA/D}}$, $I_{\mathrm{shuntA/D}}$ for the digital and analog parts, are measured, and the differences before and after the USP mechanism is triggered are compared: V_{in} and I_{in} should not change, while the others should decrease.

Instead of updating the chip config files in the case of the calibration measurements, on the contrary, the chips must be reset after the USP test, as they might be affected by the USP, causing communication problems.

Data Transmission

This test is performed on every FE to ensure that the eye opening is enough for data transmission in the detector. Module QC criteria is on the eye width.

9.2.5. Pixel Performance Tests

Pixel Performance Tests include Minimum Health Test, Tuning, and Pixel Failure Analysis. Each of the three tests comprises various YARR scans. A YARR scan aims at testing the percentage of failing pixels due a certain type of defect, or measuring a certain property. The module can also be tuned and masked. The YARR scans and the pixel performance tests are explained below.

YARR Scans

- **Digital scan**: this scan tests the digital part of the pixel. The FE chip can send digital or analog signals. In a digital scan, simple digital signals are injected as if they were the output from the analog part of the FE. YARR typically sends 100 signals, and a digital scan should be perfect with a uniform 100 hits occupancy in all pixels. A pixel is defined as digital dead if the occupancy is $< 1\,\%$ of the injections (no hits in 100 injected signals), and digital bad if the occupancy is $< 98\,\%$ or $> 102\,\%$.
- **Analog scan**: in analog scans, the FE chip sends analog signals, using a capacitor to simulate the sensor. A defined amount of charge is injected into the analog part of the FE, which is the circuit from the preamp input to the readout. The criteria for a pixel to be classified dead or bad is the same as that in the digital scan.
- **Threshold scan**: this is done by injecting voltage pulses, to simulate the signal charge from a incoming particle.

  Pulses with height V_{inj} are sent to the capacitor with a known injection capacitance C. After the capacitor, each pulse is turned into an injected charge:

  $$Q_{\mathrm{inj}} = CV_{\mathrm{inj}}. \tag{9.1}$$

  This goes through the charge sensitive amplifier, and the resulting voltage output passes the discriminator as a digital output signal if the pulse height exceeds the threshold.

In a threshold scan, a defined number of injections is done for a range of pulse heights with a certain step size, or alternatively, a certain injection charge for different threshold voltages. Whether there is a hit is determined by the discriminator response. Then, ideally, the percentage of hits vs injected charge forms a step function that reaches 100 % at a specific threshold charge value. But with noise, this is smeared to an S-shaped curve. In module QC, the injected charge is converted from the voltage (pulse height) – which is represented by a DAC value – via equation 9.1. Assuming Gaussian noise distribution, the probability of an injected charge Q_{inj} resulting in a hit is:

$$P(Q_{\text{inj}}) = \frac{1}{2} - \frac{1}{2}\text{erf}\left(\frac{Q_{\text{threshold}} - Q_{\text{inj}}}{\sqrt{2}\sigma_{\text{noise}}}\right), \tag{9.2}$$

where erf is the Gaussian error function, the $Q_{\text{threshold}}$ is the injection charge at which the probability is 50 %, which is the middle of the "S", and σ_{noise} is the width, which is the noise of the entire analog part, including the sensor. The threshold scan gives the distribution of threshold values measured from the S-curves of all pixels.

After tuning, the root mean square (RMS) of the threshold distribution should be below $50e$. A "tuning bad" pixel is defined as one with a pixel threshold that differs from the mean by more than $200e$. The requirement on the TDAC distribution is a mean within 0 ± 1, and a RMS within 10.5 ± 2.0. The equivalent noise charge (ENC) is the noise output voltage divided by the output voltage that is equivalent to a signal with one electron charge. A high ENC means a mean pixel noise > 200 and $300e$ for L0 and L1/L2, respectively. The specification varies between the inner and outer layers due to the different sensor thicknesses.

- **ToT scan**: similar to tuning, the ToT scan gives the distribution of ToT values for a certain amount of injected charge. Other than the threshold value (thus this scan is to be done after tuning), this is also related to the preamplifier setting. After a ToT tuning, each pixel's preamplifier should give the same response to the same injected charge. ToT scan and tuning are not possible for ITkPixV1.1 chips, as their ToT is binary instead of a 4 bit latch as intended. The binary output feature is to fix a bug in ITkPixV1.0 that causes high current and missing hits [197]. The intended specification for the ToT distribution after ToT tuning is that for $6000e$ test charge, the mean should be 7 ± 1, and the RMS value should be less than 1 bunch crossing.

- **Noise occupancy scan**: if a hit is fired when there was no incoming particle, this hit is noise. In a noise scan, the electronic noise is detected by the analog FE. After enabling all pixels, triggers are sent at a certain frequency, and some pixels may fire hits. The lower the threshold is, the more noise-prone the pixels are. In QC, a noisy pixel is defined as when the occupancy is $> 10^{-6}$ hits per bunch crossing in the noise scan. The noisy pixel should be masked. Noise is a result of the whole readout chain. The sensor is considered a capacitor at the preamplifier, and it induces electronic noise. If there is a disconnected bump, essentially the capacitor is disconnected, and the input of the preamp is floating, therefore there is no noise from the sensor for this pixel.

- **Disconnected bump scan**: the bump connection of a pixel is tested via injecting the neighbouring pixels. If the pixel under test is connected, it also shows signal due to crosstalk. In QC, disconnected bump is defined as when the pixel has occupancy $< 50\,\%$ of the injection.
- **Source scan**: put the module under a radioactive source, to test for disconnected bumps[15], which in QC is defined as those with occupancy < 10 hits. ITkPix modules come with the self-triggering mode, as explained in section 4.2.3.
- **Merged bump scan**: a merged bump is defined as a pixel with occupancy$> 50\,\%$ of the injections and is neighbouring another failing pixel.

Pixel Performance

Creating a Working Pixel Mask:

Proper masking should be used to keep the faulty pixels from being read out[16], which otherwise make it difficult to interpret the results.

It is possible to control the masking behaviour of the scans: enabling all pixels before the scan to obtain a new mask, adding new masked pixels to the existing mask, or not modifying the masking configuration. To create a working pixel mask, start with a digital scan with all pixel enabled, and the following tests mask the corresponding faulty pixels:

- Digital scan with new mask
- Analog scan
- Noise scan for 1 min

Minimum Health Test: a minimal set of scans that is done very often when it is necessary to check basic functionalities of the chip.

- Digital scan
- Analog scan
- Threshold scan (high range)
- ToT scan with 6000 injection charge

Tuning: to even out the charge response of each pixel, tune L0 modules to 1000e (electron charge) threshold, and L1/L2 modules to 1500e. The last threshold scan and ToT scan are post-tuning tests to check the post-tuning performance.

- Threshold scan (high range)
- ToT scan with 6000 injection charge
- Tune global threshold to 2000e
- Tune pixel threshold to 2000e

[15] In general, source or X-ray test can be used not only for checking disconnected bumps and other defects, but also for ToT and threshold calibration. The module QC procedure for ITkPixV1.1 module pre-production only uses it to test disconnected bumps.

[16] Or referred to as "disabled".

- Retune global threshold to 1000e (L0) or 1500e (L1/L2)
  (the charge targets are related to the sensor thickness, as introduced in section 4.1.1)
- Retune pixel threshold to 1000e (L0) or 1500e (L1/L2)
- Threshold scan (high resolution)
- ToT scan with 6000e injection charge

Pixel Failure Analysis: this is done after tuning, so that the pixels that are reported as bad in the analog scan are actually from bad analog behaviour instead of bad tuning.

- Electrical Pixel Failure Test: digital modules do not need to be checked for bump-bond, therefore only electrical pixel failure test applies. It catches pixels that are digitally dead/bad, analog dead/bad, or noisy. It includes:
  - Digital scan with new mask
  - Analog scan
  - Threshold scan (high resolution)
  - Noise scan with 10 million triggers
- Full Pixel Failure Test: in addition to the electrical pixel failure analysis, real modules need full pixel failure test, which also checks the bump-bond quality, including disconnected or merged bumps.
  - Disconnected bump scan
  - Merged bump scan with 1500e (L0) or 2000e (L1/2) injected charge
  - Zero-bias threshold scan[17]: at zero bias, the sensor is not fully depleted – only intrinsic depletion zone is present. This leads to higher capacitance[18], which results in higher noise. If the bump is disconnected, noise from the sensor no longer passes through the bump-bond. Therefore, zero-bias threshold scan is performed. After being compared to the threshold scan with biasing, if, for certain pixels, no change in the noise is observed, it indicates that these pixels have disconnected bumps.
    - High voltage (HV) off
    - Retune pixel threshold to 1000e (L0) or 1500e (L1/L2)
    - Threshold scan (high resolution)
    - HV on
    - Revert chip configs to the version before retune
  - Source scan: it is important to either mask pixels sensibly before this test, or run it right after electrical pixel failure test. This is because if the pixels are masked from e.g. disconnected bump scan, one does not know if the pixel would have functioned with source scan. In this test, pixels fail to get 10 hits are considered disconnected, but this is setup-dependent.

  The pixels that fail disconnected bump scan or source scan are considered to have disconnected bump-bonds.

The scan results, including the chip configs, are stored into LocalDB, with tags indicating to which pixel performance test they belong[19]. The analysis is performed by LocalDB on

[17] Not yet used in QC to identify disconnected bumps.
[18] As explained in section 4.2.2 and measured in section 6.1.5.
[19] Minimum Health Test (MHT), Tuning (TUN) and Pixel Failure Analysis (PFA), or locally defined tags.

the server based on the set of YARR scans, with help from the tags.

9.2.6. Thermal Cycling and Stability Test

Thermal Cycling

To test the module bump-bonds under thermal stress, perform these thermal cycles:

- 10 cycles between $-45\,°C$ and $40\,°C$.
- 1 cycle between $-55\,°C$ and $60\,°C$.
- Suggested T variation rate: 10 to $14\,°C$/min, maximum $15\,°C$/min.
- Soak time: 15 min. This is the time that the module is soaked at around the nominal T_{max} and T_{min}: $T_{max} - 5\,°C \leq T \leq T_{max} + 10\,°C$ and $T_{min} - 10\,°C \leq T \leq T_{min} + 5\,°C$.

After thermal cycling, 600 pixels with disconnected or merged bumps are allowed on each chip, and if the pixels with failed bumps are connected, maximum 50 connected ones are allowed [191].

Long Term Stability Test

For this test, power the module, bias the sensor with HV, and continuously read out the module using the DAQ system for 36 to 48 h.

9.3. Testing Setup

Setups for various tests must meet the requirements on equipment, environment, Detector Control Systems (DCS), and hardware (HW) interlock. The tests are categorised by the setup as follows: electrical QC (warm and cold), source or X-ray test, thermal cycling, and stability test.

9.3.1. Electrical QC Test

For warm test, temperature control and vacuum chuck are not required. However, the heat from module power dissipation – which is around 10 to 12 W – must be dissipated by either passive (dissipators like heat sink) or active (temperature controlling devices like Peltier or chiller) methods. The warm testing setup can be used for the cold tests, if the corresponding requirements are reached.

The requirements for warm and cold test are summarised in table 9.2. The requirement on the temperature T is wide since there is no danger of condensation at regular lab environment, and the maximum is defined by the FE chip maximum operating temperature. The module is kept in the carrier during testing for safe handling.

	Requirement
Module T (during test)	Warm: $15\,°C \leq T \leq 50\,°C$ Cold: triplets: $-25\,°C$, quads: $-15\,°C$ Stable within ± 3
Module T (whole duration)	Warm: $15\,°C < T < 65\,°C$ Cold: $-35\,°C < T < 50\,°C$
Vacuum under module	Required for cold test. $500\,\text{mbar} \leq \Delta p \leq \text{atm}$ [20] at testing T, where Δp is the difference between the pressure in the chuck and one atm
Vacuum chuck	Metal, clean, dry, roughness $< 0.6\,\mu m$ Sealing gasket: silicone rubber, do not leave residual at back of FE chips
RH	$< 60\,\%$
Dew point	Ambient: $< T_{\text{ambient}} - 5\,°C$ In carrier: $< T_{\text{chuck}} - 5\,°C$
Dry air	HEPA[21] filtered, oil free, have flow meter Warm: RH<30% at $15\,°C$ (dew point at $-2.5\,°C$) Cold: RH<3.5% at room T

Table 9.2: Setup requirements for warm and cold tests. Warm test is at room temperature and cold at $-15\,°C$. The module T is measured by the NTC mounted on the flex [198].

Cold Test

The cold test setup includes either a cold box or a climate chamber. For a cold box setup, the module (with carrier) should be tested in a box with dry air both in the box and in the carrier volume, to avoid condensation both outside and inside the carrier. The bottom of the module carrier should be taken off so that the FE chips are in contact with the vacuum chuck, and an RH measuring device must be attached to the lid. The top cover of the box and module carrier should not block radiation in the source or X-ray scan. In case of a climate chamber setup, the chamber could already come with its own RH sensor and humidity control, and the module should be without lid during testing.

Göttingen

In the local setup at Göttingen, the electrical QC testing setups are housed in a source box [103, 199] that was designed to allow performing tests with a radioactive source. At the time of this thesis, there is only one cold setup and one warm setup in the source box, with the cold setup being able to perform warm tests. The current status of the setups in the source box is shown in figure 9.1, a parallelisation is planned.

For the warm setup, the heat control and power dissipation are achieved via two fans and a heat sink.

The cold setup uses a centrally produced cooling system called the Bergen cooling unit[22] that includes a foam box and a vacuum chuck with sealing gasket. The configuration inside the foam box is illustrated in figure 9.2. The T control is via a chiller (silicone oil) connected to a cold plate, and above which, a Peltier CP85 that holds up the vacuum chuck, to which

[22] Developed at the University of Bergen.

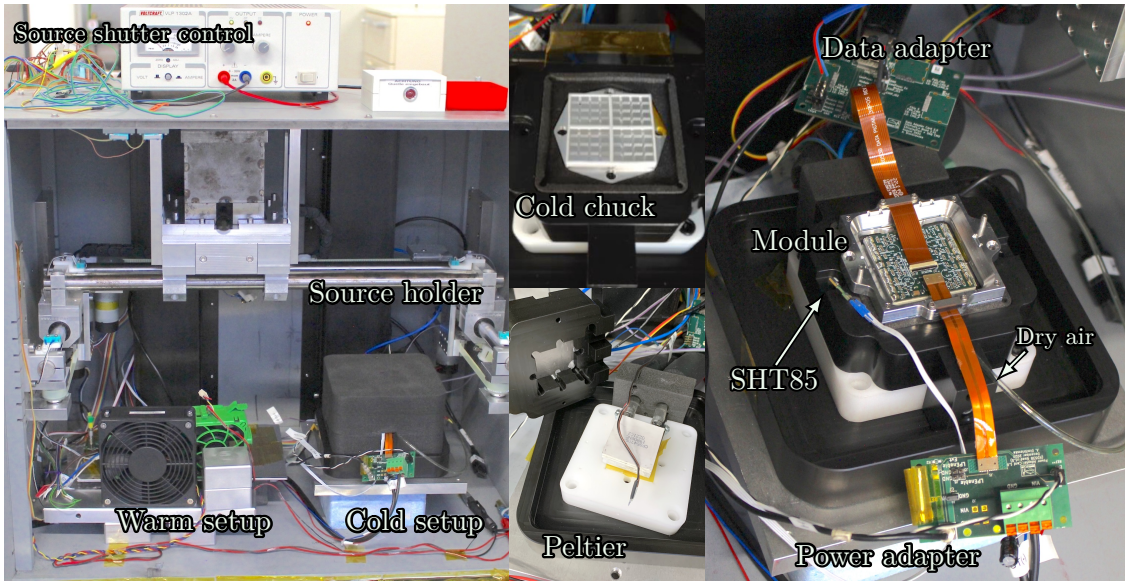

Figure 9.1: Source box setup with one warm setup and one cold setup.

the module is fixed. This setup can perform both cold and warm tests. Dry air is flushed into the module carrier. For details about dry air filtering and vacuum pump, please refer to section 7.2. The flow regulation and monitoring is with a Key Instruments MR3000 flow meter. The dry air is routed next to the cooling pipes, so that it is cooled down and the cooling dissipation from warm dry air is minimised. At room temperature and moderate dry air flow, RH $< 2\,\%$ is reached. For environmental monitoring, other than the Pt1000 sensors at the cold plate and the chuck, an SHT85 is taped at the back of the lid of the carrier. The chuck, cold plate, ambient T and ambient RH are monitored. A pressure sensor monitors the vacuum pressure. The chiller is set to $-5\,°\mathrm{C}$, after powering the module on or off, module NTC shows $T < 3\,°\mathrm{C}$, and stabilises at $1\,°\mathrm{C}$.

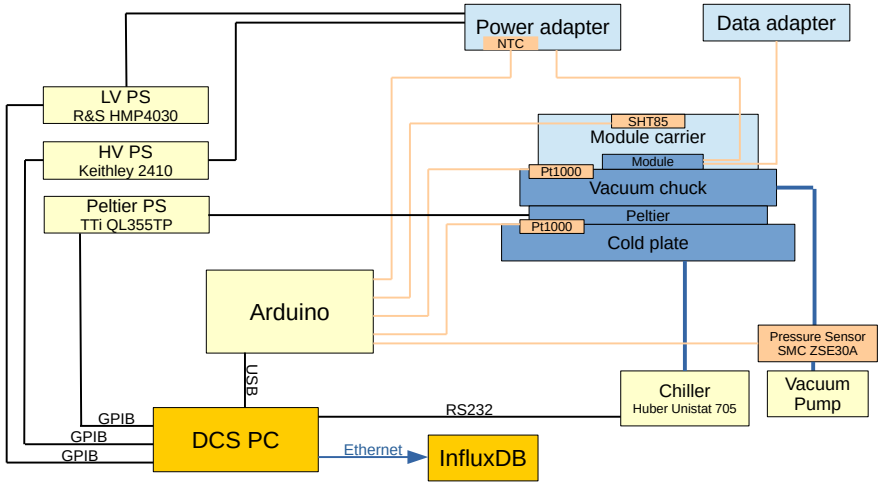

Figure 9.2: Power supply and DCS connections, and the configuration inside the cooling box for the cold setup.

Figure 9.2 also illustrates the power supply and DCS connections. An Arduino is used to read out the T and RH sensors. All monitoring tasks are based on labRemote[23], both monitoring and power supply controls are read out and run on a DCS PC, which writes necessary information to InfluxDB on a central PC, and can be viewed via Grafana.

9.3.2. Source or X-ray Test

A source or X-ray test is part of the electrical tests, but the radioactive source or X-ray tube involved results in additional requirements on the setup.

The recommended setup is: ^{90}Sr as source, with activity of around 6 MBq, and the distance between the source and the module should be 5–6 cm. This recommendation is from studies performed with 2 MBq ^{90}Sr source. Taking into account that the LV power connector and SMD capacitor has the lowest numbers of hits per min per MBq, an estimated attenuation factor of 2 from the foam box, and an attenuation factor of 2 from the mechanical wire-bond protection, the recommendation makes it possible to fulfil the required 50 hits/pixel with a measurement time of 10 to 15 min in the self-triggering mode.

The SQ requires showing test results, specifying source type, activity, minimum distance between the module and the source that allows irradiation of the full module, time estimated to obtain 50 hits/pixel, and the parallelisation plan. For X-ray setup recommendation and specifications please refer to the SQ document in ref. [178].

Göttingen

The Göttingen source box [103, 199] has a source holder mounted on a moveable gantry system that allows placing the source directly above the module. A shutter on the source chuck can be opened to allow radiation to pass through. The shutter is connected to a HW interlock and shuts off when the source box door is opened. The movement and shutter are both controlled remotely via an Arduino, which makes it possible to, after parallelisation of the setup, move the source above several modules in turns without manual intervention of the source. The distance between the source and the module can also be adjusted.

The source used is an encapsulated ^{90}Sr source, with opening to the bottom. The activity is around 10 MBq, but is mostly shielded by the encapsulation. Assuming Gaussian beam profile, and combined with the distance, the illuminated area and hit rate can be simulated and controlled.

9.3.3. Thermal Cycling

The setup requires a climate chamber (CC) or a cooling unit (CU) that perform thermal cycles with minimum range of $-55 \leq T \leq 60\,^{\circ}\text{C}$ with $\pm 2\,^{\circ}\text{C}$ uncertainty and a variation rate $\leq 0.25\,^{\circ}\text{C/s}$. T is defined as the CC T, or in case of CU setup, module T. During the

[23] https://gitlab.cern.ch/jgrosse/labRemote.git

test, the module is not powered. It is fixed to a centrally produced vacuum chuck to ensure the flatness, as the module will be glued to a flat carbon structure[24] in operation.

The environmental requirements are listed below.

- Dew point: $T_{\text{dew}} < T_{\text{chuck}}$.
- Dew point before start of test: $T_{\text{chuck}} - T_{\text{dew}}^{\text{ambient}} \geq 10\,^{\circ}\text{C}$ at room temperature. This is only applicable with continuous dry air flushing.
- Dry air: depending on the volume of theCC, the recommendation is 30 L/min at the beginning, and reduce to 13 L/min just before the start of the cycles after RH reaches the requirement.
- RH $\leq 0.1\,\%$ if no continuous dry air flushing, which corresponds to dew point $-55\,^{\circ}\text{C}$.
- Vacuum: ≥ 500 mbar.

Due to the long duration of the test (8 to 16 h), uninterruptible power supply for the dry air system and CC is recommended as a preventative measure in case of power cut. For detailed requirements on DCS and interlock, please refer to the corresponding blocks in ref. [178]. CCs are industrial instruments, and therefore no HW interlock is required, except for a lock on the door to prevent opening of the chamber when cold. CU setup has in addition vacuum and Peltier related requirements.

Göttingen

A Vötsch VT 7012 S2 shock chamber is used, the setup is shown in figure 9.3. This is normally used for bump bond thermal shock tests: it includes a hot chamber and a cold chamber, modules are put in a cage that quickly moves between the chambers, experiencing thermal shock. For thermal cycling, the shock mode cannot be used. Instead, the cycles are done only at cold chamber with an available T range of -80 to $+70\,^{\circ}\text{C}$. With an unused warm chamber on top, the cold chamber T ramps up and down slowly. Figure 9.4 shows the environmental monitoring for the cycles, and the whole duration is around 17 h.

The shock chamber has a lockable door handle and dry air inlet. For DCS monitoring, there are two monitoring sensors for ambient T and RH:

- SHT85 for T and RH, read by Arduino via I2C, the lowest possible T is $-45\,^{\circ}\text{C}$.
- HS1101LF RH sensor, which is capacitance based. The stray capacitance adversely affects the precision, but this sensor has a wider working range in T. The frequency is measured via an Agilent meter. The T sensor is PT1000, read out via an Arduino. These T, RH and dew point measurements are labeled “alt.” (alternative) in figure 9.4.

The other sensors are: PT1000 for chuck T, SMC ZSE30A for chuck vacuum, and module NTC for module T, all read out via Arduino analog pins. The shock chamber also provides measurements for the chambers.

[24] This structure is referred to as a “cell”, as mentioned in section 7.1.1.

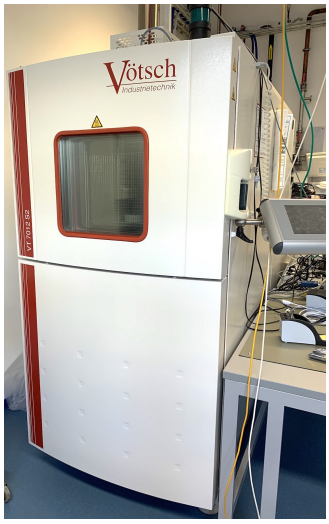

(a) Vötsch VT 7012 S2 shock chamber.

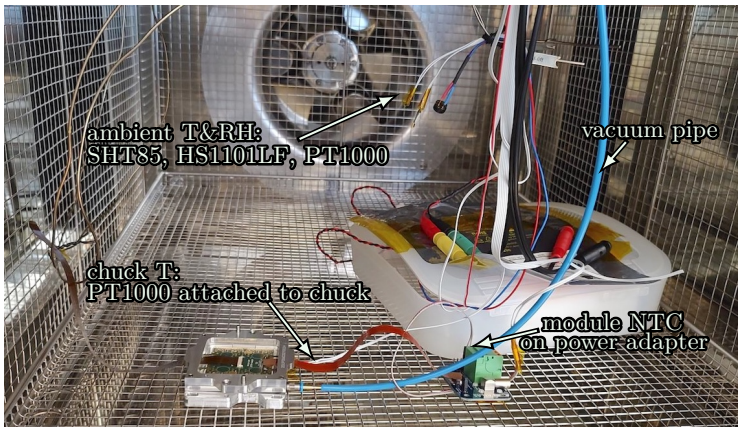

(b) The configuration inside the chamber.

Figure 9.3: The thermal cycling setup. A vacuum pressure sensor SMC ZSE30A connected to the vacuum pipe is outside the chamber and not visible in the photos.

The DCS reading and control are via labRemote, InfluxDB and Grafana, same as descried in the cold setup section, and the chamber can be controlled via the interlock in case of dew point or overheating problems.

9.3.4. Stability Test

The stability test is performed at room temperature. It can use the warm setup, or other setups with temperature control.

Göttingen

The stability tests are planned to be done in a Vötsch VTM 4004 climate chamber with T range -40 to $180\,^{\circ}\mathrm{C}$, together with a heat sink and dry air flushing. The power supplies and environmental monitoring system are similar to that described in the other setups.

9.3.5. DCS and Interlock

A SW interlock should come with the DCS. In addition, a HW interlock is also required.

For SW interlock, the requirements and the parameters to be monitored and logged vary slightly for different setups, mainly including the voltage and current of power supplies and multimeters, module NTC T, chuck T, RH in carrier, vacuum pressure, and ambient T and RH.

Overall, the DCS should show visible alert and message the operator when certain parameters are out of specification, and if critical values are reached, the SW interlock must take

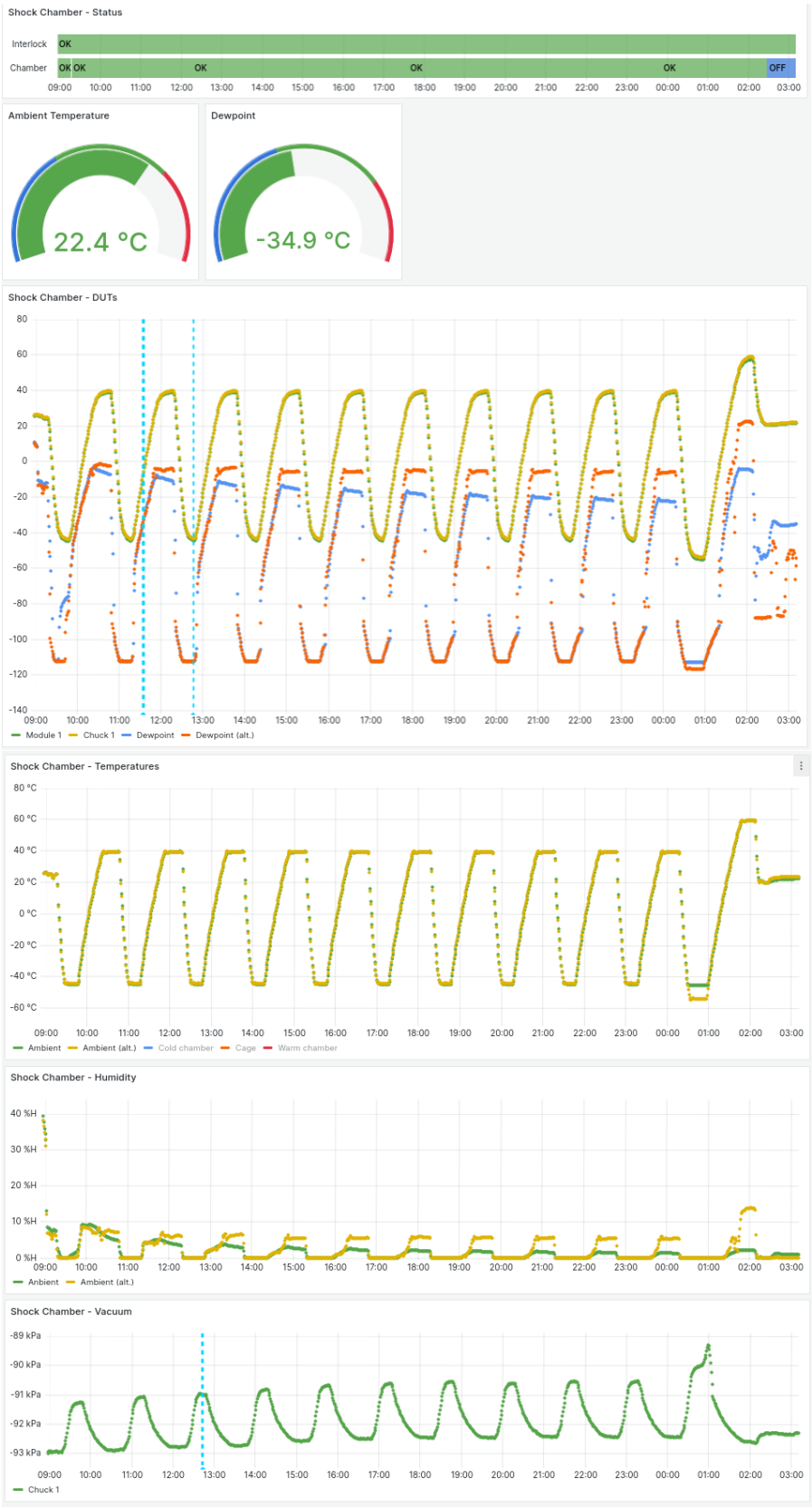

Figure 9.4: The thermal cycles and environmental monitoring. The whole duration is approximately 17 h, the RH and dew point are within specification. The dashed blue vertical lines are from DCS tests, and are no longer of relevance as the alarm threshold was later readjusted.

action, like ramping down or breaking HV, turning off LV, and turning off Peltier. The interlock should also be triggered when the lid is opened to replace the module.

An interlock normally has different statuses, like trip, armed, ready, not ready. After the SW interlock is triggered, the re-arm of the interlock should not happen automatically when the alert goes away, but only via the intervention by the testing personnel.

For the detailed requirement on e.g. the logging frequency and critical values please refer to the interlock block in [200].

A HW interlock should ideally never be triggered: the control SW should be able to counteract the condition back to desired range, and shut off the system properly like slowly ramping off HV. However, at dangerous conditions, the HW interlock is needed to directly cut the power (of module LV, HV, and e.g. Peltier). The interlock action can make use of the interlock on the power supply, or a separate board with Normally Open relays, and the setup is automatically shut off in the case of power loss.

It should be completely independent from the DCS or DAQ system, to prevent SW failure and human error: the sensors for monitoring should be read directly by the HW interlock, instead of from the database or DCS. The status and values of the setup should also be read independently, instead of through the DAQ system.

The threshold of triggering the interlock should be manually set, and the re-arm should only be possible through human intervention. If the interlock is triggered, this should be logged with a timestamp and independent from the DCS. The interlock should announce the value of the status, which can be read by the DCS or the DAQ PC. The reading should not be done by writing to the interlock like requesting information, but only by reading what was announced. The response time is recommended to be $< 250\,\text{ms}$. If DCS reads from the HW interlock, fast readout allows the SW interlock to take action before the HW interlock. Measures should be taken to prevent corrupt readings or glitches, like reading the values twice consecutively when triggered.

The DCS and SW interlock for the setups at Göttingen is as introduced in the previous sections. The HW interlock was developed, and the SQ material was submitted for review, but is out of the scope of this thesis.

9.3.6. Parallelisation

To reach the target production rate, multiple modules need to be tested at the same time. If the parallelisation of the setup is simply via duplicating the same testing systems, parallelisation qualification is needed. If equipment such as the chiller or interlock is shared, a qualification for the parallelisation is required.

In terms of DAQ for the electrical QC, it is possible to configure the FW and SW so that one PCIe card can be used to read out four modules at the same time, as introduced in section 6.2.4. Available config files and SW releases could provide possibility for sites to read multiple modules from the PCIe card.

The SQ requires showing parallel readout using the correct FW version and connectivity file in YARR scan console, correct correspondence between the results and the modules both locally and on the PDB with no data corruption, and the plan and timeline of the parallelisation.

The planned parallelisation in Göttingen[25] is to duplicate the Bergen cooling unit in the source box, the planned arrangement and the illuminated area from the moveable source is shown in figure 9.5.

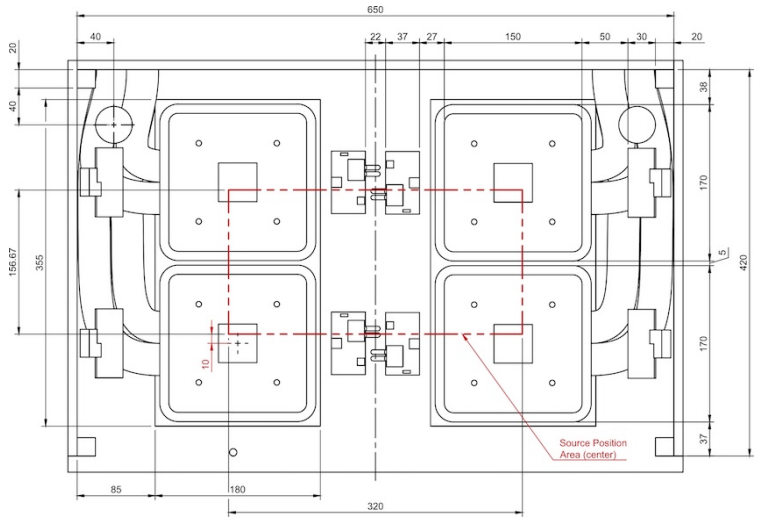

Figure 9.5: Drawing of the planned parallelisation in the source box.

9.4. Results

As mentioned in section 8.6, 16 modules were assembled at Göttingen. After wire-bonding at Bonn, Q6, Q11 and Q12 were sent back for QC testing.

The basic status of these modules is summarised in table 9.3. Q6 has one or two failing FE chips, and therefore has failed QC, no further tests were done after the initial warm tests. Q11 has a faulty core column, which is explained in section 9.4.1. As the QC testing for Q11 is ongoing, the cold test results are unfortunately beyond the cope of this thesis. Q12 is the only module among the three that has four fully functioning chips. Testing of Q12 is intended as cross-check with Bonn, where BDAQ [201] instead of YARR is used for DAQ. The testing personnel at Göttingen was not aware of the results from Bonn, to keep the independence of the cross-check. After a few initial warm tests, Q12 was sent back to Bonn for more measurements.

[25] Designed by Ruben Förster, to be published.

	Warm	Cold	V_{in} warm [V]	V_{in} cold [V]
Q6	Chip3 fails	-	1.704	–
Q11	1 core column disabled on chip2	To be tested	1.689	1.680
Q12	All chips work, no core col issue	1 failed chip	1.772	–

Table 9.3: Testing results of Q6, Q11 and Q12. V_{in} for Q12 passed the QC requirement.

9.4.1. Core Column Issue

Multiple testing sites encountered the core column issue. This refers to some FE chips failing YARR scans, and only working after disabling some columns via a designated config parameter[26]. The columns to disable are identified during debugging simply via trials. For the modules affected by this issue, this effect was not observed on the wafer probing level of the FE chips. Therefore, this not purely a chip issue. Investigations are being made in the module community to correlate the issue with the type of modules, hybridisation vendors and processes, chip manufacturing processes, chip position on wafer, and the position of the problematic core columns on the chips.

This issue also occurred in the tests at Göttingen, figure 9.6 shows an example from Q11. The YARR scan shows a pattern on chip2 that indicates readout problem, which disappeared after a faulty core column was disabled.

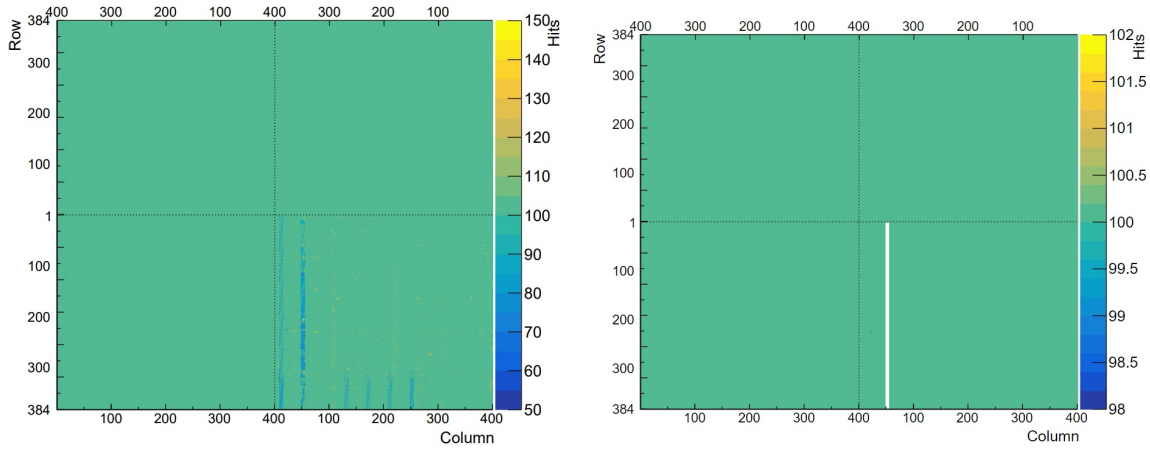

(a) Before disabling core column: pattern indicating problem.

(b) 1 core column disabled, the other pixels are good with 100 hits.

Figure 9.6: Core column issue of Q11.

[26] EnCoreCol0 to 3, the disabled columns are determined via calculating from binary to decimal and specifying the decimal number. A 16 digit binary number correspond to 16 core columns, each core column is 8 pixel columns. If all enabled, this correspond to all 1s in the 16 digits, and the number 65535 is specified. EnCoreCol0, 1, and 2 can specify the maximum 65535, the last one is maximum 63, which corresponds to the other two core columns.

9.4.2. First Power-up

All three tested modules are outer barrel L2 modules. As mentioned in section 9.2.1, they should be powered in constant current mode at 5.88 A, ideally with a voltage limit within 2.2 V. However, with the local setup, a 2.2 V limit on LV power supply was insufficient due to the thin wires causing high voltage. This resulted in readout problems that manifest as a pattern in the digital scan. After increasing the voltage limit to 3.7 V to give a larger overhead, the pattern disappeared and a perfect digital scan was obtained. See figure 9.7 for a comparison of the digital scan results from chip2 of Q12 before and after increasing the voltage limit. The V_{in} of all three modules are summarised in table 9.3.

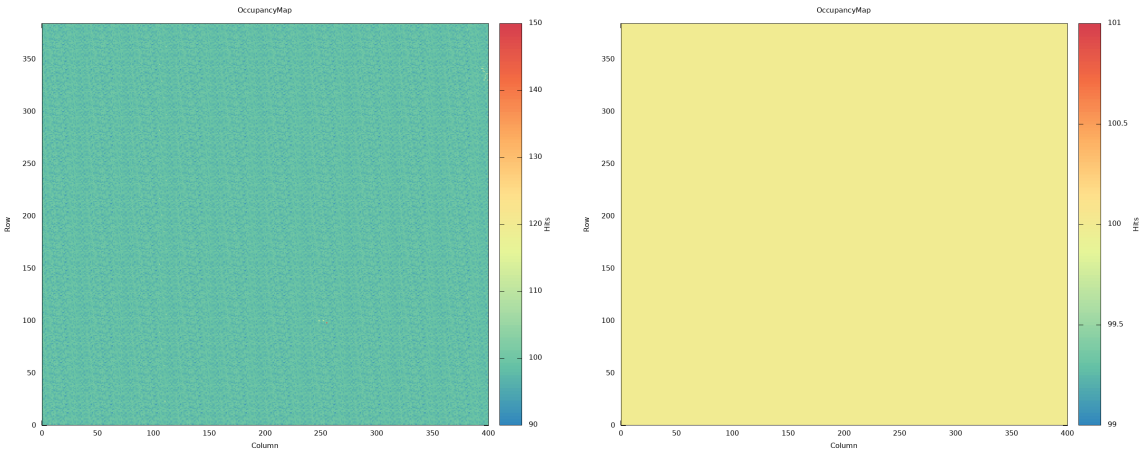

(a) Before (b) After

Figure 9.7: Digital scan (on Q12 chip2) succeeded after increasing voltage limit on the LV power supply.

9.4.3. Sensor *IV*

Sensor *IV* was measured at module level for Q11. A comparison between the *IV* curves taken at sensor, BM, and module stages is shown in figure 9.8. The sensor level *IV* was measured by the sensor vendor, and the BM level measurement before assembly is presented in figure 8.33.

Overall, there is no breakdown or change in shape on the sensor *IV* curves at any stage. From sensor to BM level, the overall leakage current increased by a factor of four. However, since leakage current is temperature dependent[27], and the environmental monitoring information from the sensor vendor is unavailable, it is unclear if the increase is caused by the hybridisation procedure, or simply from different measurement temperatures.

Between the BM and module levels, the *IV* curve shifted lower. This can be attributed to temperature differences: during BM probing[28], the temperature monitoring sensor is taped to the chuck, and the limitation in thermal contact results in the recorded temperature

[27] As discussed in section 4.2.2.
[28] The probe station setup is detailed in section 6.1.3.

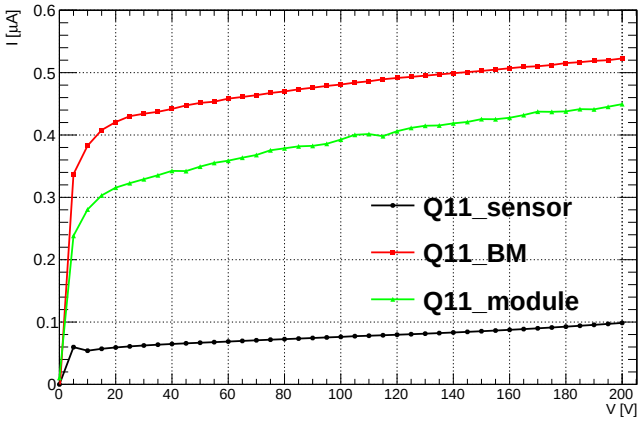

Figure 9.8: Comparison of Q11 leakage current vs voltage at the sensor, BM, and module levels. The results are not corrected for temperature (see text).

being higher than the actual temperature of the chuck and BM. In the module testing setup, however, the module NTC provides the temperature measurement. With the module being fixed by vacuum onto the chuck, therefore having good thermal contact, the temperature measurement by module NTC is more accurate.

9.4.4. Simple Electrical Tests

Simple electrical test results for the three modules are summarised in table 9.4. Q6 results were obtained before the implementation of a procedure to update the chip config files, and before the completion of USP and data transmission tests.

Test	Q6	Q11	Q12
SN	20UPGM22110094	20UPGM22110096	20UPGM22110081
ADC calibration	✓	✓	✓
Analog Readback	✗	✗	✗
SLDO Qualificaiton	✓	✓	✗
Vcal Calibration	✓	✓	✓
Injection Capacitance	✓	✓	✓
Low Power Mode	✗	✗	✗
Overvoltage Protection	✗	✗	✗
Undershunt Protection	–	✗	✗
Data Transmission	–	✓	✓

Table 9.4: Simple Electrical Test results for Q6, Q11 and Q12.

All three modules passed ADC calibration, Vcal calibration and Injection capacitance, and Q6 and Q11 in addition passed SLDO. USP and Data transmission were performed on Q11 and Q12, both modules passed data transmission. However, failing of some tests does not necessarily mean that the modules are problematic. This is explained in the following part regarding the corresponding tests.

Q11, as the remaining functioning module that will undergo further testing, is introduced in detail in the following as an example. Other than the results presented in this section, more figures and analysis summaries can be found in appendix C for completeness. The results for all the four chips on Q11 are summarised in table 9.5. Only chip2 passed analog readback, and chips 1 and 4 passed OVP.

	Chip1	Chip2	Chip3	Chip4
Name	0x17939	0x17969	0x17989	0x17979
ADC calibration	✓	✓	✓	✓
Analog Readback	✗	✓	✗	✗
SLDO Qualificaiton	✓	✓	✓	✓
Vcal Calibration	✓	✓	✓	✓
Injection Capacitance	✓	✓	✓	✓
Low Power Mode	✗	✗	✗	✗
Overvoltage Protection	✓	✗	✗	✓
Undershunt Protection	✗	✗	✗	✗
Data Transmission	✓	✓	✓	✓

Table 9.5: Q11 simple electrical test results for all four chips.

ADC Calibration

All modules passed the ADC calibration requirements. Example of V_{cal} vs ADC and the analysis summary for chip1 on Q11 is shown in figure 9.9. The analysis tool automatically compares the result with the QC criteria, which is included in the summary. The results for all the chips can be found in appendix C.1.

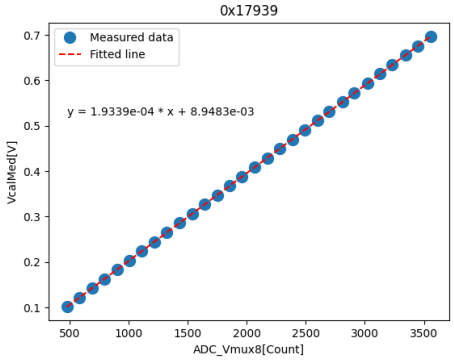

ADC_CALIBRATION for 0x17939

Parameter	Analysis result	QC criteria	Pass
ADC_CALIBRATION_SLOPE	0.193	[0.15, 0.224]	True
ADC_CALIBRATION_OFFSET	9.0	[-9, 31]	True
ADC_CALIBRATION_LINEARITY	0.47	[0.0, 4.0]	True
ADC_ANAGND30_MEAN	0.017	[0.015, 0.023]	True

Figure 9.9: ADC calibration curve and analysis results for Q11 chip1.

Analog Readback

Only chip2 on Q11 passed the analog readback QC criteria. To show an example of failed tests, the V_{DDD} vs trim value plots for both chip1 and chip2 are shown in figure 9.10. For chip1, V_{DDD} no longer increase linearly with higher trim values, and therefore has failed the QC criteria. This is not the case for chip2.

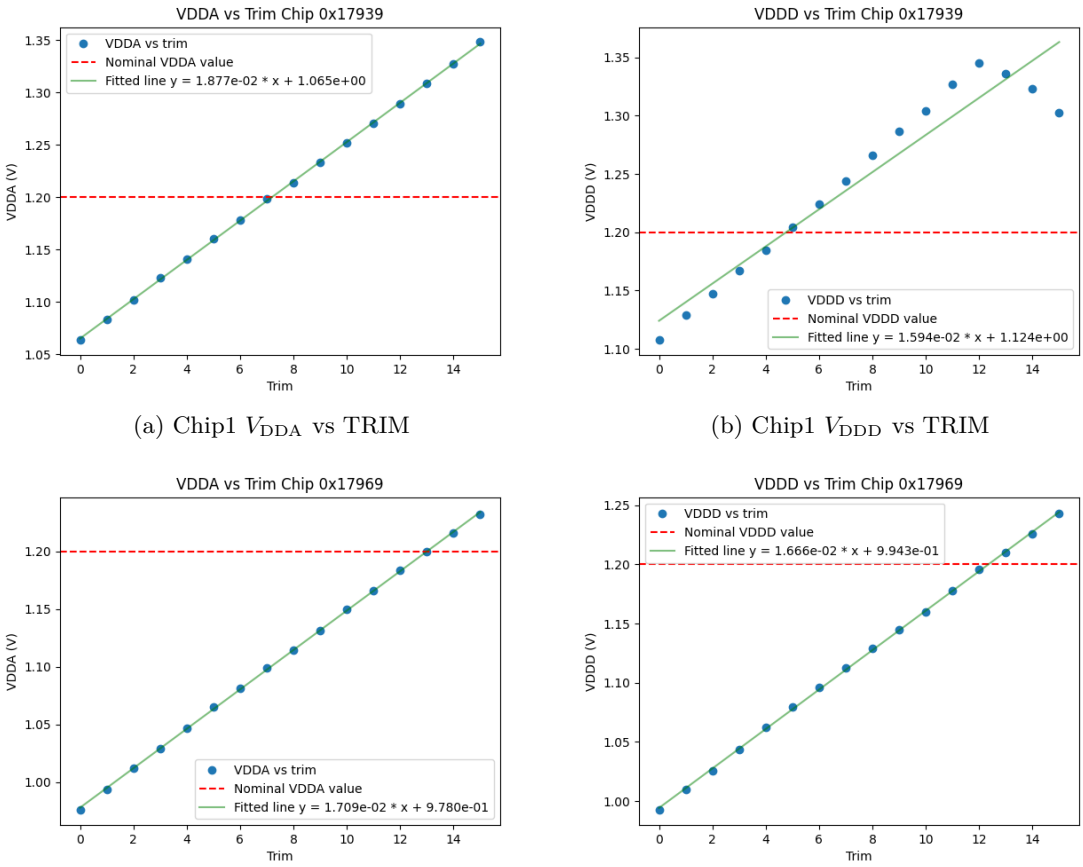

(a) Chip1 V_{DDA} vs TRIM

(b) Chip1 V_{DDD} vs TRIM

(c) Chip2 V_{DDA} vs TRIM

(d) Chip2 V_{DDD} vs TRIM

Figure 9.10: Analog readback results: V_{DDA} and V_{DDD} vs trip value for Q11 chip1 and 2. The response of chip1 is not linear at high trim values.

All the measurements results and the summary, including a comprehensive list of parameters and the QC criteria, are included in appendix C.2.

SLDO Qualification

All chips on Q11 passed the SLDO qualification. The results for chip1 are shown in figure 9.11, every QC criterion is passed, showing that all SLDO-related currents and voltages are within the required range. The results for chip2, analysis summary for all the four chips, and – as the *VI* curve illustrates the behaviour of the voltage versus constant current – the *VI* curves for all chips are included in appendix C.3.

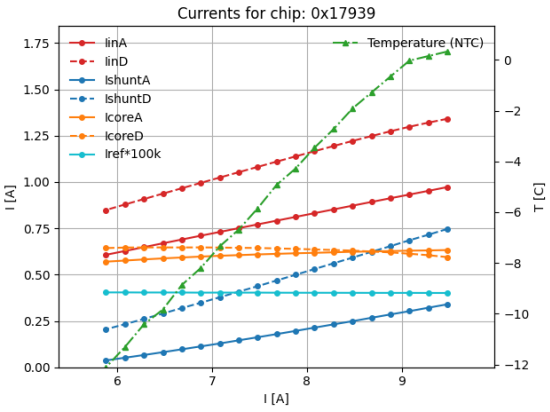

(a) II

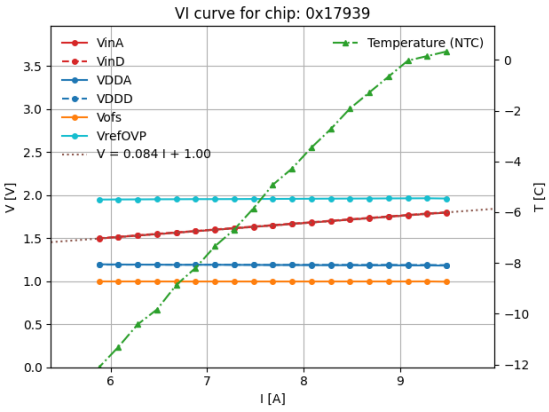

(b) VI

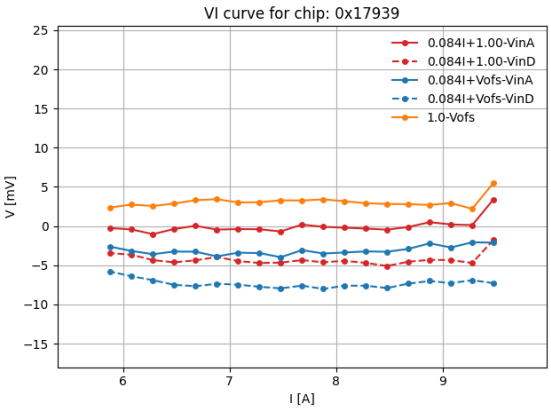

(c) VI residual

SLDO for 0x17939

Parameter	Analysis result	QC criteria	Pass
SLDO_LINEARITY	0.005	[0.0, 0.035]	True
SLDO_VINA_VIND	-0.01	[-0.01, 0.01]	True
SLDO_VDDA	1.2	[1.19, 1.21]	True
SLDO_VDDD	1.19	[1.19, 1.21]	True
SLDO_VINA	1.496	[1.468, 1.518]	True
SLDO_VIND	1.499	[1.468, 1.518]	True
SLDO_VOFFS	1.0	[0.99, 1.01]	True
SLDO_IINA	0.607	[0.567, 0.626]	True
SLDO_IIND	0.849	[0.846, 0.905]	True
SLDO_IREF	4.0	[3.7, 4.3]	True
SLDO_ISHUNTA	0.037	[0.006, 999]	True
SLDO_ISHUNTD	0.205	[0.128, 999]	True

(d) Summary

Figure 9.11: SLDO qualification of Q11 chip1.

Vcal Calibration

The calibration succeeded for all four chips. Figure 9.12 shows the linear behaviour of V_{cal} vs DAC and the analysis summary for chip1. Results for the other chips can be found in appendix C.4.

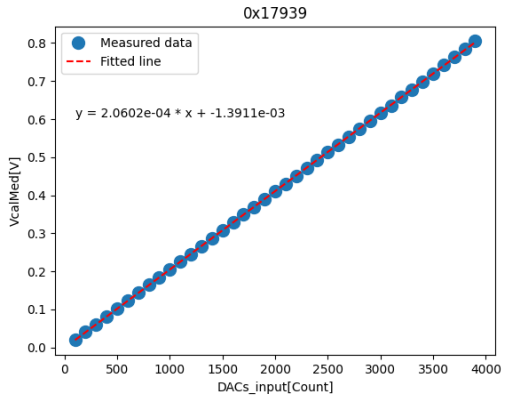

VCAL_CALIBRATION for 0x17939

Parameter	Analysis result	QC criteria	Pass
VCAL_MED_SLOPE	0.21	[0.16, 0.24]	True
VCAL_MED_OFFSET	-1.0	[-23, 17]	True
VCAL_MED_LINEARITY	0.99	[0.0, 4.0]	True
VCAL_HIGH_SLOPE	0.21	[0.16, 0.24]	True
VCAL_HIGH_OFFSET	-1.0	[-23, 17]	True
VCAL_HIGH_LINEARITY	0.35	[0.0, 4.0]	True
VCAL_HIGH_SLOPE_SMALL_RANGE_RATIO	0.5	[0.49, 0.51]	True
VCAL_MED_SLOPE_SMALL_RANGE_RATIO	0.5	[0.49, 0.51]	True

Figure 9.12: V_{cal} calibration results in the lower range for Q11 chip1.

Injection Capacitance

The injection capacitance QC criterion is 6.74–9.0 fF. The measured values for Q11 are 7.82, 7.68, 7.61, and 7.65 fF for the four chips, and they all passed QC. The figures showing all the measurements for Q11 chip1 can be found in appendix C.5.

Low Power Mode

Figure 9.13 presents the LP mode results. V_{ofs} is low for all chips, and this is a common observation among the module testing sites. A possible reason is the saturation of circuit when V_{ofs} value approaches 1.5 V. Further investigation is needed.

LP_MODE for 0x17939

Parameter	Analysis result	QC criteria	Pass
LP_VINA	1.479	[1.468, 1.518]	True
LP_VIND	1.481	[1.468, 1.518]	True
LP_VOFFS	1.303	[1.304, 1.354]	False
LP_IINA	0.22	[0.18, 0.22]	True
LP_IIND	0.3	[0.28, 0.32]	True
LP_ISHUNTA	0.0707	[0.0001, 0.1]	True
LP_ISHUNTD	0.0914	[0.0001, 0.1]	True

(a) Chip1

LP_MODE for 0x17969

Parameter	Analysis result	QC criteria	Pass
LP_VINA	1.482	[1.468, 1.518]	True
LP_VIND	1.481	[1.468, 1.518]	True
LP_VOFFS	1.299	[1.304, 1.354]	False
LP_IINA	0.22	[0.18, 0.22]	True
LP_IIND	0.32	[0.28, 0.32]	True
LP_ISHUNTA	0.0897	[0.0001, 0.1]	True
LP_ISHUNTD	0.0817	[0.0001, 0.1]	True

(b) Chip2

LP_MODE for 0x17989

Parameter	Analysis result	QC criteria	Pass
LP_VINA	1.481	[1.468, 1.518]	True
LP_VIND	1.481	[1.468, 1.518]	True
LP_VOFFS	1.301	[1.304, 1.354]	False
LP_IINA	0.22	[0.18, 0.22]	True
LP_IIND	0.31	[0.28, 0.32]	True
LP_ISHUNTA	0.0882	[0.0001, 0.1]	True
LP_ISHUNTD	0.0773	[0.0001, 0.1]	True

(c) Chip3

LP_MODE for 0x17979

Parameter	Analysis result	QC criteria	Pass
LP_VINA	1.483	[1.468, 1.518]	True
LP_VIND	1.482	[1.468, 1.518]	True
LP_VOFFS	1.301	[1.304, 1.354]	False
LP_IINA	0.22	[0.18, 0.22]	True
LP_IIND	0.31	[0.28, 0.32]	True
LP_ISHUNTA	0.0792	[0.0001, 0.1]	True
LP_ISHUNTD	0.0846	[0.0001, 0.1]	True

(d) Chip4

Figure 9.13: Low Power Mode results of Q11.

Overvoltage Protection

Figure 9.14 shows the OVP results for all chips of Q11. The chips that failed this test show slightly lower V_{ref} and higher digital I_{in}.

OVERVOLTAGE_PROTECTION for 0x17939

Parameter	Analysis result	QC criteria	Pass
OVP_VINA	1.9	[1.9, 2.1]	True
OVP_VIND	1.9	[1.9, 2.1]	True
OVP_VREFOVP	1.96	[1.95, 2.05]	True
OVP_IINA	0.729	[0.636, 0.781]	True
OVP_IIND	1.022	[0.855, 1.045]	True

(a) Chip1

OVERVOLTAGE_PROTECTION for 0x17969

Parameter	Analysis result	QC criteria	Pass
OVP_VINA	1.9	[1.9, 2.1]	True
OVP_VIND	1.9	[1.9, 2.1]	True
OVP_VREFOVP	1.94	[1.95, 2.05]	False
OVP_IINA	0.73	[0.636, 0.781]	True
OVP_IIND	1.053	[0.855, 1.045]	False

(b) Chip2

OVERVOLTAGE_PROTECTION for 0x17989

Parameter	Analysis result	QC criteria	Pass
OVP_VINA	1.9	[1.9, 2.1]	True
OVP_VIND	1.9	[1.9, 2.1]	True
OVP_VREFOVP	1.93	[1.95, 2.05]	False
OVP_IINA	0.729	[0.636, 0.781]	True
OVP_IIND	1.044	[0.855, 1.045]	True

(c) Chip3

OVERVOLTAGE_PROTECTION for 0x17979

Parameter	Analysis result	QC criteria	Pass
OVP_VINA	1.9	[1.9, 2.1]	True
OVP_VIND	1.9	[1.9, 2.1]	True
OVP_VREFOVP	1.95	[1.95, 2.05]	True
OVP_IINA	0.727	[0.636, 0.781]	True
OVP_IIND	1.033	[0.855, 1.045]	True

(d) Chip4

Figure 9.14: Overvoltage Protection analysis results for Q11.

Undershunt Protection

Figure 9.15 shows USP results for all chips of Q11. The differences before and after the USP mechanism for V_{ref} (especially V_{refA}) and V_{DDA} are much lower than required.

UNDERSHUNT_PROTECTION for 0x17939

Parameter	Analysis result	QC criteria	Pass
USP_VREFA_DIFF	0.001	[0.03, 0.15]	False
USP_VREFD_DIFF	0.059	[0.03, 0.15]	True
USP_VINA_DIFF	0.001	[-0.005, 0.005]	True
USP_VIND_DIFF	0.003	[-0.005, 0.005]	True
USP_VDDA_DIFF	0.003	[0.05, 0.2]	False
USP_VDDD_DIFF	0.12	[0.05, 0.2]	True
USP_IINA_DIFF	-0.0	[-0.005, 0.005]	True
USP_IIND_DIFF	-0.001	[-0.005, 0.005]	True
USP_ISHUNTA_DIFF	0.055	[0.05, 0.1]	True
USP_ISHUNTD_DIFF	0.087	[0.05, 0.1]	True

(a) Chip1

UNDERSHUNT_PROTECTION for 0x17969

Parameter	Analysis result	QC criteria	Pass
USP_VREFA_DIFF	0.002	[0.03, 0.15]	False
USP_VREFD_DIFF	0.028	[0.03, 0.15]	False
USP_VINA_DIFF	0.001	[-0.005, 0.005]	True
USP_VIND_DIFF	0.003	[-0.005, 0.005]	True
USP_VDDA_DIFF	0.004	[0.05, 0.2]	False
USP_VDDD_DIFF	0.059	[0.05, 0.2]	True
USP_IINA_DIFF	-0.0	[-0.005, 0.005]	True
USP_IIND_DIFF	-0.001	[-0.005, 0.005]	True
USP_ISHUNTA_DIFF	0.066	[0.05, 0.1]	True
USP_ISHUNTD_DIFF	0.077	[0.05, 0.1]	True

(b) Chip2

UNDERSHUNT_PROTECTION for 0x17989

Parameter	Analysis result	QC criteria	Pass
USP_VREFA_DIFF	0.0	[0.03, 0.15]	False
USP_VREFD_DIFF	0.059	[0.03, 0.15]	True
USP_VINA_DIFF	0.001	[-0.005, 0.005]	True
USP_VIND_DIFF	0.004	[-0.005, 0.005]	True
USP_VDDA_DIFF	0.001	[0.05, 0.2]	False
USP_VDDD_DIFF	0.121	[0.05, 0.2]	True
USP_IINA_DIFF	-0.0	[-0.005, 0.005]	True
USP_IIND_DIFF	-0.001	[-0.005, 0.005]	True
USP_ISHUNTA_DIFF	0.064	[0.05, 0.1]	True
USP_ISHUNTD_DIFF	0.072	[0.05, 0.1]	True

(c) Chip3

UNDERSHUNT_PROTECTION for 0x17979

Parameter	Analysis result	QC criteria	Pass
USP_VREFA_DIFF	-0.0	[0.03, 0.15]	False
USP_VREFD_DIFF	0.042	[0.03, 0.15]	True
USP_VINA_DIFF	0.001	[-0.005, 0.005]	True
USP_VIND_DIFF	0.003	[-0.005, 0.005]	True
USP_VDDA_DIFF	0.0	[0.05, 0.2]	False
USP_VDDD_DIFF	0.087	[0.05, 0.2]	True
USP_IINA_DIFF	-0.0	[-0.005, 0.005]	True
USP_IIND_DIFF	-0.001	[-0.005, 0.005]	True
USP_ISHUNTA_DIFF	0.055	[0.05, 0.1]	True
USP_ISHUNTD_DIFF	0.078	[0.05, 0.1]	True

(d) Chip4

Figure 9.15: Undershunt Protection analysis results for Q11.

Data Transmission

All chips passed the Data Transmission test, the result for chip1 is shown in figure 9.16, and the results for the other three chips are in appendix C.6.

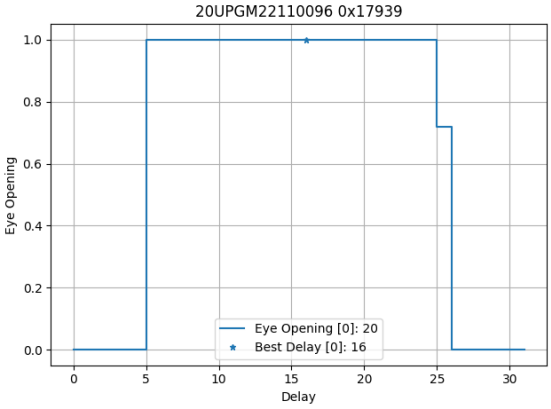

DATA_TRANSMISSION for 0x17939

Parameter	Analysis result	QC criteria	Pass
EYE_WIDTH0	20	[3, 32]	True

Figure 9.16: Data Transmission analysis results for Q11 chip1.

9.4.5. Pixel Performance

Minimum Health Test

Chip1, 3 and 4 of Q11 passed the Minimum Health Test, and chip2 failed due to the core column issue. The number of failing pixels in different categories, map of failed pixels on the chip, and the analysis results and QC criteria for chip1 are presented in figure 9.17. The number of pixels that are categorised analog bad, fail the threshold fit, or have high ENC are within specification. Results for the other chips are presented in appendix C.7.

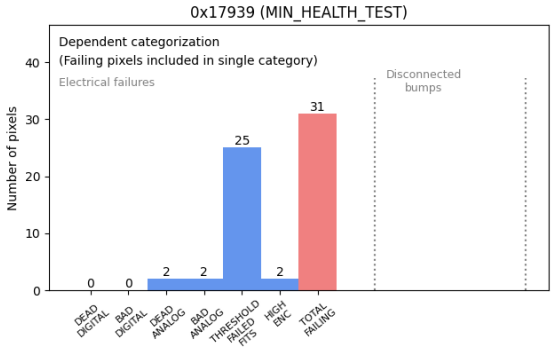

(a) Faulty pixels.

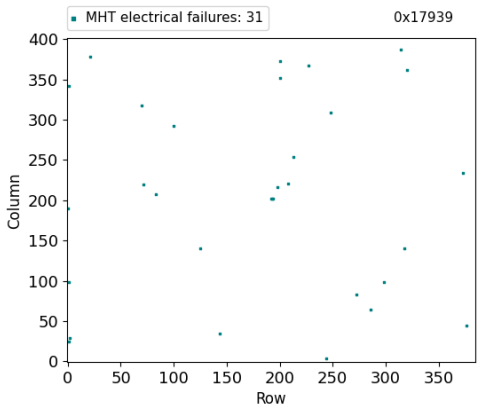

(b) Pixels with electrical failures.

MIN_HEALTH_TEST for 0x17939

Parameter	Analysis result	QC criteria	Pass
BAD_ANALOG_INTEGRATED	4	[0, 153.6]	True
THRESHOLD_FAILED_FITS_INDEPENDENT	29	[0, 1536]	True
HIGH_ENC_INDEPENDENT	2	[0, 1536]	True

(c) Analysis summary.

Figure 9.17: Minimum Health Test for Q11 chip1.

Tuning

Figure 9.18 shows the threshold distribution and S-curve before tuning, as well as the threshold distribution, S-curve, noise distribution, and threshold map after tuning.

The threshold distributions for the four chips before tuning are roughly centred around 2500e, but are slightly shifted between each other. The S-curve is widely smeared. After tuning, the threshold distributions are centred at slightly lower than the target 1500e, the shape is narrower, and the distribution of the four chips overlap with each other. The noise distribution centres at around 100e, which is well separated from the peak at 1500e threshold, showing that the signal and noise can be separated by the threshold setting, providing clean signal. The threshold map after tuning illustrates the position of the pixels that are not tuned well. The line at chip2 is the disabled core column.

The tuning did not pass QC, however, according to the summary, as in figure 9.19, the failed items are the untuned mean value of the threshold distribution and the tuned TDAC

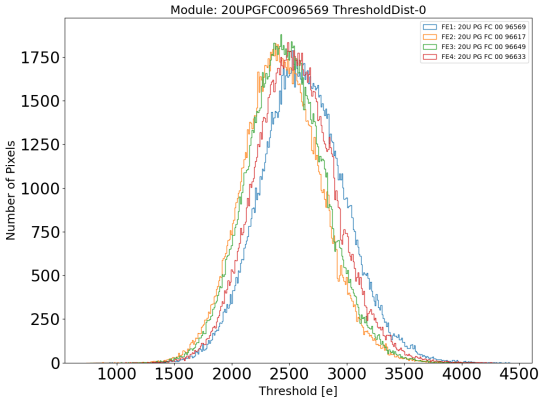

(a) Threshold distribution before tuning.

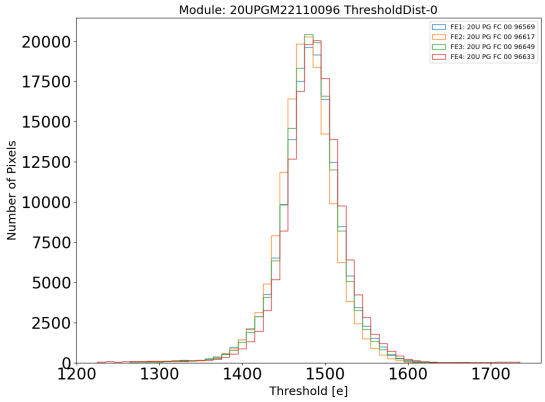

(b) Threshold distribution after tuning.

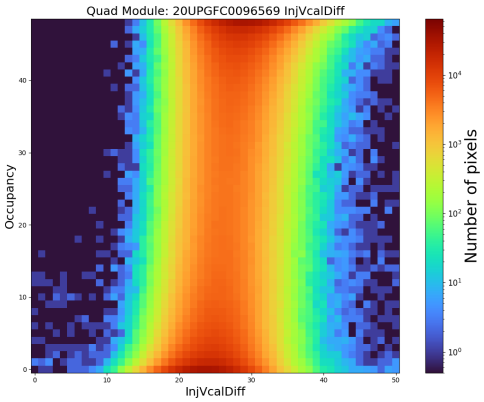

(c) S-curve before.

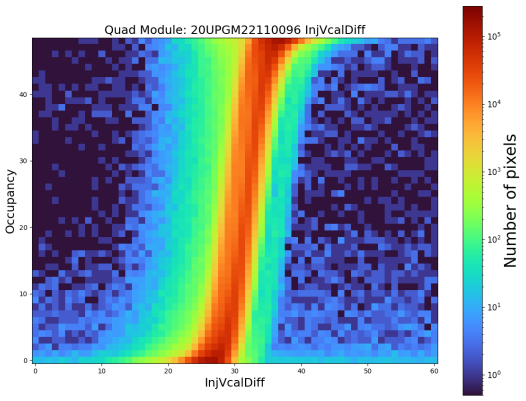

(d) S-curve after.

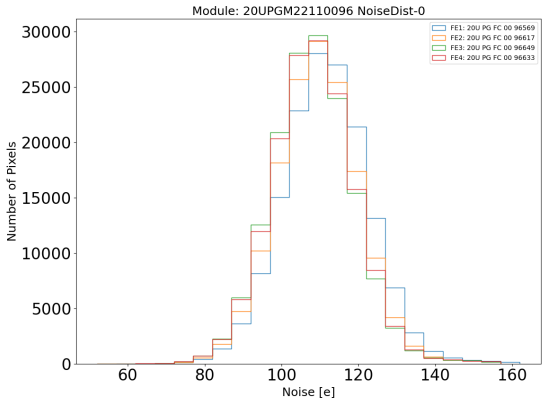

(e) Noise distribution after.

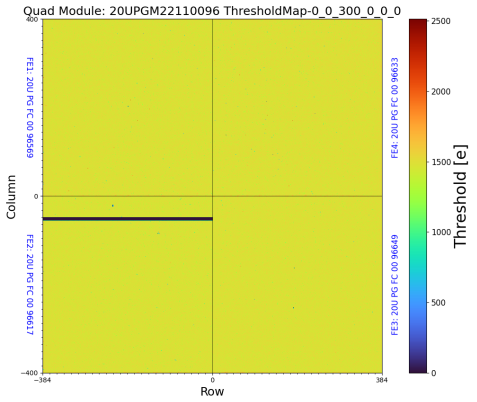

(f) Threshold map after.

Figure 9.18: Tuning of Q11: the threshold distribution and S-curve before and after tuning, and the noise distribution and threshold map after tuning.

distribution. The untuned mean is out of specification as tuning was performed multiple times on this module, therefore, the mean before tuning is already around 1500, instead of 2500 as shown in figure 9.18(a). The TDAC register is used for tuning the pixel thresholds, and the distribution should ideally be centred around 0 with a narrow width. The values

at the minimum and maximum (−15 and 15) should be minimised, which can be controlled by the global threshold tuning. However, a looser requirement on TDAC distribution could still achieve a good tuning result, as the case for Q11. Therefore, Q11 not passing the tuning QC test is a result of the testing procedure and the tight TDAC distribution specification, instead of actual module problem.

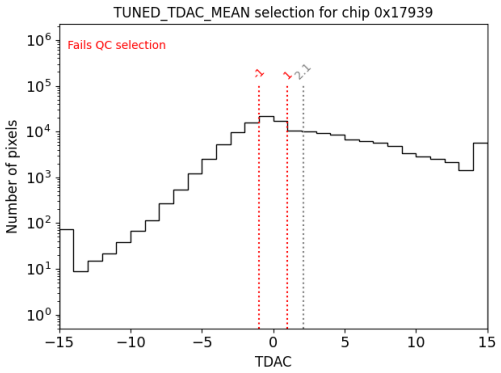

(a) TDAC distribution.

TUNING for 0x17939

Parameter	Analysis result	QC criteria	Pass
UNTUNED_THRESHOLD_MEAN	1488.0	[1700, 2700]	False
UNTUNED_THRESHOLD_SIGMA	78.0	[0, 400]	True
UNTUNED_THRESHOLD_FAILED_FITS	29	[0, 1536]	True

TUNING for 0x17939

Parameter	Analysis result	QC criteria	Pass
TUNED_THRESHOLD_MEAN	1479.6	[1350, 1650]	True
TUNED_THRESHOLD_SIGMA	48.0	[0, 50]	True
TUNED_TDAC_MEAN	2.1	[-1, 1]	False
TUNED_TDAC_SIGMA	4.9	[8.5, 12.5]	False
TUNED_TOT_MEAN	7.0	[6, 8]	True
TUNED_TOT_SIGMA	0.1	[0, 1]	True

(b) Analysis summary.

Figure 9.19: Q11 tuning QC results: TDAC distribution and analysis summary. The mean threshold before tuning is out of specification as tuning was already performed before.

Pixel Failure Analysis

Self-trigger source scan and disconnected bump scan was performed on Q12. The hit map for the disconnected bump scan is shown in figure 9.20. The scan reported 295 failed pixels.

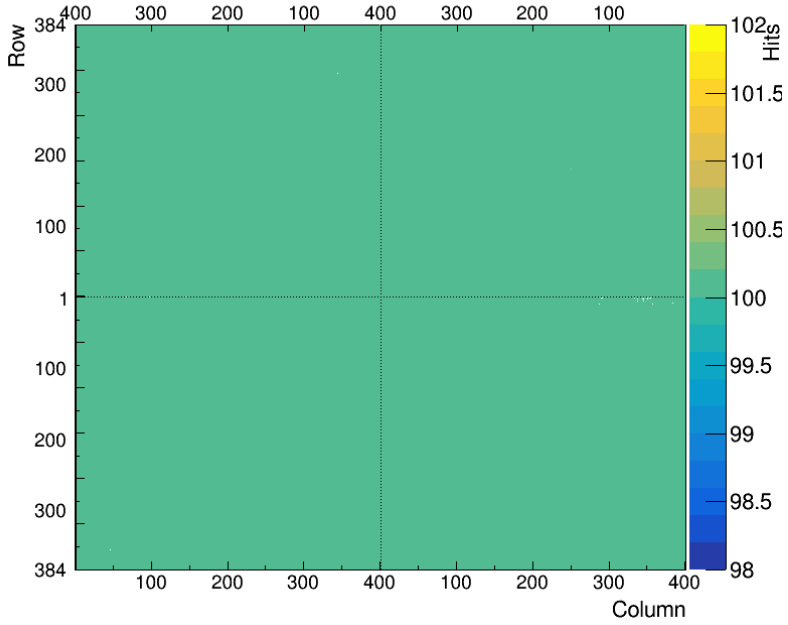

Figure 9.20: Disconnected bump scan for Q12. 295 failing pixels.

The hit map shows that the failed pixels are mainly at the boundary between chip2 and 3, and very few are between chip4 and 1.

Figure 9.21 shows the source scan result. Pixels with no hits were observed between chip2 and 3, which is consistent with the result of disconnected bump scan. The areas with lower hits correspond to the SMD components, the hit numberss are especially low at the HV capacitor, data connector, and power connector. This is because ^{90}Sr emits β particles with predominantly 0.5 MeV energy, and less probable 2 MeV. The 0.5 MeV β particles are easily absorbed, leaving less hits at the area with SMD components.

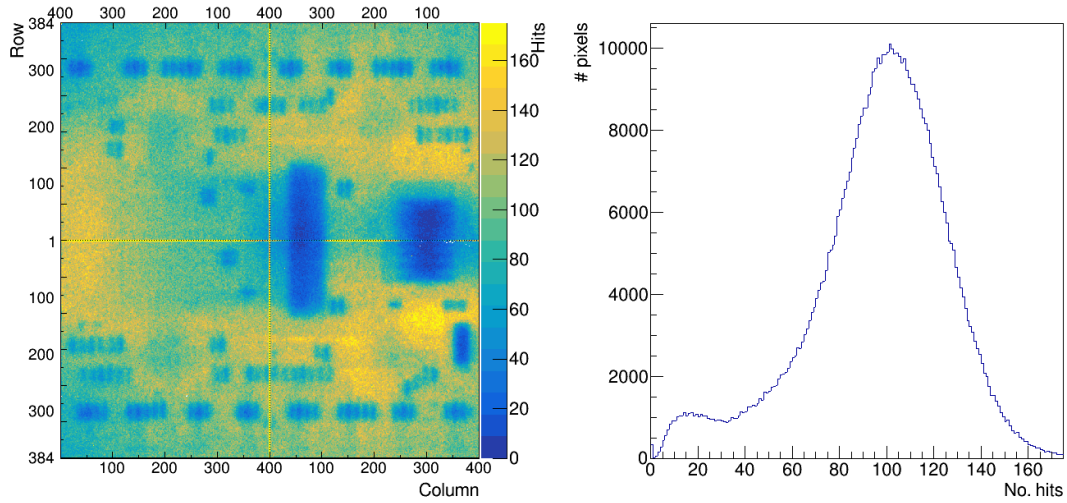

Figure 9.21: 50 min self trigger source scan on Q12 at approximately 25 cm below the source.

From the hit distribution, it can be seen that there is a small peak at 0 hits. According to the QC criteria, a disconnected pixel is defined as a pixel with < 10 hits. However, whether this can be achieved and the amount of time it takes to reach it depends on the setup. With a radioactive source in the lab, it can be difficult for the radiation to penetrate the components on the top of the flex. This is not a problem in the detector, since the incoming particle are highly relativistic and are considered mip, as explained in section 4.1.1. Practically, with a longer source scan, the peak of the hit distribution would move further to the right. If there is a gap between the distribution and the 0 hit bin, the pixels in the bin with 0 hits can be considered disconnected.

9.5. Conclusions and Outlook

For module full QC tests, a uniform testing procedure, common software tools for measurements and analysis, and a database were developed by the module testing community and provided to all testing sites. The SQ is ongoing, where the testing sites demonstrate their capabilities of performing QC tests.

In this chapter, the QC tests were explained in detail, the SQ requirements and testing setups at Göttingen were introduced, and testing results for three modules were presented.

As a testing site, Göttingen has passed the SQ blocks regarding thermal cycling setup and DCS. SQ for warm and cold tests will be passed pending approval of the HW interlock, which has been submitted for review. The planned testing setup parallelisation was shown. The digital module test block was also passed, while qualification for the full QC block is pending, until the release of the SQ document. The testing setup and procedure is continuing to be developed, to achieve streamlined and automated testing.

Using the common tools and following the required procedure, three assembled modules – Q6, Q11 and Q12 – were tested. Q6 has failing chips, and testing stopped at the initial warm stage. Q12 has also undergone warm test, to cross-check with results from Bonn, which uses BDAQ instead of YARR as the DAQ software. Q11 was tested in the initial warm stage, and the electrical test results were presented. One core column on chip2 was disabled to achieve proper functionality, and the reason for the core column issue is currently under investigation in the module testing community. Among the simple electrical tests, Q11 passed QC on ADC calibration, SLDO qualification, Vcal calibration, injection capacitance, and data transmission. One out of four chips in addition passed SLDO qualification, and two chips passed overvoltage protection. The minimum health test showed a small number of faulty pixels, and the module passed QC requirements. Tuning was successfully performed, as indicated by the resulting threshold distribution. As part of pixel failure analysis, disconnected bump scan and source scan was performed on Q12, revealing the disconnected bumps. It is important to note that there are various reasons a test might fail the QC criteria. Some failures are due to the measurements and have been resolved with updated DAQ software. The QC specifications may be overly tight and not entirely suitable. These issues were also encountered by other testing sites, and the module community is actively investigating the reasons and developing solutions.

For future tests, cross-checking of results on the same module between testing sites is essential. For Göttingen, this is planned for Q12 with Bonn. Testing of Q11 will continue, including cold test, source scan with a longer duration, and merged bump and zero-bias threshold scans for pixel failure analysis. More simple electrical tests are being developed, such as link sharing, which tests inter-chip communication. Long-term stability test and thermal cycling is also planned.

In the future, more modules will be sent to or assembled at Göttingen for QC tests as well as thermal shock tests in the shock chamber, providing larger statistics. Results from all testing sites will be pushed to PDB, and a systematical analysis can be performed using all the results, to provide information for production. In the production stage, ITkPixV2 modules can be tested with the same infrastructure, DCS and DAQ software, bringing results with proper ToT information, and providing fully functioning modules for the detector.

CHAPTER 10

Conclusions and Outlook

The Large Hadron Collider (LHC) at CERN is being upgraded to the High Luminosity LHC to enhance sensitivity to particle physics phenomena, test the Standard Model, precisely measure various parameters of particles and their processes, and attempt to find new physics beyond the Standard Model. The upgraded ATLAS ITk pixel detector aims at maintaining or improving the tracking and vertexing performance of the ATLAS ID even under HL-LHC conditions. This is especially important for b-tagging, which is crucial for physics analyses.

In order to produce modules with high performance for the ITk pixel detector, within the scope of this thesis, sensors went through quality assurance (QA) and test-beam measurements, an assembly tooling was developed to attach the sensor-FE chip hybrid with the printed circuit board, modules were assembled in pre-production, and are now under quality control (QC) tests. Site Qualification (SQ) documentation was written, and ITk sites are getting qualified for their respective tasks. Göttingen, as both an assembly and a testing site for outer barrel modules, is fully qualified for the lab infrastructure and database SQ blocks, as well as various assembly and testing sub-blocks. Work for the remaining blocks is ongoing. These lead to good progress towards production.

10.1. Sensor

Pre-production sensor characterisation measurements were carried out by various sites on sensors from three vendors in different types and thicknesses, both before and after irradiation. The planar sensor results for sensors produced by HPK and Micron were presented in this thesis. *IV* measurements on HPK diodes showed leakage current level and breakdown status within specification. Measurements on HPK (150 µm) and Micron 100 µm quad sensors are consistent with the results from the vendor. Six quad sensors from

both vendors for both thicknesses that were tested to be good in the QA were irradiated, and the IV after irradiation is also within specification.

The leakage current stability of unirradiated HPK diodes, and irradiated Micron sensors and test structures (TS) for both thicknesses is within specification. However, the fluctuation of unirradiated Micron 100 µm sensors does not pass the QA criteria.

The depletion voltages V_{dep} measured via bulk capacitance vs voltage measurements are within specification. The results were used during BM reception tests in assembly to determine the nominal V_{dep}, at which the leakage current should be compared with the specification. Measurements on irradiated sensors were also made, and showed no obvious linear or plateau regions that reveal V_{dep}. Further studies with assistance from simulation softwares (SW) will allow investigation of the reason and improve understanding of radiation damage effects on Si and sensor depletion.

Inter-pixel resistance measurements on HPK strip TS are within specification. More studies are needed for the measurements on inter-pixel TS, to properly calculate the inter-pixel resistance as a cross-check to the strip TS results. Measurements on poly-Si TS should also be further analysed, to investigate poly-Si resistance from different designs.

With the sensor pre-production QA results, a production readiness review was held. For planar sensors, HPK and Micron 150 µm sensors passed the review and moved on to production. However, Micron 100 µm sensors needed more investigation due to the leakage current stability problem. Baking test was conducted later, but did not improve stability. This problem will continue to be closely monitored at module level, for assembled modules equipped with this type of sensor.

In test-beam campaigns, unirradiated and irradiated modules were tested. For the first time, Corryvreckan was used for ITk pixel modules as reconstruction and analysis SW. Investigations and studies were conducted within the work for this thesis, to determine reasonable procedure and parameter choices, and efficiency vs bias voltage and in-pixel efficiency results were obtained for an unirradiated module equipped with an HPK 150 µm sensor. The efficiency at 20 V reverse bias voltage is lower than that at 40 V, but is already above the required limit. Further increasing the bias voltage does not continue to increase the efficiency. The measured efficiency results were shown to be related to the reference modules: using FEI4 as reference results in an efficiency approximately 0.2 % higher than that calculated using an ITkPixV1.1 module. This difference is consistent and independent of bias voltages from 20 to 120 V. However, further studies on the spacial cut and masking results are needed to draw meaningful conclusions. Disabling pixels with no hits or excessive hits also results in the efficiency being 0.1 to 0.2 % higher than without masking, as expected. Data was taken also with different thresholds, and in later test-beam campaigns, unirradiated modules with Micron 100 µm sensors and irradiated modules were tested. Reconstruction and analysis of these data can be performed to investigate the behaviour of Micron 100 µm sensors with leakage current stability issues in beam, as well as the effect of irradiation on the efficiency.

10.2. Assembly

Based on results from the ITk Pixel Quad Assembly Tooling V1 used for RD53A assembly, tooling V2 was developed. The performance was demonstrated with both dummy and real components. The xy-alignment, thickness, and flatness of the glued samples are within specification. The stencil tool, in combination with the stencil, applies a repeatable amount of glue on the flex. Extensive studies on different stencil patterns achieved higher glue coverage and good structural integrity. During testing, temporary kapton tape masking was used as a solution for the problem with glue seepage into HV hole, and a procedure was developed to avoid the tape hindering the setting of target glue thickness. This solution was tested and found reliable. During gluing tests, one of the tabs connecting the flex body to the flex frame was found to be a weak point, and problem with the SMD components clashing with the flex jig cutout was identified, leading to changes in design on the flex tabs and the flex jig cutout of the tooling. After the adaptations, damages to the flex can be avoided, and setting of the glue thickness is influenced less by the SMD components.

The common tooling designed, manufactured, and tested at Göttingen makes it possible to assemble over ten thousand quad modules in pre-production and production, with good and consistent alignment and dimensions independent of the assembly personnel.

Within the work for this thesis, the BM *IV* sub-block for the assembly SQ documentation was written, and SQ materials from assembly sites on the quad module component reception tests were reviewed. All assembly sites were qualified for these sub-blocks. Tooling V2 were sent to assembly sites. These bring the pre-production module assembly, and the upcoming production on good track.

Göttingen is qualified for module component reception tests. The assembly block was passed partially, and the wire-bonding and backside flatness parts are in progress. 17 quad components were received and tested at Göttingen, and 16 were assembled with good alignment and thickness. In production, Göttingen will produce around 600 quad modules for the outer barrel of the ITk pixel detector.

10.3. Module QC

Following the SQ requirements, testing setups for module full QC tests are being developed, and the testing procedures practiced. The warm, cold, source, and thermal cycling testing setups, DCS with SW interlock, and digital module QC tests fulfilled SQ requirements. The hardware interlock SQ material was submitted.

Three modules assembled at Göttingen and Bonn were tested. Testing experience shows that proper powering of modules and keeping the SW tools up-to-date are also important for performing reliable QC tests and producing results that actually reflect the module quality. Some FE chips function properly only after disabling one or more core columns, and the modules function worse in cold tests: FE chips that function well in warm may no longer work in cold. Testing results showed that no chips passed the low power mode

and undershunt protection QC tests. In low power mode, the offset voltage is consistently lower than the specification. For tuning, modules that are successfully tuned with good threshold distribution can still fail the QC criteria, as the TDAC distribution QC criteria is tight, and the module might have been tuned multiple times, therefore not fulfilling the pre-tuning requirements.

These findings are in line with experiences from other testing sites. Various investigations are ongoing in the module testing community on the issues emerged in pre-production, including pin-pointing the reason for the core column issue and the degraded performance in cold temperature, bug fixing in central SW tools, and defining adequate QC criteria. With more testing results from all sites, common issues and tendencies are expected to be found, and problems will be addressed. The results will also provide important information for making sensible decisions and specifications for production modules.

Future module QC testing at Göttingen will benefit from setup parallelisation and automated testing procedures, to achieve streamlined testing that reaches the required production rate. Undershunt protection, data transmission, link sharing, full pixel failure analysis, cold electrical QC tests, thermal cycling, and stability test will be performed. More pre-production ITkPixV1.1 modules will be produced and tested. In production, ITkPixV2 modules will come with bug fixes, which will bring new features and characteristics, therefore interesting QC testing results, and provide unprecedented performance for the ITk pixel detector.

Bibliography

[1] Y. Tian et al., *ATLAS ITk Pixel Pre-production Planar Sensor Characterisation for the HL-LHC Upgrade*, in: *Proceedings of 10th International Workshop on Semiconductor Pixel Detectors for Particles and Imaging — PoS(Pixel2022)* (Santa Fe, New Mexico, USA, Dec. 12–16, 2022), **420**, 067, ATL-ITK-PROC-2023-006

[2] Š. Hadžić, *Production and performance of silicon pixel modules with planar sensors for the ATLAS ITk upgrade*, urn:nbn:de:bvb:19-319588, PhD thesis, University of Munich, 2023

[3] S. Möbius, *Pixel Detector Studies for the ATLAS ITk Upgrade for the HL-LHC*, II.Physik-UniGö-Diss-2022/03, PhD thesis, University of Göttingen, 2022

[4] J. J. Thomson, *XL. Cathode Rays*, Phil. Mag. **44** (1897) 293

[5] M. Planck, *Über das Gesetz der Energieverteilung im Normalspectrum*, Ann. Phys. **309** (1901) 553

[6] S. L. Glashow, *Partial-symmetries of weak interactions*, Nucl. Phys. **22** (1961) 579

[7] S. Weinberg, *A Model of Leptons*, Phys. Rev. Lett. **19** (1967) 1264

[8] A. Salam, *Weak and Electromagnetic Interactions*, Conf. Proc. C **680519** (1968) 367

[9] S. L. Glashow, J. Iliopoulos, and L. Maiani, *Weak Interactions with Lepton-Hadron Symmetry*, Phys. Rev. D **2** (1970) 1285

[10] G. 't Hooft, *Renormalization of massless Yang-Mills fields*, Nucl. Phys. B **33** (1971) 173

[11] G. 't Hooft, *Renormalizable Lagrangians for massive Yang-Mills fields*, Nucl. Phys. B **35** (1971) 167

[12] H. Georgi and S. L. Glashow, *Unified Weak and Electromagnetic Interactions without Neutral Currents*, Phys. Rev. Lett. **28** (1972) 1494

[13] G. 't Hooft and M. Veltman, *Regularization and renormalization of gauge fields*, Nucl. Phys. B **44** (1972) 189

[14] G. 't Hooft and M. Veltman, *Combinatorics of gauge fields*, Nucl. Phys. B **50** (1972) 318

[15] D. J. Gross and F. Wilczek, *Ultraviolet Behavior of Non-Abelian Gauge Theories*, Phys. Rev. Lett. **30** (1973) 1343

[16] H. D. Politzer, *Reliable Perturbative Results for Strong Interactions?*, Phys. Rev. Lett. **30** (1973) 1346

[17] H. David Politzer, *Asymptotic freedom: An approach to strong interactions*, Phys. Rept. **14** (1974) 129

[18] ATLAS Collaboration, *The ATLAS Experiment at the CERN Large Hadron Collider*, JINST **3** (2008) S08003

[19] CMS Collaboration, *The CMS experiment at the CERN LHC*, JINST **3** (2008) S08004

[20] LHCb Collaboration, *The LHCb Detector at the LHC*, JINST **3** (2008) S08005

[21] ALICE Collaboration, *The ALICE experiment at the CERN LHC*, JINST **3** (2008) S08002

[22] ATLAS Collaboration, *Observation of a new particle in the search for the Standard Model Higgs boson with the ATLAS detector at the LHC*, Phys. Lett. B **716** (2012) 1

[23] CMS Collaboration, *Observation of a new boson at a mass of 125 GeV with the CMS experiment at the LHC*, Phys. Lett. B **716** (2012) 30

[24] U. Baur, T. Plehn, and D. L. Rainwater, *Measuring the Higgs Boson Self Coupling at the LHC and Finite Top Mass Matrix Elements*, Phys. Rev. Lett. **89** (2002) 151801

[25] U. Baur, T. Plehn, and D. L. Rainwater, *Determining the Higgs Boson Selfcoupling at Hadron Colliders*, Phys. Rev. D **67** (2003) 033003

[26] U. Baur, T. Plehn, and D. L. Rainwater, *Probing the Higgs selfcoupling at hadron colliders using rare decays*, Phys. Rev. D **69** (2004) 053004

[27] F. Gianotti et al., *Physics potential and experimental challenges of the LHC luminosity upgrade*, Eur. Phys. J. C **39** (2005) 293

[28] *Report on the Physics at the HL-LHC, and Perspectives for the HE-LHC*, CERN Yellow Reports: Monographs, CERN-2019-007, 2019

[29] *High-Luminosity Large Hadron Collider (HL-LHC): Technical Design Report V. 0.1*, CERN Yellow Reports: Monographs, CERN-2017-007-M, 2017

[30] R. L. Workman et al. (Particle Data Group), *Review of Particle Physics*, PTEP **2022** (2022) 083C01

[31] A. Quadt, *Top quark physics at hadron colliders*, Eur. Phys. J. C **48** (2006) 835

[32] P. W. Anderson, *Plasmons, Gauge Invariance, and Mass*, Phys. Rev. **130** (1963) 439

[33] P. Higgs, *Broken symmetries, massless particles and gauge fields*, Phys. Lett. **12** (1964) 132

[34] F. Englert and R. Brout, *Broken Symmetry and the Mass of Gauge Vector Mesons*, Phys. Rev. Lett. **13** (1964) 321

[35] G. S. Guralnik, C. R. Hagen, and T. W. B. Kibble, *Global Conservation Laws and Massless Particles*, Phys. Rev. Lett. **13** (1964) 585

[36] J. Woithe, G. J. Wiener, and F. F. V. der Veken, *Let's have a coffee with the Standard Model of particle physics!*, Phys. Educ. **52** (2017) 034001

[37] A. D. Sakharov, *Violation of CP Invariance, C asymmetry, and baryon asymmetry of the universe*, Pisma Zh. Eksp. Teor. Fiz. **5** (1967) 32

[38] T. D. Lee and C. N. Yang, *Question of Parity Conservation in Weak Interactions*, Phys. Rev. **104** (1956) 254

[39] C. S. Wu et al., *Experimental Test of Parity Conservation in Beta Decay*, Phys. Rev. **105** (1957) 1413

[40] J. H. Christenson et al., *Evidence for the* 2π *Decay of the* K_2^0 *Meson*, Phys. Rev. Lett. **13** (1964) 138

[41] M. Kobayashi and T. Maskawa, *CP Violation in the Renormalizable Theory of Weak Interaction*, Prog. Theor. Phys. **49** (1973) 652

[42] A. Abashian et al. (Belle Collaboration), *Measurement of the CP violation parameter* $\sin 2\phi_1$ *in* B_d^0 *meson decays*, Phys. Rev. Lett. **86** (2001) 2509

[43] B. Aubert et al. (BABAR Collaboration), *Observation of CP Violation in the* B^0 *Meson System*, Phys. Rev. Lett. **87** (2001) 091801

[44] Planck Collaboration, *Planck 2018 results. VI. Cosmological parameters*, A&A **641** (2020) A6, Erratum: A&A 652 (2021) C4

[45] J. Alexander et al., *Dark Sectors 2016 Workshop: Community Report*, in: FERMILAB-CONF-16-421, 2016

[46] B. Batell, M. Pospelov, and A. Ritz, *Exploring portals to a hidden sector through fixed targets*, Phys. Rev. D **80** (2009)

[47] P. Fayet, *Effects of the spin-1 partner of the goldstino (gravitino) on neutral current phenomenology*, Phys. Lett. B **95** (1980) 285

[48] P. Fayet, *The fifth interaction in grand-unified theories: A new force acting mostly on neutrons and particle spins*, Phys. Lett. B **172** (1986) 363

[49] P. Fayet, *A new long-range force?*, Phys. Lett. B **171** (1986) 261

[50] J. Batley et al. (NA48/2 Collaboration), *Search for the dark photon in* $\pi 0$ *decays*, Phys. Lett. B **746** (2015) 178

[51] LHCb Collaboration, *Search for Dark Photons Produced in 13 TeV pp Collisions*, Phys. Rev. Lett. **120** (2018)

[52] M. J. Duff, *Kaluza-Klein theory in perspective*, in: *The Oskar Klein Centenary Nobel Symposium* (Stockholm, Sweden, Sept. 19–21, 1994), 22, NI-94-015, CTP-TAMU-22-94

[53] E. Witten, *String theory dynamics in various dimensions*, Nucl. Phys. B **443** (1995) 85

[54] G. R. Dvali, G. Gabadadze, and G. Senjanovic, *Constraints on extra time dimensions*, *The Many Faces of the Superworld: Yuri Golfand Memorial Volume*, ed. by M. A. Shifman, NYU-TH-99-08-02, WORLD SCIENTIFIC, 1999, 525, ISBN: 9789812793850

[55] R. Sundrum, *Fat gravitons, the cosmological constant and submillimeter tests*, Phys. Rev. D **69** (2004) 044014

[56] D. J. Kapner et al., *Tests of the gravitational inverse-square law below the dark-energy length scale*, Phys. Rev. Lett. **98** (2007) 021101

[57] I. Antoniadis et al., *New dimensions at a millimeter to a Fermi and superstrings at a TeV*, Phys. Lett. B **436** (1998) 257

[58] N. Arkani-Hamed, S. Dimopoulos, and G. R. Dvali, *The Hierarchy problem and new dimensions at a millimeter*, Phys. Lett. B **429** (1998) 263

[59] ATLAS Collaboration, *Search for TeV-scale gravity signatures in high-mass final states with leptons and jets with the ATLAS detector at* $\sqrt{s} = 13$ *TeV*, Phys. Lett. B **760** (2016) 520

[60] ATLAS Collaboration, *Combined measurements of Higgs boson production and decay using up to* 139 fb^{-1} *of proton-proton collision data at* $\sqrt{s} = 13$ *TeV collected with the ATLAS experiment*, ATLAS-CONF-2021-053, 2021

[61] E. Asakawa et al., *Higgs boson pair production in new physics models at hadron, lepton, and photon colliders*, Phys. Rev. D **82** (2010) 115002

[62] S. Di Vita et al., *A global view on the Higgs self-coupling at lepton colliders*, JHEP **02** (2018) 178

[63] H. Haseroth et al., *History, developments and recent performance of the CERN Linac 1*, in: *16th International Linear Accelerator Conference*, LINAC 92 (Ottawa, Ontario, Canada, Aug. 23–28, 1992), 58, CERN-PS-92-53-HI

[64] H. Haseroth, *The CERN heavy ion facility*, Conf. Proc. C **940627** (1995) 138

[65] J. Vollaire et al., *Linac4 design report*, CERN Yellow Reports: Monographs, CERN-2020-006, 2020

[66] L. Evans and P. Bryant, *LHC Machine*, JINST **3** (2008) S08001

[67] E. Lopienska, *The CERN accelerator complex, layout in 2022. Complexe des accélérateurs du CERN en janvier 2022*, CERN-GRAPHICS-2022-001, 2022, General Photo

[68] *Design Study of the Large Hadron Collider (LHC): A Multiparticle Collider in the LEP Tunnel*, CERN Yellow Reports: Monographs, CERN-91-03, CERN-YELLOW-91-03, 1991

[69] M. Bajko et al., *Report of the Task Force on the Incident of 19th September 2008 at the LHC*, LHC-PROJECT-Report-1168, CERN-LHC-PROJECT-Report-1168, 2009

[70] L. Arnaudon et al., *Effects of terrestrial tides on the LEP beam energy*, Nucl. Instrum. Meth. A **357** (1995) 249

[71] E. Todesco and J. Wenninger, *Large Hadron Collider momentum calibration and accuracy*, Phys. Rev. Accel. Beams **20** (2017) 081003

[72] ATLAS ITk Collaboration, *LHC/HL-LHC Plan (last update January 2025)*, https://hilumilhc.web.cern.ch/content/hl-lhc-project (visited on Mar. 12, 2025)

[73] J. Gareyte, *LHC main parameters*, Part. Accel. **50** (1995) 61

[74] R. M. Bianchi (ATLAS Collaboration), *ATLAS experiment schematic illustration*, ATLAS-PHOTO-2022-055, 2022, General Photo

[75] *Event Displays from Collision Data*, https://twiki.cern.ch/twiki/bin/view/AtlasPublic/EventDisplayRun2Collisions (visited on Feb. 16, 2021)

[76] J. Pequenao and P. Schaffner, *How ATLAS detects particles: diagram of particle paths in the detector*, CERN-EX-1301009, 2013

[77] A. M. Rodriguez Vera and J. Antunes Pequenao, *ATLAS Detector Magnet System*, ATLAS-PHOTO-2021-029, 2021, General Photo

[78] M. Brice, *ATLAS barrel detector*, CERN-EX-0305043, 2003

[79] T. Kawamoto et al., *New Small Wheel Technical Design Report*, CERN-LHCC-2013-006, ATLAS-TDR-020, 2013

[80] The ATLAS IBL Collaboration, *Production and Integration of the ATLAS Insertable B-Layer*, JINST **13** (2018) T05008

[81] M. Aleksa et al., *ATLAS Liquid Argon Calorimeter Phase-I Upgrade: Technical Design Report*, CERN-LHCC-2013-017, ATLAS-TDR-022, 2013

[82] ATLAS Collaboration, *Technical Design Report for the Phase-I Upgrade of the ATLAS TDAQ System*, CERN-LHCC-2013-018, ATLAS-TDR-023, 2013

[83] L. Adamczyk et al., *Technical Design Report for the ATLAS Forward Proton Detector*, CERN-LHCC-2015-009, ATLAS-TDR-024, 2015

[84] ATLAS Collaboration, *Technical Design Report for the Phase-II Upgrade of the ATLAS Muon Spectrometer*, CERN-LHCC-2017-017, ATLAS-TDR-026, 2017

[85] ATLAS Collaboration, *Technical Design Report for the Phase-II Upgrade of the ATLAS TDAQ System*, CERN-LHCC-2017-020, ATLAS-TDR-029, 2017

[86] ATLAS Collaboration, *Technical Design Report: A High-Granularity Timing Detector for the ATLAS Phase-II Upgrade*, CERN-LHCC-2020-007, ATLAS-TDR-031, 2020

[87] ATLAS Collaboration, *Technical Design Report for the ATLAS Inner Tracker Pixel Detector*, CERN-LHCC-2017-021, ATLAS-TDR-030, 2017

[88] ATLAS Collaboration, *Technical Design Report for the ATLAS Inner Tracker Strip Detector*, CERN-LHCC-2017-005, ATLAS-TDR-025, 2017

[89] ATLAS Collaboration, *Expected tracking and related performance with the updated ATLAS Inner Tracker layout at the High-Luminosity LHC*, ATL-PHYS-PUB-2021-024, 2021

[90] Y. Fukuda et al. (Super-Kamiokande), *The Super-Kamiokande detector*, Nucl. Instrum. Meth. A **501** (2003) 418, ed. by V. A. Ilyin, V. V. Korenkov, and D. Perret-Gallix

[91] H. Bethe, *Zur Theorie des Durchgangs schneller Korpuskularstrahlen durch Materie (Theory of the Passage of Fast Corpuscular Rays Through Matter)*, Ann. Phys. **397** (1930) 325

[92] F. Bloch, *Zur Bremsung Rasch Bewegter Teilchen beim Durchgang durch Materie*, Ann. Phys. **408** (1933) 285

[93] F. Bloch, *Bremsvermögen von Atomen mit mehreren Elektronen*, Z. Phys. **81** (1933) 363

[94] P. H. Barrett et al., *Interpretation of Cosmic-Ray Measurements Far Underground*, Rev. Mod. Phys. **24** (1952) 133

[95] L. D. Landau, *On the Energy Loss of Fast Particles by Ionisation*, J. Phys. (USSR) **8** (1944) 201

[96] M. J. Berger and S. M. Seltzer, *Tables of Energy Losses and Ranges of Electrons and Positrons*, NASA SP-3012, Scientific and Technical Information Division, National Aeronautics and Space Administration, 1964

[97] H. Kolanoski and N. Wermes, *Particle Detectors*, Oxford University Press, 2020, ISBN: 978-0-19-885836-2

[98] Y.-S. Tsai, *Pair Production and Bremsstrahlung of Charged Leptons*, Rev. Mod. Phys. **46** (1974) 815, Erratum: Rev. Mod. Phys. 49 (1977) 421

[99] B. Rossi, *High Energy Particles*, Prentice-Hall, 1952

[100] H. Jansen et al., *Performance of the EUDET-type beam telescopes*, EPJ Tech. Instrum. **3** (2016) 7

[101] G. R. Lynch and O. I. Dahl, *Approximations to multiple Coulomb scattering*, Nucl. Instrum. Meth. B **58** (1991) 6

[102] L. Rossi et al., *Pixel Detectors: From Fundamentals to Applications*, Particle Acceleration and Detection, Berlin: Springer, 2006, ISBN: 978-3-642-06652-8

[103] H. C. Beck, *Development of Pixel Module Assembly Processes for the Phase 2 Upgrade of the ATLAS Detector and Test Beam Measurements with Diamond Pixel Detectors*, II.Physik-UniGö-Diss-2019/08, PhD thesis, University of Göttingen, 2020

[104] C. Grah, *Pixel detector modules using MCM-D technology*, Nucl. Instrum. Meth. A **465** (2001) 211

[105] L. Paolozzi et al., *Picosecond Avalanche Detector — working principle and gain measurement with a proof-of-concept prototype*, JINST **17** (2022) P10032

[106] J. Schmidt et al., *Pixel detector hybridisation with anisotropic conductive films*, JINST **18** (2023) C01040

[107] W. Shockley, *Currents to conductors induced by a moving point charge*, J. Appl. Phys. **9** (1938) 635

[108] A. Chilingarov, *Temperature dependence of the current generated in Si bulk*, JINST **8** (2013) P10003

[109] A. Vasilescu and G. Lindström, *Notes on the fluence normalisation based on the NIEL scaling hypothesis*, ROSE/TN/2000-02, 2000

[110] M. Moll et al., *Relation between microscopic defects and macroscopic changes in silicon detector properties after hadron irradiation*, Nucl. Instrum. Meth. B **186** (2002) 100

[111] G. Lindström et al. (ROSE/CERN-RD48 Collaboration), *Radiation hard silicon detectors – developments by the RD48 (ROSE) Collaboration*, Nucl. Instrum. Meth. A **466** (2001) 308

[112] M. Moll, E. Fretwurst, and G. Lindström (ROSE/CERN-RD48 Collaboration), *Leakage current of hadron irradiated silicon detectors – material dependence*, Nucl. Instrum. Meth. A **426** (1999) 87

[113] R. Wunstorf, *Systematische Untersuchungen zur Strahlenresistenz von Silizium-Detektoren für die Verwendung in Hochenergiephysik-Experimenten*, DESY-2013-00725, PhD thesis, University of Hamburg, 1992

[114] M. Moll, *Radiation damage in silicon particle detectors: Microscopic defects and macroscopic properties*, DESY-THESIS-1999-040, PhD thesis, University of Hamburg, 1999

[115] J. Srour and J. McGarrity, *Radiation effects on microelectronics in space*, Proc. IEEE **76** (1988) 1443

[116] J. R. Schwank et al., *Radiation Effects in MOS Oxides*, IEEE Trans. Nucl. Sci. **55** (2008) 1833

[117] C. T. Sah, *Origin of Interface States and Oxide Charges Generated by Ionizing Radiation*, IEEE Trans. Nucl. Sci. **23** (1976) 1563

[118] G. F. Derbenwick and B. L. Gregory, *Process Optimization of Radiation-Hardened CMOS Integrated Circuits*, IEEE Trans. Nucl. Sci. **22** (1975) 2151

[119] E. Fretwurst et al. (RD2 Collaboration), *Reverse annealing of the effective impurity concentration and long term operational scenario for silicon detectors in future collider experiments*, Nucl. Instrum. Meth. A **342** (1994) 119

[120] M. Moll, E. Fretwurst, and G. Lindström (ROSE/CERN-RD48 Collaboration), *Investigation on the improved radiation hardness of silicon detectors with high oxygen concentration*, Nucl. Instrum. Meth. A **439** (2000) 282

[121] M. Boscardin et al., *Advances in 3D Sensor Technology by Using Stepper Lithography*, Front. in Phys. **8** (2021) 647

[122] J. Chistiansen and M. Garcia-Sciveres, *RD Collaboration Proposal: Development of pixel readout integrated circuits for extreme rate and radiation*, CERN-LHCC-2013-008, LHCC-P-006, 2013

[123] M. Garcia-Sciveres (RD53 Collaboration), *The RD53A Integrated Circuit*, CERN-RD53-PUB-17-001, 2017

[124] M. Garcia-Sciveres, F. Loddo, and J. Christiansen (RD53 Collaboration), *RD53B Manual*, CERN-RD53-PUB-19-002, 2019

[125] M. Garcia-Sciveres (RD53 Collaboration), *RD53C Chip Manual*, CERN-RD53-PUB-24-001, 2024

[126] M. Mironova (For the RD53 Collaboration), *Measurements of the radiation damage to the ITkPixV1 chip in X-ray irradiations*, Nucl. Instrum. Meth. A **1039** (2022) 166947

[127] T. Gleisberg et al., *Event generation with SHERPA 1.1*, JHEP **2009** (2009) 007

[128] ATLAS Collaboration, *Software Performance of the ATLAS Track Reconstruction for LHC Run 3*, ATL-PHYS-PUB-2021-012, 2021

[129] H. M. Gray, *The Charged Particle Multiplicity at Center of Mass Energies from 900 GeV to 7 TeV measured with the ATLAS Experiment at the Large Hadron Collider*, CaltechTHESIS:11232010-093045913, PhD thesis, California Institute of Technology, 2010

[130] ATLAS Collaboration, *Early Inner Detector Tracking Performance in the 2015 data at $\sqrt{s}$ = 13 TeV*, ATL-PHYS-PUB-2015-051, 2015

[131] ATLAS Collaboration, *Development of ATLAS Primary Vertex Reconstruction for LHC Run 3*, ATL-PHYS-PUB-2019-015, 2019

[132] J. Shelton, *Jet Substructure*, in: *Proceedings of the 2012 Theoretical Advanced Study Institute in Elementary Particle Physics: Searching for New Physics at Small and Large Scales*, TASI 2012 (Boulder, Colorado, USA, June 4–29, 2012), 303, ed. by M. Schmaltz and E. Pierpaoli, arXiv: 1302.0260 [hep-ph]

[133] ATLAS Collaboration, *Performance of jet substructure techniques for large-R jets in proton-proton collisions at $\sqrt{s}$ = 7 TeV using the ATLAS detector*, JHEP **09** (2013) 076

[134] S. Catani et al., *Longitudinally-invariant $k_\perp$-clustering algorithms for hadron-hadron collisions*, Nucl. Phys. B **406** (1993) 187

[135] S. D. Ellis and D. E. Soper, *Successive combination jet algorithm for hadron collisions*, Phys. Rev. D **48** (1993) 3160

[136] Y. L. Dokshitzer et al., *Better jet clustering algorithms*, JHEP **08** (1997) 001

[137] M. Wobisch and T. Wengler, *Hadronization corrections to jet cross-sections in deep inelastic scattering*, in: *Proceedings of Workshop on Monte Carlo Generators for HERA Physics* (Hamburg, Germany, Apr. 27–30, 1998), PITHA-99-16, ed. by A. T. Doyle et al.

[138] M. Cacciari, G. P. Salam, and G. Soyez, *The anti-k_t jet clustering algorithm*, JHEP **2008** (2008) 063

[139] ATLAS Collaboration, *Jet reconstruction and performance using particle flow with the ATLAS Detector*, Eur. Phys. J. C **77** (2017) 466

[140] ATLAS Collaboration, *Optimisation and performance studies of the ATLAS b-tagging algorithms for the 2017-18 LHC run*, ATL-PHYS-PUB-2017-013, 2017

[141] ATLAS Collaboration, *ATLAS b-jet identification performance and efficiency measurement with $t\bar{t}$ events in pp collisions at $\sqrt{s} = 13$ TeV*, Eur. Phys. J. C **79** (2019) 970

[142] ATLAS Collaboration, *Measurement of the associated production of a top-antitop-quark pair and a Higgs boson decaying into a $b\bar{b}$ pair in pp collisions at $\sqrt{s} = 13$ TeV using the ATLAS detector at the LHC*, Eur. Phys. J. C **85** (2025) 210

[143] ATLAS Collaboration, *A Continuous Calibration of the ATLAS Flavor-Tagging Classifiers via Optimal Transportation Maps*, ATLAS-COM-CONF-2024-025, 2024

[144] ATLAS ITk Collaboration, *Planar Pixels Tendering Specification document*, ATLAS Internal Note, `https://edms.cern.ch/document/2570161/1`, AT2-IP-ES-0022 v.1, 2021

[145] S. Passaggio (on behalf of the ATLAS ITk Collaboration), *The ATLAS ITk Pixel Detector: status and roadmap*, in: *Talk at the 13th International Hiroshima Symposium on the Development and Application of Semiconductor Tracking Detectors*, HSTD13 (Vancouver, Canada, Dec. 3–8, 2023), ATL-ITK-SLIDE-2023-636

[146] K. Nakamura et al., *Development of a radiation tolerant fine pitch planar pixel detector by HPK/KEK*, Nucl. Instrum. Meth. A **924** (2019) 64

[147] S. Terzo (on behalf of the ATLAS Collaboration), *ATLAS ITk pixel detector overview*, in: *Proceedings of 40th International Conference on High Energy physics — PoS(ICHEP2020)* (Prague, Czech Republic, July 28–Aug. 6, 2020), **390**, 878, ATL-ITK-PROC-2020-007

[148] J.-C. Beyer, *Optimisation of pixel modules for the ATLAS inner tracker at the high-luminosity LHC*, urn:nbn:de:bvb:19-239390, PhD thesis, University of Munich, 2019

[149] S. Terzo (on behalf of the ATLAS Collaboration), *Novel pixel sensors for the Inner Tracker upgrade of the ATLAS experiment*, in: *Talk at the 6th International Conference on Technology and Instrumentation in Particle Physics*, TIPP 2023 (Cape Town, South Africa, Sept. 4–8, 2023), ATL-ITK-SLIDE-2023-438

[150] R. L. Bates et al., *Charge collection studies and electrical measurements of heavily irradiated 3D double-sided sensors and comparison to planar strip detectors*, IEEE Trans. Nucl. Sci. **58** (2011) 3370

[151] Private communication, Dec. 14, 2022

[152] R. Marco-Hernández, *A portable readout system for silicon microstrip sensors*, Nucl. Instrum. Meth. A **623** (2010) 207

[153] M. S. Alam et al., *The ATLAS Silicon Pixel Sensors*, ATL-INDET-99-012, CERN-EP-99-152, 2001

[154] S. Spannagel et al., *Allpix^2: A modular simulation framework for silicon detectors*, Nucl. Instrum. Meth. A **901** (2018) 164

[155] G. Calderini et al., *Qualification of the first pre-production 3D FBK sensors with ITkPixV1 readout chip*, in: *Proceedings of 10th International Workshop on Semiconductor Pixel Detectors for Particles and Imaging — PoS(Pixel2022)*, Pixel2022 (Santa Fe, New Mexico, USA, Dec. 12–16, 2022), ATL-ITK-PROC-2023-005

[156] D. Banerjee et al., *The North Experimental Area at the Cern Super Proton Synchrotron*, CERN-ACC-NOTE-2021-0015, 2021

[157] L. Gatignon, *Design and Tuning of Secondary Beamlines in the CERN North and East Areas*, CERN-ACC-Note-2020-0043, 2020

[158] V. Baggiolini et al., *The CESAR Project using J2EE for Accelerator Controls*, in: *Proceedings of the 9th International Conference on Accelerator and Large Experimental Physics Control Systems*, ICALEPCS 2003 (Gyeongju, Korea, Oct. 13–17, 2003), CERN-AB-2004-001-CO

[159] EUDET Consortium, *Infrastructure for Detector Research and Development towards the International Linear Collider*, arXiv: 1201.4657 [physics.ins-det], 2012

[160] I. Rubinskiy (on behalf of EUDET, AIDA Consortia), *An EUDET/AIDA Pixel Beam Telescope for Detector Development*, in: *Proceedings of 2nd International Conference on Technology and Instrumentation in Particle Physics 2011*, TIPP 2011 (Chicago, Illinois, USA, June 9–14, 2011), AIDA-CONF-2015-035, ed. by T. Liu

[161] Y. Teng et al., *Development of the Readout Electronics for a MAPS-Based Beam Telescope*, IEEE Trans. Nucl. Sci. **70** (2023) 82

[162] J. Brau et al., *Lycoris — A large-area, high resolution beam telescope*, JINST **16** (2021) P10023

[163] C. Hu-Guo et al., *First reticule size MAPS with digital output and integrated zero suppression for the EUDET-JRA1 beam telescope*, Nucl. Instrum. Meth. A **623** (2010) 480

[164] *EUDAQ2 – A Flexible Data Acquisition Software Framework for Common Test Beams*, JINST **14** (2019) P10033

[165] D. Cussans, *Description of the JRA1 Trigger Logic Unit (TLU), v0.2c*, EUDET-Memo-2009-4, 2009

[166] P. Ahlburg et al., *EUDAQ – A Data Acquisition Software framework for Common Beam Telescopes*, JINST **15** (2020) P01038

[167] S. Spannagel, *Test Beam Measurements for the Upgrade of the CMS Pixel Detector and Measurement of the Top Quark Mass from Differential Cross Sections*, DESY-THESIS-2016-010, PhD thesis, DESY, 2016

[168] G. Claus, *DAQ Systems based on NI COTS for pixels sensors characterization in beam test (FlexRIO at EUDET for MIMOSA Particle Detector)*, in: National Instruments Big Physics Symposium (Austin, Texas, USA, Aug. 1, 2011), 2011

[169] EUDAQ Development Team, *EUDAQ User Manual*, for EUDAQ version v1.7, 2016

[170] M. Backhaus et al., *Development of a versatile and modular test system for ATLAS hybrid pixel detectors*, Nucl. Instrum. Meth. A **650** (2011) 37

[171] T. Heim, *Performance of the Insertable B-Layer for the ATLAS Pixel Detector during Quality Assurance and a Novel Pixel Detector Readout Concept based on PCIe*, CERN-THESIS-2016-085, PhD thesis, University of Wuppertal, 2016

[172] T. Bisanz, *Test beam studies of pixel detector prototypes for the ATLAS-Experiment at the High Luminosity Large Hadron Collider*, Presented 18 Dec 2018, II.Physik-UniGö-Diss-2018/03, University of Göttingen, 2019

[173] D. Dannheim et al., *Corryvreckan: a modular 4D track reconstruction and analysis software for test beam data*, JINST **16** (2021) P03008

[174] T. Bisanz et al., *EUTelescope: A modular reconstruction framework for beam telescope data*, JINST **15** (2020) P09020

[175] C. Kleinwort, *General broken lines as advanced track fitting method*, Nucl. Instrum. Meth. A **673** (2012) 107

[176] Y. Liu, *EUDAQ2 User Manual*, AIDA-2020-NOTE-2018-001, 2018

[177] ATLAS ITk Collaboration, *Production Flow and QA/QC of Modules*, ATLAS Internal Note, https://edms.cern.ch/document/2659984/1, AT2-IP-QA-0011, 2023

[178] ATLAS ITk Collaboration, *Site Qualification*, ATLAS Internal Note, https://edms.cern.ch/document/2786305/1, AT2-IP-QA-0015, 2023

[179] ATLAS ITk Collaboration, *ITk-reports dashboard*, (visited on Feb. 1, 2024)

[180] ATLAS ITk Collaboration, *ITk Pixel Module Site Qualification – Cleanroom Standards*, ATLAS Internal Note, https://edms.cern.ch/document/2810169/1, AT2-IP-QA-0016, 2023

[181] R. Plackett, R. L. Bates, and J. E. Metcalfe, *LAB_SHIP*, ATLAS Internal Note, https://edms.cern.ch/document/2817082/1, AT2-IP-QA-0045 v.1, 2023

[182] J. T. Taylor, *Parylene coating*, ATLAS Internal Note, https://edms.cern.ch/document/2786311/1, AT2-IP-QA-0019 v.1, 2023

[183] ATLAS ITk Collaboration, *Pixel bare Module, Sensor and FE chip Engineering DWG*, ATLAS Internal Note, https://edms.cern.ch/document/1932682/12, AT2-IP-EP-0009 v.12, 2024

[184] *Parylene Coating and Masking Procedures*, ATLAS Internal Note, https://edms.cern.ch/document/2648146/1, AT2-IP-AP-0002, 2021

[185] D. A. Feito et al., *Design Overview of the Loaded Local Supports for the ITk Pixel Outer Barrel*, ATLAS Internal Note, https://edms.cern.ch/document/2822664/1, AT2-IP-ER-0046 v.1, 2023

[186] ATLAS ITk Collaboration, *Araldite 2021*, ATLAS Internal Note, https://edms.cern.ch/document/2664113/1, AT2-IP-AN-0004 v.1, 2021

[187] ATLAS ITk Collaboration, *Wire Bond Protection (OB) Assembly and QC Procedures*, ATLAS Internal Note, https://edms.cern.ch/document/2648149/1, AT2-IP-AP-0005 v.1, 2021

[188] ATLAS ITk Collaboration, *WBMP & SR MODULE TOOL – SHORT VERSION*, ATLAS Internal Note, https://edms.cern.ch/document/3030110/1, AT2-IP-OM-0054 v.1, 2023

[189] ATLAS ITk Collaboration, *DRAWING FOLDER - WBMP & SR MODULE TOOL - STENCIL ASSEMBLY*, ATLAS Internal Note, https://edms.cern.ch/document/3030113/1, AT2-IP-OM-0075, 2024

[190] ATLAS ITk Collaboration, *Pixel Quad Module Assembly DWG*, ATLAS Internal Note, https://edms.cern.ch/document/2363543/10, AT2-IP-ED-0010 v.10, 2023

[191] ATLAS ITk Collaboration, *Technical Specification for ITk pixel modules*, ATLAS Internal Note, https://edms.cern.ch/document/2019657/2, AT2-IP-ES-0009 v.2, 2022

[192] ATLAS ITk Collaboration, *Pixel Module Assembly DWG*, ATLAS Internal Note, https://edms.cern.ch/document/2363543/5, AT2-IP-ED-0010 v.5, 2022

[193] ATLAS ITk Collaboration, *ITkPix assembly tooling including instruction*, ATLAS Internal Note, https://edms.cern.ch/document/2615861/1, AT2-IP-ED-0021, 2022

[194] ATLAS ITk Collaboration, *Module Flex PCB QC*, ATLAS Internal Note, https://edms.cern.ch/document/2786309/1, AT2-IP-QA-0018 v.1, 2023

[195] ATLAS ITk Collaboration, *Assembled quad module metrology tool*, ATLAS Internal Note, https://edms.cern.ch/document/2739409/1, AT2-IP-ED-0031 v.1, 2024

[196] ATLAS ITk Collaboration, *Digital module tests*, ATLAS Internal Note, https://edms.cern.ch/document/2786321/1, AT2-IP-QA-0025 v.1, 2023

[197] Mark Hendrik Standke, *Hybrid Pixel Readout Chip Verification, Characterization and Wafer Level Testing for the ATLAS-ITK Upgrade at the HL-LHC*, urn:nbn:de:hbz:5-71232, PhD thesis, University of Bonn, 2023

[198] S. D'Auria, *Testing set-up*, ATLAS Internal Note, https://edms.cern.ch/document/2786319/1, AT2-IP-QA-0024 v.1, 2023

[199] T. Hüser, *Module tests for the ATLAS pixel detector*, II.Physik-UniGö-BSc-2018/01, BSc thesis, University of Göttingen, 2018

[200] ATLAS ITk Collaboration, *Interlock for module test setup*, ATLAS Internal Note, https://edms.cern.ch/document/2794452/1, AT2-IP-QA-0031 v.1, 2023

[201] M. Daas et al., *BDAQ53, a versatile pixel detector readout and test system for the ATLAS and CMS HL-LHC upgrades*, Nucl. Instrum. Meth. A **986** (2021) 164721

Acknowledgements

There are so many persons to whom I want to say thank you, and this acknowledgement quickly turned long. First of all, thanks to my supervisor, Prof. Dr. Arnulf Quadt, for taking me into your group and providing great opportunities during my study here. This work entails all that I wanted: hands-on work, fundamental physics, not to mention the opportunities of trips to conferences and workshops, all that have brought interesting academic exposure, and the chances of seeing and doing good and important work. I appreciate your support for my academic career, and in addition, the care for my life in Göttingen over the difficulties that I could face and sometimes have faced as an international. I knew that I can always ask you for perspectives and help.

Ten thousand thanks to PD[1] Dr. Jörn Große-Knetter and Dr. Hua Ye for the direct supervision of my day-to-day work, for being so reliable and always giving good advice. Thank you for your guidance. To Dr. Silke Möbius, who taught me things like how to use the probe station[2] when I started lab work. Despite that you were also a PhD student back then, you were like half a postdoc to me. Thanks to my first year qualification task local supervisor Dr. Elizaveta Shabalina, for explaining physics analysis related questions to me, for the support through the project, and for the insights on general academic life and career. I am very thankful to have you all as not only my mentors, but hopefully also my dear friends.

So much thanks to PD Dr. Jörn Große-Knetter, Dr. Silke Möbius, Dr. Ali Skaf, Dr Hua Ye, Dr. Marcello Bindi, Dr. Elizaveta Shabalina, Dr. Baptiste Ravina, and Dr. Steffen Korn for providing the crucial support of proof-reading to this thesis. Thank Chris Scheulen for the reference checking and Dr. Knut Zoch for the thesis template.

I would also like to thank my thesis advisory committee for going through the process with me, my reviewers for reading and correcting the thesis, and my examination board[3]. It is never easy to figure out a common time slot that works for everyone, thank you for all the

[1] By the time of the correction of this thesis, apl. Prof.

[2] Which I have used extensively these years, as you can see in section 6.1.

[3] The names are neatly listed at the back of the title page.

niceties in the process of making it happen!

Thanks to my co-workers and to my collaborators in the ITk pixel realm, for the work we did together, the explanations and answers when I needed to figure things out, and the nice discussions and suggestions, which I very much enjoyed. Thanks to Tim Kanngießer for the discussions and explanations on the tooling related items, to Dr. Jörn Lange for the initial help like finding me a place to live in Göttingen when I first arrived, and to Karin for having taken me in.

谢谢我的父母宋华和田双喜。从小我的选择就或许并不主流，谢谢你们很少干涉我，而是一直爱我、支持我，陪我玩，让我度过无忧无虑的童年，比如一起去旅游、爬山、玩雪、下棋、吃饭……你们是我一生中最重要的人。我爱你们。[4]

Thanks to my friends Natasha[5], Zhiying[6], and friends from the institute: Sreelakshmi[7], Saidev[8], Chris[9], Matthew[10], Andrés[11], Theresa[12], Ishan[13] …[14], and everyone else in the institute, who has cared about me and helped me. You made working in the institute like simply hanging out with friends. The pub quizzes[15], coffee breaks[16], trips, other hanging-outs, and 11:30 lunches created really enjoyable memories.

This – which now sounds a bit like a will or an award speech – is a milestone that is also an opportunity to think back through the happiness and hardship, thank the persons in my life and the journeys we've had together. There are so many other memories and persons that I want to write about, perhaps I just say: thank you. I deeply appreciate every one of you, and have learned a lot from the unique precious qualities in you. I hope we will do more interesting things together in the future!

Wishing you everything well,

屿颂

[4]Thanks to my parents 宋华 and 田双喜. Perhaps my wishes have been unconventional since when I was a child, thank you for having rarely interfered, but instead always loved me, supported me, spent time with me, and have been there for me. You gave me a happy and carefree childhood: travelling, hiking, playing with snow, playing board games, eating... You are the most important persons in my life. I love you.

[5]Great memories and fun: food, cake, exercise, talk, trip...:D.

[6]ITk buddy... thanks for the chats and for cooking for me when we I visited.

[7]Thank you my dear friend, I hope I'm as wise as you. I will not write out all the time and memories we had together, as it will be too many, and we will have more together!

[8]We should play more board games and badminton, and watch more films (Star Wars)!

[9]Thanks for the great memories: watching & talking about science fiction stuff, camping – something I've always wanted to do. And the rest. The food you made was great!

[10]We had great times hanging out and potluck-ing! Wishing you happiness.

[11]I should make trips and learn about things like you do :D

[12]I've been wearing the "Mastermind" bracelet you made me when writing this thesis.

[13]Thanks for being so very social and bringing everybody in, which made a big difference to my life in Göttingen. You helped and taught me a lot, and brought a lot of fun!

[14]A lot of names that have already shown up before e.g. in the list of proof-readers.

[15]You need to change that team name :P

[16]Thanks Jörn for hosting coffee every day.

APPENDIX A

Additional Figures for Sensor Characterisation

A.1. Photo of Micron test structures

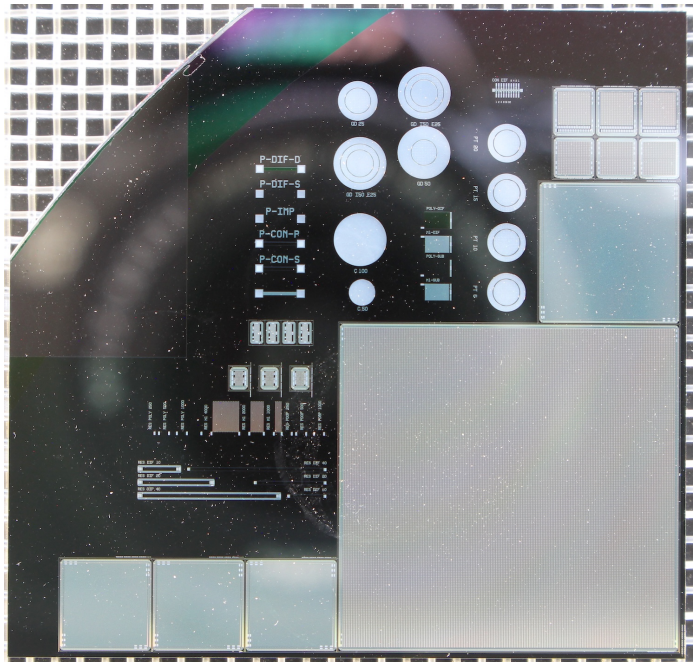

Figure A.1: Micron 100 µm TS die from wafer 0121, irradiated with $2 \times 10^{15}\,\mathrm{n_{eq}/cm^2}$ fluence. The biggest structure on this die is TSF2 – a mini sensor.

A.2. *IV* from probing different pads of the same diode

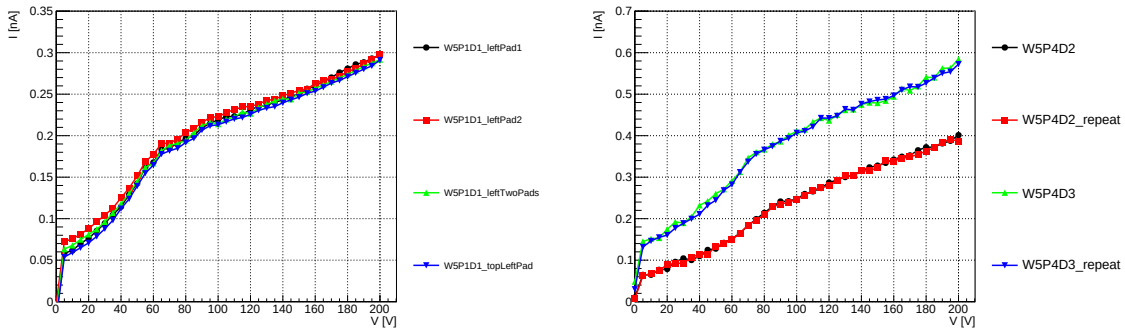

(a) Probe different pads.

(b) Repeated measurements using same pads.

Figure A.2: Probing different pads on the diode W5P1D1 from HPK. The curves do not differ more than simply repeating the measurements.

A.3. *CV* of unirradiated Micron quad sensors

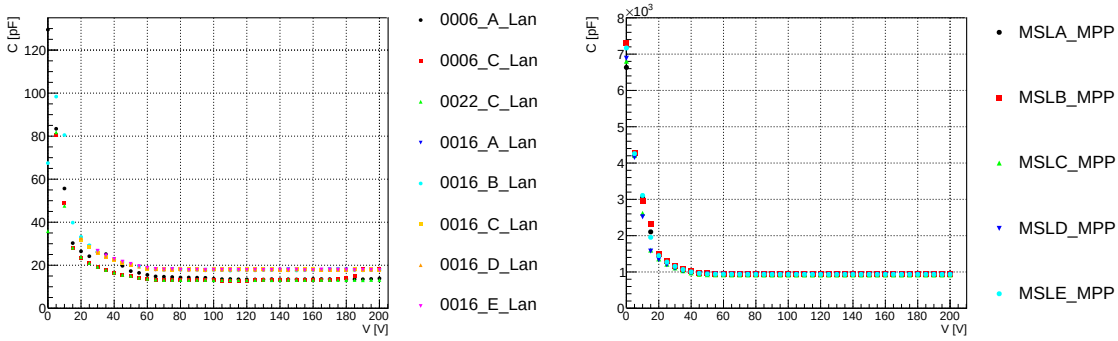

(a) *CV* of Micron 150 µm sensors.

(b) *CV* of Micron 100 µm sensors.

Figure A.3: *CV* of unirradiated Micron quad sensors with two thicknesses.

APPENDIX B

Additional Figures for Assembly

B.1. Different flexes: un-populated or by a different vendor

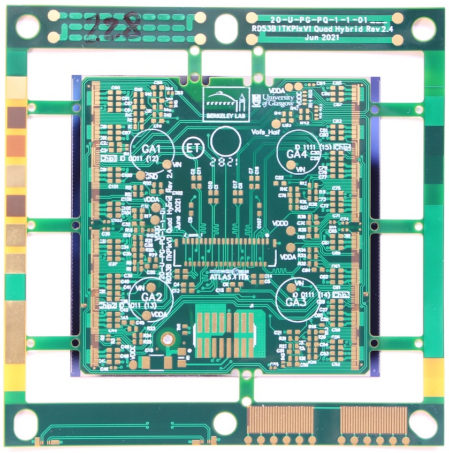

(a) Un-populated Flex v2.4 (glued to Si dummy).

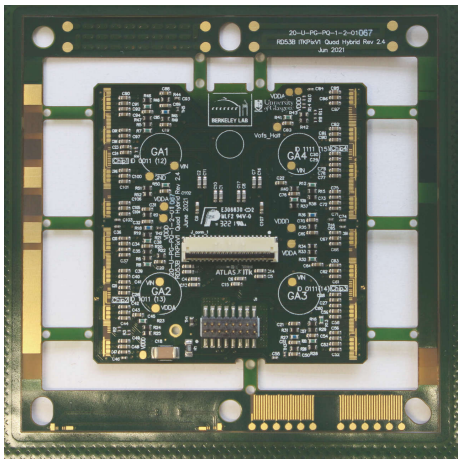

(b) Populated Flex v2.4 from a different vendor.

Figure B.1: Two flavours of flex.

B.2. Brass flex dummy and Si bare module dummy

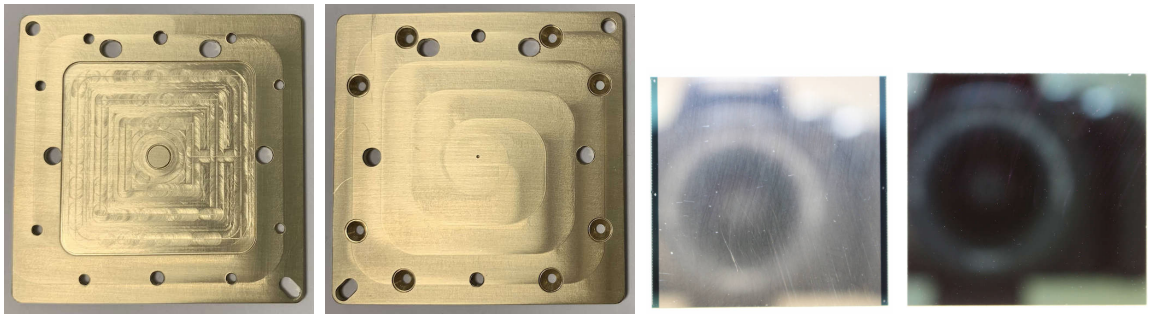

Figure B.2: Brass flex dummy and Si dummy, front and back sides.

B.3. Si dummy Visual Inspection

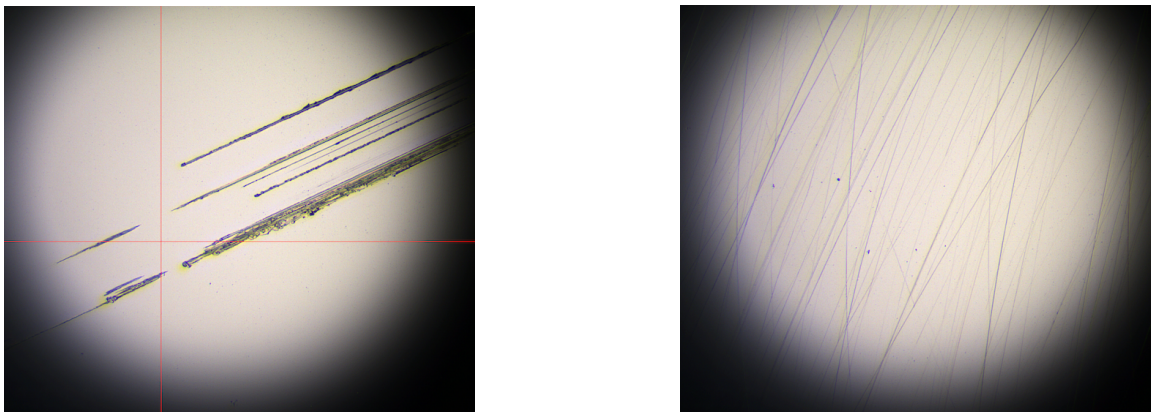

(a) Scratches.

(b) Scratches from cleaning.

Figure B.3: Example photos of defects found in Si dummy visual inspection.

B.4. *CV* of quad bare modules

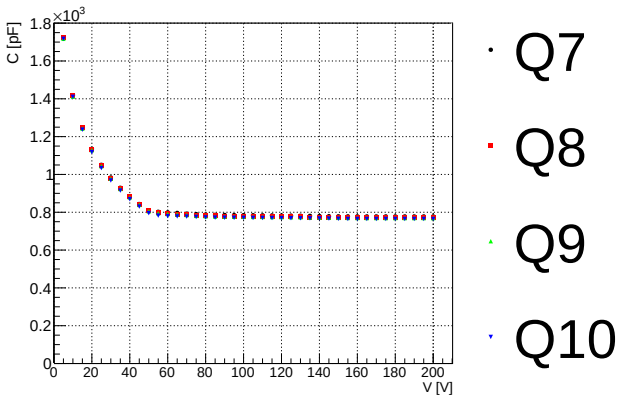

Figure B.4: *CV* for quad bare module 7–10.

APPENDIX C

Additional Figures for Module Quality Control

C.1. ADC Calibration

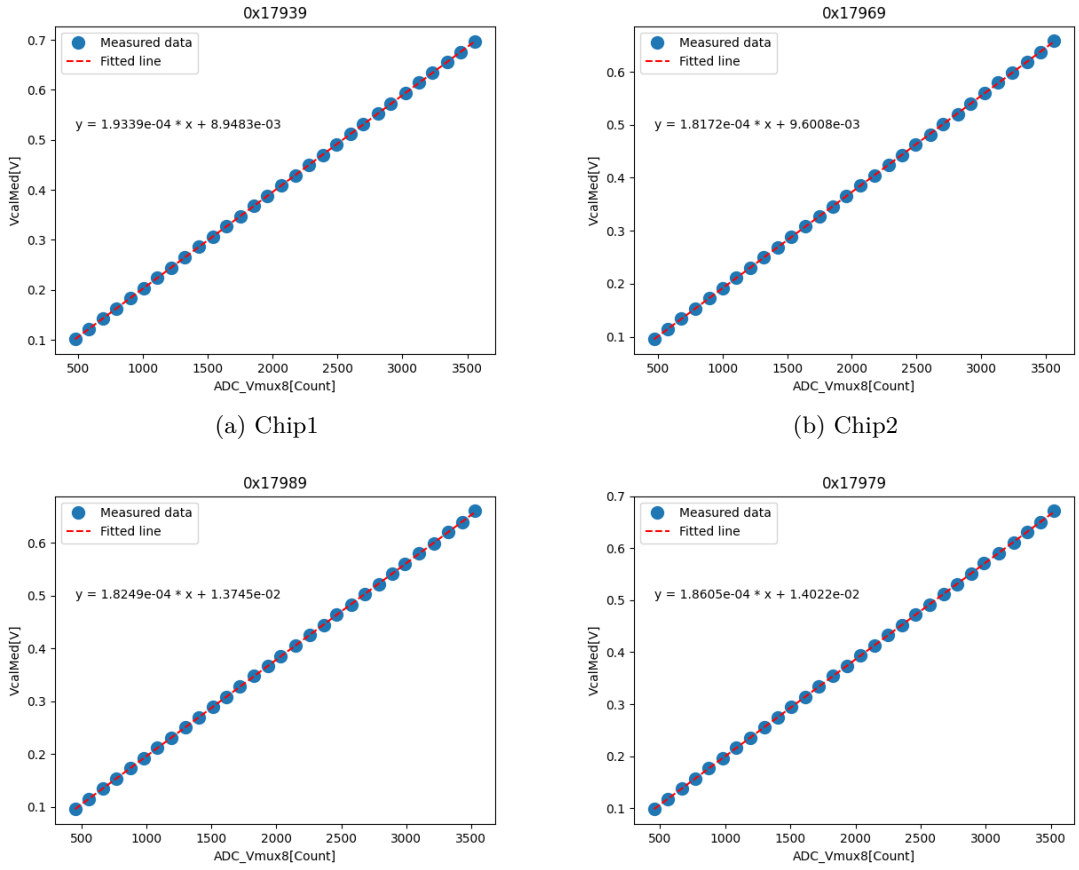

(a) Chip1

(b) Chip2

(c) Chip3

(d) Chip4

Figure C.1: ADC calibration results for all chips of Q11.

ADC_CALIBRATION for 0x17939

Parameter	Analysis result	QC criteria	Pass
ADC_CALIBRATION_SLOPE	0.193	[0.15, 0.224]	True
ADC_CALIBRATION_OFFSET	9.0	[-9, 31]	True
ADC_CALIBRATION_LINEARITY	0.47	[0.0, 4.0]	True
ADC_ANAGND30_MEAN	0.017	[0.015, 0.023]	True

(a) Chip1

ADC_CALIBRATION for 0x17969

Parameter	Analysis result	QC criteria	Pass
ADC_CALIBRATION_SLOPE	0.182	[0.15, 0.224]	True
ADC_CALIBRATION_OFFSET	10.0	[-9, 31]	True
ADC_CALIBRATION_LINEARITY	0.68	[0.0, 4.0]	True
ADC_ANAGND30_MEAN	0.017	[0.015, 0.023]	True

(b) Chip2

ADC_CALIBRATION for 0x17989

Parameter	Analysis result	QC criteria	Pass
ADC_CALIBRATION_SLOPE	0.182	[0.15, 0.224]	True
ADC_CALIBRATION_OFFSET	14.0	[-9, 31]	True
ADC_CALIBRATION_LINEARITY	0.77	[0.0, 4.0]	True
ADC_ANAGND30_MEAN	0.018	[0.015, 0.023]	True

(c) Chip3

ADC_CALIBRATION for 0x17979

Parameter	Analysis result	QC criteria	Pass
ADC_CALIBRATION_SLOPE	0.186	[0.15, 0.224]	True
ADC_CALIBRATION_OFFSET	14.0	[-9, 31]	True
ADC_CALIBRATION_LINEARITY	0.6	[0.0, 4.0]	True
ADC_ANAGND30_MEAN	0.017	[0.015, 0.023]	True

(d) Chip4

Figure C.2: ADC calibration results for all chips of Q11 - summary of analysis results.

C.2. Analog Readback

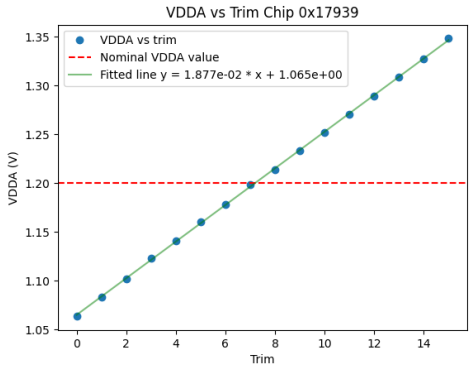

(a) 0x17939 VDDA TRIM

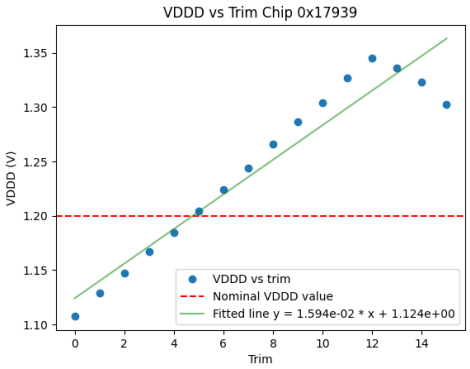

(b) 0x17939 VDDD TRIM

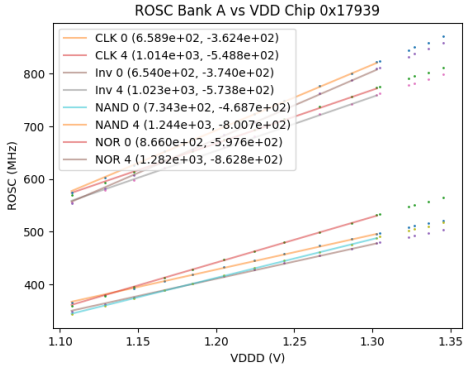

(c) 0x17939 ROSC vs VDDD Bank A

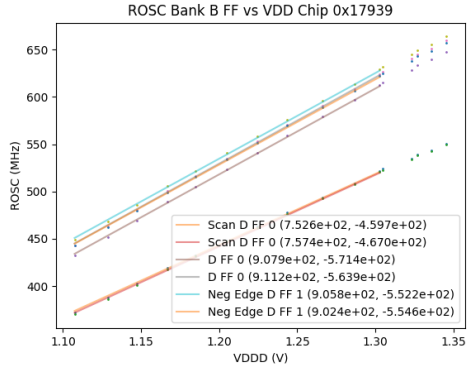

(d) 0x17939 ROSC vs VDDD Bank B FF

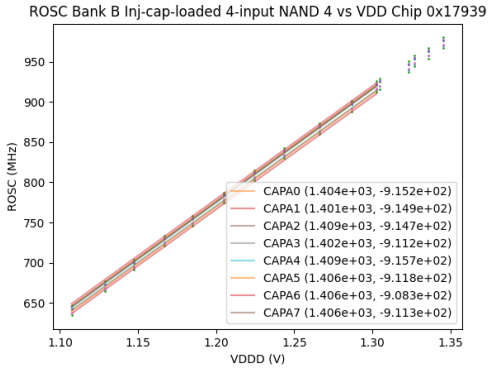

(e) 0x17939 ROSC vs VDDD Bank B Inj-cap-loaded 4-input NAND 4

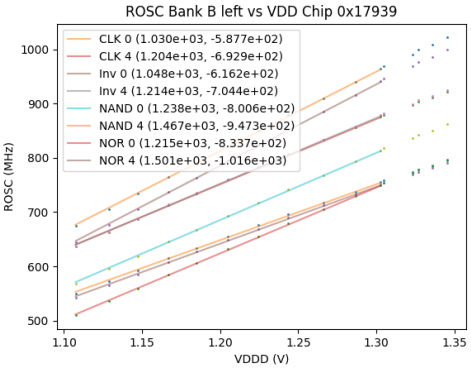

(f) 0x17939 ROSC vs VDDD Bank B left

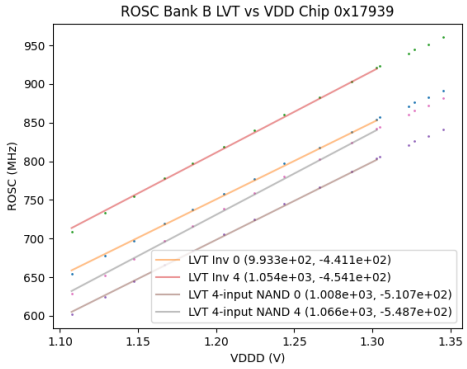

(g) 0x17939 ROSC vs VDDD Bank B LVT

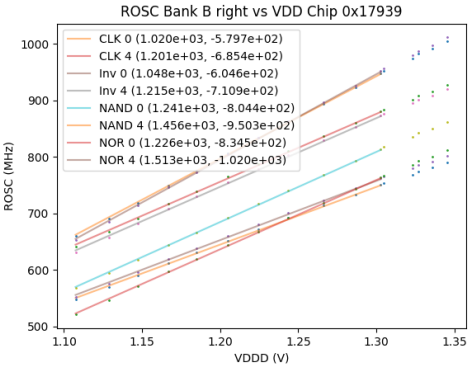

(h) 0x17939 ROSC vs VDDD Bank B right

Figure C.3: Analog readback results for chip1 of Q11.

ANALOG_READBACK for 0x17939

Parameter	Analysis result	QC criteria	Pass
Iref	4e-06	[3.7e-06, 4.3e-06]	True
CdrVcoMainBias	8.76e-05	[7.87e-05, 9.47e-05]	True
CdrVcoBuffBias	5.11e-05	[3.94e-05, 5.77e-05]	True
ICdrCP	4.3e-06	[3.2e-06, 4.8e-06]	True
ICdrFD	4.1e-05	[3.26e-05, 4.55e-05]	True
CdrBuffBias	2.09e-05	[1.74e-05, 2.13e-05]	True
CMLDrivTap1Bias	3.99e-05	[1e-05, 6e-05]	True
CMLDrivMainBias	7.38e-05	[6.32e-05, 8.26e-05]	True
IDiffPreMain	4.82e-05	[3.72e-05, 5.75e-05]	True
IDiffPreampComp	6.57e-05	[5.34e-05, 7.52e-05]	True
IDiffComp	5.3e-05	[4.07e-05, 6.16e-05]	True
IDiffVth2	8.74e-05	[7.28e-05, 9.67e-05]	True
IDiffVth1Main	7.45e-05	[3.51e-05, 9.77e-05]	True
IDiffLcc	8.6e-05	[6.94e-05, 9.61e-05]	True
IDiffFB	8.42e-05	[6.3e-05, 0.000107]	True
IDiffPreampLeft	8.74e-05	[7.28e-05, 9.97e-05]	True
IDiffVth1Left	7.03e-05	[4.7e-05, 8.86e-05]	True
IDiffPreampRight	4.54e-05	[3.64e-05, 5.75e-05]	True
IDiffPreampTopLeft	4.75e-05	[3.49e-05, 5.91e-05]	True
IDiffVth1Right	6.9e-05	[4.33e-05, 9.11e-05]	True
IDiffPreampTop	4.71e-05	[3.49e-05, 6e-05]	True
IDiffPreampTopRight	4.7e-05	[3.44e-05, 5.9e-05]	True
GADC	0.781	[0.703, 0.924]	True
VcalDac	0.842	[0.668, 0.987]	True
AnaGND30	0.017	[0.015, 0.023]	True
VrefCore	0.451	[0.435, 0.49]	True
VrefOVP	1.962	[1.857, 2.152]	True
VrefA	0.591	[0.563, 0.628]	True
VrefD	0.589	[0.561, 0.62]	True
Vofs	1.0	[0.99, 1.01]	True
ChipNTC_vs_ExtExt	-2.0	[-2, 2]	True

(a) Summary 1

ANALOG_READBACK for 0x17939

Parameter	Analysis result	QC criteria	Pass
AR_VDDA_VS_TRIM_2	1.102	[0.0, 1.2]	True
AR_VDDA_VS_TRIM_13	1.309	[1.2, 2.0]	True
AR_VDDA_VS_TRIM_1_STEP_SIZE	0.02	[0.013, 0.024]	True
AR_VDDA_VS_TRIM_2_STEP_SIZE	0.018	[0.013, 0.024]	True
AR_VDDA_VS_TRIM_3_STEP_SIZE	0.021	[0.013, 0.024]	True
AR_VDDA_VS_TRIM_4_STEP_SIZE	0.018	[0.013, 0.024]	True
AR_VDDA_VS_TRIM_5_STEP_SIZE	0.019	[0.013, 0.024]	True
AR_VDDA_VS_TRIM_6_STEP_SIZE	0.018	[0.013, 0.024]	True
AR_VDDA_VS_TRIM_7_STEP_SIZE	0.02	[0.013, 0.024]	True
AR_VDDA_VS_TRIM_8_STEP_SIZE	0.016	[0.013, 0.024]	True
AR_VDDA_VS_TRIM_9_STEP_SIZE	0.019	[0.013, 0.024]	True
AR_VDDA_VS_TRIM_10_STEP_SIZE	0.019	[0.013, 0.024]	True
AR_VDDA_VS_TRIM_11_STEP_SIZE	0.019	[0.013, 0.024]	True
AR_VDDA_VS_TRIM_12_STEP_SIZE	0.018	[0.013, 0.024]	True
AR_VDDA_VS_TRIM_13_STEP_SIZE	0.02	[0.013, 0.024]	True
AR_VDDA_VS_TRIM_14_STEP_SIZE	0.019	[0.013, 0.024]	True
AR_VDDA_VS_TRIM_15_STEP_SIZE	0.021	[0.013, 0.024]	True
AR_VDDD_VS_TRIM_2	1.147	[0.0, 1.2]	True
AR_VDDD_VS_TRIM_13	1.336	[1.2, 2.0]	True
AR_VDDD_VS_TRIM_1_STEP_SIZE	0.021	[0.013, 0.024]	True
AR_VDDD_VS_TRIM_2_STEP_SIZE	0.018	[0.013, 0.024]	True
AR_VDDD_VS_TRIM_3_STEP_SIZE	0.02	[0.013, 0.024]	True
AR_VDDD_VS_TRIM_4_STEP_SIZE	0.018	[0.013, 0.024]	True
AR_VDDD_VS_TRIM_5_STEP_SIZE	0.02	[0.013, 0.024]	True
AR_VDDD_VS_TRIM_6_STEP_SIZE	0.019	[0.013, 0.024]	True
AR_VDDD_VS_TRIM_7_STEP_SIZE	0.019	[0.013, 0.024]	True
AR_VDDD_VS_TRIM_8_STEP_SIZE	0.022	[0.013, 0.024]	True
AR_VDDD_VS_TRIM_9_STEP_SIZE	0.021	[0.013, 0.024]	True
AR_VDDD_VS_TRIM_10_STEP_SIZE	0.018	[0.013, 0.024]	True
AR_VDDD_VS_TRIM_11_STEP_SIZE	0.023	[0.013, 0.024]	True
AR_VDDD_VS_TRIM_12_STEP_SIZE	0.018	[0.013, 0.024]	True
AR_VDDD_VS_TRIM_13_STEP_SIZE	-0.01	[0.013, 0.024]	False
AR_VDDD_VS_TRIM_14_STEP_SIZE	-0.013	[0.013, 0.024]	False
AR_VDDD_VS_TRIM_15_STEP_SIZE	-0.02	[0.013, 0.024]	False

(b) Summary 2

ANALOG_READBACK for 0x17939

Parameter	Analysis result	QC criteria	Pass
AR_ROSC_SLOPE_0	659.0	[580, 790]	True
AR_ROSC_SLOPE_1	1014.0	[900, 1220]	True
AR_ROSC_SLOPE_2	654.0	[580, 780]	True
AR_ROSC_SLOPE_3	1023.0	[900, 1220]	True
AR_ROSC_SLOPE_4	734.0	[670, 820]	True
AR_ROSC_SLOPE_5	1244.0	[1140, 1400]	True
AR_ROSC_SLOPE_6	866.0	[790, 970]	True
AR_ROSC_SLOPE_7	1282.0	[1170, 1430]	True
AR_ROSC_SLOPE_8	1030.0	[910, 1220]	True
AR_ROSC_SLOPE_9	1020.0	[920, 1210]	True
AR_ROSC_SLOPE_10	1204.0	[1070, 1420]	True
AR_ROSC_SLOPE_11	1201.0	[1070, 1420]	True
AR_ROSC_SLOPE_12	1048.0	[950, 1230]	True
AR_ROSC_SLOPE_13	1048.0	[950, 1230]	True
AR_ROSC_SLOPE_14	1214.0	[1080, 1430]	True
AR_ROSC_SLOPE_15	1215.0	[1080, 1430]	True
AR_ROSC_SLOPE_16	1238.0	[1140, 1390]	True
AR_ROSC_SLOPE_17	1241.0	[1140, 1380]	True
AR_ROSC_SLOPE_18	1467.0	[1350, 1620]	True
AR_ROSC_SLOPE_19	1456.0	[1340, 1370]	False
AR_ROSC_SLOPE_20	1215.0	[1120, 1350]	True
AR_ROSC_SLOPE_21	1226.0	[1130, 1200]	False
AR_ROSC_SLOPE_22	1501.0	[1390, 1500]	False
AR_ROSC_SLOPE_23	1513.0	[1390, 1500]	False
AR_ROSC_SLOPE_24	753.0	[690, 860]	True
AR_ROSC_SLOPE_25	757.0	[690, 860]	True
AR_ROSC_SLOPE_26	908.0	[830, 1040]	True
AR_ROSC_SLOPE_27	911.0	[830, 1030]	True
AR_ROSC_SLOPE_28	906.0	[820, 1040]	True
AR_ROSC_SLOPE_29	902.0	[820, 1040]	True
AR_ROSC_SLOPE_30	993.0	[860, 1230]	True
AR_ROSC_SLOPE_31	1054.0	[910, 1300]	True
AR_ROSC_SLOPE_32	1008.0	[900, 1180]	True
AR_ROSC_SLOPE_33	1066.0	[940, 1250]	True
AR_ROSC_SLOPE_34	1404.0	[1290, 1570]	True
AR_ROSC_SLOPE_35	1401.0	[1290, 1570]	True
AR_ROSC_SLOPE_36	1409.0	[1300, 1560]	True
AR_ROSC_SLOPE_37	1402.0	[1300, 1560]	True
AR_ROSC_SLOPE_38	1409.0	[1290, 1560]	True
AR_ROSC_SLOPE_39	1406.0	[1300, 1560]	True
AR_ROSC_SLOPE_40	1406.0	[1300, 1560]	True
AR_ROSC_SLOPE_41	1406.0	[1300, 1560]	True
AR_ROSC_SLOPE_FRACPASS	0.9	[0.5, 1.0]	True

(c) Summary 3

ANALOG_READBACK for 0x17939

Parameter	Analysis result	QC criteria	Pass
AR_ROSC_OFFSET_0	-362.0	[-500, -270]	True
AR_ROSC_OFFSET_1	-549.0	[-760, -420]	True
AR_ROSC_OFFSET_2	-374.0	[-500, -290]	True
AR_ROSC_OFFSET_3	-574.0	[-770, -440]	True
AR_ROSC_OFFSET_4	-469.0	[-550, -410]	True
AR_ROSC_OFFSET_5	-801.0	[-940, -700]	True
AR_ROSC_OFFSET_6	-598.0	[-670, -520]	True
AR_ROSC_OFFSET_7	-863.0	[-980, -750]	True
AR_ROSC_OFFSET_8	-588.0	[-780, -460]	True
AR_ROSC_OFFSET_9	-580.0	[-770, -460]	True
AR_ROSC_OFFSET_10	-693.0	[-900, -540]	True
AR_ROSC_OFFSET_11	-685.0	[-910, -540]	True
AR_ROSC_OFFSET_12	-616.0	[-800, -500]	True
AR_ROSC_OFFSET_13	-605.0	[-800, -510]	True
AR_ROSC_OFFSET_14	-704.0	[-910, -570]	True
AR_ROSC_OFFSET_15	-711.0	[-920, -560]	True
AR_ROSC_OFFSET_16	-801.0	[-920, -720]	True
AR_ROSC_OFFSET_17	-804.0	[-940, -700]	True
AR_ROSC_OFFSET_18	-947.0	[-1090, -850]	True
AR_ROSC_OFFSET_19	-950.0	[-1090, -850]	True
AR_ROSC_OFFSET_20	-834.0	[-940, -740]	True
AR_ROSC_OFFSET_21	-834.0	[-940, -740]	True
AR_ROSC_OFFSET_22	-1016.0	[-1160, -890]	True
AR_ROSC_OFFSET_23	-1020.0	[-1160, -900]	True
AR_ROSC_OFFSET_24	-460.0	[-570, -400]	True
AR_ROSC_OFFSET_25	-467.0	[-570, -400]	True
AR_ROSC_OFFSET_26	-571.0	[-680, -490]	True
AR_ROSC_OFFSET_27	-564.0	[-680, -500]	True
AR_ROSC_OFFSET_28	-552.0	[-690, -470]	True
AR_ROSC_OFFSET_29	-555.0	[-680, -470]	True
AR_ROSC_OFFSET_30	-441.0	[-690, -290]	True
AR_ROSC_OFFSET_31	-454.0	[-700, -280]	True
AR_ROSC_OFFSET_32	-511.0	[-690, -410]	True
AR_ROSC_OFFSET_33	-549.0	[-730, -420]	True
AR_ROSC_OFFSET_34	-915.0	[-1050, -810]	True
AR_ROSC_OFFSET_35	-915.0	[-1050, -820]	True
AR_ROSC_OFFSET_36	-915.0	[-1040, -820]	True
AR_ROSC_OFFSET_37	-911.0	[-1040, -820]	True
AR_ROSC_OFFSET_38	-916.0	[-1050, -820]	True
AR_ROSC_OFFSET_39	-912.0	[-1050, -810]	True
AR_ROSC_OFFSET_40	-908.0	[-1050, -820]	True
AR_ROSC_OFFSET_41	-911.0	[-1050, -820]	True
AR_ROSC_OFFSET_FRACPASS	1.0	[0.5, 1.0]	True

(d) Summary 4

ANALOG_READBACK for 0x17939

Parameter	Analysis result	QC criteria	Pass
AR_ROSC_MAX_RESIDUAL_0	1.0	[0, 5]	True
AR_ROSC_MAX_RESIDUAL_1	2.0	[0, 5]	True
AR_ROSC_MAX_RESIDUAL_2	1.0	[0, 5]	True
AR_ROSC_MAX_RESIDUAL_3	2.0	[0, 5]	True
AR_ROSC_MAX_RESIDUAL_4	1.0	[0, 5]	True
AR_ROSC_MAX_RESIDUAL_5	2.0	[0, 5]	True
AR_ROSC_MAX_RESIDUAL_6	1.0	[0, 5]	True
AR_ROSC_MAX_RESIDUAL_7	2.0	[0, 5]	True
AR_ROSC_MAX_RESIDUAL_8	2.0	[0, 5]	True
AR_ROSC_MAX_RESIDUAL_9	2.0	[0, 5]	True
AR_ROSC_MAX_RESIDUAL_10	2.0	[0, 5]	True
AR_ROSC_MAX_RESIDUAL_11	2.0	[0, 5]	True
AR_ROSC_MAX_RESIDUAL_12	2.0	[0, 5]	True
AR_ROSC_MAX_RESIDUAL_13	2.0	[0, 5]	True
AR_ROSC_MAX_RESIDUAL_14	3.0	[0, 5]	True
AR_ROSC_MAX_RESIDUAL_15	2.0	[0, 5]	True
AR_ROSC_MAX_RESIDUAL_16	2.0	[0, 5]	True
AR_ROSC_MAX_RESIDUAL_17	2.0	[0, 5]	True
AR_ROSC_MAX_RESIDUAL_18	2.0	[0, 5]	True
AR_ROSC_MAX_RESIDUAL_19	2.0	[0, 5]	True
AR_ROSC_MAX_RESIDUAL_20	2.0	[0, 5]	True
AR_ROSC_MAX_RESIDUAL_21	2.0	[0, 5]	True
AR_ROSC_MAX_RESIDUAL_22	2.0	[0, 5]	True
AR_ROSC_MAX_RESIDUAL_23	2.0	[0, 5]	True
AR_ROSC_MAX_RESIDUAL_24	1.0	[0, 5]	True
AR_ROSC_MAX_RESIDUAL_25	1.0	[0, 5]	True
AR_ROSC_MAX_RESIDUAL_26	1.0	[0, 5]	True
AR_ROSC_MAX_RESIDUAL_27	2.0	[0, 5]	True
AR_ROSC_MAX_RESIDUAL_28	2.0	[0, 5]	True
AR_ROSC_MAX_RESIDUAL_29	2.0	[0, 5]	True
AR_ROSC_MAX_RESIDUAL_30	2.0	[0, 5]	True
AR_ROSC_MAX_RESIDUAL_31	3.0	[0, 5]	True
AR_ROSC_MAX_RESIDUAL_32	2.0	[0, 5]	True
AR_ROSC_MAX_RESIDUAL_33	2.0	[0, 5]	True
AR_ROSC_MAX_RESIDUAL_34	2.0	[0, 5]	True
AR_ROSC_MAX_RESIDUAL_35	2.0	[0, 5]	True
AR_ROSC_MAX_RESIDUAL_36	2.0	[0, 5]	True
AR_ROSC_MAX_RESIDUAL_37	2.0	[0, 5]	True
AR_ROSC_MAX_RESIDUAL_38	2.0	[0, 5]	True
AR_ROSC_MAX_RESIDUAL_39	2.0	[0, 5]	True
AR_ROSC_MAX_RESIDUAL_40	2.0	[0, 5]	True
AR_ROSC_MAX_RESIDUAL_41	2.0	[0, 5]	True
AR_ROSC_MAX_RESIDUAL_FRACPASS	1.0	[0.5, 1.0]	True

(e) Summary 5

Figure C.4: Analog readback results for chip1 of Q11 - analysis summaries. Please refer to the online version and zoom in.

C.3. SLDO Qualification

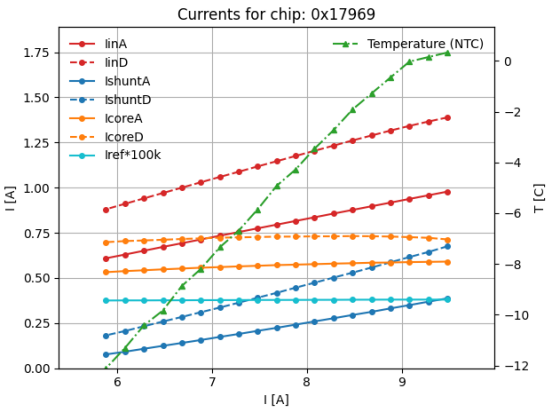

(a) II

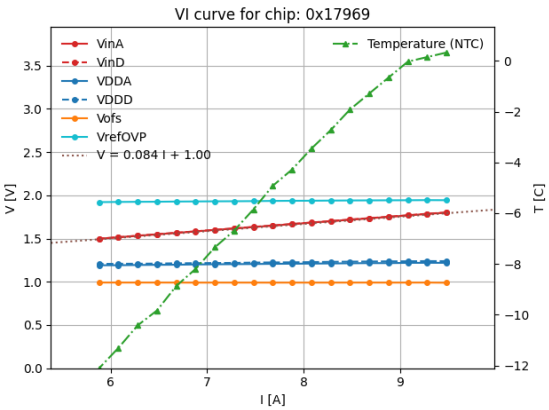

(b) VI

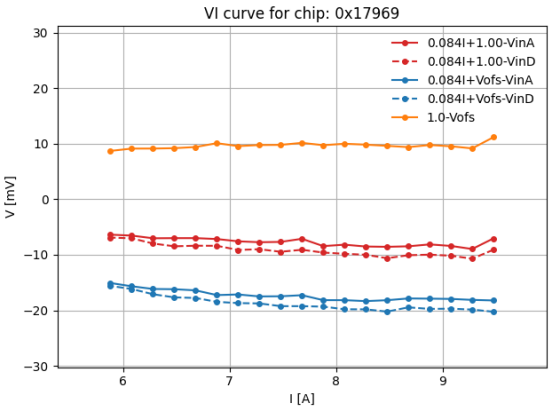

(c) VIresidual

SLDO for 0x17969

Parameter	Analysis result	QC criteria	Pass
SLDO_LINEARITY	0.018	[0.0, 0.035]	True
SLDO_VINA_VIND	-0.0	[-0.01, 0.01]	True
SLDO_VDDA	1.19	[1.19, 1.21]	True
SLDO_VDDD	1.21	[1.19, 1.21]	True
SLDO_VINA	1.498	[1.468, 1.518]	True
SLDO_VIND	1.499	[1.468, 1.518]	True
SLDO_VOFFS	0.99	[0.99, 1.01]	True
SLDO_IINA	0.609	[0.567, 0.626]	True
SLDO_IIND	0.881	[0.846, 0.905]	True
SLDO_IREF	3.8	[3.7, 4.3]	True
SLDO_ISHUNTA	0.077	[0.006, 999]	True
SLDO_ISHUNTD	0.182	[0.128, 999]	True

(d) Summary

Figure C.5: SLDO qualification for Q11 chip2.

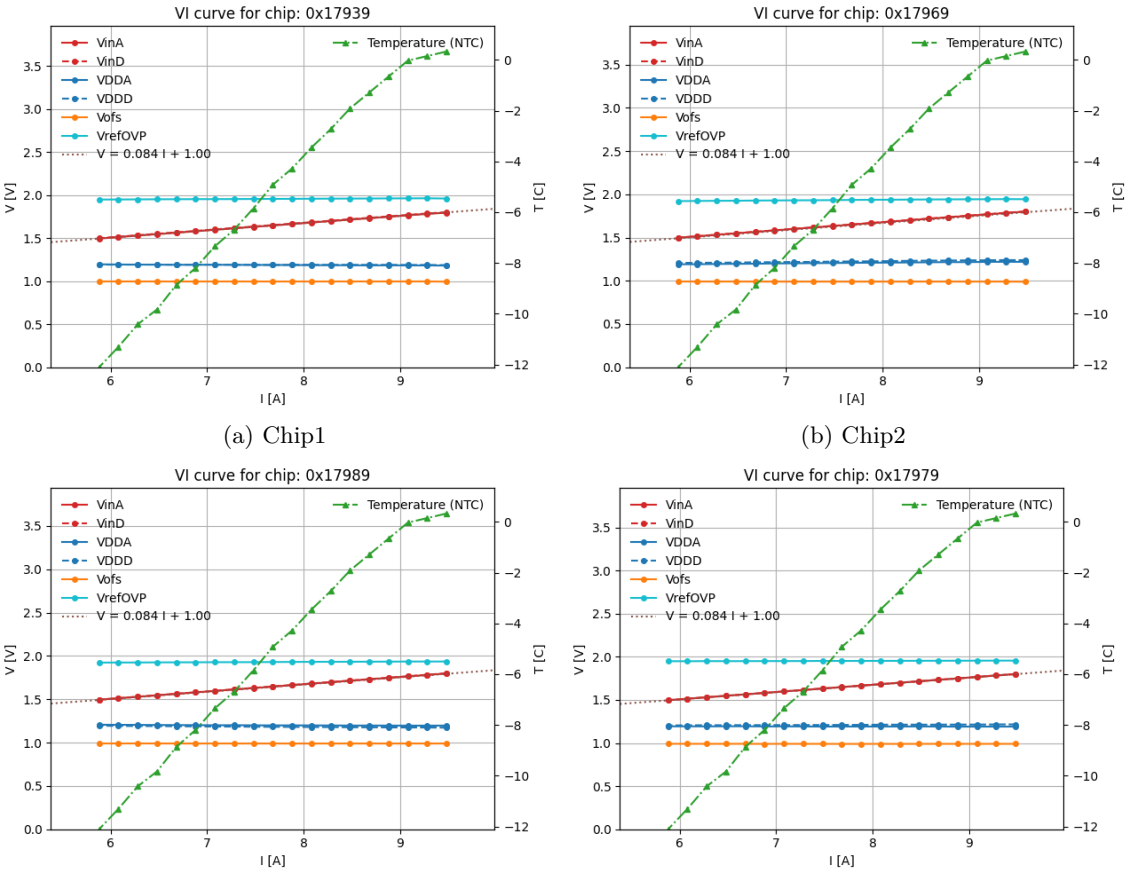

(a) Chip1

(b) Chip2

(c) Chip3

(d) Chip4

Figure C.6: SLDO *VI* results for all chips of Q11.

SLDO for 0x17939

Parameter	Analysis result	QC criteria	Pass
SLDO_LINEARITY	0.005	[0.0, 0.035]	True
SLDO_VINA_VIND	-0.01	[-0.01, 0.01]	True
SLDO_VDDA	1.2	[1.19, 1.21]	True
SLDO_VDDD	1.19	[1.19, 1.21]	True
SLDO_VINA	1.496	[1.468, 1.518]	True
SLDO_VIND	1.499	[1.468, 1.518]	True
SLDO_VOFFS	1.0	[0.99, 1.01]	True
SLDO_IINA	0.607	[0.567, 0.626]	True
SLDO_IIND	0.849	[0.846, 0.905]	True
SLDO_IREF	4.0	[3.7, 4.3]	True
SLDO_ISHUNTA	0.037	[0.006, 999]	True
SLDO_ISHUNTD	0.205	[0.128, 999]	True

(a) Chip1

SLDO for 0x17969

Parameter	Analysis result	QC criteria	Pass
SLDO_LINEARITY	0.018	[0.0, 0.035]	True
SLDO_VINA_VIND	-0.0	[-0.01, 0.01]	True
SLDO_VDDA	1.19	[1.19, 1.21]	True
SLDO_VDDD	1.21	[1.19, 1.21]	True
SLDO_VINA	1.498	[1.468, 1.518]	True
SLDO_VIND	1.499	[1.468, 1.518]	True
SLDO_VOFFS	0.99	[0.99, 1.01]	True
SLDO_IINA	0.609	[0.567, 0.626]	True
SLDO_IIND	0.881	[0.846, 0.905]	True
SLDO_IREF	3.8	[3.7, 4.3]	True
SLDO_ISHUNTA	0.077	[0.006, 999]	True
SLDO_ISHUNTD	0.182	[0.128, 999]	True

(b) Chip2

SLDO for 0x17989

Parameter	Analysis result	QC criteria	Pass
SLDO_LINEARITY	0.015	[0.0, 0.035]	True
SLDO_VINA_VIND	-0.0	[-0.01, 0.01]	True
SLDO_VDDA	1.21	[1.19, 1.21]	True
SLDO_VDDD	1.19	[1.19, 1.21]	True
SLDO_VINA	1.495	[1.468, 1.518]	True
SLDO_VIND	1.495	[1.468, 1.518]	True
SLDO_VOFFS	0.99	[0.99, 1.01]	True
SLDO_IINA	0.608	[0.567, 0.626]	True
SLDO_IIND	0.872	[0.846, 0.905]	True
SLDO_IREF	4.0	[3.7, 4.3]	True
SLDO_ISHUNTA	0.056	[0.006, 999]	True
SLDO_ISHUNTD	0.192	[0.128, 999]	True

(c) Chip3

SLDO for 0x17979

Parameter	Analysis result	QC criteria	Pass
SLDO_LINEARITY	0.011	[0.0, 0.035]	True
SLDO_VINA_VIND	0.0	[-0.01, 0.01]	True
SLDO_VDDA	1.19	[1.19, 1.21]	True
SLDO_VDDD	1.2	[1.19, 1.21]	True
SLDO_VINA	1.497	[1.468, 1.518]	True
SLDO_VIND	1.497	[1.468, 1.518]	True
SLDO_VOFFS	0.99	[0.99, 1.01]	True
SLDO_IINA	0.603	[0.567, 0.626]	True
SLDO_IIND	0.859	[0.846, 0.905]	True
SLDO_IREF	4.0	[3.7, 4.3]	True
SLDO_ISHUNTA	0.058	[0.006, 999]	True
SLDO_ISHUNTD	0.186	[0.128, 999]	True

(d) Chip4

Figure C.7: SLDO summary for all chips of Q11.

C.4. Vcal Calibration

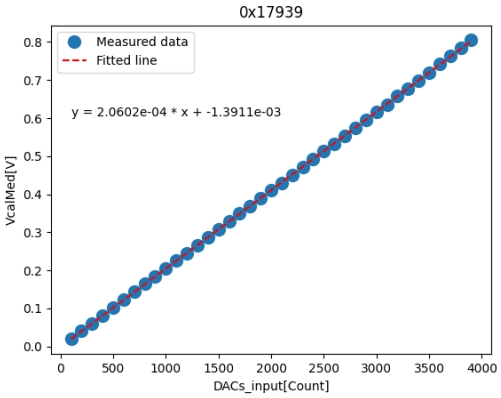

(a) MED

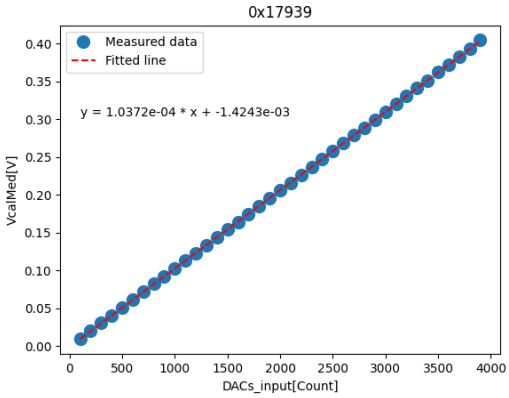

(b) MED small range

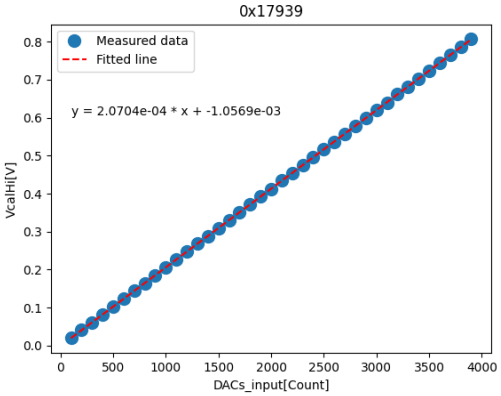

(c) High

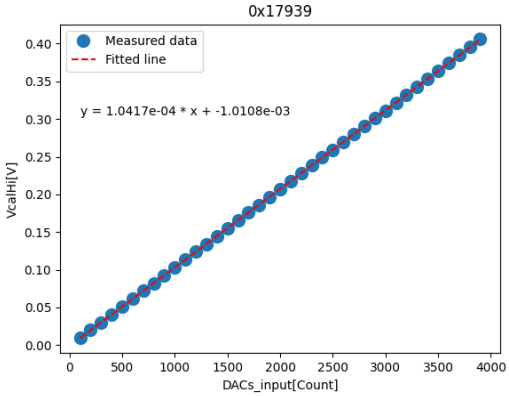

(d) High small range

VCAL_CALIBRATION for 0x17939

Parameter	Analysis result	QC criteria	Pass
VCAL_MED_SLOPE	0.21	[0.16, 0.24]	True
VCAL_MED_OFFSET	-1.0	[-23, 17]	True
VCAL_MED_LINEARITY	0.99	[0.0, 4.0]	True
VCAL_HIGH_SLOPE	0.21	[0.16, 0.24]	True
VCAL_HIGH_OFFSET	-1.0	[-23, 17]	True
VCAL_HIGH_LINEARITY	0.35	[0.0, 4.0]	True
VCAL_HIGH_SLOPE_SMALL_RANGE_RATIO	0.5	[0.49, 0.51]	True
VCAL_MED_SLOPE_SMALL_RANGE_RATIO	0.5	[0.49, 0.51]	True

(e) Summary

Figure C.8: V_{cal} calibration results for Q11 chip1.

C.5. Injection Capacitance

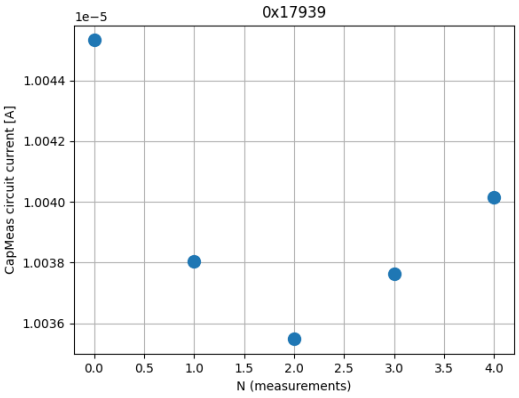

(a) Circuit current

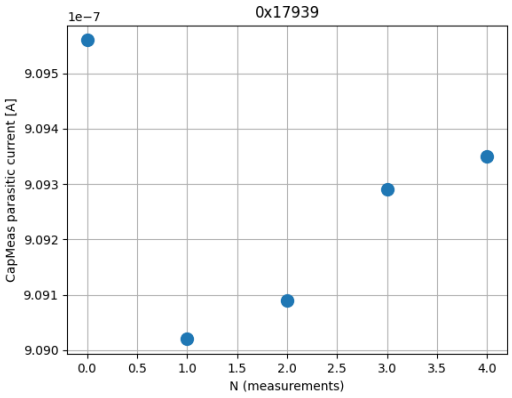

(b) Parasitic current

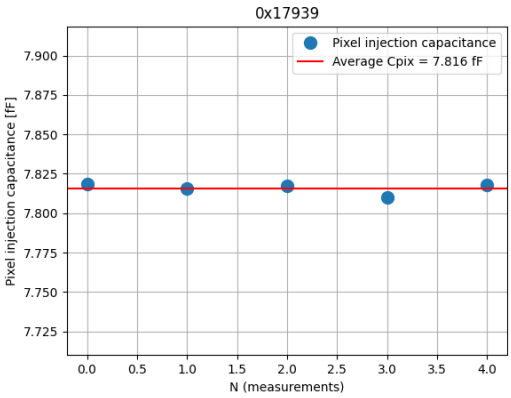

(c) Pixel injection capacitance

INJECTION_CAPACITANCE for 0x17939

Parameter	Analysis result	QC criteria	Pass
INJ_CAPACITANCE	7.82	[6.74, 9.0]	True

(d) Summary

Figure C.9: Injection Capacitance results for Q11 chip1.

C.6. Data Transmission

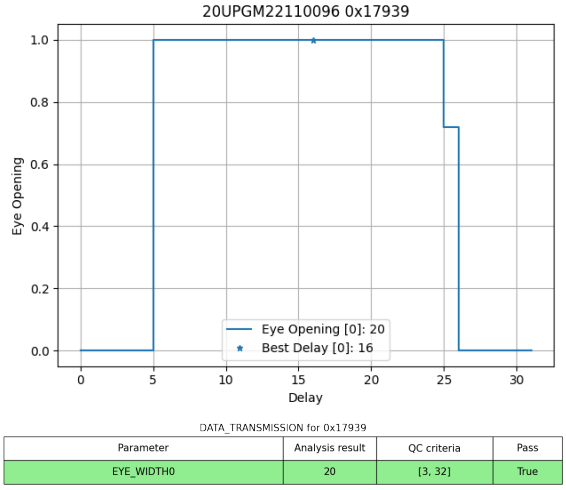

DATA_TRANSMISSION for 0x17939

Parameter	Analysis result	QC criteria	Pass
EYE_WIDTH0	20	[3, 32]	True

(a) Chip1

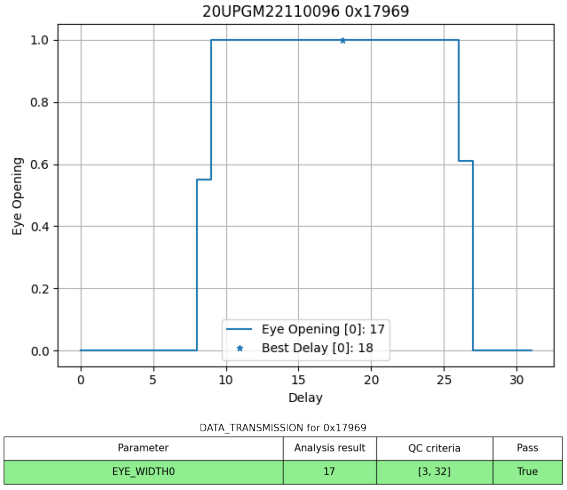

DATA_TRANSMISSION for 0x17969

Parameter	Analysis result	QC criteria	Pass
EYE_WIDTH0	17	[3, 32]	True

(b) Chip2

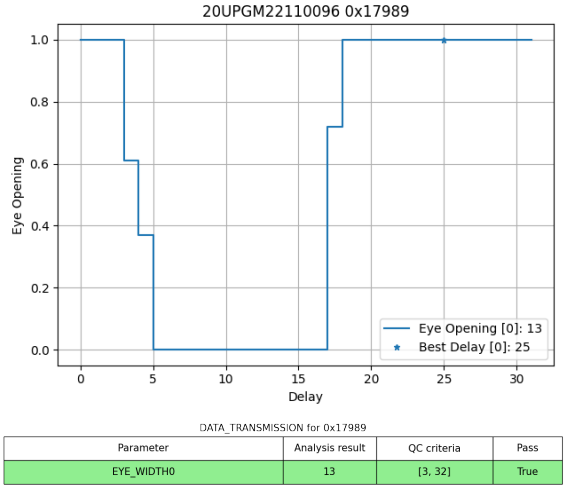

DATA_TRANSMISSION for 0x17989

Parameter	Analysis result	QC criteria	Pass
EYE_WIDTH0	13	[3, 32]	True

(c) Chip3

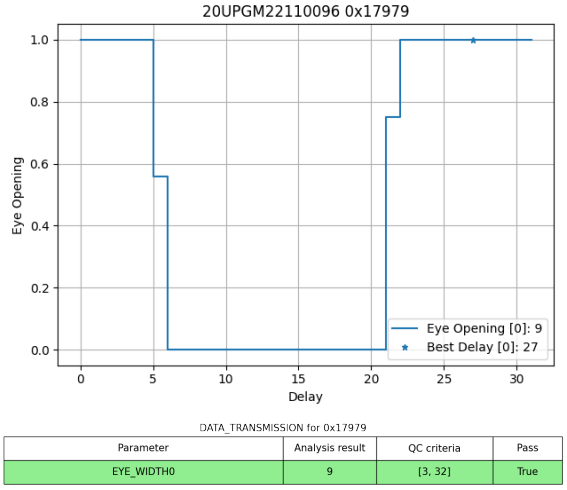

DATA_TRANSMISSION for 0x17979

Parameter	Analysis result	QC criteria	Pass
EYE_WIDTH0	9	[3, 32]	True

(d) Chip4

Figure C.10: Data Transmission results for Q11.

C.7. Minimum Health Test

It is worth mentioning that in these results, most pixels on chip2 failed tuning. This problem was resolved after updating the SWs to the latest version – chip2 still does not meet QC requirements due to the core column issue and remaining failed pixels, but the chip is no longer dominated by non-functional pixels. This shows the importance of keeping an updated version of DAQ and analysis SW, as well as using the same version across all testing sites.

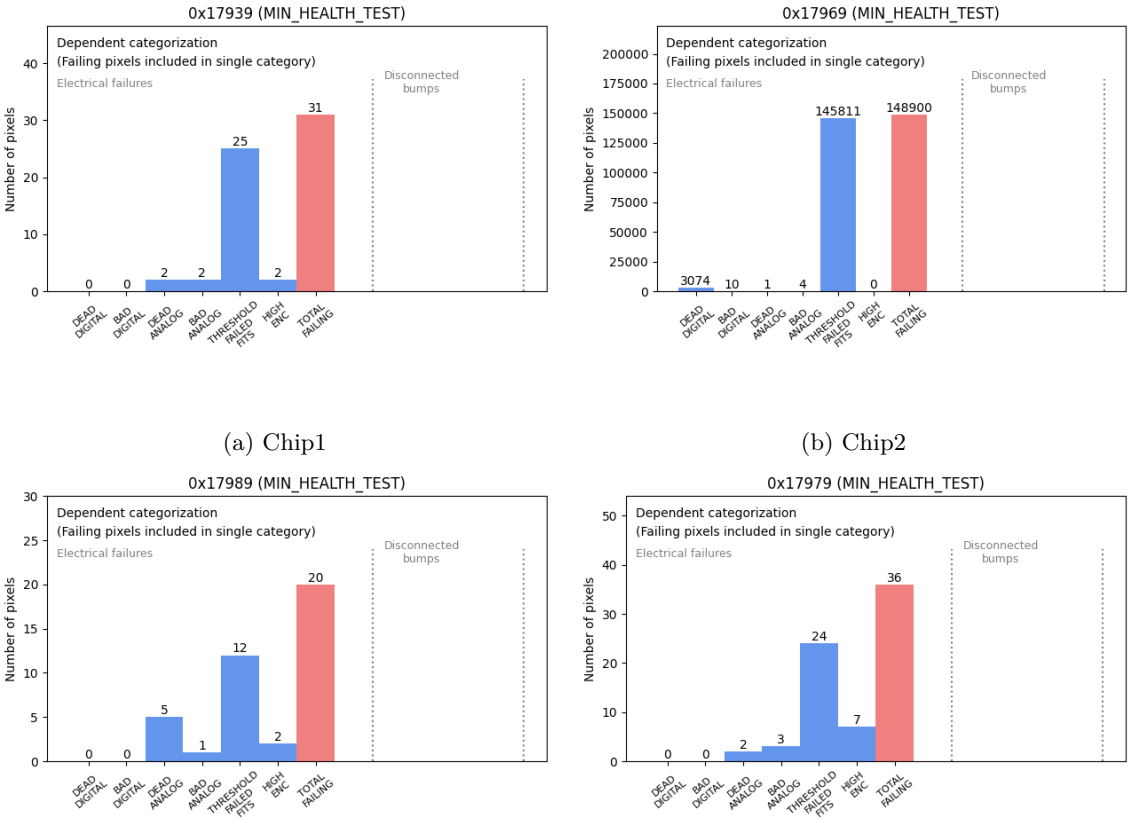

(a) Chip1

(b) Chip2

(c) Chip3

(d) Chip4

Figure C.11: Faulty pixels found in the Minimum Health Test of Q11.

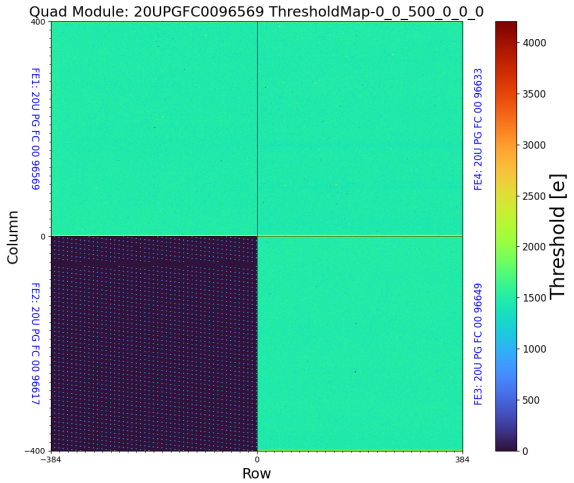

Figure C.12: Threshold map given by the threshold scan used in the Minimum Health Test of Q11 initial warm test, showing obvious readout error on chip2.

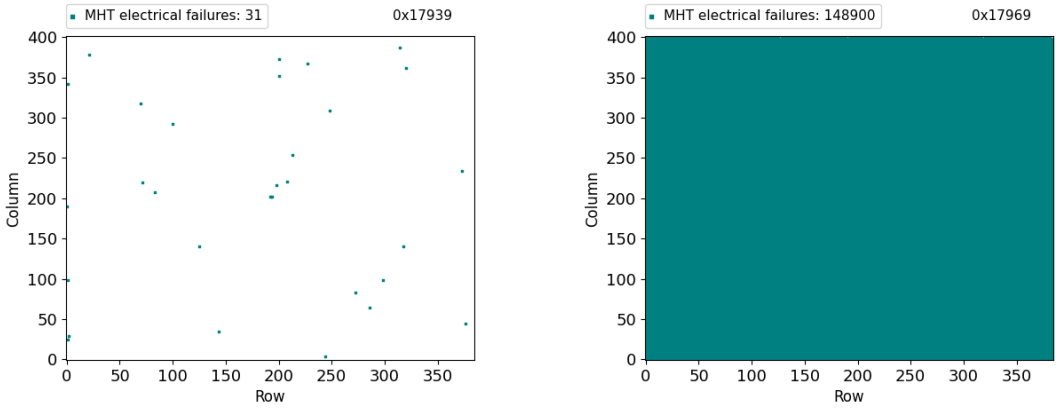

(a) Chip1

(b) Chip2

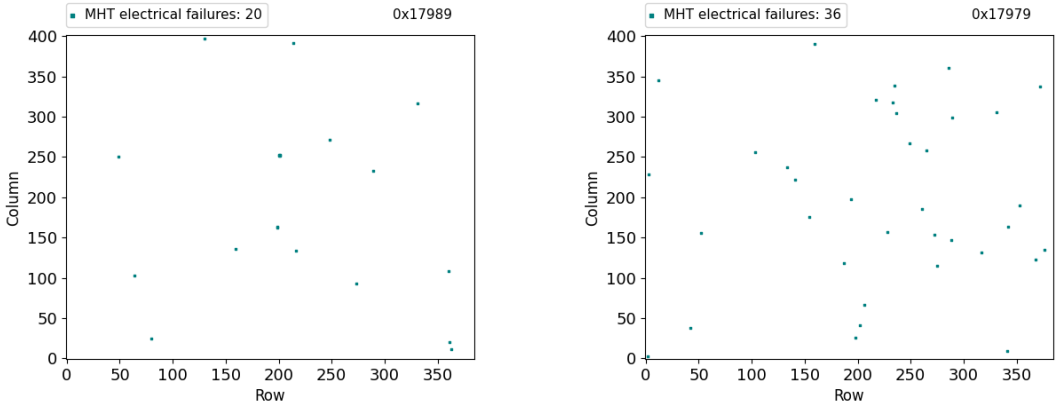

(c) Chip3

(d) Chip4

Figure C.13: Pixels with electrical failures in Minimum Health Test of Q11. Chip2 did not pass QC due to failed tuning. This problem disappeared after SW update.

MIN_HEALTH_TEST for 0x17939

Parameter	Analysis result	QC criteria	Pass
BAD_ANALOG_INTEGRATED	4	[0, 153.6]	True
THRESHOLD_FAILED_FITS_INDEPENDENT	29	[0, 1536]	True
HIGH_ENC_INDEPENDENT	2	[0, 1536]	True

(a) Chip1

MIN_HEALTH_TEST for 0x17969

Parameter	Analysis result	QC criteria	Pass
BAD_ANALOG_INTEGRATED	3089	[0, 153.6]	False
THRESHOLD_FAILED_FITS_INDEPENDENT	148900	[0, 1536]	False
HIGH_ENC_INDEPENDENT	0	[0, 1536]	True

(b) Chip2

MIN_HEALTH_TEST for 0x17989

Parameter	Analysis result	QC criteria	Pass
BAD_ANALOG_INTEGRATED	6	[0, 153.6]	True
THRESHOLD_FAILED_FITS_INDEPENDENT	18	[0, 1536]	True
HIGH_ENC_INDEPENDENT	2	[0, 1536]	True

(c) Chip3

MIN_HEALTH_TEST for 0x17979

Parameter	Analysis result	QC criteria	Pass
BAD_ANALOG_INTEGRATED	5	[0, 153.6]	True
THRESHOLD_FAILED_FITS_INDEPENDENT	29	[0, 1536]	True
HIGH_ENC_INDEPENDENT	7	[0, 1536]	True

(d) Chip4

Figure C.14: Analysis summary of Minimum Health Test for Q11.